core
Continuous Resolution and
Deracemization of Chiral
Compounds by Crystallization

Crystallization in Multicomponent Chiral Systems: Thermodynamic Characterization and Guidelines for Chiral Resolution of Racemic Compounds with Cocrystallization

Maxime D. Charpentier

Supervisors: Prof. Joop H. Ter Horst
Dr. Karen Johnston

University of Strathclyde
Glasgow

CMAC
FUTURE MANUFACTURING
RESEARCH HUB

Thesis submitted in satisfaction with the requirements of the
Strathclyde Institute of Pharmacy and Biomedical Sciences at the
University of Strathclyde for the Degree of Doctor of Philosophy.

March 2023

DECLARATION

This thesis is the result of the author’s original research. It has been composed by the author and has not been previously submitted for examination which has led to the award of a degree.

The copyright of this thesis belongs to the author under the terms of the United Kingdom Copyright Acts as qualified by University of Strathclyde Regulation 3.50. Due acknowledgement must always be made of the use of any material contained in, or derived from, this thesis.

Charpentier

Glasgow, 02.03.2023

Maxime Charpentier Place, Date

ACKNOWLEDGMENTS

First, I would like to thank my supervisors, Prof. Joop H. ter Horst and Dr. Karen Johnston, for their guidance throughout this PhD. Bringing this project to a successful conclusion was a challenging experience, with a pathway that was far from linear because of obstacles and unusual situations nobody could have predicted. Fortunately, my supervisors helped me to go through these trials, by providing support and encouragement.

Additionally, I would like to thank everyone that was part of the CORE Innovative Training Network project. It was a great chance to be part of this project, and I thank the European Union and the Marie Skłodowska-Curie Actions for funding my PhD and permitting my attendance to conferences and network events. Despite I joined the network late and only lived that experience for 1 year and a half, it was very enriching, and it led to the fruitful collaborations that are presented in this thesis. Therefore, I give a special thanks to all co-authors mentioned for bringing their expertise to improve my work.

I would also like to thank the EPSRC Centre for Innovative Manufacturing in Continuous Manufacturing and Crystallization (CMAC), for supporting my research and providing their facilities and equipment.

Finally, I thank all the friends I met during this project. They made this experience wonderful from a personal point of view. It made me grow as a person by learning about various cultures and interacting with interesting personalities, and I am grateful for that. I am glad I could have counted on their friendship, inspiration, and support.

LIST OF PUBLICATIONS

The work presented in the chapters of this thesis helped to produce six publications:

1. Comparing and Quantifying the Efficiency of Cocrystal Screening Methods for Praziquantel

Authors: **Maxime D. Charpentier**, Jan-Joris Devogelaer, Arnoud Tijink, Hugo Meekes, Paul Tinnemans, Elias Vlieg, René de Gelder, Karen Johnston, and Joop H. ter Horst
Crystal Growth & Design **2022** *22* (9), 5511–5525
DOI: 10.1021/acs.cgd.2c00615

2. Multicomponent Chiral Quantification with Ultraviolet Circular Dichroism Spectroscopy: Ternary and Quaternary Phase Diagrams of Levetiracetam

Authors: **Maxime D. Charpentier**, Raghunath Venkatramanan, Céline Rougeot, Tom Leyssens, Karen Johnston, and Joop H. ter Horst
Molecular Pharmaceutics **2023** *20* (1), 616-629
DOI: 10.1021/acs.molpharmaceut.2c00825

3. Enantioselective Cocrystallization and Enantiomer Recovery Guidelines from Phase Diagram Information

Authors: **Maxime D. Charpentier**, Russell Miller, Karen Johnston, and Joop H. ter Horst
In preparation

4. Simultaneous Chiral Resolution of Two Racemic Compounds by Preferential Cocrystallization

Authors: Fuli Zhou, Oleksii Shemchuk, **Maxime D. Charpentier**, Chloé Matheys, Laurent Collard, Joop H. ter Horst, and Tom Leyssens
Angewandte Chemie International Edition **2021** *60* (37), 20264-20268
DOI: 10.1002/anie.202107804

5. Cocrystals of Praziquantel: Discovery by Network-Based Link Prediction

Authors: Jan-Joris Devogelaer, **Maxime D. Charpentier**, Arnoud Tijink, Valérie Dupray, Gérard Coquerel, Karen Johnston, Hugo Meekes, Paul Tinnemans, Elias Vlieg, Joop H. ter Horst, and René de Gelder
Crystal Growth & Design **2021** *21* (6), 3428-3437
DOI: 10.1021/acs.cgd.1c00211

6. Co-crystals of non-steroidal anti-inflammatory drugs (NSAIDs): Insight toward formation, methods, and drug enhancement

Authors: André L.C.S. Nascimento, Richard P. Fernandes, **Maxime D. Charpentier**, Joop H. ter Horst, Flávio J. Caires, and Marlus Chorilli
Particuology **2021** *58*, 227-241
DOI:10.1016/j.partic.2021.03.015

ABSTRACT

Chiral molecules are asymmetrical objects, and from this geometric property emerge enantiomers, that are a pair of non-superimposable mirror-image compounds. More than 50% of marketed drugs are chiral, and enantiomeric separation is a major research area. Enantiomers possess the same physical properties, but they interact differently with chiral receptors in the human body, which induces a different biological response. While one enantiomer has a desired therapeutic effect, its opposite-enantiomer can be inactive or produce unwanted side effects. Moreover, an inactive opposite-enantiomer in a racemic drug can be considered as an impurity representing up to 50% of the formulation, which presents economic consequences. Consequently, the manufacture of chiral active pharmaceutical ingredients (API) is regulated to prefer enantiopure drugs. Because enantioselective synthesis is not always possible, robust separation methods are required to achieve enantiomeric purity from racemic mixtures. Crystallization-based resolution processes are preferred at industrial scale because of more interesting costs. When a racemic mixture crystallizes as a stable racemic compound, one resolution strategy relies on the cocrystal engineering with an additional coformer molecule to prompt new thermodynamic equilibria more favorable. The work outlined in this thesis focuses on the thermodynamic characterization and understanding of multicomponent chiral systems to apply chiral resolution strategies of racemic compounds with cocrystallization.

In Chapter 3, the detection of new cocrystals is discussed through the investigation of results obtained during a campaign aiming to find cocrystals to resolve the racemic compound of praziquantel. A total of 30 coformers are screened with four cocrystal screening methods, which are compared thoroughly by defining quantified parameters that help to review their strengths and weaknesses. The objective of this chapter is to conclude on screening methods' efficiencies and convenience, with the view to provide relevant advice on the optimization of cocrystal screening method selection.

Chapter 4 addresses the issue of chiral quantification in multicomponent systems and presents a novel chiral quantification method using ultraviolet circular dichroism spectroscopy and multivariate partial least square models. The method is used to understand the solid-liquid equilibria in the complex quaternary system of levetiracetam enantiomers with a chiral coformer in a solvent, through the accurate determination of the full quaternary phase diagram. The aim of this chapter is to propose a new approach for multicomponent chiral quantification in order to characterize complex systems and identify the conditions permitting a chiral separation process with crystallization.

By using the acquired quaternary phase diagram, an enantioselective cocrystallization process is designed in Chapter 5 to recover levetiracetam from its racemic compound through the isolation of its enantiospecific cocrystal. This process is combined with a solvent-mediated transformation step that permits the retrieval of pure levetiracetam from its cocrystal. The objective of Chapter 5 is to propose guidelines to build and optimize chiral resolution processes with chiral cocrystallization from the understanding of phase diagram information.

While cocrystallization provides a relevant collection of strategies for the chiral resolution of stable racemic compounds, several parameters must be considered to identify the best scenario permitting the resolution of a target compound. Therefore, in Chapter 6, the key points leading to

a quick and efficient identification of the optimal resolution strategy are discussed, such as the racemic compound stability, the coformer selection methods and its chirality, and the identification of the thermodynamic equilibria compatible with a resolution. The aim of this chapter is to propose relevant guidelines for chiral resolution strategy identification with cocrystallization.

The work in this thesis deepens the knowledge about chiral resolution of racemic compounds with cocrystallization by providing relevant new tools to this research area. New approaches are introduced to screen more efficiently for new cocrystals, to quantify complex multicomponent chiral systems, to design chiral resolution processes, and to identify the parameters for choosing the optimal resolution strategies. It is hoped that these methodologies will contribute to solve the challenges of enantiomers separation.

TABLE OF CONTENTS

Chapter 1 - Introduction

1.1. Chirality

Chirality is a property of an object to not be superimposable over its mirror image by translation or rotation because of its asymmetry.[1] In chemistry, many organic molecules exhibit this property through chiral centers, the most common ones being asymmetric carbons, but the constrained conformation of certain molecules can also generate chirality.[2] The two mirror images of a chiral molecule are called enantiomers. They are distinguished by their absolute configuration at their chiral center by the Cahn-Ingold-Prelog rule that assigns priorities to substituents attached to it. Enantiomers are named R or S depending on the order of priority, if it goes clockwise or anticlockwise (Figure 1.1).[3]

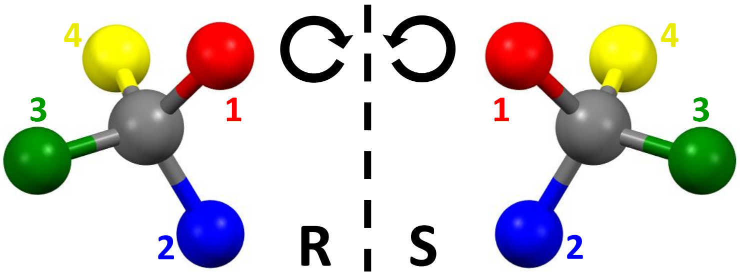

Figure 1.1: Mirror image representation of enantiomers, non-superimposable, with chiral carbon (grey) linked to four different substituents. Their priorities assigned by Cahn-Ingold-Prelog rule define their absolute configurations with the rotation priority order.

Other notations are used, such as one based on the deviation plane of polarized light by the enantiomer that can be dextrogyre (+) or levogyre (-), and one following Fischer projection priority rules that differentiates the enantiomers by the letter D or L. The samples containing only one enantiomer are said to be enantiopure, while equimolar mixtures of enantiomers are called racemates or racemic mixtures.[4] When the composition deviates from this ratio, the proportion between enantiomers is characterized by the “enantiomeric excess” value that can be computed by Equation 1.1, with R and S being mass or molar composition value in enantiomers.

$$ee(\%) = \left(\frac{|R-S|}{R+S}\right) \times\ 100 \qquad \text{Equation 1.1}$$

Because of the mirror symmetry between enantiomers, they exhibit the same physical properties such as melting points, solubility, crystal growth kinetics, or reactivity with achiral molecules.[5] However, their interaction with other chiral systems, such as the human body made of many chiral molecules (amino-acids, sugars…), is greatly different. In many cases, one enantiomer has a desired therapeutic effect with the body, while the other can have no effect, or even a harmful one.[6] This behavior difference in biological activities can lead to disasters, such as the infamous case of Thalidomide, a chiral drug given as a racemate in the 50s and 60s to pregnant women for the sedative effect associated to the R enantiomer, without knowing about the teratogenic effect of the S enantiomer.[7] The need for pure enantiomer is therefore an essential topic for chiral drugs in pharmaceutical industry, with the view to avoid any catastrophe related to the non-desired enantiomer, but also for economic reasons as the non-desired enantiomer can be considered as an impurity representing up to 50% of the formulation.[8] Consequently, the single enantiomers are strongly preferred to racemic mixtures for the marketing of a new drug, and chiral molecule separation has become a major research area in the pharmaceutical industry, with more than 50% of marketed drugs being chiral.[9-11] However, the access to pure enantiomers is challenging. In more than 50% of cases, they are obtained by stereoselective chemical reactions from asymmetric syntheses by using enantiopure precursors selected from the chiral pool (cheap available chiral molecules), chiral auxiliaries, or asymmetric catalysis,[12-16] but the cost of such techniques is expensive.[17] When non-stereoselective syntheses are used, racemic mixtures are obtained and must be separated with an additional chiral resolution technology. Often more economically favorable, these separation possibilities consist in chirally resolving the racemates by means of biocatalytic processes, chiral chromatography, or crystallization.[17-19] Crystallization is generally preferred at industrial scale as it is relatively inexpensive compared to chiral chromatography.[20, 21] Therefore, the discovery and the enhancement of chiral separation techniques by means of crystallization constitutes an active research area, and this thesis is incorporated within the framework of this issue.

1.2. Crystalline State of Organic Chiral Molecules

1.2.1. Molecular Crystals

Matter is constituted of atoms that can hold together by chemical bonds to form molecules, and the latter can arrange into four main physical states: liquid, solid, gas and plasma. In a solid, strong forces between particles pack them closely together so that they cannot move as freely as in the other states. When particles are arranged in a strict and periodic three-dimensional arrangement, they exhibit long-range order, and the material is defined as a crystal. It is the most stable state and the most ordered manner for the matter to pack. On the contrary, an amorphous material is considered thermodynamically as a liquid-like state with an infinite viscosity, as it is out of equilibrium and presents only a short-range order. According to the nature of bonds involved in the crystal packings, it is possible to classify crystals as ionic (e.g., sodium chloride), covalent (e.g., diamond), metallic (e.g., bismuth) and molecular (e.g., acetaminophen). The work from this thesis focuses on molecular crystals of organic compounds, and such crystals exhibit three main intermolecular interactions:

- Van der Waals forces that are electrostatic interactions between molecules forming permanent-permanent dipoles (Keesom forces), permanent dipole-induced dipole (Debye forces) or induced dipole-induced dipole (London forces). They are isotropic, weak (0.5 to 40 $kJ.mol^{-1}$), and depend on the distance between molecules[22-25]
- Hydrogen bonds that occur between a H atom from a strongly polar function X-H (the donor) and an atom Y of a different molecule (the acceptor). X and Y must be very electronegative atoms such as N, O, F and Cl. This attractive interaction is highly directional and comprises energy values going from 1 to 150 $kJ.mol^{-1}$ [26, 27]
- π-π stackings that happen between polarized aromatic rings with interaction patterns (parallel, perpendicular, or parallel displaced) connecting one ring region more enriched in electrons with another more depleted in electrons. Their energies, despite being difficult to characterize, are considered to be lower to 12 $kJ.mol^{-1}$ [28]

Because the energy of hydrogen bonds is much greater than others, it makes them decisive in the crystal structure. However, they are weaker than the other intermolecular interactions from other crystal types (ionic, covalent, metallic), and consequently the properties of molecular crystals differ. For instance, they usually present lower melting points, which permits the access to liquid states through moderate conditions, and therefore the study of solid-liquid equilibria.

1.2.2. Crystallography Fundamentals

The crystal packing also influences the physical properties, and the three-dimensional arrangement of molecules in the crystal can be described with crystallography. The entire crystal is considered as a mathematical object that is constructed with defined symmetry operations. The structural information are all contained in the unit-cell, which is the lowest possible volume with the highest degree of symmetry in the crystal, and it represents the building block of the crystal with translation operations.[29] Its geometry is a parallelepipedon with lattice points on its apexes, and whose parameters are defined as a, b and c, the lengths of the three independent translation vectors and α, β and γ, the angles between the edges (Figure 1.2).

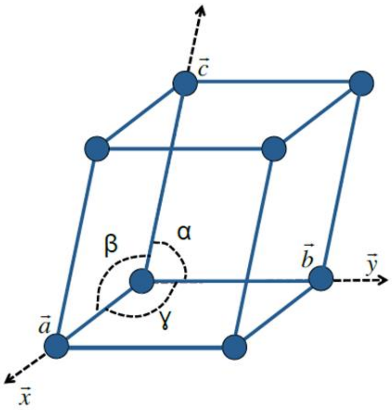

Figure 1.2: Representation of the unit-cell and its lattice parameters a, b, c, α, β and γ.[30]

A crystallographic point group is a group of symmetry operations that keep the unit-cell unmodified when they are applied.[31] 32 crystallographic point groups are defined and are the only possible combinations of the three unit-cell independent translations with ten macroscopic symmetries of rotation and inversion.[32, 33] The point groups are divided into seven crystalline systems according to common symmetry characteristics of unit-cells.[32] Nevertheless, the crystalline systems are not enough to describe all possible unit-cells as a unit-cell can contain one, two or four lattice points.[34] Four lattice modes were defined by Bravais:[35]

- Primitive mode P: one lattice point per unit-cell, with lattice point eighths in each apex
- Base-centered mode A, B or C: two lattice points per unit-cell, with two lattice point halves in the middle of faces $(\vec{b},\vec{c})$, $(\vec{a},\vec{c})$, or $(\vec{a},\vec{b})$
- Body-centered mode I: two lattice points per unit-cell, with one lattice point in the center
- Face-centered mode F: four lattice points per unit-cell, with six lattice point halves in the middle of each face

The combination of the four modes and the seven crystalline systems leads to the 14 Bravais Lattices.[34, 35] Nevertheless, additional symmetries, such as helical screw axes and glide planes, exist to describe a crystal, because the pattern can repeat in the unit-cell. Consequently, the point groups, the crystalline systems, the lattice modes, and all possible combinations of symmetry operations, lead to 230 Space Groups that are 230 different unique ways to pack the matter.[34]

A single-crystal is the macroscopic result of unit-cell translations, and it obeys to the same symmetry rules defined by its Space Group, as symmetries are preserved through the periodicity of the crystal packing.[36] The Space Group of a single-crystal can be resolved with X-ray diffraction (SC-XRD) to describe fully the packing. A set of different single-crystals of small size is defined as a crystalline powder, and it also presents symmetry elements, but because of their random orientation some structural information is lost, and it does not permit generally the Space Group resolution. However, X-ray diffraction on powders (PXRD) generates unique resulting patterns that are characteristic of the studied crystals.

1.2.3. Polymorphism of Organic Molecules

Polymorphism is the ability of a chemical substance to crystallize into different crystalline structures.[37] Polymorphs have thus the same chemical structural formula, but different crystal lattices. Therefore, their physicochemical properties, such as melting point or solubilities, are also different.[38] Polymorphism concerns at least 50% of organic compounds and is largely recognized as an essential issue for research and industry.[39-41] In the pharmaceutical industry, requirements exist to characterize polymorphism, since two polymorphs of a drug have different pharmacological properties. Additionally, risks exist that new polymorphs appear throughout a production process modification. The patent registration of known polymorphs also help the companies to protect their research and investments against industrial competition. Consequently, the FDA (Food and Drug Administration) and EMEA (European Medical Evaluation Agency) require the knowledge of polymorph properties before delivering a marketing authorization for an Active Pharmaceutical Ingredient (API). Packing polymorphism is the difference of crystal packings (Figure 1.3), but organic molecular crystals can also exhibit conformational polymorphism.[42, 43]

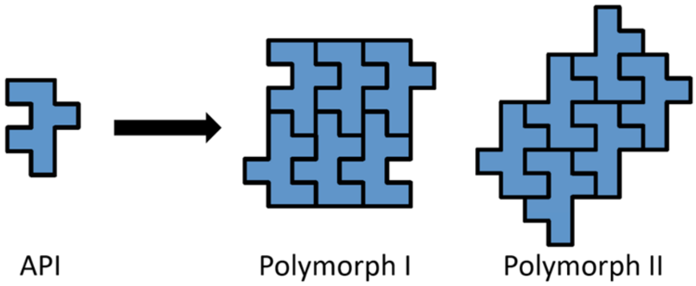

Figure 1.3: Representation of packing polymorphism for an Active Pharmaceutical Ingredient (API).

Each polymorph has its own stability conditions under defined state variables (temperature, pressure), which means that for fixed conditions, thermodynamics imposes that only one polymorph is stable, while the others are metastable.[44] Thermodynamically, the stable form is the one having the lowest Gibbs free energy G. Two types of stability relationship between polymorphs exist, as they can either be enantiotropically or monotropically related.[45] In a thermodynamic system, at constant pressure P, if one polymorph is thermodynamically stable until the melting point, then the other crystalline forms are metastable, and they are said to be in a monotropic relationship with the stable polymorph. This situation is described in Figure 1.4a through the evolution of the Gibbs free energy G with temperature T. At any T below the stable fusion $T_{f,I}$, the G curve of polymorph I is lower than G curve of polymorph II. The theoretical thermodynamic transition T_t between both polymorphs is therefore above the stable melting point $T_{f,I}$. Figure 1.4b illustrates the enantiotropic relationship, where T_t is below the stable melting point $T_{f,II}$, which gives rise to a reversible solid-solid transition between the polymorph I stable at low T, and the polymorph II stable at high T. The stability relationship between polymorphs can be determined experimentally with thermal analyses (DSC, TGA), structural characterization (X-Ray Diffraction, FTIR and Raman spectroscopy), temperature-controlled cross-seeding experiments, solubility measurements, or hot-stage microscopy. Burger and Ramberger also stated rules based on experimental interpretations, to help to determine if two polymorphs are enantiotropically or monotropically related.[45]

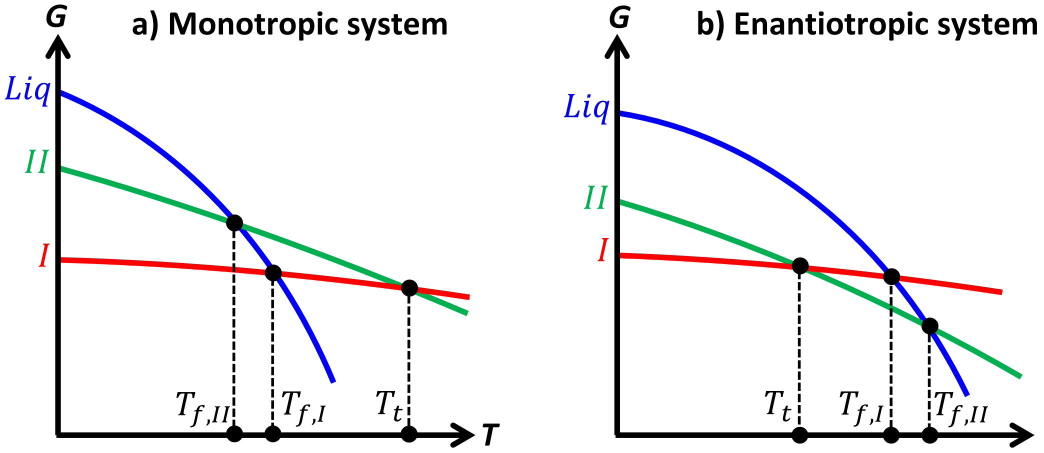

Figure 1.4: Isobaric diagrams of the Gibbs free energy G of two polymorphs (I and II) and the liquid phase (Liq) as a function of the temperature T in **a)** a monotropic system and **b)** an enantiotropic system. The stable phase is the one with the lowest G. T_t is the polymorphic transition temperature, $T_{f,I}$ the melting temperature of form I, and $T_{f,II}$ the melting temperature of form II.

1.2.4. Chirality in Crystal Structures

With regards to chiral molecules, three main solid equilibria can occur for the crystallization of a racemic mixture and are illustrated in Figure 1.5.[5] In 90 to 95 % of cases, the enantiomers arrange as a racemic compound, that is a new crystalline phase in which enantiomers coexist with an equimolar ratio in the same unit-cell. Such defined compound possesses its own crystal structure and physical properties. In 5 to 10 % of cases, a conglomerate equilibrium exists, where the two enantiomers crystallize separately as a physical mixture of their enantiopure crystals. Finally, in less than 1 % of cases, enantiomers coexist as a complete solid solution in the same isomorphous crystal structure and are randomly positioned on the crystallographic sites where they can substitute each other. However, this uncommon case is not considered in the present thesis. Derivatives of these equilibria also exist, for instance when enantiopure solids or racemic compounds exhibit polymorphism, or the possibility of partial solid solutions.[46] Such rare cases are also not considered in the present work.

Pure enantiomers, and therefore conglomerates, can only crystallize in non-centrosymmetric space groups. Among the 230 space groups, only 65 are chiral and compatible with the crystallization of one single enantiomer.[47] Both enantiomers can crystallize either in the same chiral space group, such as $P2_12_12_1$ or $P2_1$, or in space groups that are enantiomorphic, as $P3_1$ and $P3_2$. Consequently, the crystal structures are mirror images, with identical crystal packings but of opposite symmetry. That is why properties related to crystal packing such as solubility, density, or melting point, are equivalent for both enantiomers, while the ones related to the symmetry, as optical properties, are opposite. 95 % of all pure enantiomers crystallize in only four chiral space groups that are $P2_12_12_1$, $P2_1$, $C2$ and $P1$.[48] On the contrary, racemic compounds can crystallize in any space group, but they have a huge prevalence for centrosymmetric ones (more than 95% of cases reported). The most common space groups are $P2_1/c$, $C2/c$, $Pbca$ and $P\overline{1}$, and all four cases represent more than 95% of racemic compounds in centrosymmetric space groups.[49]

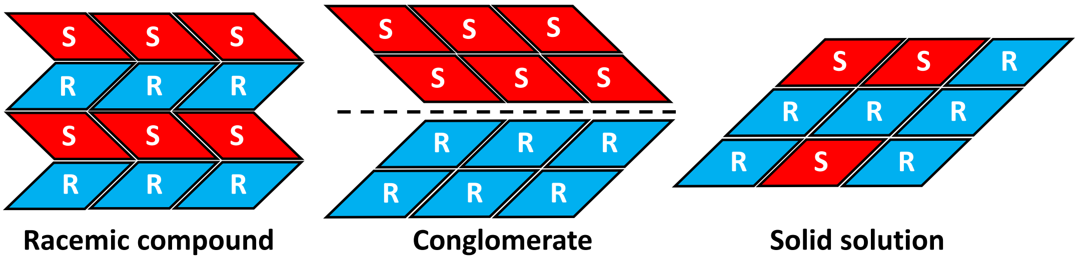

Figure 1.5: Schematic of most common solid equilibria for a racemic mixture of enantiomers: Racemic compound (left), conglomerate (middle), and complete solid solution (right).

The problematic of chiral separation directly originates from the solid equilibria possibilities, as neither the racemic compound nor the solid solution permit the enantiomeric resolution. The thermodynamic systems that present chirally pure structures, such as conglomerates, are therefore the key to design chiral resolution processes. However, when a given chiral molecule crystallizes as a stable racemic compound or solid solution, different crystallization equilibria must be found to allow the chiral resolution. For example, the chemical modification of the achiral part of the molecule can prompt new chances to obtain a conglomerate system, though it requires many steps. Another strategy relies on the engineering of multicomponent crystals with an additional molecule, to form salts, solvates or cocrystals.[50, 51]

1.3. Multicomponent Crystals

1.3.1. Classification and Properties

When two or more different components crystallize as part of the same crystal structure rather than separately, they form a multicomponent crystal.[52, 53] This definition applies to molecules that differ chemically, or from molecular structure, but not from opposite chirality. In 2016, Grothe et al. proposed a classification of multicomponent crystals based on strict definitions. They distinguish three possible types of components:[53]

- Solvent: a neutral component that is liquid at ambient conditions
- Coformer: a neutral component that is solid at ambient conditions
- Ion: a component with a nonzero formal charge

Three main classes of multicomponent crystals can then be deduced based on the association of these components:[53]

- Solvate: any crystal with a solvent molecule plus either a coformer, or at least two ions
- Cocrystal: a crystal with a coformer plus either another coformer, or at least two ions
- Salt: a crystal containing at least two ions

As multicomponent crystals can contain more than only two components, seven subclasses are defined from the overlapping of the previous classes definition to describe accurately all possible combinations of components (Figure 1.6).[53]

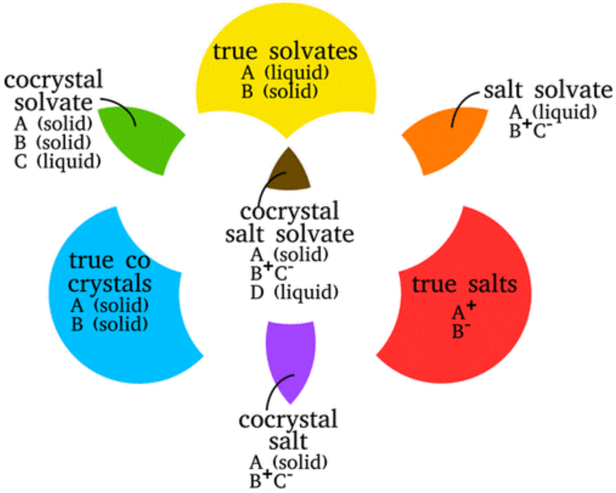

Figure 1.6: Classification scheme of multicomponent crystals from Grothe et al. (2016).[53]

The multicomponent crystals are of strong interest to the pharmaceutical industry as they permit the enhancement of drug physicochemical properties, such as solubility, bioavailability, mechanical/humidity/thermal stability, and compressibility,[54-60] without modifying their medical action, and can also be used as a separation technology.[61] Salt formation is the most common approach for properties improvement, with more than 50 % of the marketed drugs being administered as salts.[62] However, a major limitation of salts is the requirement of the target molecule to possess ionizable functions to create ionic interactions, which can be a restricting factor for the development of universal strategies, such as here in the present work for chiral separation routes. On the contrary, cocrystallization and solvate formation are always possible for organic molecules because these mechanisms involve intermolecular interactions like hydrogen bonds.[63, 64] Such interactions are made possible by common chemical functions that are good acceptors or donors, as carboxylic acids, amides, amines, alcohols, thiols, ketones or aldehydes. However, it also exists cocrystals and solvates based on other intermolecular interactions such as π-π stacking, or van der Waals interactions.[65-67] Cocrystals are generally preferred as they are more stable than solvates with temperature and have a larger accessible pool of compounds "Generally Recognized As Safe" (GRAS compounds) for coformers than solvents.[68] Although, pure target molecules can be more easily separated from a solvate than from a cocrystal.[69] In the recent years, cocrystals have become an increasingly popular topic of interest because of their easy access, their universality, and the vast scope of possibilities they offer to modify the solid state and the properties of a target molecule. This also applies to chiral separation possibilities by multicomponent crystal engineering, and that is why cocrystals constitute the main topic of the work presented in this thesis.

1.3.2. Cocrystal Screening and Characterization

The detection of new cocrystals is key to the enhancement of solid-state properties and the emergence of chiral resolution routes. Various preparation methods exist to screen for cocrystals, and they involve solid-state transformations that can be induced by energy sources that are mechanical (grinding,[70] cryomilling, and high-shear granulation), thermal (thermal treatment, crystallization from the melt, and hot-melt extrusion), or based on sound/ultrasound, microwaves, or electrical current.[71, 72] Cocrystallization can also be mediated by the presence of solvents, such as stirring slurries to induce a phase transition, cooling/evaporating/adding an antisolvent to solutions, or using supercritical fluids, spray-drying, and freeze-drying technologies.[72, 73] All these methods present advantages and disadvantages, with alternative paths to cocrystal synthesis and experimental limitations that vary with the nature of the coformers. Some techniques can also be non-applicable to certain coformers that can for instance present thermal or mechanical degradation, reactions with a component/solvent, or formation of amorphous material or unwanted phases. No cocrystallization technique has proven to be universal, but the choice of methods used for detection of cocrystal formation can be optimized. Consequently, the optimization of cocrystal screening through the identification and the selection of the most efficient methods is an important research topic. The identification and characterization of a new cocrystal is feasible by the measurement of its new properties, compared to the ones of the target molecule and the coformer. Therefore, thermal, structural, spectroscopy, and quantification techniques are investigated for cocrystal screening and characterization optimization.

1.4. Phase Diagrams of Chiral Systems

Phase diagrams are thermodynamic tools that represent the different compositional domains for the equilibrium states of a thermodynamic system. They thus permit to describe the equilibrium state of the different phases as a function of experimental conditions, such as temperature and component compositions. Moreover, they are key to design robust and reliable crystallization processes,[4, 74] especially for chiral molecule separations.[75, 76] Because phase diagrams are often encountered throughout this thesis, and their complexity increase in multicomponent chiral systems, a theoretical background must be provided for a better understanding.

1.4.1. Heterogenous Equilibria and the Phase Rule

A thermodynamic system is considered heterogeneous when it involves 2 or more phases, for instance a suspension of a crystalline phase in a solution phase. A phase is defined as a part of the system whose chemical composition and physical properties are homogeneous, being identical, on a thermodynamic length scale, in all points. Any component or a mixture of components can be found in a phase at the thermodynamic equilibrium. A system is considered at equilibrium when all its intensive properties, such as temperature, pressure, and component chemical potentials, do not evolve anymore as a function of time at given experimental conditions. Any modification enforced from outside the system, of an intensive property would therefore induce an evolution of the system towards a new equilibrium.[44] A heterogeneous system is in stable equilibrium if its total Gibbs free energy G is minimal, and a phase k in this system is stable if its Gibbs free energy G_k represents the minimum that the system can achieve. Any system that is not in equilibrium has the thermodynamic drive to move towards its equilibrium state at lower total Gibbs free energy G, releasing energy on its irreversible transformation towards equilibrium. While thermodynamics describes the distance of a system from equilibrium, it does not give information on the route and speed towards equilibrium, that is described by kinetics. The metastability state corresponds to a local minimum in Gibbs free energy $G_{local} > G,$ for which the slow kinetics allow its existence for an interim period. Given enough time, the system would then evolve to a more stable state. The Gibbs phase rule (Equation 1.2) defines the number of degrees of freedom, v, that are the number of independent intensive parameters required to define an equilibrium state, and is expressed as

$$v = C + N - \varphi \qquad \text{Equation 1.2}$$

where C is the number of independent components, N is the number of intensive parameters that the system depends on, and φ is the number of phases in equilibrium.[44] Because we are interested in chiral separation processes with crystallization, we consider only systems with $C > 1$ in the present thesis, and the phase diagrams are said to be solid-liquid as they only depict solid-liquid equilibria.

1.4.2. Chiral Binary Solid-Liquid Phase Diagrams

Thermodynamic systems containing two independent components ($C = 2$), such as two enantiomers, are defined as binary. In addition to pressure P and temperature T intensive variables, these phase diagrams are characterized by a composition variable X, expressed in mole fraction or mass fraction, that defines the relative composition between the two components. Binary systems are usually studied at constant pressure P, which leaves temperature T as the only intensive parameter that influences equilibria for a binary composition ($N = 1$). Therefore, the Gibbs phase rule (Equation 1.2), states the number of degrees of freedom v of such binary systems as: $v = 3 - \varphi$, that leads to three possible equilibria that are summarized in Table 1.1.

Table 1.1: Representation of phase equilibria in isobaric binary phase diagrams.

Equilibria	v	Representation in binary phase diagram plot
Monophasic (φ = 1)	**2**	Free surface
Biphasic (φ = 2)	**1**	Tie-line joining 2 fixed phase compositions
Triphasic (φ = 3)	**0**	Invariant point

Isobaric binary phase diagrams are represented with composition X on the x axis and temperature T on the y axis (see Figure 1.7). The liquidus (red line) represents the curve of complete melt of the system, which also includes the pure solid melting points (red points). Above this curve, all compositions are in a liquid phase (liq), that is consequently a monophasic domain ($\varphi = 1 ; v = 2$) represented as a free surface, meaning that the phase composition is the same as the overall composition. The solidus (blue line) represents the curve of the beginning of melting. Below the solidus, a composition is completely solid, and for binary compositions, it generates solid-solid biphasic domains between the stable crystals of the system ($\varphi = 2 ; v = 1$). Between the solidus and the liquidus, liquid and solid phases coexist to give rise to solid-liquid biphasic domains. At a given temperature, any overall composition point from a biphasic domain, splits between the two equilibrated phases along a tie-line, that gives the composition of each phase. An example is illustrated in Figure 1.7a, for a point o of overall composition X_o, that equilibrates a solid s, whose composition X_s is pure R crystals, and a saturated liquid l of composition X_l. The lever rule is a proportionality rule that links the fraction of two phases in equilibrium in a biphasic domain with the segment lengths ratio between the phase composition points of a tie-line.[44] For instance, in the latter example, the fraction of liquid f_l is given by Equation 1.3, and the fraction of solid f_s by Equation 1.4.

$$f_l = \frac{\overline{so}}{\overline{sl}} = \frac{|X_s - X_o|}{|X_s - X_l|} \qquad \text{Equation 1.3}$$

$$f_s = \frac{\overline{ol}}{\overline{sl}} = \frac{|X_o - X_l|}{|X_s - X_l|} \qquad \text{Equation 1.4}$$

In all cases of Figure 1.7, the solidus is a eutectic invariant. A binary eutectic invariant is a mixture of two components that can melt and solidify at a constant temperature that is lower to the melting temperature of pure components. The intersection point between the solidus and the liquidus is the eutectic composition point (green triangle). This point is called an invariant point because it equilibrates 3 phases, and therefore $v = 0$, meaning all parameters are fixed for such equilibrium. It can only happen at the fixed eutectic temperature T_{eut} and the 3 phase compositions are fixed by the solidus tie-line, on which the lever rule can be applied.

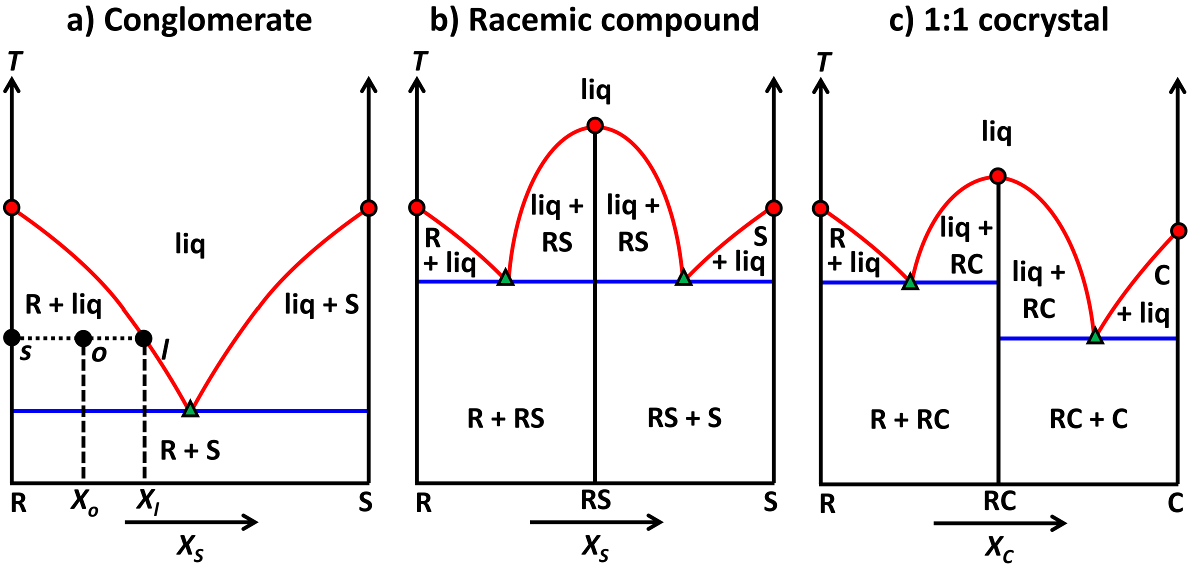

Figure 1.7: Binary phase diagrams for **a)** a conglomerate equilibrium, **b)** a racemic compound equilibrium, and **c)** a cocrystal forming system. The liquidus (red), solidus (blue), and eutectic points (green triangles) are represented. The tie-line (dotted line) shows the phase split in a biphasic domain.

Figure 1.7a represents the conglomerate equilibrium between enantiomers R and S. Because of the identical physical properties between enantiomers, it exhibits symmetry along the racemic composition. Consequently, the enantiomer melting points are identical, and the eutectic composition is the racemic composition. In the case of a racemic compound equilibrium (Figure 1.7b), the phase diagram presents an intermediate binary solid RS, that is represented by a vertical line at the corresponding stoichiometry. Such binary solid has its own crystal structure and melting point, which leads to two eutectic invariants, that are here symmetrical because of the chirality. When the system is not chiral, as a system forming a 1:1 stoichiometry cocrystal RC between an enantiomer R and a coformer C (Figure 1.7c), the eutectic compositions are no longer symmetrical, and the eutectic temperatures are not identical. One can note that on heating, both binary solids RS and RC melt in a liquid composition that is the same as the solid composition. Such melting behavior is said congruent, in opposition to non-congruent melting that can occur for other binary invariants. Though, only the eutectic equilibrium is of interest in the present study.

1.4.3. Chiral Ternary Solid-Liquid Phase Diagrams

Ternary phase diagrams depict the equilibria between three independent components ($C = 3$), such as two enantiomers in a solvent. In addition to pressure P and temperature T intensive variables, these systems are also characterized by three component composition X variables. Only two of them are independent and necessary to set an overall composition, while the third is fixed by knowing the others. For a constant pressure P, a ternary phase diagram between components A, B, and C, can be represented as the prolongation of their binary phase diagrams in a ternary composition/temperature three-dimensional space as shown in Figure 1.8. Because of the additional component, liquidus (red) and solidus (blue) lines become surfaces inside the ternary space, and biphasic domains become three-dimensional with an additional degree of freedom

($v = 2$). Similarly, eutectic lines (dashed lines) correspond to the prolongation inside the space of the binary eutectic points (green triangles) and describe a triphasic equilibrium boundary between the two neighboring solids and the saturated liquid ($v = 1$). An exact number of three binary eutectic lines converge into a ternary eutectic invariant point (green square), at which a unique saturated liquid composition is in equilibrium with three solids of the system ($v = 0$).

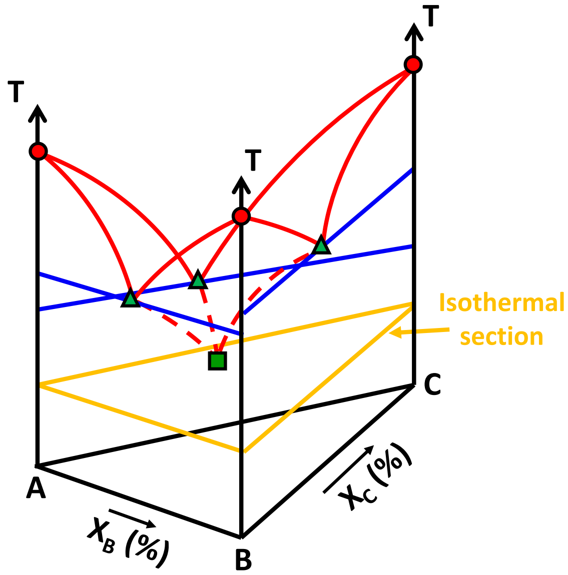

Figure 1.8: 3D representation of an isobaric ternary phase diagram, as a function of two composition variables and temperature. The liquidus (red), solidus (blue), and binary eutectic points (green triangles) are represented. The eutectic lines (dashed lines) originate from the binary eutectic points (green triangles) and converge into a ternary eutectic point (green square).

Because of the complexity in visualization of temperature dependent ternary systems, they are usually represented as isobaric and isothermal section ($N = 0$) in a bidimensional space (Figure 1.8, yellow) depending only on the two compositions X variables. The Gibbs phase rule (Equation 1.2) states the number of degrees of freedom v of such isothermal ternary section as: $v = 3 - \varphi$, which leads to three possible equilibria that are summarized in Table 1.2.

Table 1.2: Representation of phase equilibria in isobaric and isothermal ternary phase diagrams.

Equilibria	v	Representation in isothermal isobaric ternary plot
Monophasic (φ = 1)	**2**	Free surface
Biphasic (φ = 2)	**1**	Tie-line joining 2 fixed phase composition
Triphasic (φ = 3)	**0**	Tie-triangle joining 3 fixed phase compositions

An isothermal section is represented as a Gibbs composition triangle, an equilateral triangle whose apexes correspond to a pure component, and the sides to the binary section at the fixed temperature T. Any ternary composition in the triangle plot can be read with proportionality rules between the ratio of the side segments, with the segments formed from the lines parallel to the sides going through the composition point, as illustrated in Figure 1.9 (left). In the present study, the third component is often a solvent and ternary sections give solubility information, as in Figure 1.9 (right). The pure solid solubilities X_A^T and X_B^T, of A and B (red points) in solvent C at temperature T, are prolongated inside the ternary space as solubility lines (red lines). Two solubility lines converge into a eutectic composition point E (green triangle), that is a solution doubly saturated in both components A and B. Above the solubility lines, all compositions are in a liquid phase (liq), that is consequently a monophasic domain ($\varphi = 1 ; v = 2$) represented as a free surface. Below the solubility lines, the stable solids crystallize. Between one solubility line and one solid point, are defined the solid-liquid biphasic domains ($\varphi = 2 ; v = 1$), in which the equilibrium is set along a tie-line that permits to compute the phase proportions through the lever rule with the segment lengths ratio between the defined phase composition points. For instance, in Figure 1.9 (right), the suspension of overall composition o_1 equilibrates pure B solid, with a saturated liquid of composition l. The fraction of liquid f_l is given by Equation 1.5, and the fraction of solid B f_B by Equation 1.6.

$$f_l = \frac{\overline{Bo_1}}{\overline{Bl}} \qquad \text{Equation 1.5}$$

$$f_B = \frac{\overline{lo_1}}{\overline{Bl}} \qquad \text{Equation 1.6}$$

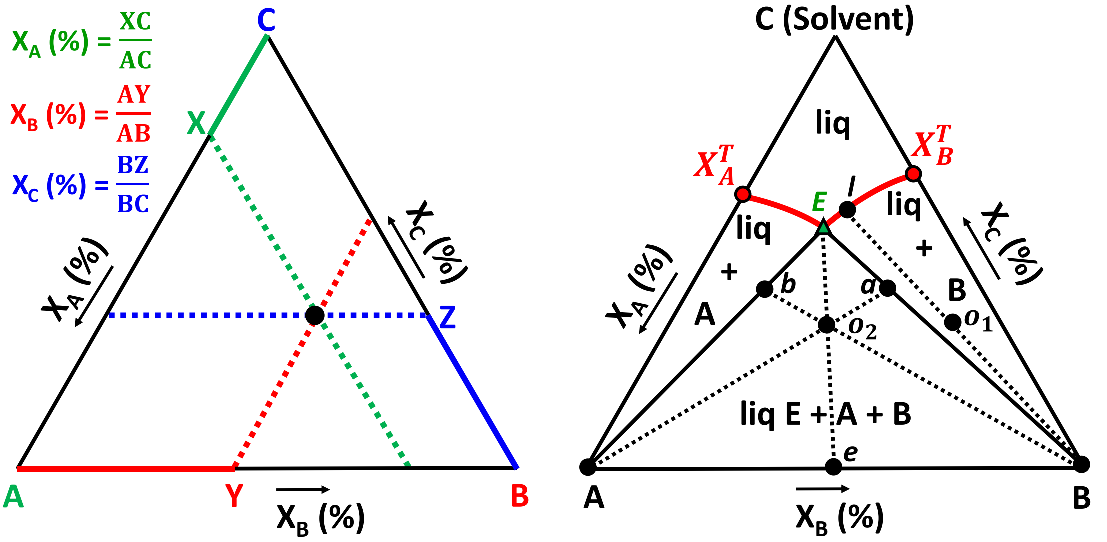

Figure 1.9: Composition determination in Gibbs composition triangle representation for ternary phase diagrams (left). Isothermal and isobaric ternary phase diagram in the case of two solids A and B with a solvent C (right), with solubility lines (red lines) and eutectic composition E (green triangle). The tie-lines (dotted lines) show the phase split in biphasic and triphasic domain.

Between the eutectic composition E and two solid points, is defined a solid-liquid triphasic domain ($\varphi = 3 ; v = 0$), that equilibrates the separated crystals of pure A and pure B in suspension in an invariant doubly saturated liquid of composition E. In this domain, all phase compositions are fixed, and the phase fraction of an overall composition can be computed by the barycenter rule applied in the tie-triangle with the segment lengths ratio between the defined points. For instance, in Figure 1.9 (right), the suspension of overall composition o_2 equilibrates a fraction of solid A f_A given by Equation 1.7, a fraction of solid B f_B given by Equation 1.8, and a fraction of liquid E f_E is given by Equation 1.9.

$$f_A = \frac{\overline{ao_2}}{\overline{aA}} \qquad \text{Equation 1.7}$$

$$f_B = \frac{\overline{bo_2}}{\overline{bB}} \qquad \text{Equation 1.8}$$

$$f_E = \frac{\overline{eo_2}}{\overline{eE}} \qquad \text{Equation 1.9}$$

When a binary solid is stable in the system, as in Figure 1.10, it possesses its own solubility line and biphasic stability domain. The additional stable solid generates two triphasic stability domains with eutectic invariant compositions E_1 and E_2. Because of the chiral symmetry, a racemic compound RS system (Figure 1.10, left) exhibits symmetry along the racemic composition. Therefore, the enantiomer solubility points are identical, and the eutectic compositions are symmetrical. When the system is not chiral, such as a 1:1 stoichiometry cocrystal RC between an enantiomer R and a coformer C (right), there is an asymmetry in the solubilities and the eutectic compositions. The position of the eutectic points is function of the cocrystal stability relative to the pure component stability, but also of the pure component solubility difference.[77] Consequently, these parameters are strongly influenced by the solvent, the temperature, and the component thermodynamic properties.[78-80] Based on the asymmetry degree between solubilities, two cases can be distinguished. The first case correspond to a congruent solubility of the binary solid when both component solubilities are of same order of magnitude. Upon solvent addition on the solid (blue dotted line), the solid nature stays unchanged until its dissolution, as in Figure 1.10 (left). On the contrary, a high asymmetry in the pure component solubilities can lead to incongruent solubility of the binary solid, which translates to a progressive modification of the solid nature upon solvent addition before the dissolution, as in Figure 1.10 (right).

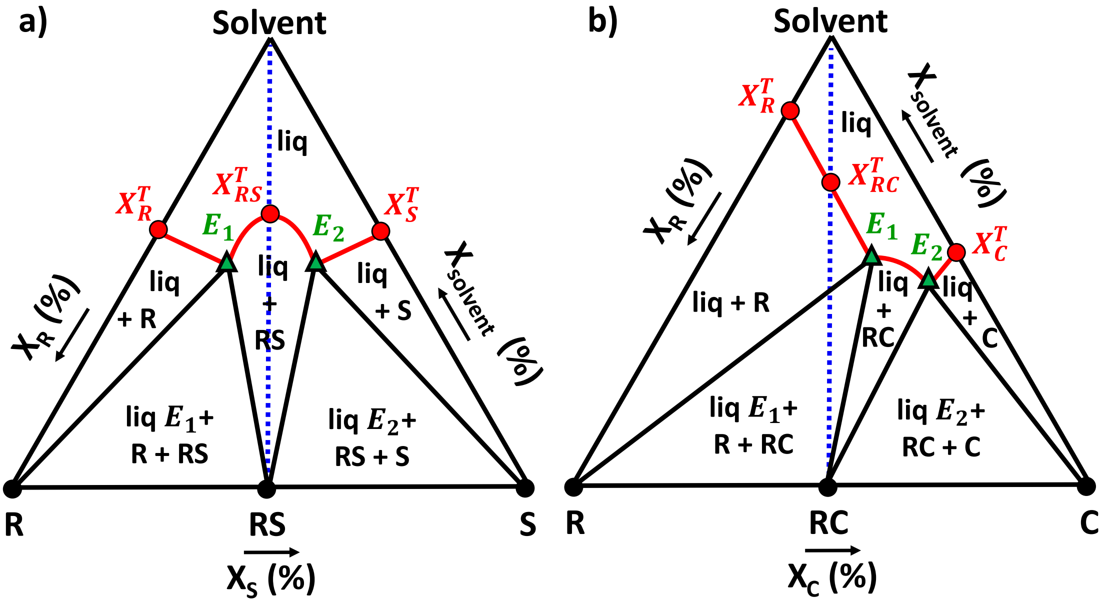

Figure 1.10: Ternary phase diagrams for **a)** a racemic compound with congruent solubility and **b)** a cocrystal forming system with incongruent solubility. The liquidus (red) and eutectic points (green triangles) are represented. The blue dotted line highlights the solvent addition line on pure binary solid.

1.4.4. Quaternary Phase Diagrams and Chiral Quantification Limitations

Quaternary phase diagrams involve four independent components ($C = 4$), and therefore, three independent composition variables X. The dependency on another variable, such as pressure P or temperature T, would add a fourth dimension that would be impossible to represent. Consequently, quaternary phase diagrams are represented as an isothermal and isobaric tetrahedron ($N = 0$), whose apexes correspond to pure components, sides to isothermal binary sections and faces to isothermal ternary sections. Any component composition from a quaternary composition can be computed with barycentric proportionality rules in the tetrahedron, with the distances from its apex and its opposite face, from the extrapolation of the rules presented in the previous sections. The Gibbs phase rule (Equation 1.2) states the number of degrees of freedom v of such system as: $v = 4 - \varphi$, which leads to four possible equilibria that are summarized in Table 1.3.

Table 1.3: Representation of phase equilibria in isobaric and isothermal quaternary phase diagrams.

v	Equilibria	Representation in isothermal isobaric quaternary plot
3	Monophasic (φ = 1)	Free volume
2	Biphasic (φ = 2)	Tie-lines joining 2 fixed compositions
1	Triphasic (φ = 3)	Tie-triangles joining 3 fixed compositions
0	Quadriphasic (φ = 3)	Tie-tetrahedron joining 4 fixed compositions

In this study, one of the four components is always a solvent, and the quaternary phase diagram gives solubility information as a function of component compositions, such as Figure 1.11 that represents the case of three pure component solids A, B, and C, forming no intermediate solid, in a solvent D. The tetrahedron shows the prolongation of solubilities and domain boundaries from the three isothermal ternaries (solid lines) inside the three-dimensional composition space (dashed lines). With the additional component, the solubility lines (red) become surfaces, and each solid possesses a three-dimensional biphasic domain of stability where phase compositions connect along tie-lines ($\varphi = 2\,; v = 2$). Above the solubility surfaces, all compositions are in a monophasic liquid phase represented as a free volume ($\varphi = 1\,; v = 3$). Eutectic lines (red dashed lines) are on the intercept of two solubility surfaces and define a line of saturated liquids in two solids from neighboring stability domains. The eutectic lines correspond to the prolongation inside the space of the eutectic points (green triangles) and delimit the boundary of a triphasic domain, by linking fixed composition saturated liquids with the two pure solids through tie-triangles ($\varphi = 3\,; v = 1$). At the intersection of exactly three eutectic lines is defined the unique quaternary invariant liquid point (green square) that equilibrates stable suspensions of the three solids in the quadriphasic domain ($\varphi = 4\,; v = 0$).

The thermodynamic system presented in Figure 1.11 corresponds to the simplest case that can be encountered. Indeed, the quaternary phase diagrams become much more complex when intermediate solids are stable in the system, as for instance a racemic compound or a cocrystal. In this study focusing on the chiral resolution of racemic compounds with cocrystallization, at least two more solids must be characterized, which complicates greatly the solid-liquid equilibria. Moreover, to truly understand and optimize a chiral resolution process of a racemic compound with a resolving agent in a solvent it is often necessary to know the data from the corresponding quaternary phase diagram.[81-85] Therefore, deepening the knowledge about complex multicomponent chiral phase diagrams constitutes an active research area. However, their characterization require analytical methods to quantify different chiral molecules in solution, which is often a limitation.

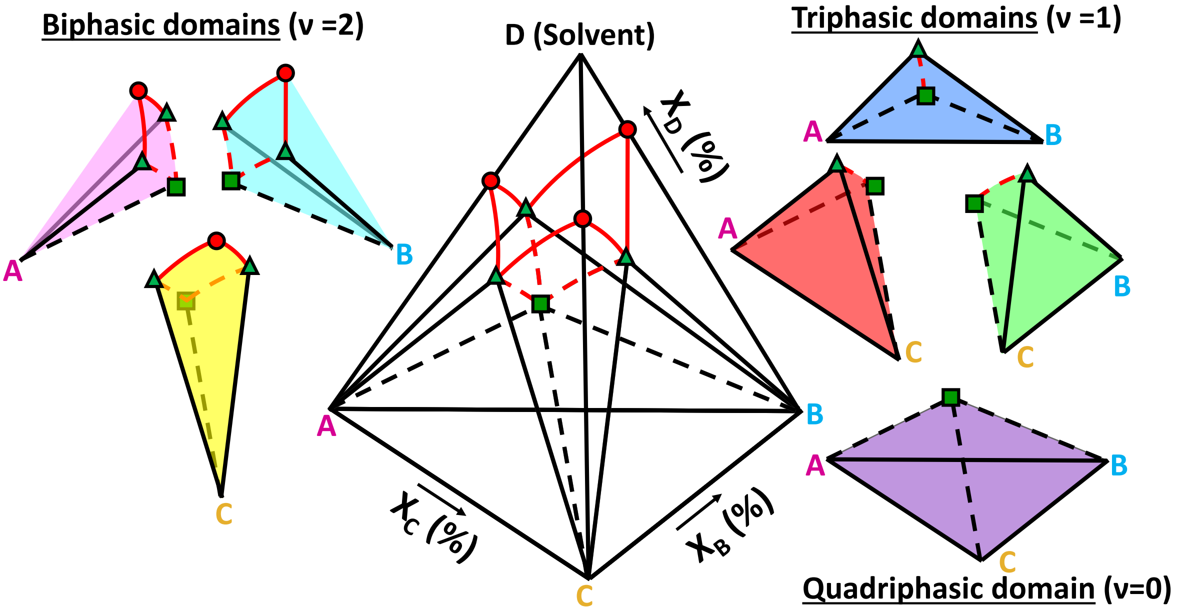

Figure 1.11: 3D tetrahedron representation of an isobaric and isothermal quaternary phase diagram, as a function of three independent composition variables, for a system of three solids A, B, and C, forming no intermediate solid, in a solvent D. The solid lines correspond to solubility information from the related isothermal ternary sections, and the dashed lines to the solubility information inside the quaternary space. The liquidus lines (red) delimit the solubility surfaces of each solid, and therefore their biphasic stability domains. The eutectic lines (red dashed lines) originate from the eutectic points in the ternaries (green triangles) and delimit the equilibrium liquid composition lines that are saturated in two solids from adjacent domains, and therefore the corresponding triphasic domain. At the intersection of three eutectic lines is the quaternary invariant point (green square) corresponding to the liquid composition saturated in the three neighboring solids. This unique composition tops the corresponding quadriphasic domain.

1.5. Crystallization in Solution

Optimal parameters can be selected from the knowledge of the phase diagrams to design crystallization processes that equilibrate a solid of interest in suspension in a saturated solution. The solid can then be separated with a phase separation method, for instance a filtration. Therefore, crystallization in solution can be defined as a separation technology with a first-order phase transition from a disordered liquid to an ordered crystalline phase. Three successive steps occur during the crystallization mechanism: the establishment of a supersaturation, the nucleation and the crystal growth.[74]

1.5.1. Supersaturation and Driving Force

The solubility is defined as the maximum quantity of solid that can be dissolved in a solvent for a given temperature T. The resulting solution composition corresponds to a thermodynamic equilibrium and is said saturated with the crystalline phase. The solubility is function of the composition and the temperature, and it can be fitted with the Van 't Hoff equation (Equation 1.10), with X^* being the mole fraction solubility composition at temperature T (in K). This equation describes an ideal solubility behavior by using as fitting parameters the heat of fusion ΔH^f (in J.mol^{-1}), the melting temperature T_f (in K), and R the universal gas constant (8.314 J.mol^{-1}.K^{-1}). The non-ideality of a system, for instance when a component solubility is influenced significantly by the presence of other components, causes a deviation in the Van ‘t Hoff equation fit.

$$\ln(X^*) = -\frac{\Delta H^f}{R}\left(\frac{1}{T} - \frac{1}{T_f}\right) \qquad \text{Equation 1.10}$$

When the solution composition X is lower than the solubility X^* at a given T, the solution is said undersaturated, and when it is higher, it is said supersaturated. Supersaturation is a necessary condition for crystallization because it corresponds to the driving force of this phenomenon. It is possible to quantify the supersaturation, for instance by expressing it as the supersaturation ratio S (Equation 1.11).[74]

$$S = \frac{X}{X^*} \qquad \text{Equation 1.11}$$

Usually, the solubility X^* increases with T, as in Figure 1.12 that represents an increasing solubility curve (red) for a binary system of a solute and a solvent. Three zones can be differentiated. In the stable zone, below the solubility curve, the solution is undersaturated and crystallization cannot happen. An addition of solid would result in its dissolution until the solution composition reaches the saturation value X^* for a given T. When going beyond the solubility curve, for values of X being higher than the solubility X^*, the solution becomes supersaturated. However, if a supersaturation is required for crystallization, it is not enough to initiate it. When the supersaturation is low, the system can indeed stay in a metastable equilibrium for a certain induction time. A limit has been set by Ostwald under the solubility curve (blue dashed line) which defines the metastable limit, and consequently the metastable zone width (MSZW) for a given T.[86] In the metastable zone, crystallization can occur, but it is not instantaneous. Nevertheless, adding seed crystals within this zone can induce crystallization. The metastable zone depends on the compound, the solvent, and experimental conditions. If the supersaturation is increased further to the Ostwald metastable limit, the labile zone is reached. In this zone, spontaneous crystallization occurs.

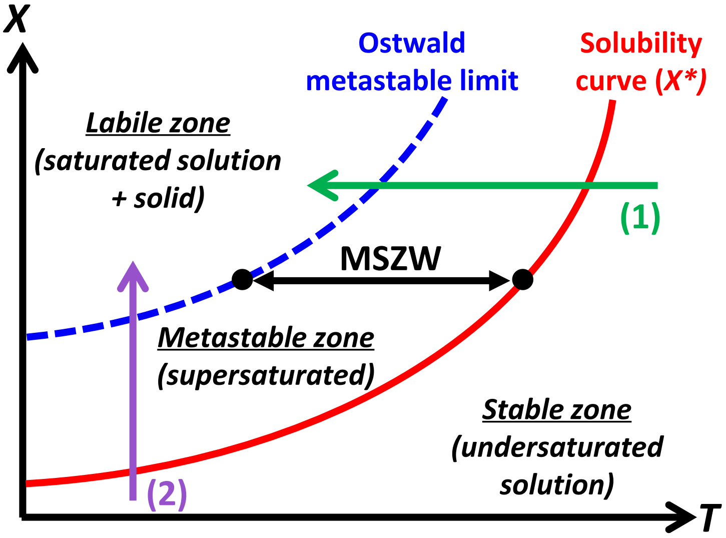

Figure 1.12: Representation of a binary system between a solvent and a solute showing the solubility curve X^*(red solid line) and Ostwald metastable limit (blue dashed line) as a function of temperature T. The supersaturation can progressively be induced through different pathways, as for instance by (1) cooling (green arrow) and (2) evaporating the solvent (purple arrow).

The supersaturation of a crystallization medium can be augmented by different methods that consist in moving the system out of its equilibrium state, with the increase of the concentration or the decrease of the solubility. For instance, this can be done by cooling a solution under its solubility at a given temperature (Figure 1.12, green path 1) or by evaporating the solvent (Figure 1.12, purple path 2). Other ways are possible such as by addition of an antisolvent, pH variation, or a chemical reaction between two components to make a compound less soluble.

1.5.2. Nucleation

Nucleation is the first step towards the formation of crystals. It refers to the formation of stable nuclei, which are groups of particles that respect the crystal packing and have the possibility to grow into crystals. Two types of nucleation can be considered.[4] Primary nucleation corresponds to the formation of nuclei from a supersaturated solution without some already existing.[87] It is said homogeneous if nuclei appear inside the solution volume, otherwise it is said heterogeneous if induced by a solid interface or impurities presence.[88, 89] Primary nucleation is often observed for highly supersaturated solution, for instance in the labile zone. The second nucleation type is called secondary nucleation, and it occurs for lower supersaturations. It corresponds to the nuclei formation from particles that are already inside the solution, for example from the attrition of particles, contact nucleation, or crystal seeding.[4, 87]

As soon as the supersaturation is high enough for the molecules to aggregate, nuclei can form. However, they will not all form a crystal. According to the Classical Nucleation Theory (CNT), the nucleation phenomenon is a competition between two terms influencing the Gibbs free energy G of the system.[4] For a nucleus considered spherical of radius r, the G variation associated to its formation is called $\mathit{\Delta G}_{nucleation}$ and is given by Equation 1.12, with $\Delta \mathrm{G_v}$ the G variation per unit of volume relative to the starting phase, and γ the surface tension between the solution and the nucleus.

$$\mathit{\Delta G}_{nucleation} = \frac{4}{3}\pi \mathrm{r}^3 \Delta \mathrm{G_v} + 4\pi \mathrm{r}^2 \gamma \qquad \text{Equation 1.12}$$

The left term of Equation 1.12 is linked to the creation of a volume through the agglomeration of particles, which causes a diminution of G. The right term describes the creation of solution/nucleus interfaces, that causes an increase in G proportional to the surface. The competition between the two terms can be represented as a function of the radius r of the nucleus (Figure 1.13), with the volume term (red) and surface energies term (blue) of opposite signs, and their sum $\mathit{\Delta G}_{nucleation}$ (green). Because of that competition between volume and surface creation, the $\mathit{\Delta G}_{nucleation}$ goes through a maximum, which defines the energy barrier $\mathit{\Delta G}^*$ that the nucleus must overcome to be stable. $\mathit{\Delta G}^*$ is the maximum value of $\mathit{\Delta G}_{nucleation}$ when the nucleus reaches a critical radius r^*. Consequently, if the size of the nucleus is below the critical size ($r < r^*$), the energy brought to the nucleus is not sufficient to make it stable and it will dissolve in the solution. On the contrary, if the nucleus is above the critical size ($r > r^*$), the nucleus is stable and can continue to grow to decrease the free energy G. This phenomenon occurs for both homogeneous and heterogeneous nucleation. In the case of heterogeneous nucleation, the interface nucleus/solvent is smaller, so the $\mathit{\Delta G}^*$ value is lowered, and heterogeneous nucleation is more likely to occur than homogeneous nucleation.

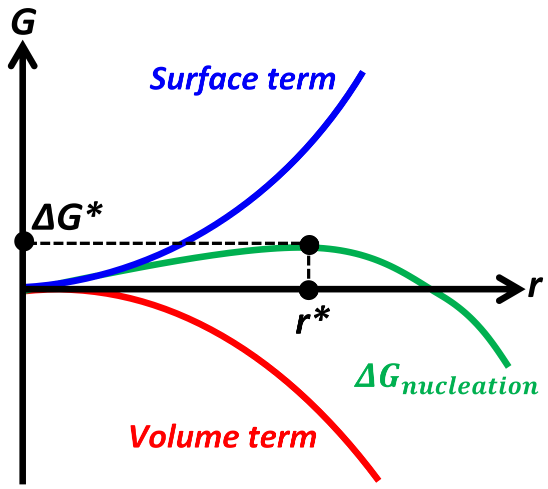

Figure 1.13: Free energy G variation associated with the nucleation of a nucleus sphere of radius r.

1.5.3. Crystal Growth

After a nucleus reaches the critical size r^*, its crystal growth can occur. Crystal growth can be defined as the increase of a particular dimension of the crystal over time, for instance with the linear growth rate.[90] Growth rates are different for all crystal faces because the intermolecular interactions involved are different, which influences the final morphology of grown crystals. Faces with the lowest growth rates are the prevalent ones. Growth rates are influenced by the crystal packing, the impurities, and the interface interactions. Several models have been proposed to explain the crystal morphologies when they grow, such as Bravais-Friedel-Donnay-Harker theory (BFDH) and Periodic Bond Chains theory (PBC).[91, 92] Both nucleation and crystal growth occur simultaneously while supersaturation exists. The molecules in solution dock to the surfaces and incorporate into the crystal. Two major growth mechanisms, named as bidimensional nucleation growth mechanism and spiral growth mechanism, can occur depending on the roughness of the surface and supersaturation levels.[93-95]

1.5.4. Kinetics and Ostwald Rule of Stages

Kinetics plays an important role during a crystallization process, and reaching the most stable equilibrium may not be straightforward. It is very common to reach first a metastable equilibrium that will transform into a more stable one under a sufficient time. This phenomenon is called Ostwald rule of stages, and even though it is only supported by experimental observations, this rule is valid in most of cases. It states that during processes, it is not the most stable state with the lowest amount of free energy G that is initially formed, but the least stable state lying nearest in free energy G to the original step.[86] Therefore, because the Gibbs free energy difference ΔG between two equilibrium states is often weak (a few kJ/mol),[37] during crystallization there is a competition between the minimization of the free energy G and the tendency of the system to reach the nearest metastable equilibrium. A metastable equilibrium permits a faster route to decrease G for the system, through the formation of a kinetic crystalline phase with a low activation energy barrier $\Delta G_{kinetic}$. On the other hand, the thermodynamic crystalline phase is the most stable because its final energy state G is the lowest that the system can achieve. However, its activation energy barrier $\Delta G_{thermodynamic}$ can be much higher, and consequently the thermodynamic crystalline phase can take more or less of time to form. This can lead to long interim periods for the kinetic metastable equilibrium to exist.

1.6. Chiral Separation Techniques with Crystallization

The focus of this study is on the crystallization processes that permit the chiral separation of racemic mixtures. It is an active research topic with various existing techniques based on either thermodynamics or kinetics to isolate an enantiomer of interest. Nonetheless, the selection of the most efficient method relies strongly on the properties of the target enantiomer, such as its crystallization equilibria, its ability to form certain types of multicomponent crystals, and its possible racemization with a racemizing agent.

1.6.1. Chiral Separation Techniques in Conglomerates

When racemic mixtures crystallize as a stable conglomerate of enantiopure crystals, the chiral discrimination is occurring at the solid state, and crystallization-based resolution techniques are applicable to isolate the enantiopure crystal of interest. Preferential crystallization is the most frequent technique to separate a conglomerate, but deracemization processes offer new perspectives for chiral systems that can racemize in solution, with techniques like Viedma ripening, temperature-cycling, and second-order asymmetric transformation (SOAT).[96-109] When the target enantiomer does not crystallize as a stable conglomerate, a resolution strategy consists in generating chemical derivatives, or forming multicomponent crystals, like cocrystals, with an achiral resolution agent. The aim is to screen for new crystallization equilibria and find a stable conglomerate to apply the techniques mentioned. The motivation relies essentially on the conglomerate statistics (5 to 10% occurrence), with the logic being that the more some new systems are screened, the higher is the chance to find a conglomerate. On the contrary, when a racemic crystal is stable, the chiral resolution through crystallization at the racemic composition is difficult or even impossible, but in rare cases a metastable separation process can be performed in the metastable conglomerate equilibrium.[110, 111]

1.6.1.1. Preferential Crystallization (PC)

Preferential crystallization is a kinetically driven and stereoselective crystallization technique that can be applied in conglomerate systems to design resolution processes.[110, 112-114] Normally, a supersaturated racemic solution in a conglomerate would lead to the simultaneous crystallization of both enantiopure crystals to reach the triphasic equilibrium in the corresponding ternary phase diagram. However, one of the enantiopure crystal can be preferentially crystallized for a certain time through the addition of its seed crystals. The enantiopure seeding has for effect to trigger the system to reach the closest metastable equilibrium, which corresponds to the crystallization of the enantiopure crystal in equilibrium with a metastable saturated solution from the extension of its solubility curve in the triphasic domain. With an appropriate process design, the enantiopure solid can then be collected by filtration. Because this technique is performed out of equilibrium, it is very sensitive to crystallization kinetics and requires a careful control of the experimental parameters to avoid the crystallization of the counter-enantiomer. The challenge relies in the selection of the operating conditions, to balance between the yield optimization and the duration of the operating window permitting the process. Therefore, both crystallization kinetics and the corresponding ternary phase diagrams must be known. Preferential crystallization is the chiral separation technique of choice when accessible, but it is often used in a fractional manner that causes long experimental times and increased costs.[115] It also has the limitation of a theoretical maximum resolution yield that cannot exceed 50 % because the counter-enantiomer cannot convert into the enantiomer of interest.

1.6.1.2. Deracemization Techniques

Deracemization techniques are the combination of a racemization in solution with a crystallization that leads to a chiral discrimination at the solid state.[116, 117] Consequently, deracemization processes can only be designed in a stable conglomerate. The racemization is defined as the reversible conversion of an enantiomer into its counter-enantiomer, occurring spontaneously in certain solvents, or by a chemical reaction with a racemizing agent, that is usually a strong base.[112, 118] The consequence of the racemization is that the composition of the solution remains racemic, even when an enantiopure crystal of interest is crystallized. Because the counter-enantiomer is converted to the target enantiomer, the maximum resolution yield is not limited to 50 %, and the risk of crystallization of the counter-enantiomer is hampered. This allows to reach high yields and high purities, with the theoretical possibility to reach a 100 % yield of enantiopure material. For instance, second-order asymmetric transformation (SOAT) is a deracemization technique resulting of the combination of preferential crystallization (PC) with racemization in solution.[18, 119, 120] In SOAT, the crystallization of the enantiopure crystal does not cause an excess of the counter-enantiomer in solution, which makes SOAT to not rely on a kinetic equilibrium contrary to PC, and therefore avoid the crystallization of the counter-enantiomer. Other deracemization techniques, such as Viedma ripening and temperature-cycling, are based on a spontaneous symmetry breaking of a suspension of chiral crystals that undergoes an energy flux creating slight local imbalances of the enantiomeric excess or the crystal size distribution.[21, 104, 105, 117, 121-131] For Viedma ripening, also called attrition-enhanced deracemization, the energy flux is brought by grinding the suspension, while temperature-cycling relies on temperature oscillations, but other energy sources can be used to induce attrition, such as ultrasounds or microwaves.[132-134] The principle relies on a dynamic equilibrium between dissolution and crystallization that favors the dissolution of small crystals and the growth of large crystals to minimize the interfacial energy.[135-137] Therefore, a racemic suspension of crystals from opposite chirality in a conglomerate can be brought to a single enantiopurity with an appropriate process design that would favor the growth of the enantiopure crystals of interest, while the counter-enantiomer crystals are dissolved and racemized in the saturated solution. However, such processes are limited to conglomerate forming systems that can racemize rapidly in solution and are rather difficult to scale up for industrial use.[124, 136, 138]

1.6.2. **Dissymmetry Creation via Multicomponent Chiral Crystal Formation**

In most cases, the racemic mixtures crystallize inevitably as a stable racemic crystal, and an alternative crystallization-based resolution method is to generate multicomponent chiral crystals with a chiral resolving agent. This creates a dissymmetry in the solid physicochemical properties in the thermodynamic system, and consequently permits the separation of the solid containing the enantiomer of interest. For target chiral molecules that can be ionized, the most popular resolution technique is the formation of diastereomeric salts with a chiral salt-former, also called Classical resolution or Pasteurian resolution.[5, 76, 102, 112, 139-141] With this technique, a chiral acid or base is added to a racemic mixture to break the symmetry and transform the enantiomeric pair into a diastereomeric pair. By exploiting the difference in solubility of the two diastereomeric salts with an appropriate process design, the less soluble salt can be isolated from crystallization at the racemic composition. Then, the pure enantiomer can be recovered from the isolated salt by a physical separation of its chiral salt-former. Due to its simplicity and its efficiency, this technique is the most applied at industrial scale, although its maximum resolution yield is limited to 50 % if it is not coupled with racemization in solution.[142, 143] However, this technique has a strong limitation because it can only be applied to enantiomers that possess a strong enough acidic or basic function to form a salt.[102]

The cocrystallization with a chiral coformer offers an excellent solution to the limitation of salts and is applicable to all enantiomers because cocrystals form through strong intermolecular interactions, like hydrogen bonds, that are universal.[63, 64, 144] Therefore, the cocrystallization with a chiral coformer always generate a resolution possibility, by the formation of a diastereomeric pair of enantiopure cocrystals, or even an enantiospecific cocrystal.[50, 51, 81, 82, 84, 145, 146] Enantiospecificity relates to the formation of a new multicomponent crystal with only one enantiomer, while the counter-enantiomer does not interact in the solid state with the chiral resolving agent.[82, 147-149] Contrary to salts, cocrystals show much more often enantiospecificity due to the weaker nature of the hydrogen bonding.[150] Both diastereomeric pairs and enantiospecific cocrystals are suitable for the design of chiral resolution processes exploiting the solubility differences of the solids in the system, similar to Pasteurian resolution.[151, 152] An isolated cocrystal can also be deconstructed to recover the pure enantiomer, as with salts. Nonetheless, while salts require recrystallization with another acid or base to form an unwanted conjugated waste salt, a cocrystal involves neutral molecules only and thus prevents the generation of waste during its deconstruction.[153-155] This offers interesting recycling possibilities of the coformer for reusage, which is advantageous for process economics. Moreover, if the enantiomers can racemize with a racemizing agent, it was proved recently that a cocrystallization-induced spontaneous deracemization process can be designed to improve consequently the resolution yield.[51, 156] Consequently, the chiral resolution of stable racemic compounds with chiral cocrystallization is an expanding research area offering great prospects in terms of yield, applicability, and universality of the methods.

1.7. Aims and Objectives

Over the past decades, cocrystallization has gained a significant popularity because of its convenient accessibility, universality, and the extensive potential it offers to alter the solid-state properties of a target compound. Cocrystals become particularly relevant for the generation of chiral resolution possibilities, with enantiomeric separation being a major research area because of the different biological response of enantiomers while their physical properties are identical. When a racemic mixture of enantiomers crystallizes as a stable racemic compound that prevents the chiral separation, cocrystallization is applicable for every target chiral molecule to prompt new chiral separation possibilities. The cocrystallization with an achiral coformer can lead to a conglomerate equilibrium of enantiopure cocrystals, in which crystallization-based resolution techniques can be applied, such as preferential crystallization and deracemization techniques. With a chiral coformer, the generated solid equilibria are either a diastereomeric pair of enantiopure cocrystals, or an enantiospecific cocrystal, and both possibilities are favorable to design a separation process exploiting the dissymmetry in the solid physicochemical properties. However, as raised in the previous sections, many research questions are linked to the chiral resolution of racemic compounds by cocrystallization. First, because not all cocrystals generate resolution possibilities, the optimization of the detection of new cocrystals with efficient screening methods is key to the emergence of chiral resolution routes, and consequently it constitutes an active research topic. Then, the thermodynamic systems constituted of two enantiomers, a coformer, and a solvent, become complex when intermediate solids like racemic compounds and cocrystals are formed. The related phase diagrams, necessary to the understanding of solid-liquid equilibria and the design of resolution processes, are difficult to characterize because of the current limitations of chiral quantification methods. Moreover, deepening the knowledge about the use of such complex phase diagrams is essential to design robust crystallization processes in solution, from the isolation of a cocrystal to the recovery of a pure enantiomer. Finally, because of the variety in the collection of strategies applicable for the resolution of racemic compounds with cocrystallization, the influence of different parameters must be discussed to precise the selection of an optimal strategy.

The main aim of this thesis is to investigate the challenges related to the thermodynamic characterization and understanding of multicomponent chiral systems, to apply chiral resolution strategies of racemic compounds with cocrystallization. This aim is broken down into four different chapter objectives, as illustrated in Figure 1.14. Each chapter contributes to the overall aim through a proposed optimization of cocrystal screening methods, a novel analytical technique for the chiral quantification in complex systems, a guideline for the design and optimization of enantioselective cocrystallization resolution processes leading to pure enantiomer recovery, and finally a discussion on the parameters influencing a strategy selection for the resolution of racemic compounds with cocrystallization.

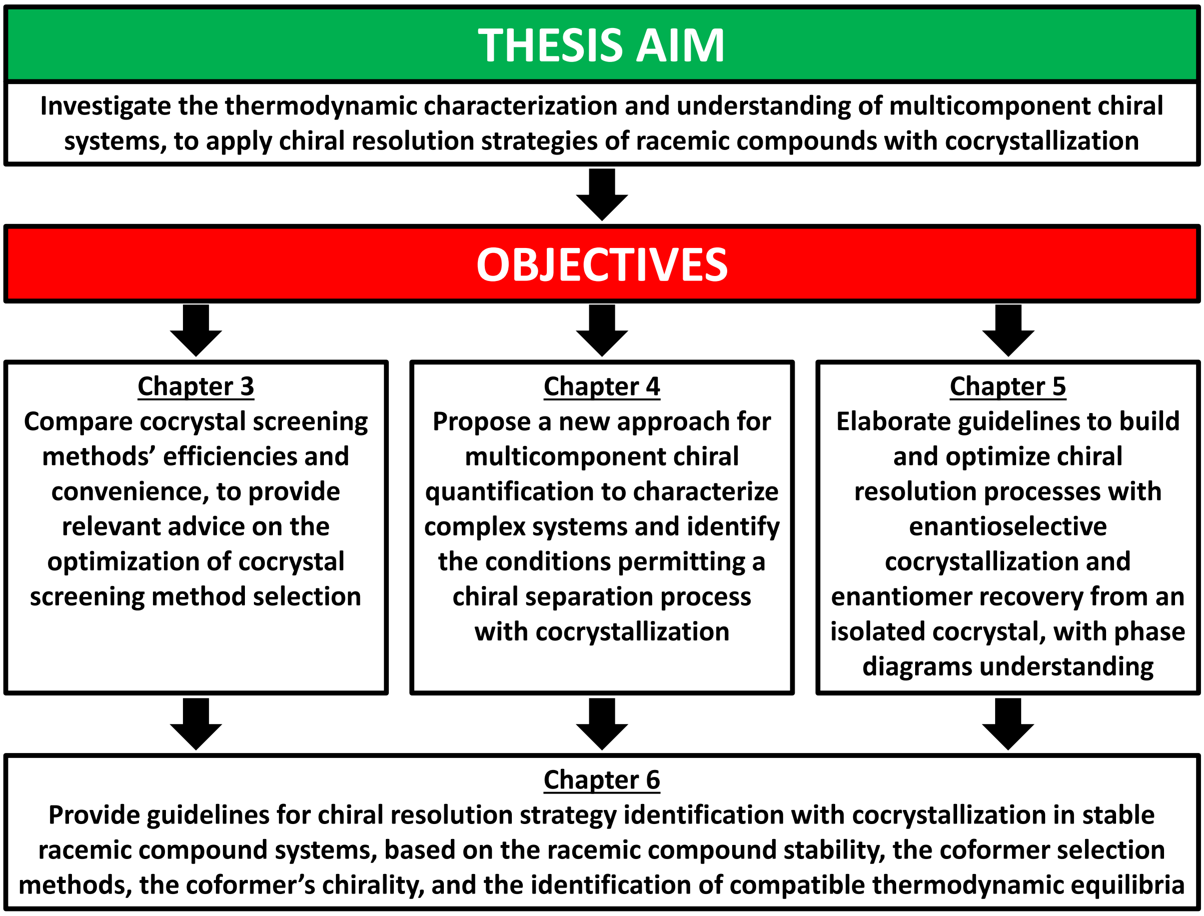

Figure 1.14: Overview of the main aim of this thesis, broken down into chapter objectives.

Chapter 3: Comparing and Quantifying the Efficiency of Cocrystal Screening Methods for Praziquantel. Pharmaceutical cocrystals are highly interesting due to their effect on physicochemical properties and their role in separation technologies, particularly for chiral molecules. The detection of new cocrystals is a challenge, and robust screening methods are required. Because numerous techniques exist that differ in their cocrystallization mechanisms, their efficiencies depend on the coformers investigated. **Therefore, the objective in this chapter is to compare cocrystal screening methods' efficiencies and convenience, to provide relevant advice on the optimization of cocrystal screening method selection.** For this purpose, the results obtained during a campaign aiming to find cocrystals to resolve the racemic compound of praziquantel are investigated. A total of 30 coformers are screened with four cocrystal screening methods, which are compared thoroughly by defining quantified parameters that help to review their strengths and weaknesses.

Chapter 4: Multicomponent Chiral Quantification with Ultraviolet Circular Dichroism Spectroscopy: Ternary and Quaternary Phase Diagrams of Levetiracetam. A technique to enable the chiral separation of racemic compounds is to create an asymmetry in the thermodynamic system by generating chiral cocrystal(s) with a chiral coformer and using the solubility differences to enable separation through crystallization from solution. However, the solid-liquid equilibria in such quaternary systems are complex to characterize and require analytical methods able to quantify different chiral molecules in solution. **The objective in this chapter is to propose a new approach for multicomponent chiral quantification to characterize complex systems and identify the conditions permitting a chiral separation process with cocrystallization.** A novel chiral quantification method is developed, which is based on ultraviolet circular dichroism spectroscopy and multivariate partial least square models. The method is used to understand the solid-liquid equilibria in the complex quaternary system of levetiracetam enantiomers with a chiral coformer in a solvent, through the accurate determination of the full quaternary phase diagram.

Chapter 5: Enantioselective Cocrystallization and Enantiomer Recovery Guidelines from Phase Diagram Information. Enantiopure cocrystals are very useful to enable separation processes for chiral molecules, particularly when racemic mixtures crystallize as stable racemic compounds. Moreover, cocrystals offer interesting possibilities of enantiomer and coformer recovery when they are deconstructed in optimal conditions. Nonetheless, the related multicomponent chiral phase diagrams, which are necessary to build efficient processes, are complex to work with and are influenced by various parameters. **Therefore, the objective in this chapter is to elaborate guidelines to build and optimize chiral resolution processes with enantioselective cocrystallization and enantiomer recovery from an isolated cocrystal, with the understanding of phase diagrams.** For that purpose, by using the full quaternary phase diagram acquired in Chapter 4, an enantioselective cocrystallization process is designed and optimized to recover levetiracetam from its racemic compound through the isolation of its enantiospecific cocrystal. This process is combined with a solvent-mediated transformation step that is developed to permit the retrieval of pure levetiracetam from its cocrystal.

Chapter 6: Cocrystallization Opportunities for Chiral Resolution of Racemic Compounds. Cocrystallization provides a relevant collection of strategies for the chiral resolution of stable racemic compounds, but several parameters must be considered to identify the best scenario permitting the resolution of a target compound. Indeed, the enantiomers can interact in many ways with the coformers, and not all scenarios lead to thermodynamic systems permitting the chiral separation. **The aim of this chapter is to provide guidelines for chiral resolution strategy identification with cocrystallization in stable racemic compound systems, based on the racemic compound stability, the coformer selection methods, the coformer's chirality, and the identification of compatible thermodynamic equilibria.** To this end, all the key points mentioned are discussed thoroughly, with the view to understand the parameters leading to a quick and efficient identification of the optimal resolution strategy. The proposed guidelines facilitate the design of a chiral resolution by cocrystallization.

1.8. References

(1) Coquerel, G. Chiral Discrimination in the Solid State: Applications to Resolution and Deracemization. In *Advances in Organic Crystal Chemistry*, Springer, 2015; pp 393-420.
(2) Collet, A.; Crassous, J.; Dutasta, J.-P.; Guy, L. *Molécules chirales: stéréochimie et propriétés*; L'Editeur: EDP Sciences, 2006.
(3) Cahn, R. S.; Ingold, C.; Prelog, V. Specification of Molecular Chirality. *Angewandte Chemie-International Edition* **1966**, *5* (4), 385-&.
(4) Mullin, J. W. *Crystallization*; Elsevier, 2001.
(5) Jacques, J.; Collet, A.; Wilen, S. H. *Enantiomers, racemates, and resolutions*; Wiley, 1981.
(6) Nguyen, L. A.; He, H.; Pham-Huy, C. Chiral drugs: an overview. *Int J Biomed Sci* **2006**, *2* (2), 85-100.
(7) Reddy, I. K.; Mehvar, R. *Chirality in drug design and development*; CRC Press, 2004.
(8) Ariens, E. J. Stereochemistry, a basis for sophisticated nonsense in pharmacokinetics and clinical pharmacology. *Eur J Clin Pharmacol* **1984**, *26* (6), 663-668.
(9) Li, Z. J.; Grant, D. J. Relationship between physical properties and crystal structures of chiral drugs. *Journal of Pharmaceutical Sciences* **1997**, *86* (10), 1073-1078.
(10) Saigo, K.; Sakai, K. Resolution of Chiral Drugs and Drug Intermediates by Crystallisation. *Chirality in drug research* **2006**, 127-154.
(11) Li, Z. J.; Grant, D. J. Relationship between physical properties and crystal structures of chiral drugs. *J Pharm Sci* **1997**, *86* (10), 1073-1078.
(12) Savile, C. K.; Janey, J. M.; Mundorff, E. C.; Moore, J. C.; Tam, S.; Jarvis, W. R.; Colbeck, J. C.; Krebber, A.; Fleitz, F. J.; Brands, J.; et al. Biocatalytic asymmetric synthesis of chiral amines from ketones applied to sitagliptin manufacture. *Science* **2010**, *329* (5989), 305-309.
(13) Blaser, H. U. The chiral pool as a source of enantioselective catalysts and auxiliaries. *Chemical reviews* **1992**, *92* (5), 935-952.
(14) Masamune, S.; Choy, W.; Petersen, J. S.; Sita, L. R. Double asymmetric synthesis and a new strategy for stereochemical control in organic synthesis. *Angewandte Chemie International Edition in English* **1985**, *24* (1), 1-30.
(15) Ager, D. J.; Prakash, I.; Schaad, D. R. 1, 2-Amino alcohols and their heterocyclic derivatives as chiral auxiliaries in asymmetric synthesis. *Chemical Reviews* **1996**, *96* (2), 835-876.
(16) Noyori, R. Asymmetric catalysis: science and opportunities (Nobel lecture). *Angew Chem Int Ed Engl* **2002**, *41* (12), 2008-2022.
(17) Caner, H.; Groner, E.; Levy, L.; Agranat, I. Trends in the development of chiral drugs. *Drug Discov Today* **2004**, *9* (3), 105-110.
(18) Sheldon, R. A. *Chirotechnology: industrial synthesis of optically active compounds*; CRC press, 1993.
(19) Beesley, T. E.; Scott, R. P. *Chiral chromatography*; John Wiley & Sons, 1999.
(20) van der Meijden, M. W.; Leeman, M.; Gelens, E.; Noorduin, W. L.; Meekes, H.; van Enckevort, W. J. P.; Kaptein, B.; Vlieg, E.; Kellogg, R. M. Attrition-Enhanced Deracemization in

the Synthesis of Clopidogrel - A Practical Application of a New Discovery. *Organic Process Research & Development* **2009**, *13* (6), 1195-1198.
(21) Suwannasang, K.; Flood, A. E.; Coquerel, G. A Novel Design Approach To Scale Up the Temperature Cycle Enhanced Deracemization Process: Coupled Mixed-Suspension Vessels. *Crystal Growth & Design* **2016**, *16* (11), 6461-6467.
(22) Parsegian, V. A. *Van der Waals forces : a handbook for biologists, chemists, engineers, and physicists*; Cambridge University Press, 2006.
(23) Gavezzotti, A. Molecular Aggregation, International Union of Crystallography Monographs on Crystallography. Oxford University Press: 2006.
(24) Desiraju, G. R. Current challenges in crystal engineering. In *Implications of Molecular and Materials Structure for New Technologies*, Springer, 1999; pp 321-339.
(25) Dunitz, J. D. Weak Interactions in Molecular Crystals. In *Implications of Molecular and Materials Structure for New Technologies*, Springer, 1999; pp 175-184.
(26) Gilli, G.; Gilli, P. *The nature of the hydrogen bond: outline of a comprehensive hydrogen bond theory*; Oxford University Press, 2009.
(27) Steiner, T. The hydrogen bond in the solid state. *Angew Chem Int Ed Engl* **2002**, *41* (1), 49-76.
(28) Hunter, C. A.; Lawson, K. R.; Perkins, J.; Urch, C. J. J. o. t. C. S., Perkin Transactions 2. Aromatic interactions. **2001**, (5), 651-669.
(29) West, A. R. *Basic solid state chemistry*; John Wiley & Sons Incorporated, 1999.
(30) Clevers, S. Développement des méthodes optiques in-situ pour la caractérisation de solides organiques cristallisés. **2014**,
(31) Van Meerssche, M.; Feneau-Dupont, J. *Introduction à la cristallographie et à la chimie structurale*; Oyez, 1976.
(32) Smith, C. S. Macroscopic symmetry and properties of crystals. In *Solid State Physics*, Vol. 6; Elsevier, 1958; pp 175-249.
(33) Giacovazzo, C.; Monaco, H. L.; Artioli, G.; Viterbo, D.; Ferraris, G.; Giacovazzo, C. *Fundamentals of crystallography*; Oxford University Press Oxford, 2002.
(34) Hahn, T.; Shmueli, U.; Arthur, J. W. *International tables for crystallography*; Reidel Dordrecht, 1983.
(35) Bravais, A. *Etudes cristallographiques*; Gauthier-Villars, 1866.
(36) Dunitz, J. D. *X-ray Analysis and the Structure of Organic Molecules*; Verlag Helvetica Chimica Acta, 1995.
(37) Bernstein, J. *Polymorphism in Molecular Crystals 2e*; International Union of Crystal, 2020.
(38) Threlfall, T. L. Analysis of Organic Polymorphs - a Review. *Analyst* **1995**, *120* (10), 2435-2460.
(39) Haleblian, J.; McCrone, W. Pharmaceutical applications of polymorphism. *J Pharm Sci* **1969**, *58* (8), 911-929.
(40) Hilfiker, R. *Polymorphism in the pharmaceutical industry*; Wiley Online Library, 2006.
(41) Hilfiker, R.; Blatter, F.; von Raumer, M. J. P. i. t. p. i. Relevance of solid-state properties for pharmaceutical products. **2006**, *1*, 1.
(42) Bernstein, J.; Hagler, A. J. J. o. t. A. C. S. Conformational polymorphism. The influence of crystal structure on molecular conformation. **1978**, *100* (3), 673-681.
(43) Cruz-Cabeza, A. J.; Bernstein, J. Conformational polymorphism. *Chem Rev* **2014**, *114* (4), 2170-2191.
(44) Ricci, J. E. *phase rule and heterogeneous equilibrium*; 1951.

(45) Burger, A.; Ramberger, R. J. M. A. On the polymorphism of pharmaceuticals and other molecular crystals. I. **1979**, *72* (3-4), 259-271.

(46) Coquerel, G. Review on the heterogeneous equilibria between condensed phases in binary systems of enantiomers. *Enantiomer* **2000**, *5* (5), 481-498.

(47) Brock, C. P.; Dunitz, J. D. Towards a Grammar of Crystal Packing. *Chemistry of Materials* **2002**, *6* (8), 1118-1127.

(48) Belsky, V.; Zorkii, P. J. A. C. S. A. C. P., Diffraction, Theoretical; Crystallography, G. Distribution of organic homomolecular crystals by chiral types and structural classes. **1977**, *33* (6), 1004-1006.

(49) Belsky, V. K.; Zorkii, P. M. Distribution of organic homomolecular crystals by chiral types and structural classes. *Acta Crystallographica Section A* **1977**, *33* (6), 1004-1006.

(50) Harmsen, B.; Leyssens, T. Enabling enantiopurity: combining racemization and dual-drug co-crystal resolution. *Crystal Growth & Design* **2018**, *18* (6), 3654-3660.

(51) Guillot, M.; de Meester, J.; Huynen, S.; Collard, L.; Robeyns, K.; Riant, O.; Leyssens, T. Cocrystallization-Induced Spontaneous Deracemization: A General Thermodynamic Approach to Deracemization. *Angew Chem Int Ed Engl* **2020**, *59* (28), 11303-11306.

(52) Barbour, L. J.; Das, D.; Jacobs, T.; Lloyd, G. O.; Smith, V. J. J. S. C. F. M. t. N. Concepts and nomenclature in chemical crystallography. **2012**,

(53) Grothe, E.; Meekes, H.; Vlieg, E.; ter Horst, J. H.; de Gelder, R. Solvates, Salts, and Cocrystals: A Proposal for a Feasible Classification System. *Crystal Growth & Design* **2016**, *16* (6), 3237-3243.

(54) Shefter, E.; Higuchi, T. Dissolution Behavior of Crystalline Solvated and Nonsolvated Forms of Some Pharmaceuticals. *J Pharm Sci* **1963**, *52* (8), 781-791.

(55) Shevchenko, A.; Miroshnyk, I.; Pietila, L. O.; Haarala, J.; Salmia, J.; Sinervo, K.; Mirza, S.; van Veen, B.; Kolehmainen, E.; Nonappa; et al. Diversity in Itraconazole Cocrystals with Aliphatic Dicarboxylic Acids of Varying Chain Length. *Crystal Growth & Design* **2013**, *13* (11), 4877-4884.

(56) Lin, Y.; Yang, H.; Yang, C.; Wang, J. Preparation, characterization, and evaluation of dipfluzine-benzoic acid co-crystals with improved physicochemical properties. *Pharm Res* **2014**, *31* (3), 566-578.

(57) Almarsson, Ö.; Zaworotko, M. J. Crystal engineering of the composition of pharmaceutical phases. Do pharmaceutical co-crystals represent a new path to improved medicines? *Chemical communications* **2004**, (17), 1889-1896.

(58) Remenar, J. F.; Morissette, S. L.; Peterson, M. L.; Moulton, B.; MacPhee, J. M.; Guzman, H. R.; Almarsson, O. Crystal engineering of novel cocrystals of a triazole drug with 1,4-dicarboxylic acids. *J Am Chem Soc* **2003**, *125* (28), 8456-8457.

(59) Schultheiss, N.; Newman, A. Pharmaceutical Cocrystals and Their Physicochemical Properties. *Cryst Growth Des* **2009**, *9* (6), 2950-2967.

(60) Friscic, T.; Jones, W. Benefits of cocrystallisation in pharmaceutical materials science: an update. *J Pharm Pharmacol* **2010**, *62* (11), 1547-1559.

(61) Urbanus, J.; Roelands, C. P. M.; Verdoes, D.; Jansens, P. J.; ter Horst, J. H. Co-Crystallization as a Separation Technology: Controlling Product Concentrations by Co-Crystals. *Crystal Growth & Design* **2010**, *10* (3), 1171-1179.

(62) Schultheiss, N.; Newman, A. Pharmaceutical cocrystals and their physicochemical properties. *Crystal growth and design* **2009**, *9* (6), 2950-2967.

(63) Bond, A. D. What is a co-crystal? *CrystEngComm* **2007**, *9* (9), 833-834.

(64) Alhalaweh, A.; George, S.; Basavoju, S.; Childs, S. L.; Rizvi, S. A. A.; Velaga, S. P. Pharmaceutical cocrystals of nitrofurantoin: screening, characterization and crystal structure analysis. *CrystEngComm* **2012**, *14* (15), 5078-5088.

(65) Cinčić, D.; Friščić, T.; Jones, W. J. C. A. E. J. Isostructural Materials Achieved by Using Structurally Equivalent Donors and Acceptors in Halogen-Bonded Cocrystals. **2008**, *14* (2), 747-753.

(66) Pedireddi, V. R.; Jones, W.; Chorlton, A. P.; Docherty, R. Creation of crystalline supramolecular arrays: A comparison of co-crystal formation from solution and by solid state grinding. *Chemical Communications* **1996**, (8), 987-988.

(67) Shen, Q. J.; Pang, X.; Zhao, X. R.; Gao, H. Y.; Sun, H.-L.; Jin, W. J. J. C. Phosphorescent cocrystals constructed by 1, 4-diiodotetrafluorobenzene and polyaromatic hydrocarbons based on C–I··· π halogen bonding and other assisting weak interactions. **2012**, *14* (15), 5027-5034.

(68) Wood, P. A.; Feeder, N.; Furlow, M.; Galek, P. T. A.; Groom, C. R.; Pidcock, E. Knowledge-based approaches to co-crystal design. *Crystengcomm* **2014**, *16* (26), 5839-5848.

(69) Griesser, U. J. The Importance of Solvates. In *Polymorphism*, 2006; pp 211-233.

(70) Trask, A. V.; Jones, W. Crystal engineering of organic cocrystals by the solid-state grinding approach. *Organic Solid State Reactions* **2005**, *254*, 41-70.

(71) Shaikh, R.; Singh, R.; Walker, G. M.; Croker, D. M. Pharmaceutical Cocrystal Drug Products: An Outlook on Product Development. *Trends Pharmacol Sci* **2018**, *39* (12), 1033-1048.

(72) Lin, S. Y. Mechanochemical Approaches to Pharmaceutical Cocrystal Formation and Stability Analysis. *Curr Pharm Des* **2016**, *22* (32), 5001-5018.

(73) Leyssens, T.; ter Horst, J. H. 9. Solution co-crystallisation and its applications. In *Multi-Component Crystals*, De Gruyter, 2017; pp 205-236.

(74) Coquerel, G. Crystallization of molecular systems from solution: phase diagrams, supersaturation and other basic concepts. *Chem Soc Rev* **2014**, *43* (7), 2286-2300.

(75) Cascella, F.; Seidel-Morgenstern, A.; Lorenz, H. Exploiting Ternary Solubility Phase Diagrams for Resolution of Enantiomers: An Instructive Example. *Chemical Engineering & Technology* **2020**, *43* (2), 329-336.

(76) Marchand, P.; Lefèbvre, L. c.; Querniard, F.; Cardinaël, P.; Perez, G.; Counioux, J.-J.; Coquerel, G. Diastereomeric resolution rationalized by phase diagrams under the actual conditions of the experimental process. *Tetrahedron: Asymmetry* **2004**, *15* (16), 2455-2465.

(77) Rodríguez-Hornedo, N.; Nehm, S. J.; Seefeldt, K. F.; Pagán-Torres, Y.; Falkiewicz, C. J. Reaction Crystallization of Pharmaceutical Molecular Complexes. *Molecular Pharmaceutics* **2006**, *3* (3), 362-367.

(78) Ter Horst, J.; Deij, M.; Cains, P. Discovering new co-crystals. *Crystal Growth & Design* **2009**, *9* (3), 1531-1537.

(79) Chiarella, R. A.; Davey, R. J.; Peterson, M. L. Making Co-CrystalsThe Utility of Ternary Phase Diagrams. *Crystal Growth & Design* **2007**, *7* (7), 1223-1226.

(80) Childs, S. L.; Rodriguez-Hornedo, N.; Reddy, L. S.; Jayasankar, A.; Maheshwari, C.; McCausland, L.; Shipplett, R.; Stahly, B. C. Screening strategies based on solubility and solution composition generate pharmaceutically acceptable cocrystals of carbamazepine. *Crystengcomm* **2008**, *10* (7), 856-864.

(81) Harmsen, B.; Leyssens, T. Dual-Drug Chiral Resolution: Enantiospecific Cocrystallization of (S)-Ibuprofen Using Levetiracetam. *Crystal Growth & Design* **2017**, *18* (1), 441-448.

(82) Springuel, G.; Leyssens, T. Innovative Chiral Resolution Using Enantiospecific Co-Crystallization in Solution. *Crystal Growth & Design* **2012**, *12* (7), 3374-3378.

(83) Song, L.; Leng, F.; Robeyns, K.; Leyssens, T. Quaternary phase diagrams as a tool for ionic cocrystallization: the case of a solid solution between a racemic and enantiopure ionic cocrystal. *CrystEngComm* **2020**, *22* (14), 2537-2542.

(84) Springuel, G.; Collard, L.; Leyssens, T. Ternary and quaternary phase diagrams: key tools for chiral resolution through solution cocrystallization. *CrystEngComm* **2013**, *15* (39), 7951-7958.

(85) Zhou, F.; Shemchuk, O.; Charpentier, M. D.; Matheys, C.; Collard, L.; Ter Horst, J. H.; Leyssens, T. Simultaneous Chiral Resolution of Two Racemic Compounds by Preferential Cocrystallization*. *Angew Chem Int Ed Engl* **2021**, *60* (37), 20264-20268.

(86) Ostwald, W. J. Z. f. p. C. Studien über die Bildung und Umwandlung fester Körper. **1897**, *22* (1), 289-330.

(87) Ter Horst, J. H.; Schmidt, C.; Ulrich, J. Fundamentals of industrial crystallization. In *Handbook of Crystal Growth*, Elsevier, 2015; pp 1317-1349.

(88) Gibbs, J. *The Collected Works. Vol. 1. Thermodynamics*; Yale University Press, 1948.

(89) Söhnel, O.; Garside, J. *Precipitation: basic principles and industrial applications*; Butterworth-Heinemann, 1992.

(90) Myerson, A. *Handbook of industrial crystallization*; Butterworth-Heinemann, 2002.

(91) Donnay, J. D. H.; Harker, D. A new law of crystal morphology extending the law of bravais. *American Mineralogist* **1937**, *22* (5), 446-467.

(92) Hartman, P. *Crystal growth: an introduction*; North Holland, 1973.

(93) Hartman, P.; Perdok, W. J. A. C. On the relations between structure and morphology of crystals. I. **1955**, *8* (1), 49-52.

(94) Stranski, I. N. J. Z. f. p. C. Zur theorie des kristallwachstums. **1928**, *136* (1), 259-278.

(95) Bennema, P. Spiral Growth and Surface Roughening - Developments since Burton, Cabrera and Frank. *Journal of Crystal Growth* **1984**, *69* (1), 182-197.

(96) Belletti, G.; Tortora, C.; Mellema, I. D.; Tinnemans, P.; Meekes, H.; Rutjes, F.; Tsogoeva, S. B.; Vlieg, E. Photoracemization-Based Viedma Ripening of a BINOL Derivative. *Chemistry* **2020**, *26* (4), 839-844.

(97) Sakai, K.; Hirayama, N.; Tamura, R. *Novel optical resolution technologies*; Springer, 2007.

(98) Suwannasang, K.; Flood, A. E.; Rougeot, C.; Coquerel, G. Using Programmed Heating–Cooling Cycles with Racemization in Solution for Complete Symmetry Breaking of a Conglomerate Forming System. *Crystal Growth & Design* **2013**, *13* (8), 3498-3504.

(99) Li, W. W.; Spix, L.; de Reus, S. C. A.; Meekes, H.; Kramer, H. J. M.; Vlieg, E.; ter Horst, J. H. Deracemization of a Racemic Compound via Its Conglomerate-Forming Salt Using Temperature Cycling. *Crystal Growth & Design* **2016**, *16* (9), 5563-5570.

(100) Sogutoglu, L. C.; Steendam, R. R.; Meekes, H.; Vlieg, E.; Rutjes, F. P. Viedma ripening: a reliable crystallisation method to reach single chirality. *Chem Soc Rev* **2015**, *44* (19), 6723-6732.

(101) Buol, X.; Caro Garrido, C.; Robeyns, K.; Tumanov, N.; Collard, L.; Wouters, J.; Leyssens, T. Chiral Resolution of Mandelic Acid through Preferential Cocrystallization with Nefiracetam. *Crystal Growth & Design* **2020**, *20* (12), 7979-7988.

(102) Lorenz, H.; Seidel-Morgenstern, A. Processes to separate enantiomers. *Angew Chem Int Ed Engl* **2014**, *53* (5), 1218-1250.

(103) Kellogg, R. M. Practical Stereochemistry. *Acc Chem Res* **2017**, *50* (4), 905-914.

(104) Maggioni, G. M.; Fernández-Ronco, M. P.; van der Meijden, M. W.; Kellogg, R. M.; Mazzotti, M. Solid state deracemisation of two imine-derivatives of phenylglycine derivatives

via high-pressure homogenisation and temperature cycles. *CrystEngComm* **2018**, *20* (27), 3828-3838.

(105) Breveglieri, F.; Maggioni, G. M.; Mazzotti, M. Deracemization of NMPA via temperature cycles. *Crystal Growth & Design* **2018**, *18* (3), 1873-1881.

(106) Belletti, G.; Meekes, H.; Rutjes, F.; Vlieg, E. Role of Additives during Deracemization Using Temperature Cycling. *Cryst Growth Des* **2018**, *18* (11), 6617-6620.

(107) Harfouche, L. C.; Couvrat, N.; Sanselme, M.; Brandel, C.; Cartigny, Y.; Petit, S.; Coquerel, G. Discovery of New Proxyphylline-Based Chiral Cocrystals: Solid State Landscape and Dehydration Mechanism. *Crystal Growth & Design* **2020**, *20* (6), 3842-3850.

(108) Neurohr, C.; Marchivie, M.; Lecomte, S.; Cartigny, Y.; Couvrat, N.; Sanselme, M.; Subra-Paternault, P. Naproxen–Nicotinamide Cocrystals: Racemic and Conglomerate Structures Generated by CO2 Antisolvent Crystallization. *Crystal Growth & Design* **2015**, *15* (9), 4616-4626.

(109) Wacharine-Antar, S.; Levilain, G.; Dupray, V.; Coquerel, G. Resolution of (±)-Imeglimin-2,4-dichlorophenylacetate Methanol Solvate by Preferential Crystallization. *Organic Process Research & Development* **2010**, *14* (6), 1358-1363.

(110) Levilain, G.; Coquerel, G. Pitfalls and rewards of preferential crystallization. *CrystEngComm* **2010**, *12* (7), 1983-1992.

(111) Harfouche, L. C.; Brandel, C.; Cartigny, Y.; Ter Horst, J. H.; Coquerel, G.; Petit, S. Enabling Direct Preferential Crystallization in a Stable Racemic Compound System. *Mol Pharm* **2019**, *16* (11), 4670-4676.

(112) Lorenz, H.; Seidel-Morgenstern, A. Processes to separate enantiomers. *Angewandte Chemie International Edition* **2014**, *53* (5), 1218-1250.

(113) Lorenz, H.; Seidel-Morgenstern, A. Binary and ternary phase diagrams of two enantiomers in solvent systems. *Thermochimica Acta* **2002**, *382* (1-2), 129-142.

(114) Rougeot, C.; Hein, J. E. Application of continuous preferential crystallization to efficiently access enantiopure chemicals. *Organic Process Research & Development* **2015**, *19* (12), 1809-1819.

(115) Rekoske, J. E. Chiral separations. *American Institute of Chemical Engineers. AIChE Journal* **2001**, *47* (1), 2.

(116) Amabilino, D. B.; Kellogg, R. M. Spontaneous deracemization. *Israel Journal of Chemistry* **2011**, *51* (10), 1034-1040.

(117) Li, W. W.; Spix, L.; De Reus, S. C.; Meekes, H.; Kramer, H. J.; Vlieg, E.; Ter Horst, J. H. Deracemization of a racemic compound via its conglomerate-forming salt using temperature cycling. *Crystal Growth & Design* **2016**, *16* (9), 5563-5570.

(118) Bada, J. L.; Miller, S. L. Racemization and the origin of optically active organic compounds in living organisms. *Biosystems* **1987**, *20* (1), 21-26.

(119) Oketani, R.; Hoquante, M.; Brandel, C.; Cardinael, P.; Coquerel, G. Resolution of an Atropisomeric Naphthamide by Second-Order Asymmetric Transformation: A Highly Productive Technique. *Organic Process Research & Development* **2019**, *23* (6), 1197-1203.

(120) Oketani, R.; Marin, F.; Tinnemans, P.; Hoquante, M.; Laurent, A.; Brandel, C.; Cardinael, P.; Meekes, H.; Vlieg, E.; Geerts, Y. Deracemization in a Complex Quaternary System with a Second-Order Asymmetric Transformation by Using Phase Diagram Studies. *Chemistry–A European Journal* **2019**, *25* (61), 13890-13898.

(121) Kellogg, R. M. Practical stereochemistry. *Accounts of Chemical Research* **2017**, *50* (4), 905-914.

(122) Steendam, R. R.; Brouwer, M. C.; Huijs, E. M.; Kulka, M. W.; Meekes, H.; van Enckevort, W. J.; Raap, J.; Rutjes, F. P.; Vlieg, E. Enantiopure isoindolinones through Viedma ripening. *Chemistry–A European Journal* **2014**, *20* (42), 13527-13530.
(123) Engwerda, A. H.; Meekes, H.; Kaptein, B.; Rutjes, F.; Vlieg, E. Speeding up Viedma ripening. **2016**,
(124) Sögütoglu, L.-C.; Steendam, R. R.; Meekes, H.; Vlieg, E.; Rutjes, F. P. Viedma ripening: a reliable crystallisation method to reach single chirality. *Chemical Society Reviews* **2015**, *44* (19), 6723-6732.
(125) Xiouras, C.; Ter Horst, J. H.; Van Gerven, T.; Stefanidis, G. D. Coupling Viedma ripening with racemic crystal transformations: mechanism of deracemization. *Crystal Growth & Design* **2017**, *17* (9), 4965-4976.
(126) Noorduin, W. L.; Kaptein, B.; Meekes, H.; van Enckevort, W. J.; Kellogg, R. M.; Vlieg, E. Fast attrition-enhanced deracemization of naproxen by a gradual in situ feed. *Angewandte Chemie* **2009**, *121* (25), 4651-4653.
(127) van der Meijden, M. W.; Leeman, M.; Gelens, E.; Noorduin, W. L.; Meekes, H.; van Enckevort, W. J.; Kaptein, B.; Vlieg, E.; Kellogg, R. M. Attrition-enhanced deracemization in the synthesis of clopidogrel-a practical application of a new discovery. *Organic Process Research & Development* **2009**, *13* (6), 1195-1198.
(128) Noorduin, W. L.; Izumi, T.; Millemaggi, A.; Leeman, M.; Meekes, H.; Van Enckevort, W. J.; Kellogg, R. M.; Kaptein, B.; Vlieg, E.; Blackmond, D. G. Emergence of a single solid chiral state from a nearly racemic amino acid derivative. *Journal of the American Chemical Society* **2008**, *130* (4), 1158-1159.
(129) Noorduin, W. L.; Meekes, H.; van Enckevort, W. J.; Millemaggi, A.; Leeman, M.; Kaptein, B.; Kellogg, R. M.; Vlieg, E. Complete Deracemization by Attrition-Enhanced Ostwald Ripening Elucidated. *Angewandte Chemie International Edition* **2008**, *47* (34), 6445-6447.
(130) Noorduin, W. L.; van Enckevort, W. J.; Meekes, H.; Kaptein, B.; Kellogg, R. M.; Tully, J. C.; McBride, J. M.; Vlieg, E. The driving mechanism behind attrition-enhanced deracemization. *Angewandte Chemie International Edition* **2010**, *49* (45), 8435-8438.
(131) Viedma, C. Chiral symmetry breaking during crystallization: complete chiral purity induced by nonlinear autocatalysis and recycling. *Physical review letters* **2005**, *94* (6), 065504.
(132) Xiouras, C.; Fytopoulos, A.; Jordens, J.; Boudouvis, A. G.; Van Gerven, T.; Stefanidis, G. D. Applications of ultrasound to chiral crystallization, resolution and deracemization. *Ultrasonics Sonochemistry* **2018**, *43*, 184-192.
(133) Rougeot, C.; Guillen, F.; Plaquevent, J.-C.; Coquerel, G. Ultrasound-enhanced deracemization: toward the existence of agonist effects in the interpretation of spontaneous symmetry breaking. *Crystal Growth & Design* **2015**, *15* (5), 2151-2155.
(134) Cameli, F.; Xiouras, C.; Stefanidis, G. D. Intensified deracemization via rapid microwave-assisted temperature cycling. *CrystEngComm* **2018**, *20* (21), 2897-2901.
(135) Voorhees, P. W. The theory of Ostwald ripening. *Journal of Statistical Physics* **1985**, *38*, 231-252.
(136) Noorduin, W. L.; Vlieg, E.; Kellogg, R. M.; Kaptein, B. From Ostwald ripening to single chirality. *Angewandte Chemie International Edition* **2009**, *48* (51), 9600-9606.
(137) Noorduin, W. L.; Meekes, H.; Bode, A. A.; van Enckevort, W. J.; Kaptein, B.; Kellogg, R. M.; Vlieg, E. Explanation for the emergence of a single chiral solid state during attrition-enhanced Ostwald ripening: survival of the fittest. *Crystal Growth and Design* **2008**, *8* (5), 1675-1681.

(138) Steendam, R. R.; Ter Horst, J. H. Continuous total spontaneous resolution. *Crystal Growth & Design* **2017**, *17* (8), 4428-4436.

(139) Kozma, D. *CRC handbook of optical resolutions via diastereomeric salt formation*; Crc Press, 2001.

(140) Lam, W. H.; Ng, K. M. Diastereomeric salt crystallization synthesis for chiral resolution of ibuprofen. *AIChE Journal* **2007**, *53* (2), 429-437.

(141) Lorenz, H.; Perlberg, A.; Sapoundjiev, D.; Elsner, M. P.; Seidel-Morgenstern, A. Crystallization of enantiomers. *Chemical Engineering and Processing: Process Intensification* **2006**, *45* (10), 863-873.

(142) Murakami, H. From racemates to single enantiomers–chiral synthetic drugs over the last 20 years. *Novel optical resolution technologies* **2007**, 273-299.

(143) Collet, A. Resolution of racemates: did you say "classical"? *Angewandte Chemie International Edition* **1998**, *37* (23), 3239-3241.

(144) Wouters, J.; Quéré, L. *Pharmaceutical salts and co-crystals*; Royal Society of Chemistry, 2011.

(145) Springuel, G.; Robeyns, K.; Norberg, B.; Wouters, J.; Leyssens, T. Cocrystal Formation between Chiral Compounds: How Cocrystals Differ from Salts. *Crystal Growth & Design* **2014**, *14* (8), 3996-4004.

(146) Sánchez-Guadarrama, O.; Mendoza-Navarro, F.; Cedillo-Cruz, A.; Jung-Cook, H.; Arenas-García, J. I.; Delgado-Díaz, A.; Herrera-Ruiz, D.; Morales-Rojas, H.; Höpfl, H. Chiral resolution of RS-praziquantel via diastereomeric co-crystal pair formation with L-malic acid. *Crystal Growth & Design* **2016**, *16* (1), 307-314.

(147) Harmsen, B.; Leyssens, T. Dual-drug chiral resolution: enantiospecific cocrystallization of (s)-ibuprofen using levetiracetam. *Crystal Growth & Design* **2018**, *18* (1), 441-448.

(148) Springuel, G.; Norberg, B.; Robeyns, K.; Wouters, J.; Leyssens, T. Advances in Pharmaceutical Co-crystal Screening: Effective Co-crystal Screening through Structural Resemblance. *Crystal Growth & Design* **2011**, *12* (1), 475-484.

(149) Wang, J.; Peng, Y. Resolution of Halogenated Mandelic Acids through Enantiospecific Co-Crystallization with Levetiracetam. *Molecules* **2021**, *26* (18), 5536.

(150) Braga, D.; Casali, L.; Grepioni, F. The Relevance of Crystal Forms in the Pharmaceutical Field: Sword of Damocles or Innovation Tools? *International Journal of Molecular Sciences* **2022**, *23* (16), 9013.

(151) Sánchez-Guadarrama, O.; Mendoza-Navarro, F.; Cedillo-Cruz, A.; Jung-Cook, H.; Arenas-García, J. I.; Delgado-Díaz, A.; Herrera-Ruiz, D.; Morales-Rojas, H.; Höpfl, H. Chiral Resolution of RS-Praziquantel via Diastereomeric Co-Crystal Pair Formation with l-Malic Acid. *Crystal Growth & Design* **2015**, *16* (1), 307-314.

(152) Songsermsawad, S.; Nalaoh, P.; Promarak, V.; Flood, A. E. Chiral Resolution of RS-Baclofen via a Novel Chiral Cocrystal of R-Baclofen and L-Mandelic Acid. *Crystal Growth & Design* **2022**, *22* (4), 2441-2451.

(153) Urbanus, J.; Roelands, C. M.; Verdoes, D.; Jansens, P. J.; ter Horst, J. H. Co-crystallization as a separation technology: controlling product concentrations by co-crystals. *Crystal growth & design* **2010**, *10* (3), 1171-1179.

(154) Roa Engel, C. A.; Straathof, A. J.; Zijlmans, T. W.; van Gulik, W. M.; van der Wielen, L. A. Fumaric acid production by fermentation. *Applied microbiology and biotechnology* **2008**, *78* (3), 379-389.

(155) Urbanus, J.; Roelands, C. M.; Mazurek, J.; Verdoes, D.; ter Horst, J. H. Electrochemically induced co-crystallization for product removal. *CrystEngComm* **2011**, *13* (8), 2817-2819.

(156) Guillot, M.; de Meester, J.; Collard, L.; Riant, O.; Leyssens, T. Co-Crystallization-Induced Spontaneous Deracemization: An Optimization Study. *Organic Process Research & Development* **2021**, *25* (4), 884-891.

Chapter 2 – Experimental Methods

The equipment and the basic principles related to the experimental methods used to generate data are presented in this chapter. The experimental details and instrumental parameters are developed in the specific chapters where they are used.

2.1. Differential Scanning Calorimetry (DSC)

Differential Scanning Calorimetry (DSC) is a thermal method used to compare the thermal behavior of a material with a reference.[1, 2] In this thesis, the thermal analyses are performed with a DSC 214 Polyma (Netzsch Geratebau GmbH), which is a heat-flux type DSC. With this DSC type, separate aluminum pans undergo a precise temperature program in the same oven, whose atmosphere is regulated with a nitrogen gas flow. One pan contains the sample to analyze, and the other stays empty to serve as a reference. During the analysis, the temperature of the two pans is measured with two thermocouples to compute the temperature difference ΔT between the sample and the reference. From the recorded ΔT signal and the sample mass m, the specific heat flux Q absorbed by the sample is automatically computed. Thermograms are produced after the DSC analysis and consist in plots with the heat flux Q on the y-axis, and time t or temperature T on the x-axis. The thermograms generated in this thesis represent a positive heat flux Q for an increase in the y-axis (exo up). When the sample material goes through a phase transformation, such as melting or crystallization, it consumes or produces heat, and this translates as a deviation from the baseline in the thermogram. Thermal peaks are obtained, that correspond to exothermic thermal events when peaks are pointing up, and endothermic events when they are pointing down. Therefore, the thermograms provide precise thermal information, such as the temperature of a thermal phenomenon, and the enthalpy associated to it, which is computed from the integration of the peak area with regards to the baseline. In this thesis, DSC analyses are performed to assess the purity of solids in Chapter 5, and to measure the thermal behavior of binary solid mixtures in Chapter 3. The Netzsch Thermal Analyses Proteus Software is used for the data treatment. Every corresponding thermal event peak is evaluated from the determination of its enthalpy, and its onset, peak, and endset temperatures.

2.2. X-ray Powder Diffraction (XRPD)

X-Ray Powder Diffraction (XRPD) is a solid identification technique based on structural analysis of crystalline powders from their interaction with X-rays.[3, 4] When an electromagnetic wave interacts with a material whose particles are periodically arranged and separated by a distance close to the incident wavelength, the phenomenon of diffraction occurs. Because of the periodic nature of a crystal, the diffraction of X-rays occurs only for specific orientations between the wave and the material, and more precisely between the wave front and the high electronic density crystal planes that are characterized by h, k and l Miller indexes. These orientations are characteristic of the crystal packing (lattice parameters, symmetries, space group) of the investigated crystalline solid. During XRPD measurements, a powder sample is exposed to an X-ray monochromatic beam generated with an X-ray source with a certain incidence angle θ. From the other side, whether it is by transmission or reflection, a detector is measuring the intensity of the beam diffracted by the sample at an angle 2θ. Throughout the analysis, a goniometer changes the incidence angle θ, and therefore the detection angle 2θ. X-rays are diffracted by the sample when the Bragg law (Equation 2.1) is satisfied, with d_{hkl} being the reticular distance between hkl diffracting planes (i.e crystal planes of high electronic density), n a positive integer giving the diffraction order, and λ the wavelength of the incident X-ray beam.[5]

$$2d_{hkl}\sin(\theta) = n\lambda \qquad \text{Equation 2.1}$$

From a XRPD analysis, a diffractogram $I = f(2\theta)$ is obtained, which gives the measured diffracted beam intensity I on the y-axis, as a function of the angular position 2θ on the x-axis. The acquired diffraction patterns can be conceived as a unique fingerprint of a crystal packing, because they present specific diffraction peaks whose intensity and position are function of a unique spatial arrangement of the particles in the crystal packing. In this study, XRPD is used for solid phase identification. In Chapter 3, it is used to identify a new solid phase, for instance a cocrystal, by comparison with XRPD reference patterns of pure coformers after a cocrystal screening experiment. In Chapter 4, it is used to identify the nature of the solid phases obtained from filtration of equilibration experiments for phase diagrams assessment. In Chapter 5, XRPD is used to assess the structural purity and the solid form control of solids obtained from crystallization experiments. The data treatment is done with the software DIFFRAC.EVA from Bruker, and Origin Pro 2017.

2.3. Solubility Measurements

Solubility measurements constitute a large part of the results produced in this thesis. In Chapters 3 and 5, the solubility curves and Van ‘t Hoff plots of many pure components are generated with the Saturation Temperature Measurement (STM) method by using a Crystal 16 reactor. Additionally, in Chapter 3, the STM method is used as a screening method on binary mixtures of coformers to detect cocrystal formation through the apparition of a less soluble solid. In Chapters 4 and 5, the equilibration method permits phase diagrams assessment, with the solubility measurements of many multicomponent mixture suspensions equilibrated with a Polar Bear Plus reactor, whose saturated solutions are quantified with either gravimetric analysis or a spectroscopic quantification method.

2.3.1. Saturation Temperature Measurement with Crystal 16 (STM)

Crystal 16 is a multi-reactor platform designed to perform temperature-dependent studies on 16 samples simultaneously. It consists of four independent chambers, each accommodating four standard glass vials with a capacity of up to 2 mL. Within each chamber, there is a light transmission probe to detect changes in the turbidity of the vial. The temperature control is precise and permits the measurement of turbidity changes in a dispersed suspension with temperature changes in the well, by heating and cooling.[6-8] Turbidity is a measure of the light transmission through a sample. When a clear solution is present in the vial, the light passes through the sample undisturbed, resulting in maximum transmission of light (100 %). However, if a suspension is present in the sample, the light is blocked, and the transmission of light is reduced (< 100 %). By increasing the temperature T of a homogeneously stirred suspension, the crystals dissolve progressively in the solvent until the suspension turns into a clear solution and the light transmission reaches an upper limit of 100 %. This upper limit temperature, at which full dissolution is occurring, is known as the clear point temperature, also called saturation temperature T_{sat}. Therefore, for a given T_{sat} , the composition of the sample corresponds to the solubility value. When a clear solution is cooled to an adequate supersaturation, the nucleation occurs, and the presence of crystals will obstruct the transmission of light. The temperature at which this happens is the cloud point temperature. During Crystal 16 experiments, accurate temperature cycles are set so that the samples undergo different cycles of dissolution and nucleation, which precises the measurement of the solubility value. The masses of solid components and solvents used to prepare the suspension compositions are accurately weighed to precise the measure.

2.3.2. Equilibration Method with Polar Bear Plus

Polar Bear Plus from Cambridge Reactor Design is a heating and cooling platform that provides precise temperature control to ± 0.1 °C, and an efficient magnetic stirring that guarantees the samples homogeneity. The apparatus possesses interchangeable aluminum plates that present sets of wells of different volumes for multiple vials, with a corresponding insulating cover to ensure that the vials are maintained at temperature. Polar Bear Plus is used in this study to equilibrate isothermal suspensions for solubility measurements and phase diagram data points acquisition. Known compositions are prepared in vials to be stable suspensions at the selected temperature. The vials are sealed to prevent solvent evaporation. For some experiments, the suspensions are seeded with seed crystals of the stable solids from the corresponding thermodynamic system. The samples are stored isothermally under stirring for a certain equilibration time, after which the thermodynamic system is considered to have reached a solid-liquid equilibrium, with a solid phase that cannot evolve anymore and a saturated solution whose composition is fixed. The saturated solution in a vial is sampled with a syringe and a filter, to ensure that no solid particles is sampled. From a known mass of saturation solution sampled, the composition of the solution is quantified, with either gravimetric analysis or a spectroscopic analytical quantification method. Gravimetric analysis permits the measurement of the content in dissolved material of a solution through a mass balance. From a known sample solution mass, the solvent is evaporated, and the mass of solid residue is weighed. The measured masses permit to calculate the total concentration of the corresponding solution. In this study, another analytical quantification method is developed in Chapter 4 with ultraviolet-circular dichroism spectroscopy and is also used in Chapter 5. With this method, a known mass of sampled solution is diluted to the calibration range of the method and analyzed. Its light absorption is measured at different wavelengths and is proportional to the component concentrations, which permits the complete quantification of the solution.

2.4. Absorption Spectroscopy

Absorption spectroscopy is an analytical technique that is used to measure a component concentration in a sample, based on the quantized interaction of an electromagnetic radiation with matter.[9, 10] When a radiation goes through a sample, its photons can be absorbed if the photon energy E matches the energy difference ΔE required for an electronic transition between two energy levels of a molecule, which would excite the latter to a higher energy level. The photon energy is inversely proportional to the wavelength λ of the radiation, as expressed by the Planck-Einstein relation (Equation 2.2), where h is the Planck's constant, and c the speed of light.

$$E = \frac{hc}{\lambda} \qquad \text{Equation 2.2}$$

The molecular absorption of electromagnetic radiations at specific wavelengths is directly proportional to the concentration of the absorbing components contained in the sample, as expressed by the Beer-Lambert law (Equation 2.3).[11] It defines the absorbance A of a sample as a function of the molar absorptivity coefficient ε of an absorbing molecule at a given wavelength λ, the absorbing component concentration C, and l the path length the radiation travels through the sample.

$$A = \varepsilon C l \qquad \text{Equation 2.3}$$

Absorption spectroscopy is performed with a spectrometer, which consists of an electromagnetic radiation source, a monochromator, a sample cell holder, and a detector. The radiation source emits radiations over a range of wavelengths, and the monochromator selects a specific wavelength that goes through the sample. The detector measures the final intensity I of the radiation that crosses the sample and compares it to the initial intensity I_0 to compute the absorbance A as in Equation 2.4.

$$A = \log \frac{I_o}{I} \qquad \text{Equation 2.4}$$

An absorption spectrum $A = f(\lambda)$ is obtained from an experiment that is set across a range of varying wavelengths λ, and shows the change in the measured absorbance by the sample. By preparing samples of known compositions and by measuring their absorption spectra under the same experimental conditions, it is possible to calibrate a quantification method on a defined calibration range. In this thesis, absorption spectroscopy is used in Chapter 4 to develop a multicomponent chiral quantification method with ultraviolet-circular dichroism spectroscopy. The developed method is also used in Chapter 5 for the assessment of sample purities from crystallization experiments with their component quantification.

2.5. Raman Spectroscopy

Raman spectroscopy is a vibrational spectroscopy technique that gives information about the chemical composition and the molecular structure of samples. It is used in Chapter 5 to monitor the nature of solid phases in suspensions over time and solvent addition. Raman spectroscopy is based on the inelastic scattering of photons during an energy transfer between an incident radiation and irradiated molecules, which results in an energy shift of the scattered photons named Raman shift.[12] The scattering is said inelastic because the energy of the scattered photon is different from the incident photon, and this difference in energy corresponds to the energy required to excite a molecule to a different vibrational mode. With Raman spectroscopy, a laser of near-infrared light is used to bring molecules from a ground state to a higher vibration state by using more energy than required, and this triggers different types of scattering when the molecules relax after excitation.[13] Only a small fraction of the incident light is scattered inelastically with a Raman shift, which is measured by analyzing the scattered light with a Raman spectrometer. A Raman spectrum shows the intensity of the scattered radiation, as a function of the Raman shift, expressed in wavenumbers, and is characteristic of the vibrational modes of the sample molecules. The amount of energy that is transferred between the laser and the sample is thus distinctive of the material and the bonds linking its molecules. Therefore, Raman spectroscopy can be used to identify different crystal structures, even when they are made of the same molecules. However, Raman spectroscopy does not distinguish enantiopure crystal structures.

2.6. References

(1) Haines, P.; Reading, M.; Wilburn, F. Differential thermal analysis and differential scanning calorimetry. In *Handbook of thermal analysis and calorimetry*, Vol. 1; Elsevier, 1998; pp 279-361.
(2) Höhne, G. W. H.; Hemminger, W.; Flammersheim, H.-J.; Höhne, G.; Hemminger, W.; Flammersheim, H.-J. Theoretical fundamentals of differential scanning calorimeters. *Differential scanning calorimetry* **2003**, 31-63.
(3) Hammond, C. *The basics of crystallography and diffraction*; International Union of Crystallography texts on crystallography, 2015.
(4) Waseda, Y.; Matsubara, E.; Shinoda, K. *X-ray diffraction crystallography: introduction, examples and solved problems*; Springer Science & Business Media, 2011.
(5) Bragg, W. H.; Bragg, W. L. The reflection of X-rays by crystals. *Proceedings of the Royal Society of London. Series A, Containing Papers of a Mathematical and Physical Character* **1913**, *88* (605), 428-438.
(6) Srisanga, S.; ter Horst, J. H. Racemic compound, conglomerate, or solid solution: phase diagram screening of chiral compounds. *Crystal growth & design* **2010**, *10* (4), 1808-1812.
(7) Ter Horst, J.; Deij, M.; Cains, P. Discovering new co-crystals. *Crystal growth and design* **2009**, *9* (3), 1531-1537.
(8) Kongsamai, P.; Maneedaeng, A.; Flood, C.; ter Horst, J. H.; Flood, A. E. Effect of additives on the preferential crystallization of L-asparagine monohydrate. *The European Physical Journal Special Topics* **2017**, *226*, 823-835.
(9) Field, L. D.; Li, H. L.; Magill, A. M. *Organic structures from spectra*; John Wiley & Sons, 2020.
(10) Skoog, D. A.; Holler, F. J.; Crouch, S. R. *Principles of instrumental analysis*; Cengage learning, 2017.
(11) Swinehart, D. F. The beer-lambert law. *Journal of chemical education* **1962**, *39* (7), 333.
(12) Bakeev, K. A. *Process analytical technology: spectroscopic tools and implementation strategies for the chemical and pharmaceutical industries*; John Wiley & Sons, 2010.
(13) Long, D. A.; Long, D. *The Raman effect: a unified treatment of the theory of Raman scattering by molecules*; Wiley Chichester, 2002.

Chapter 3 - Comparing and Quantifying the Efficiency of Cocrystal Screening Methods for Praziquantel

Maxime D. Charpentier[1], **Jan-Joris Devogelaer**[2], **Arnoud Tijink**[2], **Hugo Meekes**[2], **Paul Tinnemans**[2], **Elias Vlieg**[2], **René de Gelder**[2], **Karen Johnston**[3], **Joop H. ter Horst**[1,4]

1. EPSRC Centre for Innovative Manufacturing in Continuous Manufacturing and Crystallization (CMAC), University of Strathclyde, Technology and Innovation Centre, 99 George Street, Glasgow G1 1RD, U.K.

2. Radboud University, Institute for Molecules and Materials, Heyendaalseweg 135, 6525AJ Nijmegen, The Netherlands

3. Department of Chemical and Process Engineering, University of Strathclyde, James Weir Building, 75 Montrose Street, Glasgow G1 1XJ, U.K.

4. Univ Rouen Normandie, Laboratoire Sciences et Méthodes Séparatives (SMS), UR 3233, F-76000 Rouen, France

Abstract

Pharmaceutical cocrystals are highly interesting due to their effect on physicochemical properties and their role in separation technologies, particularly for chiral molecules. Detection of new cocrystals is a challenge, and robust screening methods are required. As numerous techniques exist that differ in their crystallization mechanisms, their efficiencies depend on the coformers investigated. The most important parameters characterizing the methods are the (a) screenable coformer fraction, (b) coformer success rate, (c) ability to give several cocrystals per successful coformer, (d) identification of new stable phases, and (e) experimental convenience. Based on these parameters, we compare and quantify the performance of four methods: liquid-assisted grinding, solvent evaporation, saturation temperature measurements of mixtures, and a novel thermal method based on binary eutectic temperature differences after melt crystallization. These methods were used to screen 30 molecules, predicted by a network-based link prediction algorithm (described in Cryst. Growth Des. ***2021*** *21 (6), 3428-3437) as potential coformers for the target molecule praziquantel. The solvent evaporation method and the thermal method presented more drawbacks than advantages, liquid-assisted grinding emerged as the most successful and the quickest, while saturation temperature measurements provided equally good results in a slower route yielding additional solubility information relevant for future screenings, single-crystal growth, and cocrystal production processes. Seventeen cocrystals were found, with 14 showing stability, and 12 structures resolved.*

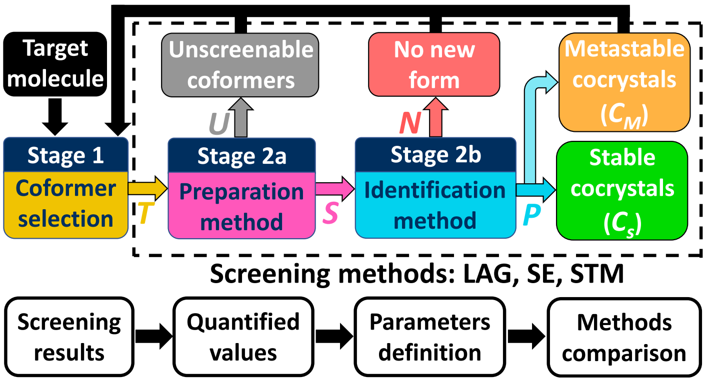

3.1. Introduction

Multicomponent crystal classes vary with the nature of the components sharing the structure, and include salts consisting of ions, solvates when one or more of the components is a solvent, or cocrystals when non-solvent neutral coformers associate as supramolecular synthons.[1-4] For structures containing more than two components, combined subclasses may also exist, for instance, cocrystal solvates.[2] Screening for multicomponent crystals, and especially cocrystals, is of strong interest to the pharmaceutical industry as it is a route toward optimization of drug physicochemical properties, such as solubility, bioavailability, mechanical/humidity/thermal stability, and compressibility,[5-11] without modifying their medical action, and can also be used as a separation technology.[12] When active pharmaceutical ingredients (APIs) are chiral, discovering solid forms can also prompt new chiral separation possibilities.[13-16] The marketing of enantiopure drugs is an essential topic because racemic mixtures, that is, equimolar ratio of enantiomers, contain only half of the active form, the other half being the opposite-enantiomer impurity, which, besides bringing economical constraints,[17] can also produce unwanted side effects.[18-20] As 90-95% of chiral systems synthetized as racemic mixtures crystallize as racemic compounds, that is, crystal structures containing both enantiomers, their chiral resolution is tricky or even impossible.[21] Introducing only achiral coformers to a racemic compound system can generate multicomponent crystals, that can either be racemic or be a conglomerate of enantiopure crystals.[22, 23] For conglomerates, chiral resolution processes are then possible such as preferential crystallization, temperature-cycling deracemization, or Viedma ripening.[24-34] On introducing a chiral coformer, a dissymmetry is induced when forming multicomponent crystals, and outcomes can be either diastereomeric pairs of enantiopure phases or enantiospecific systems, that is, only one enantiomer forms a new multicomponent crystal. Both outcomes are favorable for chiral resolution.[13-15, 35]

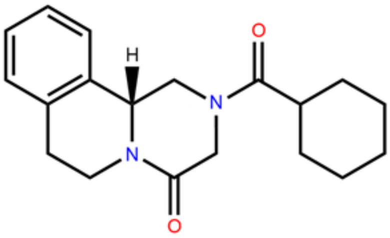

Figure 3.1: Molecular structure of Praziquantel (PZQ)

Praziquantel (PZQ) (shown in Figure 3.1), the model chiral compound of this study, presents several challenges that could be solved by multicomponent crystal formation. PZQ is the standard medicine for a parasitic worm infection named schistosomiasis causing the death of about 280,000 people annually in underdeveloped regions of Africa, South America, and Asia.[36-38] Searches for multicomponent crystals are performed either to improve the drug physicochemical properties[39-42] or to separate enantiomers with the purpose to produce an enantiopure drug.[43] Indeed, chiral resolution strategies are sought for PZQ,[43-45] currently marketed as a racemic compound, as only its R-enantiomer possesses the desired pharmaceutical action, whereas the S-enantiomer causes side effects such as a bitter taste. Moreover, the presence of the undesired enantiomer means a higher overall dosage is required that is problematic for young children, and chiral separation would lower this dosage. Screening of new multicomponent crystals is then necessary to find systems allowing enantiomeric resolution.

As PZQ does not possess ionizable functions, salt formation strategy is excluded, while cocrystallization and solvate formation are always possible for organic molecules as these mechanisms involve intermolecular interactions like hydrogen bonds.[46, 47] Cocrystals are generally preferred as they are more stable than solvates with temperature and have a larger accessible pool of compounds "Generally Recognized As Safe" (GRAS compounds) for coformers than solvate-formers,[48] although pure APIs can be more easily separated from solvates than from cocrystals.[49] Cocrystallization is, therefore, a topic of interest within the pharmaceutical industry in recent years with the emergence of many cocrystal preparation methods, which can involve transformations in the solid-state induced by energy sources that can be mechanical (grinding,[50] cryomilling, and high-shear granulation), thermal (thermal treatment, crystallization from the melt, and hot-melt extrusion), or based on sound/ultrasound, microwaves, or electrical current.[51, 52] Cocrystallization can be mediated by the presence of solvents, stirring slurries to induce a phase transition, cooling/evaporating/adding an antisolvent to undersaturated solutions, or using supercritical fluids, spray-drying, and freeze-drying technologies.[52, 53] All these methods present advantages and disadvantages, with alternative paths to cocrystal synthesis and experimental limitations that vary with the nature of the coformers. Indeed, the molar ratio between the coformers used will differ with the method, as well as the nature and amount of energy applied. Some techniques can also be non-applicable to certain coformers that can for instance present thermal or mechanical degradation, reactions with a component/solvent, or formation of amorphous material or unwanted phases. No cocrystallization technique has proven to be universal, but the choice of methods used for detection of cocrystal formation can be optimized.

A typical screening technique is liquid-assisted grinding (LAG),[54-58] which is a mechanochemical method that is based on absorption of kinetic energy to enable cocrystallization. Here, the components are ground manually or with a ball mill. Potential cocrystallization is enhanced with a small amount of solvent added as a catalyst to assist the transformation process. Solvent evaporation (SE)[55, 56, 59] is also commonly used and relies on the evaporation of a small volume of initially undersaturated solution with a volatile solvent. The evaporation gradually concentrates the compositions to drive cocrystallization. Another solvent-based screening method, that we name STM, uses saturation temperature measurements of coformer mixtures obtained via cooling crystallization.[60-63] Saturation temperatures, that is, solubilities, of coformers are measured separately and then for mixtures with compositions chosen as a function of pure coformers solubilities. A measured mixture saturation temperature that is greater than a chosen reference temperature, highlights a lower solubility, and indicates formation of a stable cocrystal. These three techniques together are often selected due to their accessibility in research labs, while utilizing very different cocrystallization mechanisms/pathways.

In this study, we aim to review the experimental screening methods by applying them in a wide screening protocol for PZQ cocrystals that involved 30 coformers selected using a network-based link prediction algorithm.[64-67] Seventeen new multicomponent cocrystals of PZQ were identified, with 12 structures resolved. The coformer prediction method using network science and single-crystal structure characterization is discussed in detail by Devogelaer et al.[67] In the present chapter, we focus on the cocrystal preparation and identification results that were obtained using the four different experimental methods: LAG, SE, STM, and a novel thermal technique based on binary eutectic temperature differences after melt crystallization (EUT). Using our screening results, we provide a thorough comparison of experimental methods with quantified parameters that are (a) the fraction of screenable coformers, (b) the coformers success rate, (c) the ability to give several cocrystals per successful coformer, and (d) the identification of new stable phases. By comparing the methods' parameters and their experimental convenience, we aim to conclude on their efficiency and provide relevant advice on optimization of cocrystal screening method selection.

3.2. Cocrystal Screening Methods

3.2.1. Materials and Experimental Protocols

(RS)-PZQ was provided by Merck KGaA (Darmstadt, Germany). The coformers used for screening are listed in the Appendix A, with their purities and chemical suppliers in Tables A1 and A2 and their molecular structures in Figure A1. For SE and LAG experiments, the following solvents with purities higher than reagent grade were used: methanol, ethanol, isopropanol, acetonitrile, acetone, and ethyl acetate. Recently purchased ethanol, acetonitrile, and ethyl acetate with purities higher than 99% were used for the STM method to minimize the introduction of impurities and water.

3.2.2. X-ray Powder Diffraction

X-ray powder diffraction (XRPD) was used to identify a new phase by comparison with reference patterns of pure coformers. For clarity, figures in this chapter contain only the XRPD reference of stable polymorphs from pure starting coformers. LAG and SE samples were placed as a thin film of powder on zero-background (557)-silicon wafers and measured with a Malvern Panalytical Empyrean diffractometer. The diffractograms were measured in Bragg-Brentano geometry (reflection mode) using monochromatic Cu Kα radiation from a sealed LFF tube and using a PIXcel3D 1x1 detector. A continuous scan was performed in the $5° < 2\theta < 30°$ range with a step size of 0.013° and a scan speed of $0.11° s^{-1}$. STM samples were analyzed using a Bruker D8 Advance II diffractometer with Debye–Scherrer transmission from Cu Kα source radiation (1.541 Å) with an operating voltage of 40 kV, current of 50 mA, a Kα1 Johansson monochromator, and a 1 mm anti-divergence slit. A scanning range of 2θ values between 4° and 35° was applied with a scan speed of $0.017° s^{-1}$.

3.2.3. Solvent Selection and Pure Component Solubility Determination

A selection of solvents able to dissolve PZQ and coformers was required to perform LAG, SE, and STM cocrystal screening experiments. As most coformers from the list are to some extent polar, the following protic and aprotic polar solvents were chosen: methanol, ethanol (EtOH), isopropanol, acetonitrile (MeCN), acetone, and ethyl acetate (AcOEt), all commonly used in industry. For LAG and SE, the most appropriate solvent from this list was always chosen, that is, solubilizing but not too much. Experimental details can be found in the Appendix A (Table A3). For STM, only EtOH, MeCN, and AcOEt are selected as they present different chemical functions and can cope with experiments at temperatures higher than 60 °C. Saturation temperatures T_{sat} (i.e solubility) of suspensions stirred at 700 rpm in 2mL vials were measured using the Crystal16 (Technobis, Alkmaar, the Netherlands) system. The following temperature profile was used: dissolution at 60 °C followed by 3 cycles of cooling to -5 °C (-0.5 °C/min) and heating to 60 °C (0.3 °C/min), with isothermal periods of 90 min at -5 °C and 30 min at 60 °C. The clear point temperature in each cycle was identified as the temperature at which the light transmission passing through a sample reached 100%. The average of the three clear point temperatures was taken as the saturation temperature T_{sat} of the sample. The saturation temperatures were fitted with the Van 't Hoff equation, allowing the estimation of any solubility of a pure component in the observed temperature range by using heat of fusion and melting temperature as fitting parameters. Solubility data and Van ’t Hoff plots for PZQ and coformers can be found in the Appendix A (Section A3).

3.2.4. Cocrystal Preparation Methods

3.2.4.1. Liquid-Assisted Grinding (LAG)

Compositions screened with LAG contain amounts of solvent substantially lower than needed to dissolve the solid phases and undergo solid conversion without going through a clear solution state. About 50 mg of stoichiometric powders (1:1 molar ratio) containing PZQ and the coformer were ground in the presence of 40 µL of solvent in a Retsch MM 400 ball mill (Retsch GmbH, Haan, Germany). Grinding was performed in 1.5 mL stainless steel jars with one 5 mm stainless steel ball per jar for 30 min with a milling frequency of 25 Hz. Final solids were analyzed with XRPD.

3.2.4.2. Solvent Evaporation (SE)

About 50 mg of a 1:1 stoichiometric mixture was prepared and dissolved in a solvent. The samples were then transferred to 10 mL glass vials, covered with parafilm in which five small holes were pierced with a needle, and left for complete evaporation of the solvent. The resulting solids were identified by XRPD.

3.2.4.3. Saturation Temperature Measurement of Mixtures (STM)

While the LAG and SE methods use samples having an arbitrary stoichiometry in coformers to screen (1:1 in this study), the STM method uses stoichiometries determined by the pure component solubilities, as the compositional range of the cocrystal stability domain in a solvent depends on these solubilities.[60] When components have different solubilities, a stoichiometric solution for cocrystal preparation is indeed not optimal and can lead to missing a new cocrystal discovery.[53] First, solubility curves of pure coformer and PZQ in the selected solvent were determined using the experimental protocol in section 3.2.3. Then, reference temperatures T_r were chosen as working temperatures higher than room temperature to ensure the isolation of a solid phase at the end of the experiment. The pure PZQ and pure coformer solubility values at a reference temperature T_r were computed from the Van ‘t Hoff plots obtained from solubility data. The computed concentrations in components were prepared experimentally to obtain samples with a stoichiometry described by the molar ratio $M_{PZQ/cof}$ between the coformer and PZQ in solution. Finally, the screening was performed for each sample by measuring the experimental saturation temperature T_{sat} of the mixtures with the experimental protocol in section 3.2.3. If T_{sat} measured for the mixtures are equal to the reference temperature T_r (ideal solution behavior) or lower (components influencing each other solubilities), it indicates that no new phase was formed. On the other hand, a saturation temperature T_{sat} higher than T_r for a mixture indicates the formation of a more stable cocrystal phase.[68] The STM method gives therefore a quantified measurement on the existence of a new cocrystal phase. After the three temperature cycles, a final cooling to -5 °C (-0.5 °C/min) was performed and the crystallized material was collected for XRPD analysis to confirm the results.

3.2.4.4. Binary Eutectic Temperature Differences after Melt Crystallization (EUT)

Thermal methods can be used for cocrystal screening with melt crystallization, such as Kofler method, for which two coformers are melted adjacent to one another, that can give rise to a cocrystal crystallizing at the interface where the compounds mix.[69, 70] EUT is a novel cocrystallization screening technique we propose, based on thermal analyses of physical mixtures with differential scanning calorimetry (DSC). Usual thermal methods involve one heating cycle in DSC on a single physical mixture to detect an exothermic event as a solid-state transition or melt-recrystallization, toward a more stable phase, that is, a cocrystal.[71-75] Here, we add a second heating after crystallization from the melt, with equilibrium ensured by an annealing step. This is done for two opposite composition ratios close to pure components, for example, 1:9 and 9:1, to prove cocrystal formation with different equilibria invariant temperatures measured, that are usually eutectics. Indeed, in a temperature binary system, several equilibria are possible depending on the formation of intermediate phases. If no cocrystal forms, the equilibrium between both components is a eutectic equilibrium (Figure 3.2, left). The two compositions on either side of the eutectic point will then undergo a beginning of melting (solidus) at the exact same temperature T_E that corresponds to the first endotherm in DSC heating. If a cocrystal with congruent melting forms (Figure 3.2, middle), the system behaves as two neighboring binary systems: the API and cocrystal one with a eutectic equilibrium at T_{E1}, and the coformer and cocrystal one with a eutectic equilibrium at T_{E2}. As pure API and coformer have different melting points, T_{E1} and T_{E2} are not the same. It means that the two compositions in each binary, for instance, 9:1 and 1:9 molar ratios, exhibit different first endotherms in DSC from stable equilibrium. The same behavior is observed for a cocrystal system with non-congruent melting (Figure 3.2, right), except that the invariant events natures are different: one is a peritectic at temperature T_P and the other a eutectic at temperature T_{E1}. It is important to note that during first heating, solid-state transition or melt-recrystallization can still be measured as proof of cocrystallization as for the other usual thermal techniques.

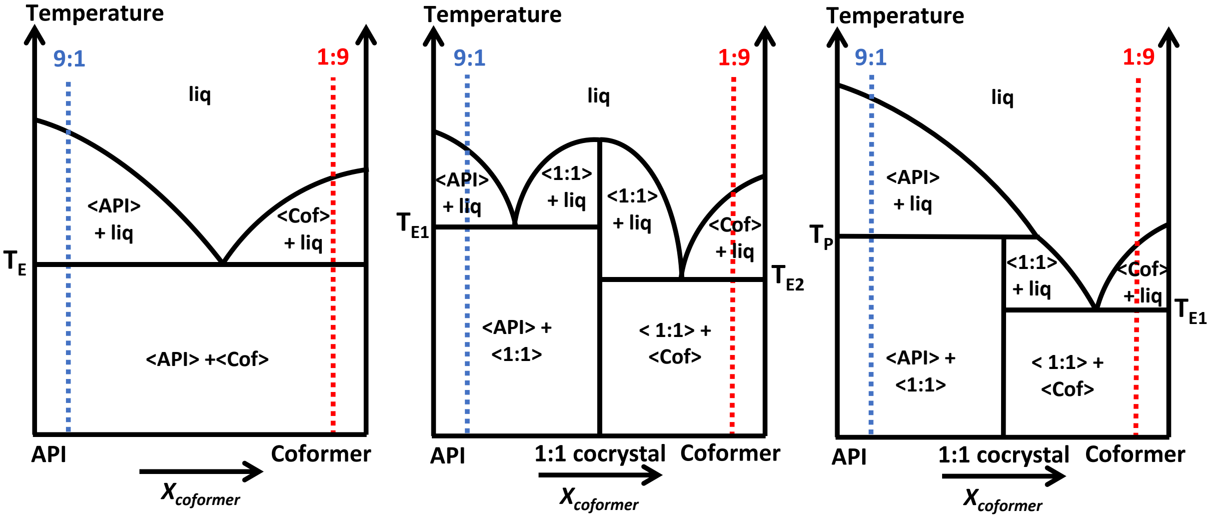

Figure 3.2: Binary phase diagrams between an API and a coformer, in the case of: no cocrystal i.e. simple eutectic equilibrium (left), a congruent melting cocrystal (middle), a non-congruent melting cocrystal (right). Vertical dashed lines correspond to compositions targeted experimentally. Each intersection between the dashed lines and a solid black line from the phase diagram corresponds to an endothermic event upon heating in the DSC.

Thermal analyses of PZQ, coformers, and physical mixtures between both, with 1:9 and 9:1 molar ratio, were performed using a Polyma214 DSC (Netzsch Geratebau GmbH). About 5 mg of solids were weighed out in aluminum pans and heated to temperatures about 20°C higher than the melting temperature (the highest pure component one for mixtures) at a heating rate of 5 °C/min. Crystallization from the melt was then performed by cooling down to 20 °C at a rate of 5 °C/min. When cooling was not sufficient, an isothermal annealing step above the glass transition of materials was added. A second heating step at 5 °C/min until melting was then performed. An inert atmosphere was maintained in the calorimeter by purging nitrogen gas.

3.3. Results

The strategy of a cocrystal screening campaign is to improve the properties of a target molecule by finding new stable cocrystals (see Figure 3.3). In the case of PZQ, the aim is to find a cocrystal system permitting chiral separation. The first stage of cocrystal screening consists of selecting appropriate coformers likely to form cocrystals with the target molecule (Figure 3.3, stage 1). This work has been covered for this PZQ cocrystal screening campaign in an article from Devogelaer et al.[67] With a network-based link prediction algorithm for coformer selection using data mining techniques applied to the Cambridge Structural Database (CSD), a list of 30 coformers was predicted and screened experimentally. The list of molecular structures and attributed ranks for each coformer can be found in the Appendix A (Section A1). The present study focuses on doing a thorough comparison of the results from screening methods LAG, SE, STM, and EUT to review their advantages and drawbacks (Figure 3.3, stage 2). The solved crystal structures of the newly found cocrystals through the screening campaign (Figure 3.3, stage 3) from single-crystal XRD information are detailed in the article from Devogelaer et al.[67]

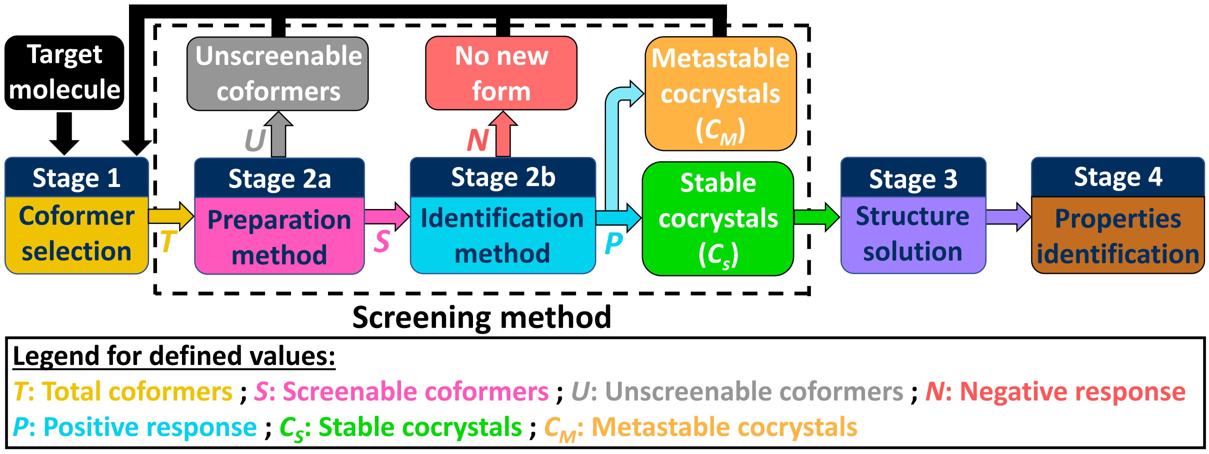

Figure 3.3: Schematic for cocrystal screening campaign stages, the strategy being to improve the properties of the target molecule by finding new stable cocrystals. In this chapter, we aim to compare different cocrystal screening methods (i.e., combination of preparation and identification techniques) by defining values resulting from stage 2. The values help to compute comparison parameters that we define as the screenable coformer fraction R_1 (Equation 3.1), the coformer success rate R_2 (Equation 3.2), the coformer pluriformity R_3 (Equation 3.3), and the new stable cocrystal coverage R_4 (Equation 3.4). We also compare methods based on their experimental convenience (time, cost, and equipment required).

In this work, we define a cocrystal screening method as the combined process of attempting to produce a solid phase with a cocrystallization preparation method and determining its nature with an identification method that will measure if the produced solid mixture possesses new properties (Figure 3.3, stage 2). Preparation and identification can either be separated in the screening procedure or included in the same experiment depending on the screening method used. In the study, we identify LAG and SE as preparation methods only (stage 2a), and the prepared solids are measured by XRPD as an identification method (stage 2b) to assess cocrystal formation or not. However, the STM method directly results in an indication whether a new phase exists or not, since a mixture forming a stable cocrystal would result in a higher saturation temperature than expected for the pure single components.[60] This means that STM is both a cocrystal preparation and an identification technique in the same experiment. Nonetheless, the new solid phases were also confirmed with XRPD for STM results.

To quantify and compare the effectiveness of the cocrystal screening methods, we propose to define quantified parameters calculated from the experimental data obtained through the different steps of Figure 3.3. Preparation methods can lead to some coformers not forming a suitable solid phase with the target molecule for later identification (amorphous or liquid), or to incompatibility with a method's limitations, for instance, when showing thermal, chemical, or mechanical degradation or solvent incompatibility. Therefore, for each preparation method (LAG, SE, and STM) tried on the total number of coformers selected for screening (T), a certain number of coformers is considered screenable (S), while the rest is unscreenable (U) by that specific method. We define for each screening method its screenable coformer fraction parameter R_1 (Equation 3.1), that is, the fraction of coformers for which a solid phase could successfully be produced and analyzed with an identification technique.

$$\text{Screenable coformer fraction: } R_1(\%) = \frac{S}{T} \times 100 \qquad \text{Equation 3.1}$$

The prepared solids with screenable coformers are analyzed with an identification technique to determine if the measured properties are different from pure coformers or not. For these coformers, a part has a positive response to cocrystallization if at least one cocrystal is identified (P), and the other part has a negative response as no cocrystal is detected (N). We can then define a coformer success rate parameter R_2 (Equation 3.2) for each screening method.

$$\text{Coformer success rate : } R_2(\%) = \frac{P}{S} \times 100 \qquad \text{Equation 3.2}$$

Newly identified cocrystals with one method can be stable when lower in energy than pure coformer mixtures, and we define their final number to be C_S. Otherwise, they are metastable if at equilibrium they cannot be isolated due to acquisition of pure coformers instead, and we define this value to be C_M for that method. In this study, generally, single-crystal growth experiments and the different screening methods under varying conditions consistently led to the same form. In those cases, it is likely that the obtained form and thus also the obtained crystal structure[67] is the stable form under the conditions of the experiment. However, these results do not guarantee that the new form is the thermodynamic stable form, and accurate stability studies in future research will have to confirm the hypotheses. One successful coformer can result in more than one new cocrystal identified, for instance, two cocrystals of different stoichiometries, different stabilities, or solvated or not. Therefore, we define a coformer pluriformity parameter R_3 (Equation 3.3) that quantifies a screening method's ability to give more than one new cocrystal per successful coformer.

$$\text{Coformer pluriformity : } R_3(\%) = \frac{C_S + C_M - P}{P} \times 100 \qquad \text{Equation 3.3}$$

In the end of a cocrystal screening campaign, only new stable cocrystals found with one method (C_S) are interesting in most cases for further research. By defining C^{tot} as the total of cocrystals (stable and metastable), found with all methods combined during the screening campaign, we characterize the new stable cocrystal coverage parameter R_4 (Equation 3.4) that describes the fraction of new stable cocrystals identified with one method.

$$\text{New stable cocrystal coverage : } R_4(\%) = \frac{C_S}{C^{tot}} \times 100 \qquad \text{Equation 3.4}$$

To review and compare the screening method results in the case of the present PZQ screening study, we use these defined parameters and discuss the methods' convenience, in terms of experiment time, material cost, and equipment required.

3.3.1. LAG

The solvents used in LAG are listed in the Appendix A Table A3 and were chosen as being able to solubilize both PZQ and the coformer screened. LAG experiments typically result in a powder or a slurry that can then be analyzed with XRPD to identify potential cocrystal formation. However, for the three coformers 3-hydroxybenzoic acid (**16**), 3-nitrobenzoic acid (**25**), and 4-nitrophenol (**26**), LAG resulted in the formation of an oil or amorphous phase and the absence of a measurable XRPD pattern. These mixtures do not show crystallization even after a period of 90 days. Although these coformers have relatively high melting temperatures, an explanation could be that the binary melting temperatures of these coformers' system are below the room temperature, preventing crystal formation as the melt would be the stable phase. Otherwise, crystallization kinetics of any solid phase could be very slow, resulting in an out-of-equilibrium phase. The cocrystal preparation experiments of these three coformer systems are inconclusive about cocrystal existence as no solid could be obtained for the XRPD analysis, and hence are considered unscreenable with LAG. Therefore, $S = 27$ for the LAG method, setting its screenable coformers fraction parameter R_1 to be 90%.

With LAG experiments, 11 coformers out of the 27 screenable ones show a positive response in cocrystallization ($P = 11$), setting the coformer success rate parameter R_2 to be 41%. As an example of positive screening experiment, the coformer 3,5-dinitrobenzoic acid (**13**), shown in Figure 3.4 (green), indicates a significantly different XRPD pattern compared to that of the pure coformer (dark blue) and PZQ (red). We note a complete conversion into the new phase as there is no trace of either the pure coformer or PZQ peaks in the pattern. New patterns are also identified for salicylic acid (**5**, Figure A3), 1,4-diiodotetrafluorobenzene (**6**, Figure A4), 4-hydroxybenzoic acid (**7**, Figure A5), 4-aminosalicylic acid (**12**, Figure A6), hydroquinone (**15**, Figure 3.7 green), vanillic acid (**20**, Figure 3.5 green), 2,5-dihydroxybenzoic acid (**22**, Figure 3.6 green), 3,5-dihydroxybenzoic acid (**24**, Figure A13), 2,4-dihydroxybenzoic acid (**28**, Figure 3.10 green), and orcinol (**29**, Figure A16). No evidence of cocrystal formation is found for 16 other screened coformers as the XRPD patterns indicate the presence of already known solid phases from coformers and PZQ ($N = 16$).

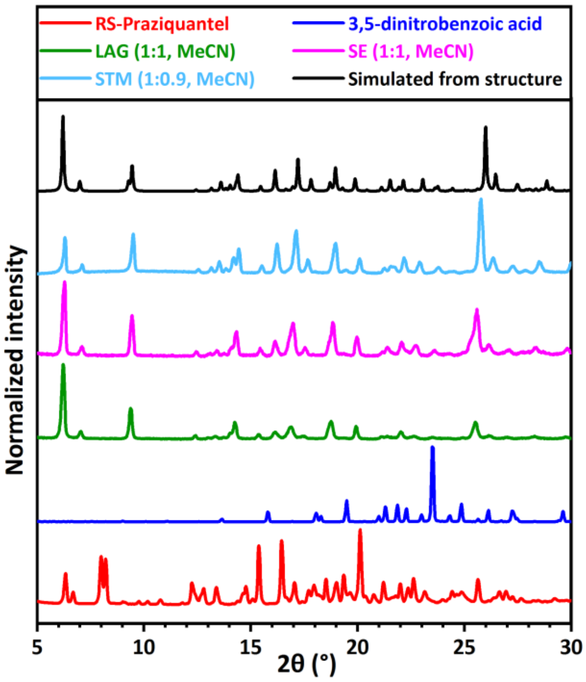

Figure 3.4: XRPD patterns for RS-PZQ, 3,5-dinitrobenzoic acid, and solid phases obtained from their mixtures after LAG, SE, and STM (with the corresponding solvent and molar ratio between the coformer and PZQ $M_{PZQ/cof}$). The simulated powder pattern from the resolved cocrystal (CCDC 2054491[67]) is added for comparison. This new pattern is identified for the LAG, SE, and STM experiments.

In most cases, systems screened with LAG in multiple solvents result in the same solid phase formation. However, XRPD patterns can differ depending on the solvent used. This is the case in our study of PZQ and vanillic acid (**20**) which gives different XRPD patterns in LAG for EtOH and MeCN, as shown in green patterns in Figure 3.5. Another example is 2,5-dihydroxybenzoic acid (**22**), as shown in Figure 3.6, that has two new, different patterns with LAG in acetone and MeCN (green). Possible explanations are the formation of a cocrystal and a cocrystal solvate or two stable cocrystals of different stoichiometries or a stable cocrystal and a metastable cocrystal of the same stoichiometry (polymorphism). In total, 13 new cocrystal XRPD patterns are identified using LAG for 11 positive coformers, setting its coformer pluriformity parameter $R_3$to be 18%.

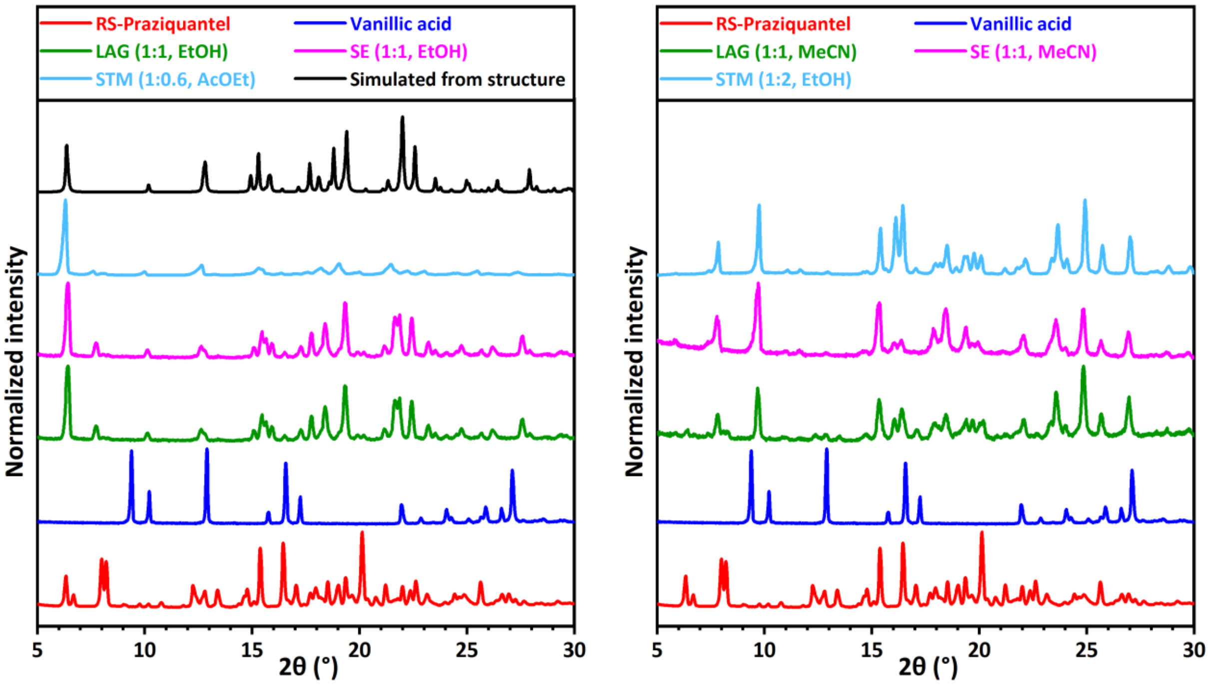

Figure 3.5: XRPD patterns for RS-PZQ, vanillic acid (**20**), and solid phases obtained from their mixtures after LAG, SE, and STM (with the corresponding solvent and molar ratio $M_{PZQ/cof}$ between the coformer and PZQ). The simulated powder pattern from the resolved cocrystal (CCDC 2054490[67]) is added for comparison. Two new patterns, one presented in the left graph and the other in the right graph, are identified for LAG, SE, and STM depending on the solvent used.

The solved crystal structures from single-crystal X-ray diffraction information help to conclude on the nature of the new crystals formed, that is, cocrystal, cocrystal solvate, and their stoichiometries. Among the 13 new XRPD patterns identified using LAG, single-crystal growth experiments confirm 12 new cocrystal structures where the simulated patterns correspond to those obtained from the LAG experiments. Eight coformers are identified as forming 1:1 molar stoichiometry cocrystals with PZQ: 1,4-diiodotetrafluorobenzene (**6**), 4-hydroxybenzoic acid (**7**), 4-aminosalicylic acid (**12**), hydroquinone (**15**), vanillic acid (**20**), 2,5-dihydroxybenzoic acid (**22**), 2,4-dihydroxybenzoic acid (**28**), and orcinol (**29**). Four coformers are identified as forming 1:1:1 cocrystal solvates with PZQ and a solvent. Three of these solvates are with MeCN: 4-aminosalicylic acid (**12**), 2,5-dihydroxybenzoic acid (**22**), and 3,5-dihydroxybenzoic acid (**24**). The fourth is a cocrystal hydrate unexpectedly obtained with salicylic acid (**5**) even if water is not used here as a solvent. Indeed, acetone is used in this case for grinding, which leads to an oil transition stage that crystallizes upon contact with ambient humidity from air. Two distinctly new XRPD patterns, presented in Figure 3.5, were obtained using the coformer vanillic acid in LAG. The phase produced in LAG using the solvent EtOH (green, left) is a 1:1 cocrystal, whose structure is solved by single-crystal XRD. The other phase was produced in LAG using the solvent MeCN (green, right), but the single-crystal growth experiments were not successful in producing this cocrystal form.

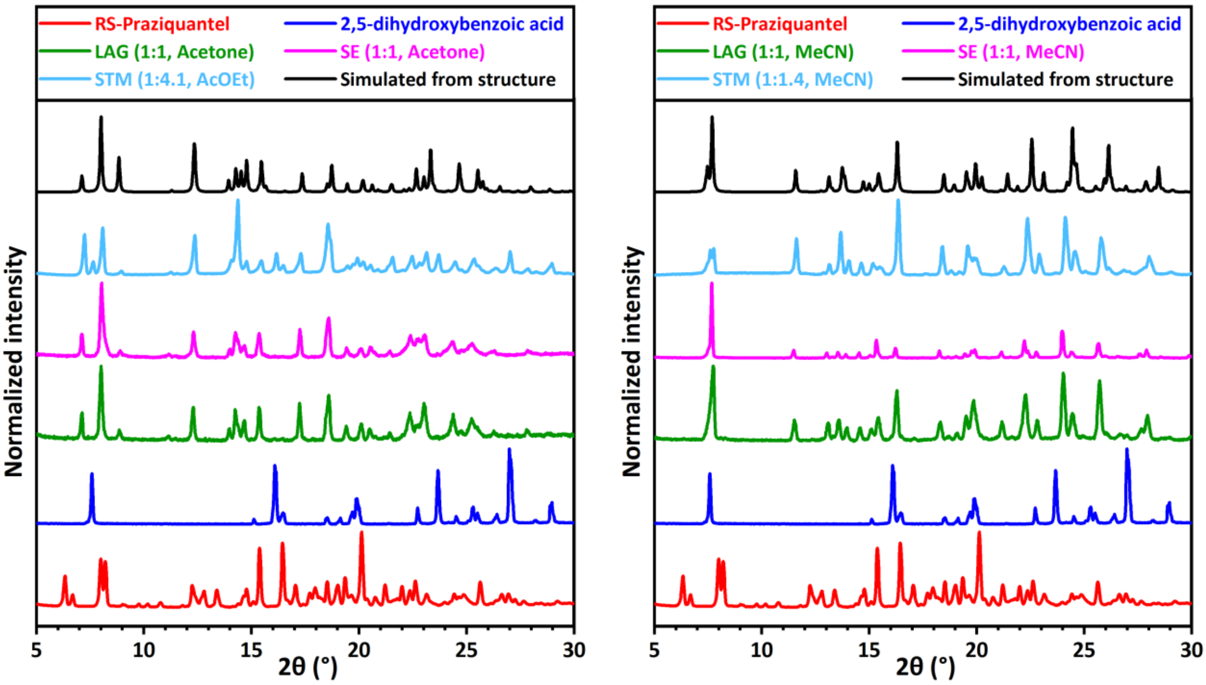

Figure 3.6: XRPD patterns for RS-PZQ, 2,5-dihydroxybenzoic acid, and solid phases obtained from their mixtures after LAG, SE and STM (with the corresponding solvent and molar ratio $M_{PZQ/cof}$ between coformer and PZQ). The simulated powder patterns from resolved cocrystal (CCDC 2054489,[67] left) and resolved cocrystal solvate (CCDC 2054487,[67] right) are added for comparison. Two new patterns, one presented in the left graph and the other in the right graph, are identified for LAG, SE and STM depending on the solvent used.

3.3.2. SE

SE experiments require solvents in which both the coformer and PZQ have a substantial solubility and evaporate relatively quickly under ambient conditions. The solvents were screened, and those used for SE for each coformer are listed in the Appendix A Table A3. Three coformers, namely, terephthalic acid (**8**), isophthalic acid (**10**), and phthalic acid (**18**) do not have a suitable solvent as only DMF is found to dissolve them but does not evaporate under ambient conditions. Therefore, these coformers are unscreenable by the SE method due to solvent incompatibility. The other coformers were tested for solid mixture preparation. Successful preparation attempts result in a powder or a slurry that can be analyzed with XRPD to confirm cocrystal formation. Nine coformer systems, namely, benzoic acid (**3**), *trans*-cinnamic acid (**14**), 3-hydroxybenzoic acid (**16**), anthranilic acid (**17**), D-tartaric acid (**19**), 3-nitrobenzoic acid (**25**), 4-nitrophenol (**26**), 1-hydroxy-2-naphtoic acid (**27**), and orcinol (**29**), result in oils/amorphous materials and therefore no solid phases identifiable with XRPD analysis. It is unlikely that after complete evaporation, the stable equilibrium for these mixtures is the liquid state at room temperature. Therefore, these issues are due to fast crystallization kinetics caused by fast evaporation resulting in an amorphous state or due to trapping of the remaining solvent in a liquor that becomes too viscous to permit complete evaporation. These coformers are also considered unscreenable as SE preparation attempts are unsuccessful, and no conclusion about cocrystal existence for these systems is possible. Therefore, $S = 18$ for the SE method, setting its screenable coformer fraction parameter $R_1$to be 60%.

With SE experiments, 10 coformers out of the 18 screenable ones show a positive response in cocrystallization ($P = 10$), setting the coformer success rate parameter R_2 to be 56%. It includes the result of the coformer 3,5-dinitrobenzoic acid (**13**) with PZQ, as shown in Figure 3.4 (pink). This new pattern is the same as the one obtained with LAG for this system (green). New patterns are also identified for PZQ with pimelic acid (**4**, Figure A2), salicylic acid (**5**, Figure A3), 1,4-diiodotetrafluorobenzene (**6**, Figure A4), 4-hydroxybenzoic acid (**7**, Figure A5), hydroquinone (**15**, Figure 3.7 pink), vanillic acid (**20**, Figure 3.5 pink), 2,5-dihydroxybenzoic acid (**22**, Figure 3.6 pink), 3,5-dihydroxybenzoic acid (**24**, Figure A13), and 2,4-dihydroxybenzoic acid (**28**, Figure 3.10 pink). No evidence of cocrystal formation is found for the eight other screened coformers as the XRPD patterns indicate the presence of already known solid phases from coformers and PZQ ($N = 8$).

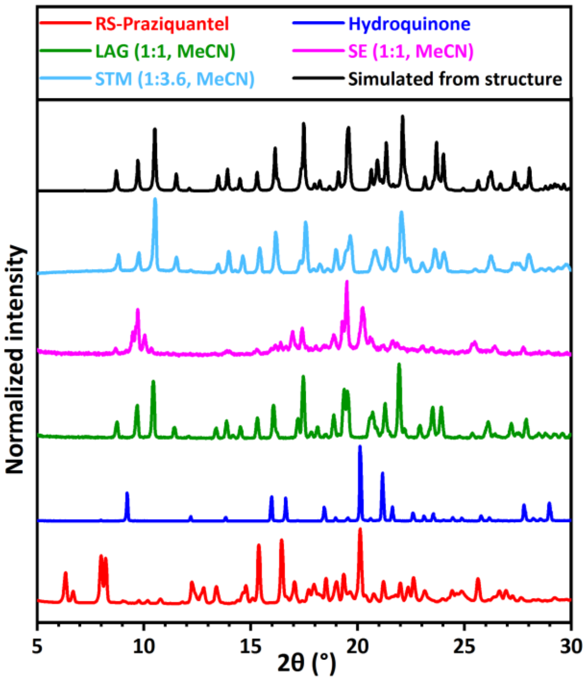

Figure 3.7: XRPD patterns for RS-PZQ, hydroquinone, and solid phases obtained from their mixtures after LAG, SE, and STM (with the corresponding solvent and molar ratio $M_{PZQ/cof}$ between coformer and PZQ). The simulated powder pattern from the resolved cocrystal (CCDC 2054497[67]) is added for comparison. This new pattern is identified for LAG and STM. SE presents a different new pattern (corresponding structure has not been characterized; so no simulated powder pattern is shown).

In total, 12 new cocrystal XRPD patterns are identified using SE for 10 positive coformers, setting its coformer pluriformity parameter $R_3$to be 20%. As in the case of LAG, the two coformers, vanillic acid (**20**, Figure 3.5) and 2,5-dihydroxybenzoic acid (**22**, Figure 3.6) give new XRPD patterns that depend on the solvent used. The same solvents with the same 1:1 ratio between PZQ and the coformer are used in LAG and SE, so the results are consistent between the two methods.

However, the new XRPD patterns with SE for hydroquinone (**15**, Figure 3.7 pink) and 2,4-dihydroxybenzoic acid (**28**, Figure 3.10 pink) are not the same as the 1:1 cocrystals obtained with LAG (green), whose stabilities are indicated from consistent results with single-crystal growth experiments. These different patterns from SE results are observed, despite SE experiments being done in the same solvent with the same equimolar ratio as with LAG. No single-crystals could be grown for these phases as growth experiments result in the LAG cocrystals suspected to be stable and not the SE phases. The same problem is encountered for pimelic acid using SE (**4**, Figure A2), with a new pattern identified that shows the pimelic acid pattern containing an additional peak not corresponding to any known phase. No new pattern is identified with LAG under the same experimental conditions, and growth experiments lead to pure coformers phases and not the solid identified with SE. Therefore, the question about the nature of these three phases remains, and as they are different from the known pure coformer solids, our interpretation is that they are metastable cocrystals/cocrystal solvates. For the other coformers having a positive response to cocrystallization, the XRPD patterns with SE correspond to the same as those identified with LAG from which indications of stability are obtained from single-crystal growth experiments. However, for 4-aminosalicylic acid (**12**) in Figure 3.8, the SE result (pink) indicates no cocrystal formation as pure 4-aminosalicylic acid is obtained (dark blue pattern), contrary to LAG for the same composition.

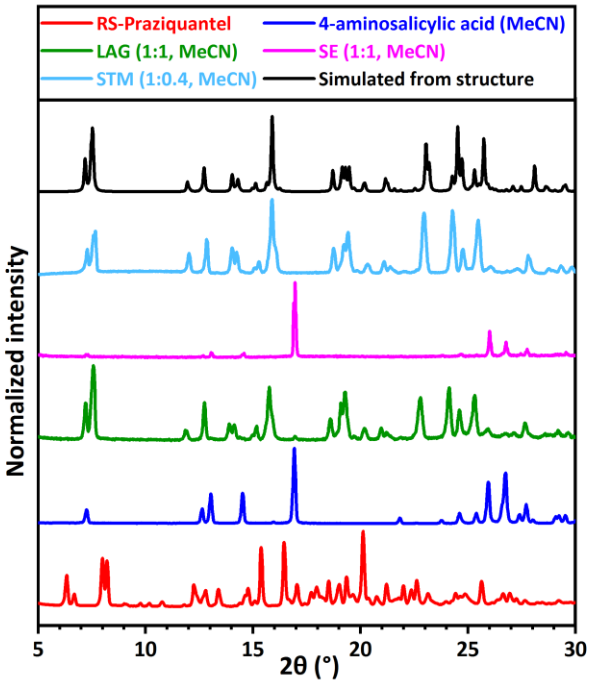

Figure 3.8: XRPD patterns for RS-PZQ, 4-aminosalicylic acid, and solid phases obtained from their mixtures after LAG, SE, and STM (with the corresponding solvent and molar ratio $M_{PZQ/cof}$ between coformer and PZQ). The simulated powder pattern from the resolved cocrystal solvate (CCDC 2054493[67]) is added for comparison. This new pattern is identified for LAG and STM but not SE.

3.3.3. STM

For STM experiments, it is necessary to find a solvent that solubilizes both the coformer and PZQ. Pure component solubility curves are acquired to choose the optimal mixture composition screened. This composition corresponds to the pure component solubilities at a reference temperature T_r, chosen arbitrarily at a temperature higher than room temperature to ensure obtaining a solid phase. The screening is done in more than one solvent, up to a maximum of three solvents, which leads to mixture molar ratios $M_{PZQ/cof}$ that vary with the solvent used. The screening strategy for STM consists of first measuring coformer solubility curves for which the Van ’t Hoff plots are presented in Figures A17 to A42 with related data tables A4 to A29 in the Appendix A Section A3. Then, mixtures with PZQ and the coformer are screened, using the following order of solvents: EtOH, MeCN, and AcOEt. Five coformer systems could not be screened with these solvents, namely, terephthalic acid (**8**), isophthalic acid (**10**), phthalic acid (**18**), D-tartaric acid (**19**), and orcinol (**29**), due to solubility issues. All solvents tried could not dissolve **8**, **10** and **18**. Solutions of **29** did not crystallize. Only EtOH could dissolve **19**, but the solubility measurements resulted in inconsistent despite multiple experiments. These coformer systems, for which no pure component solubility data can be obtained, are considered unscreenable with STM because of solvent incompatibility. Therefore, $S = 25$ for the STM method, setting its screenable coformer fraction parameter $R_1$to be 83%.

Screening experiment details are given in the Appendix A (Table A30) that summarizes screened compositions by the STM method with the corresponding molar ratio $M_{PZQ/cof}$ between the coformer and PZQ in solution. The results are indicated by the temperature difference $\Delta T = T_{sat} - T_r$ between the measured saturation temperature T_{sat} of the mixture and the reference temperature T_r. As represented in Figure 3.9, the newly identified cocrystals by the STM method show a positive ΔT, which is a strong thermodynamic indication of the formation of a more stable phase that is less soluble than both pure components. For example, a screened sample in MeCN with a concentration in PZQ of 0.3168 mol/L and 0.2834 mol/L in 3,5-Dinitrobenzoic acid experimentally dissolves at a measured $T_{sat} = 53.6\ °C$. From the Van 't Hoff plots of pure components solubility data in MeCN, a solution of pure PZQ with a concentration of 0.3168 mol/L dissolves at 30.2 °C and a solution of pure 3,5-dinitrobenzoic acid with a concentration of 0.2834 mol/L dissolves at 30.6 °C. The reference temperature T_r is defined as the highest between both, and therefore $T_r = 30.6\ °C$, giving a positive $\Delta T = 23\ °C$ for this system that assesses the formation of a cocrystal less soluble than both pure components. XRPD analyses of the samples giving positive ΔT confirm the formation of cocrystals with new patterns and assess the method's reliability (Figure 3.9, green data). When multiple experiments on the same coformer are performed in different solvents or molar ratio $M_{PZQ/cof}$, XRPD also allows to know the new solid phase it concerns. This is not the case if only saturation temperatures are used as the latter indicate cocrystal formation but do not consist of a solid form fingerprint contrary to XRPD patterns. With STM experiments, 9 coformers out of the 25 screenable ones show a positive response in cocrystallization ($P = 9$), setting the coformer success rate parameter R_2 to be 36%. This involves 1,4-diiodotetrafluorobenzene (**6**, Figure A4), 4-hydroxybenzoic acid (**7**, Figure A5), 4-aminosalicylic acid (**12**, Figure 3.8 light blue), 3,5-dinitrobenzoic acid (**13**, Figure 3.4 light blue), hydroquinone (**15**, Figure 3.7 light blue), vanillic acid (**20**, Figure 3.5 light blue), 2,5-dihydroxybenzoic acid (**22**, Figure 3.6 light blue), 3,5-dihydroxybenzoic acid (**24**, Figure A13), and 2,4-dihydroxybenzoic acid (**28**, Figure 3.10 light blue). No evidence of cocrystal formation is found for the 16 other screened coformers as the XRPD patterns indicate the presence of already known solid phases from coformers and PZQ ($N = 16$).

A false positive is observed for benzoic acid (**3**) in EtOH with a positive temperature difference of $\Delta T = 4.7\ °C$, while XRPD confirms a physical mixture of PZQ and benzoic acid (Figure 3.9, orange circle). This is probably caused by a decrease in the solubility of one component due to the other. Systems for which the measurement of ΔT is below 0 show negative response to cocrystallization (Figure 3.9, red data) and correspond to components enhancing each other's solubilities with favorable interactions. Sometimes, the effect can be substantial, for instance with 2,5-dihydroxybenzoic acid (**22**) in MeCN for which a temperature difference of $\Delta T = -45.8\ °C$ is measured. XRPD of the solids corresponding to red data always consists of pure coformers. In some cases, crystallization did not happen, and no T_{sat} data or solid phases for XRPD could be obtained: **5** in MeCN, **9** in AcOEt, **16** in EtOH/MeCN/AcOEt, **17** in EtOH/MeCN, **21** in AcOEt, and **27** in AcOEt. These experiments are considered to not result in cocrystallization and to correspond to more extreme cases of overall enhanced solubility when mixing components.

The ΔT for newly identified forms systems varies based on the relative stabilities of the new phases, going from $\Delta T = 7.1\,°C$ for a cocrystal solvate with MeCN and 4-aminosalicylic acid (**12**) to $\Delta T = 29.4\,°C$ for a cocrystal with 2,4-dihydroxybenzoic acid (**28**). For some systems, the saturation temperature is so high (beyond the boiling point of the solvent) that it could not be measured, such as cocrystals with 1,4-diiiodotetrafluorobenzene (**6**) in EtOH, 4-hydroxybenzoic acid (**7**) in MeCN, 2,5-dihydroxybenzoic acid (**22**) in MeCN, and 2,4-dihydroxybenzoic acid (**28**) in MeCN and AcOEt. To nevertheless show these experiments in Figure 3.9 (square symbols), their T_{sat} is assumed to be 60 °C, the maximum temperature in the temperature profiles. This highlights the accuracy of the detection method as stable cocrystals will be less soluble than the coformer mixture. The STM is then sufficient proof of a stable cocrystal formation, as no false negatives, that is, cocrystals confirmed by XRPD but with $\Delta T < 0$, are observed.

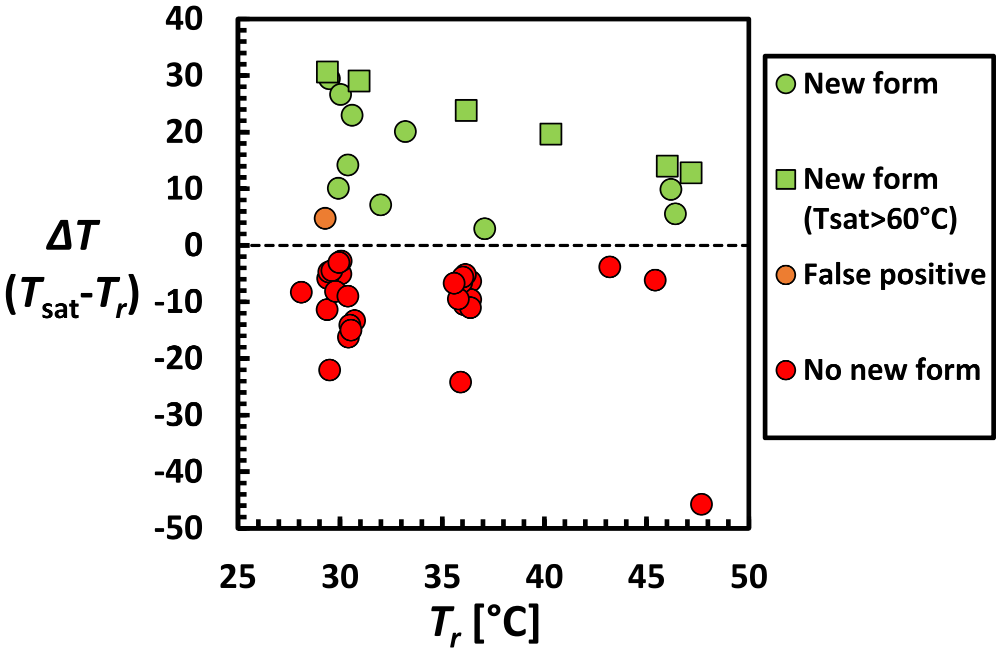

Figure 3.9: Temperature difference $\Delta T = T_{sat} - T_r$ versus the reference temperature T_r for systems investigated with the STM method. T_{sat} is the saturation temperature of mixtures containing PZQ and the coformer, both with a concentration equal to their ideal solubility at the chosen reference temperature T_r in studied solvents. A positive value of ΔT indicates potential formation of stable cocrystals, which is confirmed by XRPD (green). The STM method applied to 30 coformers results in one false positive (orange) when a positive ΔT is obtained, but XRPD indicates a coformer physical mixture. No false negatives, that is, cocrystals confirmed by XRPD with $\Delta T < 0$, are observed. Crystallization of coformer physical mixtures (red) correspond to ΔT values below 0.

In total, 12 new cocrystals are identified using STM for 9 positive coformers, setting its coformer pluriformity parameter $R_3$to be 33%. As in the case of LAG and SE, the two coformers, vanillic acid (**20**, Figure 3.5) and 2,5-dihydroxybenzoic acid (**22**, Figure 3.6), give new XRPD patterns that depend on the solvent used. This is the same for 2,4-dihydroxybenzoic acid (**28**, Figure 3.10 right, light blue), whose new pattern obtained in EtOH is specific to STM. As no single-crystal was grown for this phase, it is unclear whether it is a cocrystal of a different stoichiometry than the one confirmed by LAG or a cocrystal solvate with EtOH. However, its solubility is much lower than the pure component mixture, indicated by a high $\Delta T = 29.4\ °C$, which is a good indication of its stable nature. For the other coformers indicating positive response to cocrystallization, the XRPD patterns with STM correspond to the same as those identified with LAG from which stable cocrystals are suspected. The pattern of PZQ with 2,5-dihydroxybenzoic acid in AcOEt prepared with the STM method (Figure 3.6, left) presents extra peaks corresponding to the pure coformer pattern compared to the cocrystal simulated pattern. As the solid sample was taken from the suspension at a temperature well below its saturation temperature, the mixed XRPD pattern indicates that the sample equilibrated in a triphasic stability domain and not as a pure cocrystal in suspension.

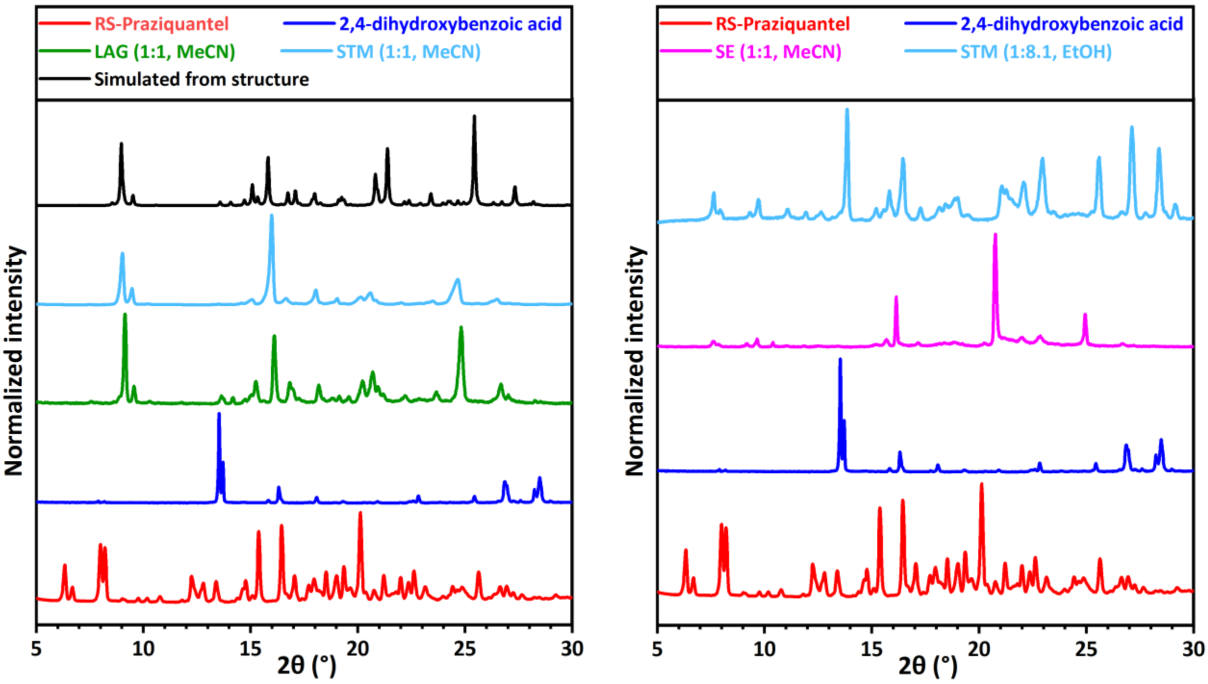

Figure 3.10: XRPD patterns for RS-PZQ, 2,4-dihydroxybenzoic acid, and solid phases obtained from their mixtures after LAG, SE, and STM (with the corresponding solvent and molar ratio $M_{PZQ/cof}$ between the coformer and PZQ). The simulated powder pattern from the resolved cocrystal (CCDC 2054494[67]) is added for comparison. This new pattern is identified for LAG and STM (left). New different patterns are also identified for SE and STM in other conditions (right), which differ from it. SE phase is suspected to be metastable.

3.3.4. EUT

EUT is a cocrystal screening strategy from the melt that would allow to obtain additional information compared to classic melt cocrystallization techniques (see Section 3.2.4.4). However, the EUT method was abandoned for the present study because of the identification of thermal degradation and crystallization kinetics problems. PZQ itself presents issues regarding crystallization from the melt (see Figure A43 in the Appendix A) as it stays amorphous between successive heating-cooling cycles, and therefore it requires long annealing steps above its glass transition (measured at about 80 °C) to crystallize. Moreover, the second heating always reveals the appearance of a parasite event as a double peak, which implies the formation of an impurity and indicates thermal degradation. The contents of DSC pans were checked and revealed a pink coloration of the PZQ samples, initially white, and, therefore, EUT method was discarded for the PZQ cocrystal screening campaign. An example of thermograms exhibiting the thermal behavior that we ideally seek with the EUT crystallization protocol from the melt for pure coformers, that is, identical first and second heating cycles, is shown in Figure A44 in the Appendix A. However, several pure coformers that were tried with the EUT protocol showed similar limitations to PZQ, with thermal degradation or metastable polymorphs crystallizing from the melt. In Figures A45 and A46 in the Appendix A, we report the thermograms obtained for a 1:9 and a 9:1 molar mixture of PZQ and coformer for EUT protocol in two binary systems. Both systems indicated cocrystal formation with other screening methods, but here, we cannot conclude on any result because of the difficulty in reaching the equilibrium state from the melt in the present conditions. While two thermal events are expected per composition at equilibrium, we observe more than two, which means the equilibrium is not reached, or even no event at all, which means there were kinetics issues to crystallize from the melt. The use of annealing steps to help reaching equilibrium from the melt would have been a great addition to the protocol but would have been too time consuming for the present PZQ cocrystal screening. Moreover, the more time at the high temperatures required would have led anyway to more degradation of the PZQ in the samples.

3.3.5. Overview of Screening Results

Table 3.1: Coformer screening results with LAG, SE, and STM methods. ✓: New XRPD pattern. Green: cocrystals showing stability. Red: physical mixture of coformers. Orange: cocrystals suspected to be metastable. Gray: unscreenable because insoluble (*i*), too soluble (*s*) or forming oils/amorphous (*o*).

	Coformer	LAG	SE	STM	New cocrystal(s) found
1	Sebacic acid	🟥	🟥	🟥	
2	Suberic acid	🟥	🟥	🟥	
3	Benzoic acid	🟥	*o*	🟥	
4	Pimelic acid	🟥	🟧 ✓	🟥	Metastable phase, from SE
5	Salicylic acid	🟩 ✓	🟩 ✓	🟥	1:1:1 cocrystal solvate H_2O
6	1,4-diiodotetrafluorobenzene	🟩 ✓	🟩 ✓	🟩 ✓	1:1 cocrystal
7	4-hydroxybenzoic acid	🟩 ✓	🟩 ✓	🟩 ✓	1:1 cocrystal
8	Terephthalic acid	🟥	*i*	*i*	
9	4-aminobenzoic acid	🟥	🟥	🟥	
10	Isophthalic acid	🟥	*i*	*i*	
11	Azelaic acid	🟥	🟥	🟥	
12	4-aminosalicylic acid	🟩 ✓	🟥	🟩 ✓	1:1:1 cocrystal solvate MeCN
13	3,5-dinitrobenzoic acid	🟩 ✓	🟩 ✓	🟩 ✓	1:1 cocrystal
14	*trans*-cinnamic acid	🟥	*o*	🟥	
15	Hydroquinone	🟩 ✓	🟧 ✓	🟩 ✓	- 1:1 cocrystal - Metastable phase, from SE
16	3-hydroxybenzoic acid	*o*	*o*	🟥	
17	Anthranilic acid	🟥	*o*	🟥	
18	Phthalic acid	🟥	*i*	*i*	
19	D-(-)-tartaric acid	🟥	*o*	*i*	
20	Vanillic acid	🟩 ✓,✓	🟩 ✓,✓	🟩 ✓,✓	- 1:1 cocrystal - 1:X cocrystal (unresolved)
21	4-nitrobenzoic acid	🟥	🟥	🟥	
22	2,5-dihydroxybenzoic acid	🟩 ✓,✓	🟩 ✓,✓	🟩 ✓,✓	- 1:1 cocrystal - 1:1:1 cocrystal solvate MeCN
23	2-fluorobenzoic acid	🟥	🟥	🟥	
24	3,5-dihydroxybenzoic acid	🟩 ✓	🟩 ✓	🟩 ✓	1:1:1 cocrystal solvate MeCN
25	3-nitrobenzoic acid	*o*	*o*	🟥	
26	4-nitrophenol	*o*	*o*	🟥	
27	1-hydroxy-2-naphtoic acid	🟥	*o*	🟥	
28	2,4-dihydroxybenzoic acid	🟩 ✓	🟧 ✓	🟩 ✓,✓	- 1:1 cocrystal - Metastable phase from SE - Stable phase from STM (unresolved)
29	Orcinol	🟩 ✓	*o*	*s*	1:1 cocrystal
30	Dodecanedioic acid	🟥	🟥	🟥	

Of the 30 coformers selected, all could be screened, and 12 indicate a positive response to cocrystallization with PZQ for a total of 17 cocrystals found with all methods combined ($C^{tot} = 17$). Table 3.1 summarizes the screening results for each coformer, and Figure 3.11 represents an overview of all values obtained for the methods, with their computed parameters for comparison. EUT results are not included as the screening protocol with the EUT method had to be abandoned. The right column in Table 3.1 contains the information of the XRPD patterns. The same XRPD patterns are identified by all methods presenting a tick. If distinctly different XRPD patterns were obtained, the additional tick is explained in the right column of Table 3.1 to clarify by what method the phase was identified. We have indications from single-crystal growth experiments that 12 cocrystalline phases might be stable, of which the structures are reviewed in the article by Devogelaer et al.[67] All 12 cocrystals are identified with LAG, and the one found for orcinol (**29**, Figure A16) is specific to LAG. With LAG, a first cocrystal for vanillic acid (20, Figure 3.5 left) is identified, the structure of which is shown from single-crystal XRD information to correspond to a 1:1 cocrystal. However, a second cocrystal for vanillic acid (**20**, Figure 3.5 right) is also discovered, whose structure was not resolved. As this second result is obtained multiple times using LAG, SE, and STM in different solvents with varied compositions, we assume that the most likely hypothesis is a second stable cocrystal with a stoichiometry different from 1:1. The possibility of a cocrystal solvate is indeed excluded as the result in obtained in multiple solvents. Also, the consistent and repeated results obtained with all methods, and particularly STM that provides equilibrated suspensions, indicate the stable nature of this second cocrystal. The stoichiometry of this cocrystal could probably be two vanillic acid molecules for one PZQ as it is prepared with the STM method in solution composition in EtOH with an excess of vanillic acid compared to PZQ (Figure 3.5). Therefore, $C_S = 13$, for LAG and this sets its new stable cocrystals coverage parameter R_4 to be 76%. With SE, 12 new cocrystals are identified, with 9 in common with LAG from which we have stability indication due to consistent results with LAG, STM, and single-crystal growth experiments. The three others correspond to specific cocrystals identified with SE for pimelic acid (**4**, Figure A2), hydroquinone (**15**, Figure 3.7), and 2,4-dihydroxybenzoic acid (**28**, Figure 3.10). These phases are considered metastable due to inconsistency with LAG and STM experiments in similar conditions, as well as single-crystals growth experiments giving more stable phases instead. Therefore, $C_M = 3$ and $C_S = 9$ for SE, and it sets its new stable cocrystal coverage parameter R_4 to be 53%. With STM, 12 new cocrystals are identified, with 11 in common with LAG from which we have stability indication due to consistent results with LAG, SE, and single-crystal growth experiments. A second cocrystal is obtained for 2,4-dihydroxybenzoic acid in EtOH (**28**, Figure 3.10), being a specific result to STM. Consistent experiments and a high ΔT value give indications of its stability, although screening experiments alone do not permit conclusions on its stoichiometry and eventual solvation. Therefore, $C_S = 12$ for STM, and this sets its new stable cocrystal coverage parameter R_4 to be 71%.

Methods	Coformers screenability	Coformers response	New cocrystals	Method's parameters
LAG	27 3	11 16	13 0	$R_1 = 90\,\%$ $R_2 = 41\,\%$ $R_3 = 18\%$ $R_4 = 76\,\%$
SE	18 12	10 8	9 3	$R_1 = 60\,\%$ $R_2 = 56\,\%$ $R_3 = 20\%$ $R_4 = 53\,\%$
STM	25 5	9 16	12 0	$R_1 = 83\,\%$ $R_2 = 36\,\%$ $R_3 = 33\%$ $R_4 = 71\,\%$
Total	30/30	12/30 18/30	C^{tot} = 14 + 3	

S : Screenable

U : Unscreenable

P : Positive response

N : Negative response

C_S : Stable cocrystals

C_M : Metastable cocrystals

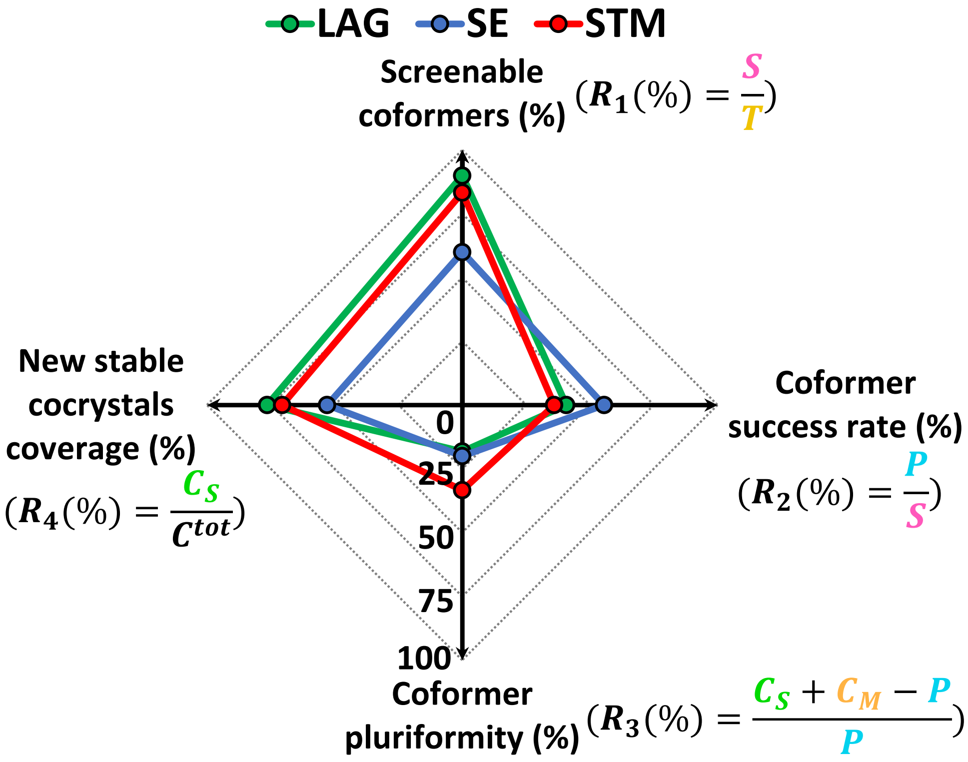

Figure 3.11: Overview of screening results per method with quantified parameters defined for comparison plotted as a web chart.

In our study, we did not obtain a cocrystal during LAG of PZQ and pimelic acid in the presence of MeCN, contrary to the LAG experiments reported by Espinosa-Lara et al.,[40] but rather a physical mixture of the raw materials (**4**, Figure A2). The XRPD pattern of our SE experiments, however, contains new diffraction peaks next to those of pimelic acid, although they are different from Espinosa-Lara et al.'s result. As we conclude on the metastability of the latter phase in our experiments, it remains unclear if a stable cocrystal with pimelic acid exists. Similarly, we did not obtain a cocrystal phase for D-tartaric acid with LAG reported by Cugovcan et al.[41] We also do not observe the recent results from Liu et al.[76] reporting cocrystals of PZQ with 3-hydroxybenzoic acid (**16**) and phthalic acid (**18**) prepared from dissolution in hot solvent followed by evaporation. Phthalic acid (**18**) is screened in our study with LAG and results in no new form, though it is uncertain if the cocrystal preparation method was efficient due to the insolubility of phthalic acid in the chosen solvents. 3-hydroxybenzoic acid (**16**) is screened with STM using three different solvents in a total of six experiments with varying molar ratios $M_{PZQ/cof}$ from 1:0.8 to 1:7.7, and all show the absence of crystallization in solution upon cooling, even at the low temperature.

3.4. Discussion

The stacked bar chart in Figure 3.12 gives a quantified overview of the ratio of positive (light blue), negative (red), and unscreenable (gray) responses of coformers for the methods and their number of new cocrystals identified during our screening. LAG allowed to cover the largest response on coformer ability to form cocrystals with PZQ, whether it is positive or negative, thereby showing the largest screenable coformer fraction (parameter R_1 = 90%). The coformers that could not be screened with LAG were due to formation of amorphous phases because of LAG's high energetic process. This limitation of LAG could be explained by the molecule mobility being too low to crystallize from an intermediate amorphous state in such conditions, because of a glass transition temperature being above the experiment temperature. Coformer success rate parameter R_2 for LAG indicates that 41% of screened coformers resulted in a positive response to cocrystallization. Multiple new forms for one coformer were obtained by changing the solvent, allowing to find cocrystals with different stoichiometries or cocrystal solvates (coformer pluriformity parameter R_3 = 18%). This demonstrates the high versatility of LAG as it does not require solubilization of the solid material, the solvent acting only as a catalytic medium and therefore a simplified solvent screening. For this reason, the cocrystal with orcinol (**29**) is specific to LAG as the coformer had solvent incompatibility with other methods, while LAG did not have this limitation. With the cocrystal(s) stability domain(s) in the ternary phase diagrams depending on pure component solubilities, using various solvents and especially ones in which solubility ratios between the coformer and API are different proves to be a conclusive strategy for optimal screening with LAG. The method also permits freedom regarding the compositions that can be screened (position of green dot in Figure 3.13 and Figure 3.14 is not fixed) and, therefore, multiple trials to access experimentally phase diagram domains where a cocrystal is stable. In this study, we limited ourselves to equimolar mixtures, but trying different ratios to investigate in-depth systems likely to present multiple forms would be relevant. With a quick experiment time (30 min), the accessibility of ball mill equipment, and low material consumption, LAG is confirmed to be highly convenient and ideal for quick and efficient screening. The acquisition of only phases suspected to be stable here with LAG is interesting to highlight, as despite constraining dynamic conditions for the system with a highly energetic milling, it always reached thermodynamic equilibrium. With a total of 13 new phases suspected to be stable that are identified with LAG, its new stable cocrystals coverage parameter R_4 of 76% is the highest.

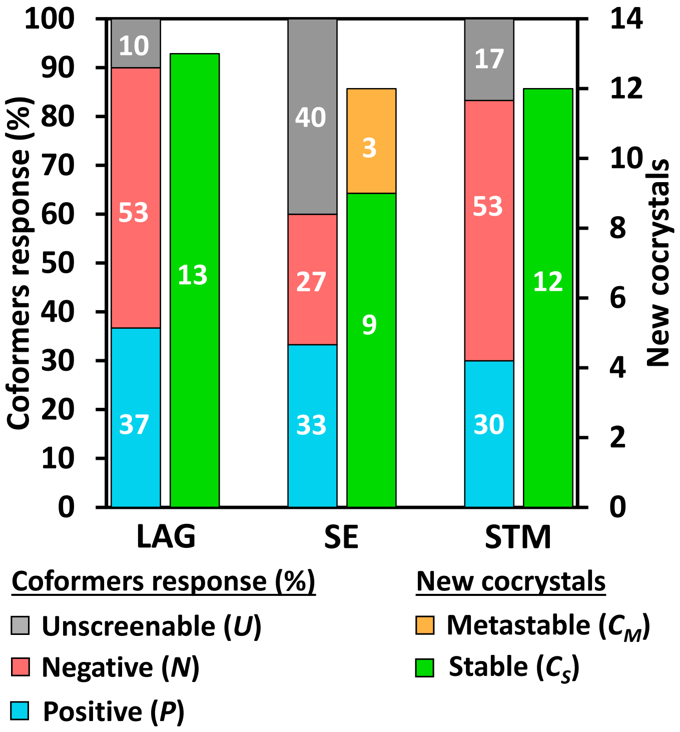

Figure 3.12: Stacked bar chart representing the ratio of positive (light blue), negative (red), and unscreenable (gray) responses for the screening methods used and their identified cocrystal number.

From Figure 3.12, the SE method presents the lowest number of conclusive responses on the coformer ability to cocrystallize, with the smallest screenable coformer fraction parameter R_1 of 60%. This is mainly due to solvent incompatibility with the coformers. SE indeed requires quick solvent screening to find solvents able to solubilize both coformers and being volatile under the screening conditions. However, additional limitations are observed during cocrystal preparation as many attempts resulted in amorphous/oil formation during evaporation. These experimental issues to reach thermodynamic equilibrium are system dependent and unpredictable, which makes SE uncertain and mainly based on trial and error. It can be explained by an evaporation rate difficult to control, inducing more easily the formation of amorphous mixtures and metastable phases. Indeed, only SE gave cocrystals we concluded to be metastable, for a total of three, with pimelic acid (**4**), hydroquinone (**15**), and 2,4-dihydroxybenzoic acid (**28**). They are considered false positives in the context of a cocrystal screening campaign, and therefore such uncertainty is generally unwanted. Furthermore, a new cocrystal solvate with 4-aminosalicylic acid (**12**) and MeCN, that is identified by LAG and STM is missed by SE (Figure 3.8). It indicates SE can also be unreliable, probably due to the pathway of its composition evolution during evaporation that can cause trouble if the cocrystal has a non-congruent solubility in a solvent (see Figure 3.13). Indeed, in this example, the first solid phase to crystallize is a pure coformer that could continue to crystallize out of equilibrium if the cocrystal is not kinetically favored, possibly skipping the apparition of the latter, especially at the end of the SE experiment in which the last solvent evaporates as there are large supersaturations and risk of possible metastable forms crystallizing out. However, the coformer success rate parameter R_2 for SE is the highest with 56% of screened coformers positive to cocrystallization. It means positive cocrystallization experiments had less issues to give a final solid with SE than negative ones. It is possibly explained by cocrystals identified in our study having a lower energetic barrier to crystallize than pure coformer solids. Nevertheless, no generalities can be concluded because of the small amount of data. SE coformer pluriformity parameter R_3 of 20% is similar to the LAG one, meaning trial and error changes of solvent allow to find different stoichiometries and solvation in cocrystals. SE is therefore a highly convenient method for quick screening, with only basic equipment required, short experiment time, and low material consumption. However, with only nine new phases found that are suspected to be stable, its new stable cocrystal coverage parameter R_4 of 53% in our study is the smallest and highlights some uncertainty and unreliability.

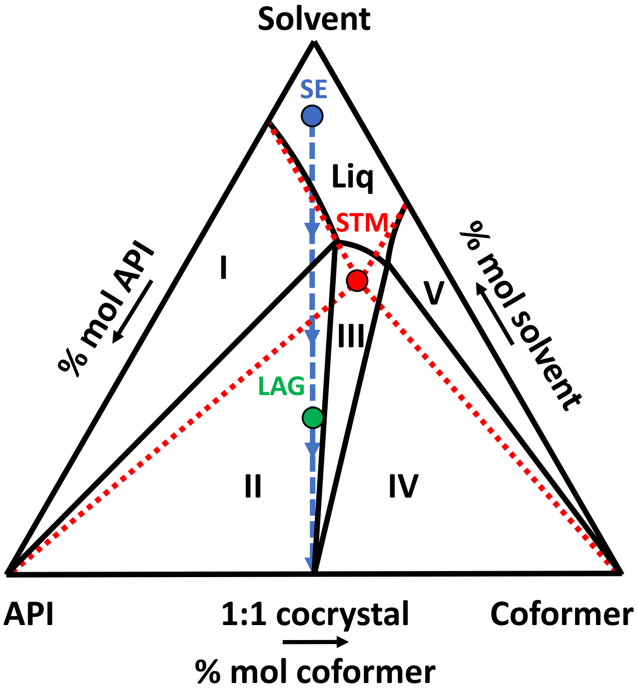

Figure 3.13: Schematic isothermal ternary phase diagram describing a 1:1 cocrystal forming system with non-congruent solubility. Regions I, III, and V are stability domains of the API, the cocrystal, and the coformer, respectively. Regions II and IV are triphasic domains between the cocrystal and a solution of eutectic composition and the API and the coformer, respectively. Liq stands for the undersaturated solution domain. The red point is the theoretical eutectic composition at that specific temperature (solution doubly saturated in API and coformer, computed from pure components ideal solubilities) chosen as the screening composition for the STM method. The green point corresponds to an arbitrary stoichiometric ratio screened by the LAG method. The blue dashed line corresponds to the crystallization pathway with the SE method from a stoichiometric undersaturated solution (blue point).

STM method gave almost as much conclusive data as LAG, with a screenable coformer fraction parameter R_1 of 83%. Despite its solvent-based nature, only five coformers could not be screened due to solvent incompatibility. However, STM is not the most convenient as it requires solvent screening and the acquisition of accurate solubility curves prior to cocrystal screening, which takes a long experimental time and consumes more material than LAG and SE. Moreover, Crystal16 or other specific equipment for solubility curve determination is necessary. STM was preferred to cooling crystallization of 1:1 molar ratio solutions that has the risk of missing new forms.[53] Indeed, STM-screened compositions are favored thermodynamically compared to arbitrary compositions as they are computed from pure component solubilities (see Figure 3.13 and Figure 3.14, red points). Throughout the cooling process, the composition equilibrates in the cocrystal stability domain due to a controlled low cooling rate and a final isothermal step. The method also guarantees the stable nature of new forms identified based on the thermodynamic principle “the less soluble, the more stable the solid phase.” The coformer success rate parameter

R_2 for STM is smaller (36%) than those for LAG and SE. The reason is the miss of the cocrystal hydrate with salicylic acid (**5**), found with LAG and SE. It could not be obtained from STM as contamination with water is not possible when using dry solvents, contrary to LAG and SE where the sample was in contact with ambient humidity. An advantage of STM is that coformers giving no new cocrystals with the method are screened accurately multiple times with varying stoichiometries by changing the solvent. Therefore, the negative results are more conclusive on the inability of these coformers to form a cocrystal with PZQ. By finding two cocrystals suspected to be stable for the coformers vanillic acid (**20**), 2,5-dihydroxybenzoic acid (**22**), and 2,4-dihydroxybenzoic acid (**28**), STM coformer pluriformity parameter R_3 is the highest with 33%. For vanillic acid (**20**), two cocrystals suspected to be stable with different stoichiometries are found, while for 2,5-dihydroxybenzoic acid (**22**), one is solvated and not the other. Nonetheless, the specific cocrystal identified with STM for 2,4-dihydroxybenzoic acid (**28**) has not been resolved, and so it is not known if it has a different stoichiometry than 1:1 or if it is a cocrystal solvate. These results highlight the efficiency with STM to use a set of solvents presenting different solubilization behaviors regarding the coformers. It induces large variation of the screened compositions that are non-equimolar while guaranteeing the equilibration in a stable cocrystallization solubility domain, allowing to find more easily non-equimolar cocrystals as illustrated in Figure 3.14. With a total of 12 new phases suspected to be stable that are identified with STM, its new stable cocrystals coverage parameter R_4 of 71% is high and comparable to LAG.

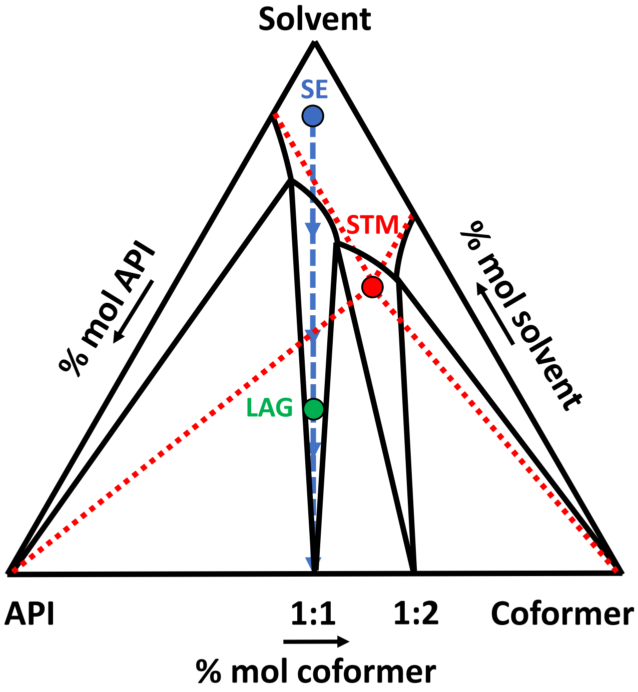

Figure 3.14: Schematic isothermal ternary phase diagram describing a system forming a 1:1 and a 1:2 cocrystal with congruent solubilities. The red point is the theoretical eutectic composition between API and the coformer at that specific temperature (solution doubly saturated in API and the coformer, computed from pure component ideal solubilities) chosen as the screening composition for the STM method. The green point corresponds to an arbitrary stoichiometric ratio screened by the LAG method. The blue dashed line corresponds to the crystallization pathway with the SE method from a stoichiometric undersaturated solution (blue point).

In the web chart in Figure 3.11, the defined parameters R_1, R_2, R_3, and R_4 are plotted for comparison of LAG, SE, and STM methods. It appears that in our screening, LAG allowed to screen the most coformers and to cover the largest number of new stable cocrystals found, making it the most successful method. STM is a close second, presenting very similar results but showing more multiple cocrystals found per positive coformer with less successful coformers than LAG. Finally, SE presents the most atypical results as due to experimental constraints, the number of screenable coformers was lowered. SE presents a high success rate among screenable coformers, but this result is balanced by the small number of new stable cocrystals covered as several metastable cocrystals were obtained.

Based on the results from our PZQ cocrystal screening campaign, we are therefore able to advise on the method selection strategy for screening optimization. Nevertheless, cocrystal screening is dependent on the studied thermodynamic systems, and it would be interesting to extend the method comparison with the same parameters on a larger number of screened systems. Despite its high convenience, the SE method was weaker than LAG, and in a context of quick screening, we recommend using LAG rather than SE as represented in Figure 3.15. The results from LAG and STM are similar, although both methods differ a lot in their principles. STM method possesses a double status of cocrystal preparation and identification technique, directly giving a quantitative indication of cocrystal formation, while for LAG, the identification must be confirmed by a XRPD measurement. LAG is highly convenient for efficient results, which makes it a powerful method ideal for quick screening. However, no information is obtained regarding single-crystal growth possibilities or application possibilities. On the contrary, STM method is not convenient for quick screening as it requires longer experimental time, more material, and solubility curve determination work prior to screening. Nonetheless, it allows to acquire a large amount of accurate solubility data (see the Appendix A) that can be collected in databases for future use. This is particularly relevant for pharmaceutical industry as the same pool of coformers are regularly used. Furthermore, when detecting a cocrystal with STM, experimental parameters to grow single-crystals are also measured as stability domains of cocrystals are identified. The same compositions can therefore be used for slow cooling crystallization or temperature cycling growth experiments. These data can also be used later, for instance, to design a cocrystal production process.

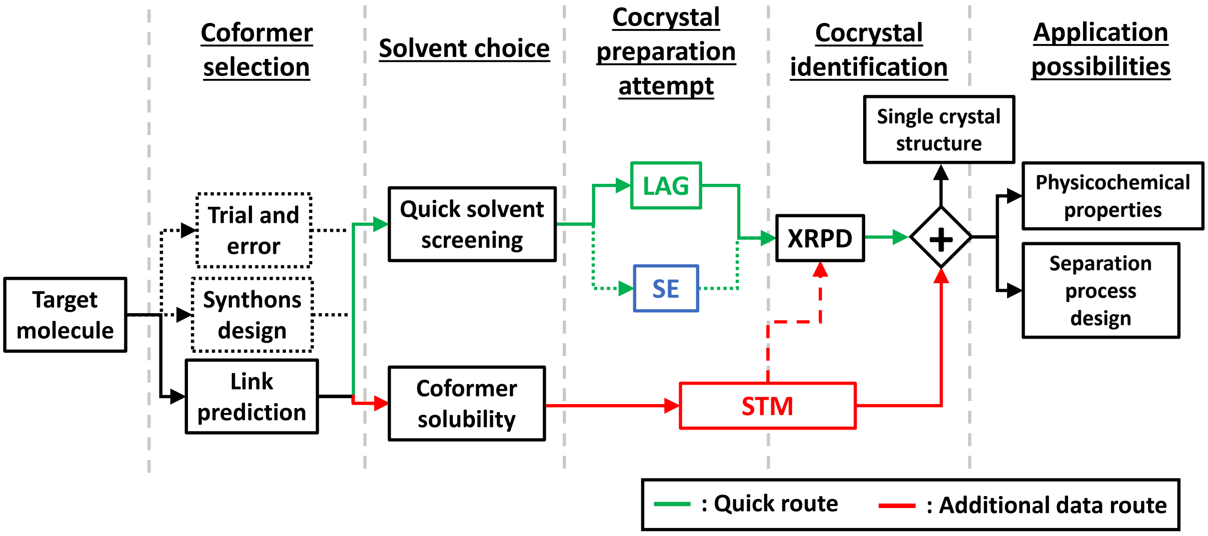

Figure 3.15: Workflow for cocrystal screening methodology advised from overall data obtained through PZQ cocrystal screening. Solid lines represent the pathways that should be preferred compared to dotted line ones that proved less efficient. Coformer selection results refer to the article from Devogelaer et al.[67] on a link prediction approach for coformer selection applied to PZQ. LAG and SE are preparation methods only, ideal for a quick screening route (green), and require the combination with an identification method, XRPD being ideal. STM is a combination of preparation and identification methods, and XRPD identification step (dashed line), even if providing relevant additional information, can be skipped to go directly to solving crystal structure from single-crystal XRD information. STM is a slow screening method but allows to acquire additional solubility data (red). STM results also give phase diagram data useful for single-crystal growth and other applications.

EUT method resulted in the thermal degradation of some samples, and therefore, did not provide results applicable in our study, and could not be included in the methods comparison. This highlights the risk of thermal based screening methods to degrade compounds, not crystallize from melt conditions, and crystallize phases out of equilibrium. However, in systems that do not degrade thermally and that have a low glass transition temperature, the EUT method could be an interesting alternative. It is an accessible method as it requires DSC equipment that is common in labs, the experiments are not time and material consuming, and it can be considered as a green technology due to the absence of organic solvents. However, it requires high purity materials for experiments. For cases such as phthalic derivatives (**8**, **10**, **18**) in the present study, for which insolubility was systematic in all solvents tried, it could have been a relevant screening alternative if PZQ was not degrading at high temperatures.

3.5. Conclusions

Four common and accessible methods with different principles in their crystallization mechanism were investigated in a vast screening for cocrystals of PZQ. The methods were applied to PZQ with 30 coformers, which were identified based on a link prediction algorithm[67] using data mining of the Cambridge Structural Database (CSD). A total of 17 cocrystals were identified, with 14 showing stability, and 12 new structures were resolved and reported.[67] The large amount of data obtained in the screening helped to compare the efficiency of the cocrystal screening methods. LAG highlighted the best results, with the largest screenable coformers fraction (90%) and the highest number of cocrystals found that are suspected to be stable (13), even though amorphous phases are obtained in a few cases. SE showed numerous limitations due to its solvent dependence and its lack of crystallization control. Less coformers were screenable (60%), a lower number of cocrystals suspected to be stable was identified (9), three metastable phases were obtained, and an existing cocrystal was missed. STM method presented results as satisfactory as LAG. Less coformers were screenable (83%), but a similar number of cocrystals suspected to be stable was detected (12), revealing a tendency to identify multiple cocrystals per successful coformers. However, STM is less convenient than LAG and SE because of time and material required with solvent screening and solubility curve measurements. Despite the innovative screening concept of EUT thermal method, investigations using this technique were stopped due to thermal degradation and difficulties in reaching equilibrium issues for many systems. Nevertheless, we highlight this method as an interesting alternative for systems that lack a suitable solvent. In summary, we advise LAG method for a quick and efficient screening route and STM for a slower route that provides relevant solubility data useful for future screenings, single-crystal growth and eventual future cocrystal production in larger scale.

3.6. Associated content

Supporting Information

The Supporting Information related to this chapter is the Appendix A.

Materials, experimental methods and conditions, powder diffractograms for new cocrystals, solubility data of coformers, and saturation temperature results of coformer mixtures.

Data availability statement

All data underpinning this chapter are openly available from the University of Strathclyde KnowledgeBase at: https://doi.org/10.15129/501763a1-4a33-4a3e-999a-84faba625cd0

3.7. Acknowledgements

This research received funding as part of the CORE ITN Project by the European Union’s Horizon 2020 Research and Innovation Program under the Marie Skłodowska-Curie grant agreement no. 722456 CORE ITN. The authors thank the EPSRC Centre for Innovative Manufacturing in Continuous Manufacturing and Crystallization (http://www.cmac.ac.uk) for support (EPSRC funding under grant reference: EP/I033459/1). We thank Dr David Maillard of Merck KGaA (Darmstadt, Germany) for providing enantiopure and racemic praziquantel.

3.8. References

(1) Duggirala, N. K.; Perry, M. L.; Almarsson, O.; Zaworotko, M. J. Pharmaceutical cocrystals: along the path to improved medicines. *Chem Commun (Camb)* **2016**, *52* (4), 640-655.
(2) Grothe, E.; Meekes, H.; Vlieg, E.; ter Horst, J. H.; de Gelder, R. Solvates, Salts, and Cocrystals: A Proposal for a Feasible Classification System. *Crystal Growth & Design* **2016**, *16* (6), 3237-3243.
(3) Aitipamula, S.; Banerjee, R.; Bansal, A. K.; Biradha, K.; Cheney, M. L.; Choudhury, A. R.; Desiraju, G. R.; Dikundwar, A. G.; Dubey, R.; Duggirala, N. Polymorphs, salts, and cocrystals: what’s in a name? *Crystal Growth & Design* **2012**, *12* (5), 2147-2152.
(4) Thipparaboina, R.; Kumar, D.; Chavan, R. B.; Shastri, N. R. Multidrug co-crystals: towards the development of effective therapeutic hybrids. *Drug Discov Today* **2016**, *21* (3), 481-490.
(5) Shefter, E.; Higuchi, T. Dissolution Behavior of Crystalline Solvated and Nonsolvated Forms of Some Pharmaceuticals. *J Pharm Sci* **1963**, *52* (8), 781-791.

(6) Shevchenko, A.; Miroshnyk, I.; Pietila, L. O.; Haarala, J.; Salmia, J.; Sinervo, K.; Mirza, S.; van Veen, B.; Kolehmainen, E.; Nonappa; et al. Diversity in Itraconazole Cocrystals with Aliphatic Dicarboxylic Acids of Varying Chain Length. *Crystal Growth & Design* **2013**, *13* (11), 4877-4884.
(7) Lin, Y.; Yang, H.; Yang, C.; Wang, J. Preparation, characterization, and evaluation of dipfluzine-benzoic acid co-crystals with improved physicochemical properties. *Pharm Res* **2014**, *31* (3), 566-578.
(8) Almarsson, Ö.; Zaworotko, M. J. Crystal engineering of the composition of pharmaceutical phases. Do pharmaceutical co-crystals represent a new path to improved medicines? *Chemical communications* **2004**, (17), 1889-1896.
(9) Remenar, J. F.; Morissette, S. L.; Peterson, M. L.; Moulton, B.; MacPhee, J. M.; Guzman, H. R.; Almarsson, O. Crystal engineering of novel cocrystals of a triazole drug with 1,4-dicarboxylic acids. *J Am Chem Soc* **2003**, *125* (28), 8456-8457.
(10) Schultheiss, N.; Newman, A. Pharmaceutical Cocrystals and Their Physicochemical Properties. *Cryst Growth Des* **2009**, *9* (6), 2950-2967.
(11) Friscic, T.; Jones, W. Benefits of cocrystallisation in pharmaceutical materials science: an update. *J Pharm Pharmacol* **2010**, *62* (11), 1547-1559.
(12) Urbanus, J.; Roelands, C. P. M.; Verdoes, D.; Jansens, P. J.; ter Horst, J. H. Co-Crystallization as a Separation Technology: Controlling Product Concentrations by Co-Crystals. *Crystal Growth & Design* **2010**, *10* (3), 1171-1179.
(13) Guillot, M.; de Meester, J.; Huynen, S.; Collard, L.; Robeyns, K.; Riant, O.; Leyssens, T. Cocrystallization-Induced Spontaneous Deracemization: A General Thermodynamic Approach to Deracemization. *Angew Chem Int Ed Engl* **2020**, *59* (28), 11303-11306.
(14) Springuel, G.; Leyssens, T. Innovative Chiral Resolution Using Enantiospecific Co-Crystallization in Solution. *Crystal Growth & Design* **2012**, *12* (7), 3374-3378.
(15) Harmsen, B.; Leyssens, T. Enabling Enantiopurity: Combining Racemization and Dual-Drug Co-crystal Resolution. *Crystal Growth & Design* **2018**, *18* (6), 3654-3660.
(16) Zhou, F.; Shemchuk, O.; Charpentier, M. D.; Matheys, C.; Collard, L.; Ter Horst, J. H.; Leyssens, T. Simultaneous Chiral Resolution of Two Racemic Compounds by Preferential Cocrystallization*. *Angew Chem Int Ed Engl* **2021**, *60* (37), 20264-20268.
(17) Ariens, E. J. Stereochemistry, a basis for sophisticated nonsense in pharmacokinetics and clinical pharmacology. *Eur J Clin Pharmacol* **1984**, *26* (6), 663-668.
(18) Reddy, I. K.; Mehvar, R. *Chirality in drug design and development*; CRC Press, 2004.
(19) Saigo, K.; Sakai, K. Resolution of Chiral Drugs and Drug Intermediates by Crystallisation. *Chirality in drug research* **2006**, 127-154.
(20) Li, Z. J.; Grant, D. J. Relationship between physical properties and crystal structures of chiral drugs. *J Pharm Sci* **1997**, *86* (10), 1073-1078.
(21) Jacques, J.; Collet, A.; Wilen, S. H. *Enantiomers, racemates, and resolutions*; Wiley, 1981.
(22) Harfouche, L. C.; Couvrat, N.; Sanselme, M.; Brandel, C.; Cartigny, Y.; Petit, S.; Coquerel, G. Discovery of New Proxyphylline-Based Chiral Cocrystals: Solid State Landscape and Dehydration Mechanism. *Crystal Growth & Design* **2020**, *20* (6), 3842-3850.
(23) Neurohr, C.; Marchivie, M.; Lecomte, S.; Cartigny, Y.; Couvrat, N.; Sanselme, M.; Subra-Paternault, P. Naproxen–Nicotinamide Cocrystals: Racemic and Conglomerate Structures Generated by CO2 Antisolvent Crystallization. *Crystal Growth & Design* **2015**, *15* (9), 4616-4626.
(24) Belletti, G.; Tortora, C.; Mellema, I. D.; Tinnemans, P.; Meekes, H.; Rutjes, F.; Tsogoeva, S. B.; Vlieg, E. Photoracemization-Based Viedma Ripening of a BINOL Derivative. *Chemistry* **2020**, *26* (4), 839-844.

(25) Sakai, K.; Hirayama, N.; Tamura, R. *Novel optical resolution technologies*; Springer, 2007.
(26) Suwannasang, K.; Flood, A. E.; Rougeot, C.; Coquerel, G. Using Programmed Heating–Cooling Cycles with Racemization in Solution for Complete Symmetry Breaking of a Conglomerate Forming System. *Crystal Growth & Design* **2013**, *13* (8), 3498-3504.
(27) Li, W. W.; Spix, L.; de Reus, S. C. A.; Meekes, H.; Kramer, H. J. M.; Vlieg, E.; ter Horst, J. H. Deracemization of a Racemic Compound via Its Conglomerate-Forming Salt Using Temperature Cycling. *Crystal Growth & Design* **2016**, *16* (9), 5563-5570.
(28) Sogutoglu, L. C.; Steendam, R. R.; Meekes, H.; Vlieg, E.; Rutjes, F. P. Viedma ripening: a reliable crystallisation method to reach single chirality. *Chem Soc Rev* **2015**, *44* (19), 6723-6732.
(29) Buol, X.; Caro Garrido, C.; Robeyns, K.; Tumanov, N.; Collard, L.; Wouters, J.; Leyssens, T. Chiral Resolution of Mandelic Acid through Preferential Cocrystallization with Nefiracetam. *Crystal Growth & Design* **2020**, *20* (12), 7979-7988.
(30) Lorenz, H.; Seidel-Morgenstern, A. Processes to separate enantiomers. *Angew Chem Int Ed Engl* **2014**, *53* (5), 1218-1250.
(31) Kellogg, R. M. Practical Stereochemistry. *Acc Chem Res* **2017**, *50* (4), 905-914.
(32) Maggioni, G. M.; Fernández-Ronco, M. P.; van der Meijden, M. W.; Kellogg, R. M.; Mazzotti, M. Solid state deracemisation of two imine-derivatives of phenylglycine derivatives via high-pressure homogenisation and temperature cycles. *CrystEngComm* **2018**, *20* (27), 3828-3838.
(33) Breveglieri, F.; Maggioni, G. M.; Mazzotti, M. Deracemization of NMPA via Temperature Cycles. *Crystal Growth & Design* **2018**, *18* (3), 1873-1881.
(34) Belletti, G.; Meekes, H.; Rutjes, F.; Vlieg, E. Role of Additives during Deracemization Using Temperature Cycling. *Cryst Growth Des* **2018**, *18* (11), 6617-6620.
(35) Harmsen, B.; Leyssens, T. Dual-Drug Chiral Resolution: Enantiospecific Cocrystallization of (S)-Ibuprofen Using Levetiracetam. *Crystal Growth & Design* **2017**, *18* (1), 441-448.
(36) Andrews, P. Praziquantel: mechanisms of anti-schistosomal activity. *Pharmacol Ther* **1985**, *29* (1), 129-156.
(37) Cioli, D.; Pica-Mattoccia, L. Praziquantel. *Parasitol Res* **2003**, *90 Supp 1* (1), S3-9.
(38) Molyneux, D. H.; Savioli, L.; Engels, D. Neglected tropical diseases: progress towards addressing the chronic pandemic. *Lancet* **2017**, *389* (10066), 312-325.
(39) Salazar-Rojas, D.; Maggio, R. M.; Kaufman, T. S. Preparation and characterization of a new solid form of praziquantel, an essential anthelmintic drug. Praziquantel racemic monohydrate. *Eur J Pharm Sci* **2020**, *146*, 105267.
(40) Espinosa-Lara, J. C.; Guzman-Villanueva, D.; Arenas-Garcia, J. I.; Herrera-Ruiz, D.; Rivera-Islas, J.; Roman-Bravo, P.; Morales-Rojas, H.; Hopfl, H. Cocrystals of Active Pharmaceutical Ingredients-Praziquantel in Combination with Oxalic, Malonic, Succinic, Maleic, Fumaric, Glutaric, Adipic, And Pimelic Acids. *Crystal Growth & Design* **2013**, *13* (1), 169-185.
(41) Cugovcan, M.; Jablan, J.; Lovric, J.; Cincic, D.; Galic, N.; Jug, M. Biopharmaceutical characterization of praziquantel cocrystals and cyclodextrin complexes prepared by grinding. *J Pharm Biomed Anal* **2017**, *137*, 42-53.
(42) Yang, S.; Liu, Q.; Ji, W.; An, Q.; Song, J.; Xing, C.; Yang, D.; Zhang, L.; Lu, Y.; Du, G. Cocrystals of Praziquantel with Phenolic Acids: Discovery, Characterization, and Evaluation. *Molecules* **2022**, *27* (6), 2022.
(43) Sánchez-Guadarrama, O.; Mendoza-Navarro, F.; Cedillo-Cruz, A.; Jung-Cook, H.; Arenas-García, J. I.; Delgado-Díaz, A.; Herrera-Ruiz, D.; Morales-Rojas, H.; Höpfl, H. Chiral Resolution

of RS-Praziquantel via Diastereomeric Co-Crystal Pair Formation with l-Malic Acid. *Crystal Growth & Design* **2015**, *16* (1), 307-314.

(44) Woelfle, M.; Seerden, J. P.; de Gooijer, J.; Pouwer, K.; Olliaro, P.; Todd, M. H. Resolution of praziquantel. *PLoS Negl Trop Dis* **2011**, *5* (9), e1260.

(45) Valenti, G.; Tinnemans, P.; Baglai, I.; Noorduin, W. L.; Kaptein, B.; Leeman, M.; Ter Horst, J. H.; Kellogg, R. M. Combining Incompatible Processes for Deracemization of a Praziquantel Derivative under Flow Conditions. *Angew Chem Int Ed Engl* **2021**, *60* (10), 5279-5282.

(46) Bond, A. D. What is a co-crystal? *CrystEngComm* **2007**, *9* (9), 833-834.

(47) Alhalaweh, A.; George, S.; Basavoju, S.; Childs, S. L.; Rizvi, S. A. A.; Velaga, S. P. Pharmaceutical cocrystals of nitrofurantoin: screening, characterization and crystal structure analysis. *CrystEngComm* **2012**, *14* (15), 5078-5088.

(48) Wood, P. A.; Feeder, N.; Furlow, M.; Galek, P. T. A.; Groom, C. R.; Pidcock, E. Knowledge-based approaches to co-crystal design. *Crystengcomm* **2014**, *16* (26), 5839-5848.

(49) Griesser, U. J. The Importance of Solvates. In *Polymorphism*, 2006; pp 211-233.

(50) Trask, A. V.; Jones, W. Crystal engineering of organic cocrystals by the solid-state grinding approach. *Organic Solid State Reactions* **2005**, *254*, 41-70.

(51) Shaikh, R.; Singh, R.; Walker, G. M.; Croker, D. M. Pharmaceutical Cocrystal Drug Products: An Outlook on Product Development. *Trends Pharmacol Sci* **2018**, *39* (12), 1033-1048.

(52) Lin, S. Y. Mechanochemical Approaches to Pharmaceutical Cocrystal Formation and Stability Analysis. *Curr Pharm Des* **2016**, *22* (32), 5001-5018.

(53) Leyssens, T.; ter Horst, J. H. 9. Solution co-crystallisation and its applications. In *Multi-Component Crystals*, De Gruyter, 2017; pp 205-236.

(54) Douroumis, D.; Ross, S. A.; Nokhodchi, A. Advanced methodologies for cocrystal synthesis. *Adv Drug Deliv Rev* **2017**, *117*, 178-195.

(55) Basavoju, S.; Bostrom, D.; Velaga, S. P. Indomethacin-saccharin cocrystal: design, synthesis and preliminary pharmaceutical characterization. *Pharm Res* **2008**, *25* (3), 530-541.

(56) Weyna, D. R.; Shattock, T.; Vishweshwar, P.; Zaworotko, M. J. Synthesis and Structural Characterization of Cocrystals and Pharmaceutical Cocrystals: Mechanochemistry vs Slow Evaporation from Solution. *Crystal Growth & Design* **2009**, *9* (2), 1106-1123.

(57) Braga, D.; Grepioni, F. Making crystals from crystals: a green route to crystal engineering and polymorphism. *Chem Commun (Camb)* **2005**, (29), 3635-3645.

(58) Trask, A. V.; Motherwell, W. D.; Jones, W. Solvent-drop grinding: green polymorph control of cocrystallisation. *Chem Commun (Camb)* **2004**, (7), 890-891.

(59) Bis, J. A.; Vishweshwar, P.; Weyna, D.; Zaworotko, M. J. Hierarchy of supramolecular synthons: Persistent hydroxyl center dot center dot center dot pyridine hydrogen bonds in cocrystals that contain a cyano acceptor. *Molecular Pharmaceutics* **2007**, *4* (3), 401-416.

(60) Ter Horst, J.; Deij, M.; Cains, P. Discovering new co-crystals. *Crystal Growth & Design* **2009**, *9* (3), 1531-1537.

(61) Manin, A. N.; Voronin, A. P.; Drozd, K. V.; Manin, N. G.; Bauer-Brandl, A.; Perlovich, G. L. Cocrystal screening of hydroxybenzamides with benzoic acid derivatives: a comparative study of thermal and solution-based methods. *Eur J Pharm Sci* **2014**, *65*, 56-64.

(62) Habgood, M.; Deij, M. A.; Mazurek, J.; Price, S. L.; ter Horst, J. H. Carbamazepine Co-crystallization with Pyridine Carboxamides: Rationalization by Complementary Phase Diagrams and Crystal Energy Landscapes. *Crystal Growth & Design* **2010**, *10* (2), 903-912.

(63) Li, W.; De Groen, M.; Kramer, H. J.; De Gelder, R.; Tinnemans, P.; Meekes, H.; Ter Horst, J. H. Screening approach for identifying cocrystal types and resolution opportunities in complex chiral multicomponent systems. *Crystal Growth & Design* **2020**, *21* (1), 112-124.

(64) Devogelaer, J. J.; Meekes, H.; Tinnemans, P.; Vlieg, E.; de Gelder, R. Co-crystal Prediction by Artificial Neural Networks*. *Angew Chem Int Ed Engl* **2020**, *59* (48), 21711-21718.
(65) Devogelaer, J.-J.; Brugman, S. J. T.; Meekes, H.; Tinnemans, P.; Vlieg, E.; de Gelder, R. Cocrystal design by network-based link prediction. *CrystEngComm* **2019**, *21* (44), 6875-6885.
(66) Devogelaer, J. J.; Meekes, H.; Vlieg, E.; de Gelder, R. Cocrystals in the Cambridge Structural Database: a network approach. *Acta Crystallogr B Struct Sci Cryst Eng Mater* **2019**, *75* (Pt 3), 371-383.
(67) Devogelaer, J. J.; Charpentier, M. D.; Tijink, A.; Dupray, V.; Coquerel, G.; Johnston, K.; Meekes, H.; Tinnemans, P.; Vlieg, E.; Ter Horst, J. H.; et al. Cocrystals of Praziquantel: Discovery by Network-Based Link Prediction. *Cryst Growth Des* **2021**, *21* (6), 3428-3437.
(68) Gagniere, E.; Mangin, D.; Puel, F.; Bebon, C.; Klein, J. P.; Monnier, O.; Garcia, E. Cocrystal Formation in Solution: In Situ Solute Concentration Monitoring of the Two Components and Kinetic Pathways. *Crystal Growth & Design* **2009**, *9* (8), 3376-3383.
(69) McNamara, D. P.; Childs, S. L.; Giordano, J.; Iarriccio, A.; Cassidy, J.; Shet, M. S.; Mannion, R.; O'Donnell, E.; Park, A. Use of a glutaric acid cocrystal to improve oral bioavailability of a low solubility API. *Pharmaceutical research* **2006**, *23*, 1888-1897.
(70) Berry, D. J.; Seaton, C. C.; Clegg, W.; Harrington, R. W.; Coles, S. J.; Horton, P. N.; Hursthouse, M. B.; Storey, R.; Jones, W.; Friščić, T.; et al. Applying Hot-Stage Microscopy to Co-Crystal Screening: A Study of Nicotinamide with Seven Active Pharmaceutical Ingredients. *Crystal Growth & Design* **2008**, *8* (5), 1697-1712.
(71) Yan, Y.; Chen, J. M.; Lu, T. B. Thermodynamics and preliminary pharmaceutical characterization of a melatonin-pimelic acid cocrystal prepared by a melt crystallization method. *Crystengcomm* **2015**, *17* (3), 612-620.
(72) Yamashita, H.; Hirakura, Y.; Yuda, M.; Teramura, T.; Terada, K. Detection of cocrystal formation based on binary phase diagrams using thermal analysis. *Pharm Res* **2013**, *30* (1), 70-80.
(73) Yamashita, H.; Hirakura, Y.; Yuda, M.; Terada, K. Coformer screening using thermal analysis based on binary phase diagrams. *Pharm Res* **2014**, *31* (8), 1946-1957.
(74) Lu, E.; Rodriguez-Hornedo, N.; Suryanarayanan, R. A rapid thermal method for cocrystal screening. *Crystengcomm* **2008**, *10* (6), 665-668.
(75) Saganowska, P.; Wesolowski, M. DSC as a screening tool for rapid co-crystal detection in binary mixtures of benzodiazepines with co-formers. *Journal of Thermal Analysis and Calorimetry* **2018**, *133* (1), 785-795.
(76) Liu, Q. W.; Yang, D. Z.; Chen, T.; Zhang, B. X.; Xing, C.; Zhang, L.; Lu, Y.; Du, G. H. Insights into the Solubility and Structural Features of Four Praziquantel Cocrystals. *Crystal Growth & Design* **2021**, *21* (11), 6321-6331.

Chapter 4 - Multicomponent Chiral Quantification with Ultraviolet Circular Dichroism Spectroscopy: Ternary and Quaternary Phase Diagrams of Levetiracetam

Maxime D. Charpentier[1], Raghunath Venkatramanan[1], Céline Rougeot[2], Tom Leyssens[3], Karen Johnston[4], Joop H. ter Horst[1,5]

1. EPSRC Centre for Innovative Manufacturing in Continuous Manufacturing and Crystallization (CMAC), University of Strathclyde, Technology and Innovation Centre, 99 George Street, Glasgow G1 1RD, U.K.

2. UCB Pharma SA, chemin du Foriest, 1420 Braine-L'Alleud, Belgium

3. Institute of Condensed Matter and Nanosciences, UCLouvain, Place L. Pasteur 1, Belgium.

4. Department of Chemical and Process Engineering, University of Strathclyde, James Weir Building, 75 Montrose Street, Glasgow G1 1XJ, U.K.

5. Univ Rouen Normandie, Laboratoire Sciences et Méthodes Séparatives (SMS), UR 3233, F-76000 Rouen, France

Abstract

Chiral molecules are challenging for the pharmaceutical industry because although physical properties of the enantiomers are the same in achiral systems, they exhibit different effects in chiral systems, such as the human body. The separation of enantiomers is desired but complex, as enantiomers crystallize most often as racemic compounds. A technique to enable the chiral separation of racemic compounds is to create an asymmetry in the thermodynamic system by generating chiral cocrystal(s) using a chiral coformer and using the solubility differences to enable separation through crystallization from solution. However, such quaternary systems are complex and require analytical methods to quantify different chiral molecules in solution. Here, we develop a new chiral quantification method using ultraviolet-circular dichroism spectroscopy and multivariate partial least squares calibration models, to build multicomponent chiral phase diagrams. Working on the quaternary system of (R)- and (S)-2-(2-oxopyrrolidin-1-yl)butanamide enantiomers with (S)-mandelic acid in acetonitrile, we measure accurately the full quaternary phase diagram for the first time. By understanding the phase stabilities of the racemic compound and the enantiospecific cocrystal, the chiral resolution of levetiracetam could be designed due to a large asymmetry in overall solubility between both sides of the racemic composition. This new method offers improvements for chiral molecule quantification in complex multicomponent chiral systems and can be applied to other chiral spectroscopy techniques.

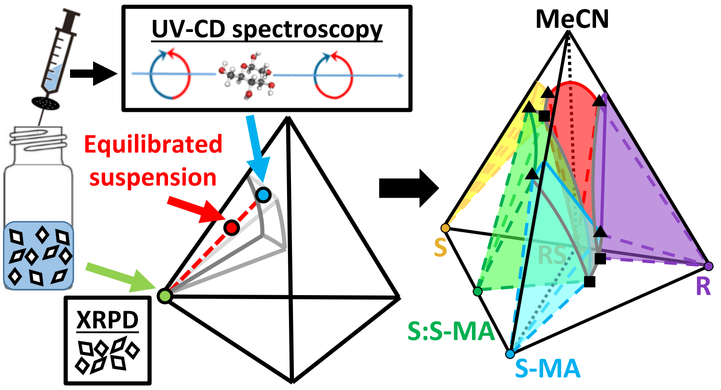

4.1. Introduction

Because of their mirror image symmetry, enantiomers exhibit the same enantiopure physical properties, such as the crystal melting point, solubility, molecular reactivity with achiral molecules, and the same response in analysis by conventional spectroscopy methods [nuclear magnetic resonance, ultraviolet (UV), and infrared].[1] However, their interaction with chiral systems, for example, a chiral drug interacting with chiral receptors in the human body, differs and hence induces different biological activities. In many cases, one enantiomer has a desired therapeutic effect, while the other may have no effect or even a harmful effect.[2-5] In addition, a non-active counter-enantiomer is an impurity that can constitute up to 50% of the product, which has economic consequences.[6] This is the case for (S)-2-(2-oxopyrrolidin-1-yl)butanamide, known commonly as levetiracetam, a nootropic drug used as an anticonvulsant to treat epilepsy.[7] Although the pure enantiomer product is desired for chiral drugs, the process of obtaining enantiopure active pharmaceutical ingredients (APIs), called chiral resolution, is challenging. Many chiral molecules are synthesized by non-stereoselective chemical reactions, leading to racemic mixtures that require separation. Crystallization is the preferred strategy at the industrial scale as it is relatively inexpensive[8, 9] and can be highly selective depending on the solid-liquid equilibria between enantiomers in solution.[1, 10] In 5-10% of cases, enantiomers crystallize separately to form a conglomerate, which is a physical mixture of enantiopure crystals that is amenable to chiral resolution processes.[11-21] However, in 90-95% of cases, a racemic crystal is formed, and chiral resolution through crystallization is difficult or even impossible.[1, 22, 23] An alternative resolution method is to generate multicomponent crystals. If chiral molecules can be ionized, Pasteurian resolution[24-26] is possible by formation of diastereomeric salts with a resolution agent. Otherwise, a conglomerate of enantiopure cocrystals or solvates can emerge using an achiral coformer or a solvent.[27-29] Finally, using a chiral coformer can either induce formation of a diastereomeric pair of enantiopure cocrystals, or an enantiospecific cocrystal.[30-35]

Understanding these multicomponent systems requires the acquisition of accurate phase diagrams that are key to designing robust and reliable crystallization processes,[36, 37] especially for chiral molecule separations.[25, 38] Phase diagrams represent compositional phase domains for equilibrium states of a system. The equilibrium state is strongly dependent on the system's intensive properties, such as temperature and overall component compositions. However, phase diagrams become more complex as the number of components increases. In the case of chiral resolution by crystallization, ternary phase diagrams are commonly used to understand the solid-liquid equilibria between enantiomers in a solvent,[32, 35, 39-41] a single enantiomer with a salt-former or a coformer,[31, 32, 35, 42] and diastereomeric salt systems.[25, 26] However, to truly understand and optimize a chiral resolution process of a racemic compound with a chiral coformer (or salt-former) in a solvent,[31, 32, 35, 43] it is necessary to know the quaternary phase diagram.

Multicomponent chiral phase diagrams increase in complexity as the number of chiral components increases because of the difficulty in quantifying them. For instance, the study of two symmetrical enantiospecific cocrystals requires the quantification of four chiral molecules in a solvent to determine the phase diagrams.[44] Therefore, accurate quantitative methods to measure the concentration of all chiral molecules and to distinguish between two enantiomers are needed. Chiral quantification methods usually involve first measuring the components' total concentration using gravimetry,[39] titration,[40] UV-vis spectroscopy[45] or achiral high-performance liquid chromatography (HPLC)[35] and then quantifying the enantiomer's concentrations using polarimetry[46] or chiral HPLC.[23, 39] Polarimetry can only characterize a single variable variation, making quantification unreliable if more than one pair of enantiomers is present,[47] and also presents issues such as low sensitivity, and influence by other components and temperature variation.[48, 49] Chiral HPLC does not have these disadvantages and is more widely used. It can quantify two enantiomers in a single step,[23, 41, 50] and for non-enantiomeric chiral molecules, quantification can be designed with both achiral and chiral HPLC methods.[32, 51] However, quantification of two enantiomers and at least one other chiral molecule increases the complexity of finding chromatography separation conditions. A combination of two different methods, such as achiral and chiral HPLC, often becomes necessary.[16, 35, 44] The requirement for multiple chromatography columns and mobile phases becomes a disadvantage, as new HPLC methods need to be developed for every chiral multicomponent system studied.[52]

An interesting alternative to analyze chiral molecules is circular dichroism (CD). This technique is based on the differential interaction of a chiral molecule with left and right circularly polarized light (Figure 4.1) and is commonly used for structure and conformation determination of chiral molecules and proteins.[53-55] Ultraviolet circular dichroism (UV-CD) is CD in UV wavelengths and has proven its efficiency to quantify enantiomers in solution.[56-59] Two signals are measured simultaneously: one is the UV signal that depends on all the molecules dissolved, and one is the CD signal that depends on the differential concentrations between the chiral compounds present. The advantage of UV-CD is that it can simultaneously detect more than one pair of enantiomers with a high sensitivity.[55, 60] The signals depend on component interactions in their spectroscopic behavior across a range of wavelengths. With the use of chemometrics[61-64] for data analysis, complex spectra can be understood. The composition information can be linked to the spectra to develop robust calibration models allowing unknown solutions to be quantified. Indeed, chemometrics on absorption spectroscopy rely on the Beer-Lambert law,[65, 66] a proportionality relation between absorbance and concentration at every wavelength measured. Therefore, multivariate methods consider the different wavelength variables to quantify the system with improved accuracy.[67] Previous quantification work with CD used a two-step approach with multivariate curve resolution (MCR) to decompose datasets into individual component spectra and estimate their relative contributions, which are later transformed into absolute trends by fitting known values and performing a two-point calibration.[68]

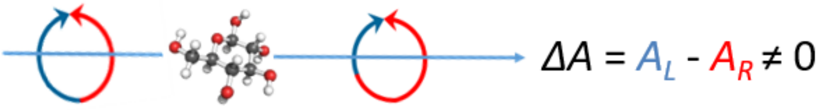

Figure 4.1: Circular dichroism: a light source composed of an equal amount of left-handed (blue) and right-handed (red) circularly polarized light, one of which is preferentially absorbed by a chiral molecule. A differential absorbance *ΔA* is measured between the absorbance of left-handed light A_L and right-handed light A_R.

In this study, we propose a new approach with multivariate partial least squares (PLS) calibration models[69, 70] to quantify chiral multicomponent systems using UV-CD spectroscopy. With this method, we determine chiral phase diagrams in the quaternary system of 2-(2-oxopyrrolidin-1-yl)butanamide enantiomers (R and S), (S)-mandelic acid (S-MA), and acetonitrile (MeCN) at 9°C. This system was previously found to have stable solid phases of the pure solutes, a stable racemic compound between enantiomers, and an enantiospecific 1:1 cocrystal between S and S-MA.[31, 35] The ternary phase diagrams of this system have until now only been estimated using limited data acquired from a combination of HPLC methods.[35] In this work, we first present a revaluation of the latter data with our method and propose a more accurate representation of the ternary phase diagrams. Then, we construct the full isothermal quaternary phase diagram for the first time, by acquiring many solubility data inside the tetrahedron plot. With the understanding of the solid phase stability and the influence of component compositions on their solubility, the chiral resolution of levetiracetam by enantioselective cocrystallization can be designed from the phase diagram data.

4.2. Experimental Methods

4.2.1. Materials

To distinguish components in the following study, the 2-(2-oxopyrrolidin-1-yl)butanamide enantiomers will be labeled **R** and **S**, and their racemic compound **RS**, the coformer S-mandelic acid **S-MA**, the enantiospecific cocrystal **S:S-MA**, and the solvent acetonitrile **MeCN** (Figure 4.2). The commonly known names are levetiracetam for S and etiracetam for RS. Levetiracetam is the biologically active enantiomer and is a medication used to treat epilepsy. R, S, and RS were provided by UCB Pharma. S-MA (≥ 99%, Sigma-Aldrich) and MeCN (HPLC grade, 100%, VWR Chemicals) were used as received. S:S-MA was crystallized by slow evaporation of a 1:1 molar ratio solution in methanol (MeOH) and confirmed by X-ray powder diffraction (XRPD). The XRPD patterns of materials used, and their references can be found in the Appendix B (Section B1). All solid phases present specific diffraction peak positions that permit assessment of their presence in solid mixtures.

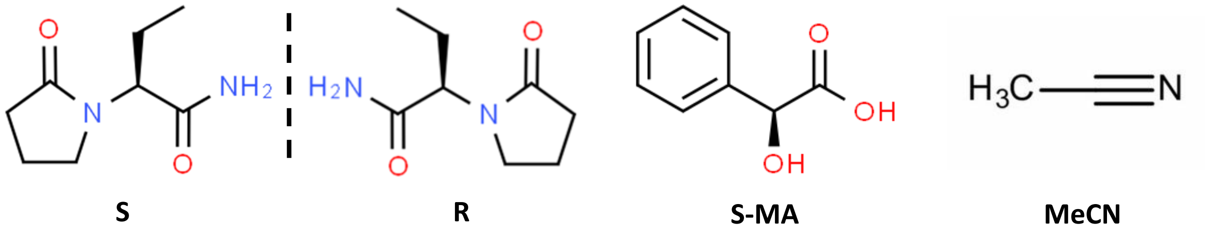

Figure 4.2: Chemical structures of the four components levetiracetam S (antiepileptic drug), its counter enantiomer R, S-mandelic acid (S-MA), and the solvent acetonitrile (MeCN).

4.2.2. X-ray Powder Diffraction

XRPD analyses were performed using a Bruker D8 Advance II diffractometer with Debye–Scherrer transmission from a Cu source radiation (1.541 Å) with an operating voltage of 40 kV, current 50 mA, Kα1 Johansson monochromator, and 1 mm anti-divergence slit. A Bruker D2 Phaser diffractometer was also used, with Bragg-Brentano reflection θ/θ geometry from a Ni filtered Cu source radiation (1.541 Å) with an operating voltage of 30 kV, current 10 mA and 0.2 mm anti-divergence slit. A scanning range of 2θ values from 4° to 35° was applied with a 0.017° step and a step time of 1 s.

4.2.3. Ultraviolet-Circular Dichroism Spectroscopy

UV-CD spectroscopy was performed using a Chirascan-Plus spectrometer from Applied Photophysics, constantly purged with a nitrogen flow. The samples were analyzed in a Hellma quartz cell with a 0.1 mm path length. Both UV and CD spectra were collected with a 0.5 nm step and 1 second per point in the 200-260 nm range. The background of pure acetonitrile was measured and automatically subtracted from the spectra using the instrument software. As the detector is saturated when solutions with a total concentration of dissolved components exceed 5 mg/mL, the calibration range is set from 0.5 to 5 mg/mL, and all samples were diluted to fall into this calibration range. The UV and CD spectra are expressed in, respectively, absorbance units and ellipticity units (ϑ), a value proportional to CD. The data were collected using Chirascan Pro data V4.4.2.0, and the analysis of the UV-CD data was done using Origin Pro 2017 and Pls_toolbox 4.0 by Eigenvector research Inc. The spectra of both UV and CD were pre-processed with first derivative baseline correction followed by a Savitzky-Golay smoothing[71] of a second-order polynomial with five window points and mean centering.[72] The spectra were otherwise free of artifacts and baseline issues, so no additional pre-processing was done.

4.2.4. Development of a Multivariate Calibration for Quantification

4.2.4.1. Calibration Samples

A multivariate calibration model using samples of known composition, i.e., calibration samples, was developed to allow the measurement of unknown composition solutions from UV-CD spectra. The chosen independent variables in the 4-component calibration samples are the mass fraction x, for R (x_R), S (x_S), and S-MA (x_{S-MA}), with the solvent MeCN mass fraction $x_{MeCN} = 1 - x_R - x_S - x_{S-MA}$. The construction of the model was to allow quantification of equilibrated samples from a quaternary phase diagram, which is a tetrahedron plot whose triangular faces are isothermal ternary phase diagrams. The calibration space, therefore, was designed to cover the entire quaternary space, consisting of the perimeter and the interior of the tetrahedron. Experimental solvent free component ratios of the calibration samples are shown in Figure 4.3. Each ratio (square) represents five calibration samples prepared by successive dilutions of the same bulk solution within the UV-CD calibration range of the molecules (0.5 to 5 mg/mL total concentration), allowing the total concentration for all components to be covered accurately. This calibration sample preparation method yields a calibration data set with 270 compositions. The 270 calibration sample compositions can be found in the Appendix B (Table B1). For each calibration sample, UV and CD spectra were measured.

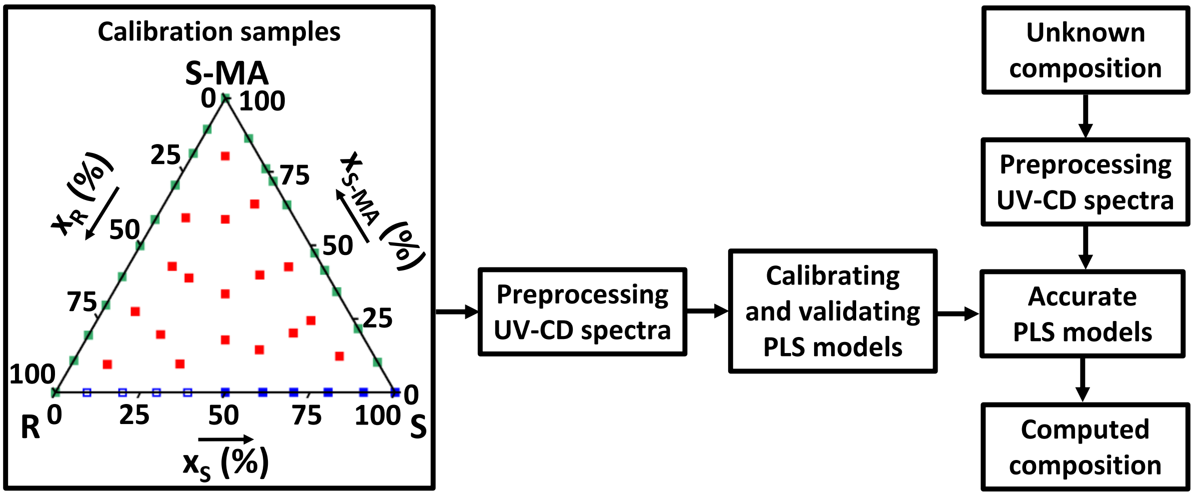

Figure 4.3: Design of the multivariate calibration, with calibration samples as input, to obtain PLS models allowing the computation of unknown compositions from their UV-CD spectra. The distribution of calibration samples is represented by their solvent free mass fraction in components. For each fraction, five solutions of varying total concentration were prepared from successive dilutions into the UV-CD calibration range (0.5 to 5 mg/mL), and the related UV and CD spectra were measured and gathered to build the model. Blue points correspond to the R/S/MeCN ternary section, open squares

being obtained from symmetry of the experimental CD spectra with S being in excess. Green points correspond to ternary sections S/S-MA/MeCN and R/S-MA/MeCN. Red points correspond to quaternary compositions containing R, S, and S-MA in MeCN.

4.2.4.2. Design of Multivariate Partial Least Squares Calibration Models

The modeling for quantitative determination of x_R, x_S and x_{S-MA} in unknown solutions, using experimental UV and CD spectra (Figure 4.3), requires a calibration using UV and CD spectra of the calibration samples. Here, we use a multivariate PLS calibration.[69, 70] Two calibration models were designed, one for the UV data and the other for CD data. Both types of signals are influenced differently by the concentration in all dissolved components (R, S, or S-MA). They both follow the Beer-Lambert proportionality law[65, 66] between absorbance and concentration at every wavelength measured. For UV spectra, because R and S absorb UV identically, two variables were defined as influencing the signal in the calibration: the total enantiomer mass fraction $x_{S+R} = x_S + x_R$ and the S-MA mass fraction x_{S-MA}. However, for CD, the two enantiomers R and S have a symmetrical response and the spectra depend on the differential mass fraction $x_{S-R} = x_S - x_R$ between enantiomers. Therefore, two variables were defined as influencing the CD spectra in the calibration: the differential mass fraction between enantiomers x_{S-R} and the mass fraction in S-MA x_{S-MA}. With x_{S+R} and x_{S-R} from UV and CD data, the enantiomeric excess

$$E = \frac{x_S - x_R}{x_S + x_R} = \frac{x_{S-R}}{x_{S+R}}$$

was computed and x_R and x_S were retrieved as

$$x_S = \frac{1+E}{2} \times x_{S+R}$$

and

$$x_R = x_{S+R} - x_S$$

Since only one enantiomer of mandelic acid (S-MA) is present, both UV and CD calibration models yield the total S-MA concentration x_{S-MA}.

After their acquisition, all spectra were pre-processed (Figure 4.3) by first derivative baseline correction followed by a Savitzky-Golay smoothing[71] of the second-order polynomial with five window points and mean centering.[72] This maintains the shape of the spectra and allows separation between the peaks and removal of artifacts, such as baseline shifts or noise,[67] thus improving the predictive performance of the calibration models. The pre-processed data of both CD and UV were partitioned into a calibration (80%) and a validation (20%) dataset using the Kennard-Stone algorithm,[73] which provides a representative split that gives a uniform distribution of samples. Finally, the multivariate calibration models were built using PLS regression[69, 70] to relate the spectral data to the compositions x_{S+R}, x_{S-R}, and x_{S-MA}. PLS is a multivariate regression method with compression of spectral data beforehand to reduce the number of variables present.[70, 74] The compressed variables obtained in PLS are referred to as latent variables (LVs). The models were validated internally and externally using cross-validation and validation datasets to test their reliability and accuracy.[61] To minimize overfitting, the optimum LVs were chosen with a maximum explained variance for cross-validation using a random subset approach with 30 data splits and 15 iterations.

To compare the model's predictions with experimental results from another quantification method, 28 compositions of different ratios in S and S-MA were analyzed simultaneously by UV-CD spectroscopy and the gravimetric method, i.e., measuring solubility by the mass difference between a solution and its solid obtained after complete evaporation.

4.2.5. Phase Diagram Construction: Equilibration Technique

The experimental compositions for equilibration were estimated at the chosen temperature of 9 °C for phase diagram construction, based on existing data.[35] These compositions were prepared in 2 mL sealed vials. After dissolution at 50 °C, they were cooled down to 9 °C and seeded with stable solid phases in the corresponding system, to form stable suspensions. All vials were stored isothermally at 9 ± 1 °C under stirring, using a Polar Bear Plus apparatus (Cambridge Reactor Design, UK) that enabled simultaneous equilibration of batches of 28 compositions. The compositions were left to equilibrate for 14 days after which the saturated solution and solid compositions were determined, which led to phase diagram points as summarized in Figure 4.4. The saturated liquid phases were sampled using a syringe with a filter. To obtain a final solution whose total component concentration is in the UV-CD calibration range for that system, a sample dilution ratio (i.e., the total mass of the dilution solvent divided by the mass of the saturated solution sample) from 10 to 300 was applied depending on the phase diagram region. Due to high dilution ratios, the liquid properties between saturated liquids and diluted samples vary a lot. Therefore, weighing of saturated liquid and added solvent was mandatory for precision, as working with volumes proved to induce a significant error in data. The diluted solutions were then analyzed by UV-CD spectroscopy. The obtained spectra were pre-processed and used as input into the model to determine the mass fractions x_R, x_S, x_{S-MA}, and x_{MeCN} of each component in the diluted solution. The saturated liquid composition for each sample was then computed using the calculated sample dilution ratio and converted to molar fraction *X* to position the experimental point in the phase diagram. The solid phases in equilibrium with the saturated liquid were analyzed by XRPD after filtration of the suspensions to conclude on the phase diagram region the point belongs to. Eutectic points and quaternary points, corresponding to solutions equilibrated with more than one solid, are identified by XRPD in which more than one solid phase is measured. When not measured experimentally, they are estimated at the intersection of extrapolated neighboring solubility curves/surfaces.

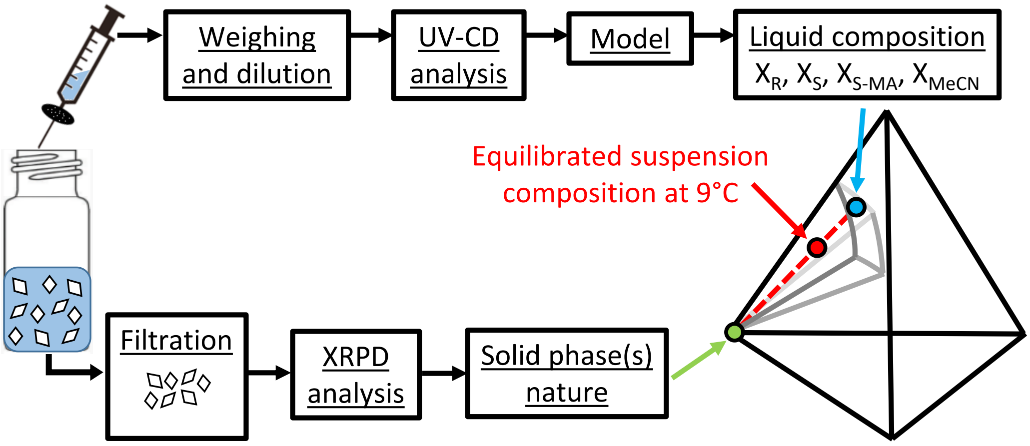

Figure 4.4: Protocol to obtain phase diagram composition from isothermal suspension at 9 °C after 14 days.

4.3. Results

Using the UV-CD spectroscopy data from calibration samples, we develop multivariate PLS calibration models to compute multicomponent chiral compositions in unknown solutions. The validated models are applied to phase diagram determination in the R/S/S-MA/MeCN quaternary system represented as a tetrahedron plot in Figure 4.5. First, we detail the results regarding the spectral data and the calibration model specificities. Then, we present the revaluation of three solid-liquid ternary phase diagrams at 9 °C, represented on the faces of the tetrahedron involving the solvent. We start with the phase diagram between R and S enantiomers forming a racemic compound RS (Figure 4.5a), then between S and S-MA forming a 1:1 enantiospecific cocrystal S:S-MA (Figure 4.5b), and next between R and S-MA forming no cocrystal (Figure 4.5c). Finally, the inside of the tetrahedron (Figure 4.5d) is investigated in detail for the first time as our models allow quantification of quaternary compositions, with the view to understand the solid phase stabilities and their solubilities as a function of component compositions.

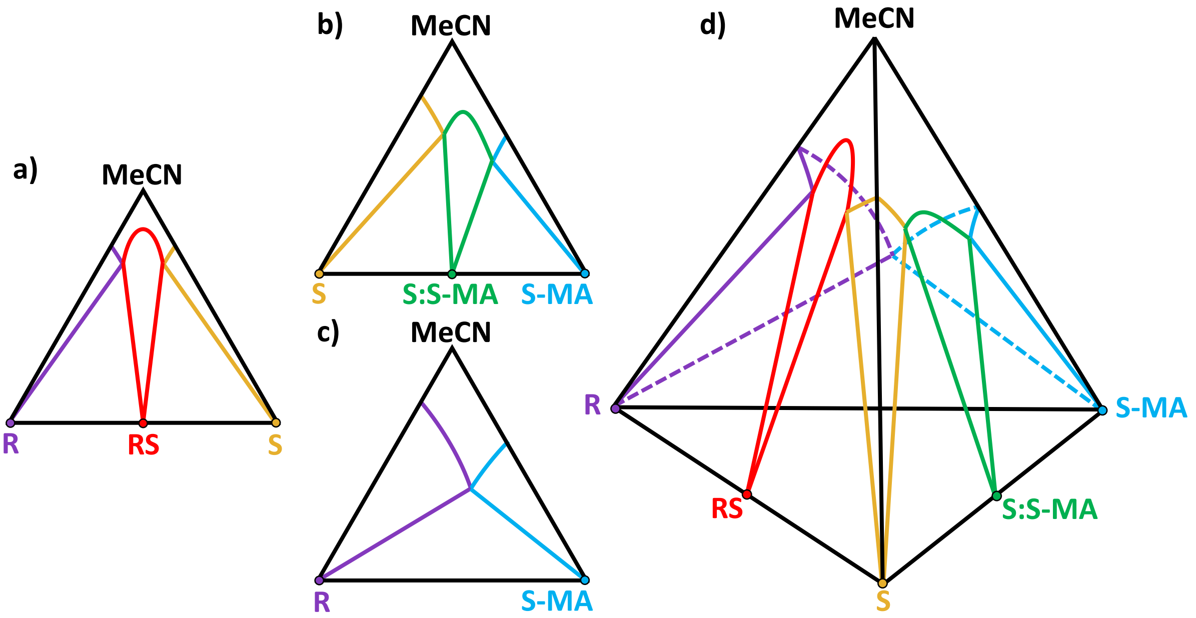

Figure 4.5 (a-d): Isothermal and isobaric schematic phase diagrams of the four-component system: (R)- and (S)-2-(2-oxopyrrolidin-1-yl)butanamide (R and S), (S)-mandelic acid (S-MA), and the solvent acetonitrile (MeCN). The ternary phase diagrams were estimated in a previous study,[35] while solubility measurements inside the tetrahedron are tackled for the first time in the present study to understand phase stability and solubility variations in the quaternary diagram.

4.3.1. Multivariate PLS Calibration Model Development from UV-CD Spectra

4.3.1.1. Spectral Data in the Quaternary System

To treat spectral data from UV and CD, defining a wavelength range where all dissolved molecules absorb UV is necessary. Since the solvent MeCN absorbs UV below 195 nm and R, S, and S-MA do not absorb above 260 nm, the optimal wavelength range is chosen to be from 200 to 260 nm. The whole region is used for composition prediction using multivariate methods. In Figure 4.6a UV spectra for several calibration samples are represented. UV spectroscopy does not distinguish between the R and S enantiomers, and both molecules yield an absorption peak below the chosen wavelength range with a large part of the tail of this peak visible from 200 to 250 nm in Figure 4.6a (yellow solid line). S-MA shows similar UV absorption behavior but additionally has a shoulder at

205 to 216 nm (Figure 4.6a, light blue solid line). Because of the significant overlap in UV spectra of pure R/S and pure S-MA, the influence of each component in R/S and S-MA mixtures is difficult to distinguish but can be observed in the resulting spectra shape. Therefore, it assesses the necessity of using multivariate calibration for modeling, as it considers the effects of composition changes on the whole wavelength range at the same time. Both the normalized spectral shape for 50% S/50% S-MA (Figure 4.6a, green dashed line) and 33.3% of R, S, and S-MA (Figure 4.6a, black dotted line) mixtures highlight this influence. The more S-MA a sample contains, the more the inflections are marked in the resulting spectra.

Figure 4.6b shows the CD spectra of the same calibration samples, where we observe that CD distinguishes both enantiomers. R and S give positive and negative symmetrical responses with peak extrema at around 230 nm (purple and yellow solid lines). The 50%/50% mixture of R and S yields a flat line signifying the presence of the equal amount of both enantiomers (red dashed line). S-MA has a positive CD spectrum with a peak at 223 nm (Figure 4.6b, light blue solid line). Significant overlap can be seen between the mixtures of R, S and S-MA, leading to different spectral shapes based on the component ratio. For instance, an equimolar ratio between R, S and S-MA results in a CD spectrum of the same shape as pure S-MA with a peak at 223 nm but with the intensity being a third, for the same total concentration (black dotted line). Therefore, despite the overlap, the shapes and intensities of the CD spectra show information on both the concentration difference between R and S and the S-MA concentration.

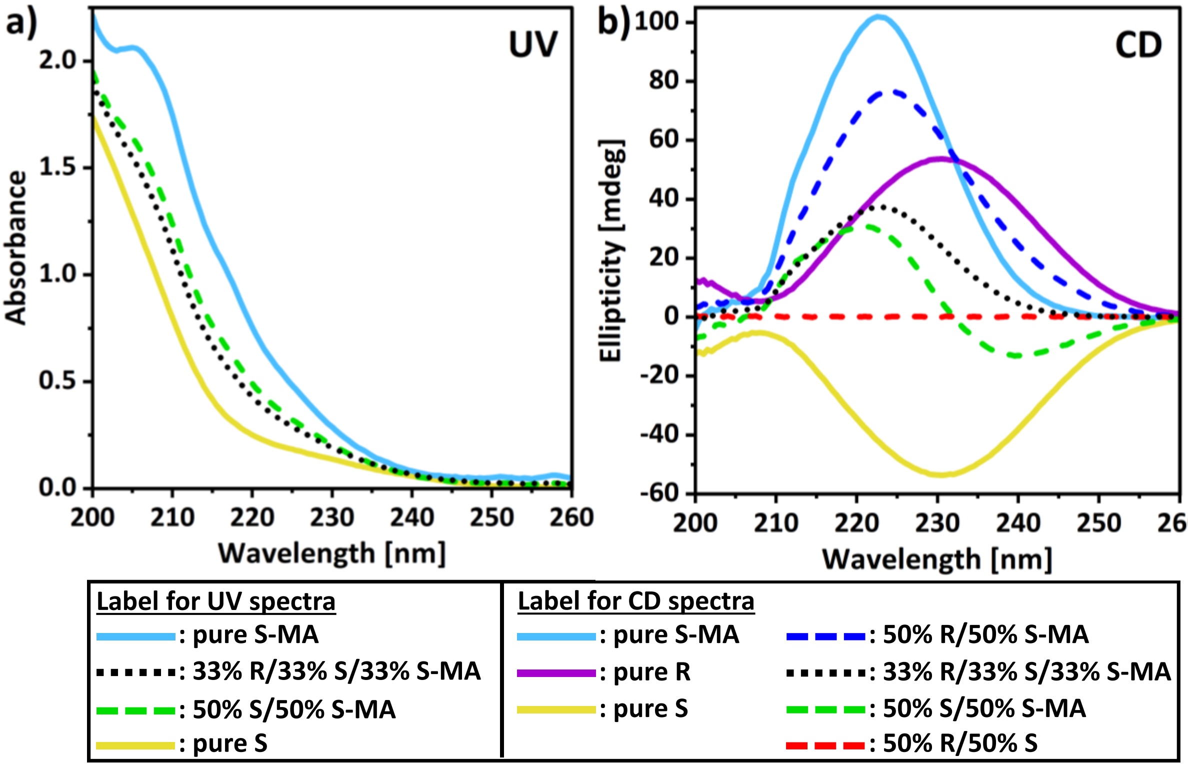

Figure 4.6: (a) UV and **(b)** CD spectra of solutions with a normalized total concentration of 4 mg/mL: pure components (solid lines), binary mixtures (dashed lines), and ternary mixtures (dotted lines).

4.3.1.2. Multivariate PLS Calibration Model Specificities

The results of PLS calibration models for the quantitative prediction of x_{S+R}, x_{S-R}, and x_{S-MA} are summarized in Table 4.1. Their reliabilities and accuracies were evaluated internally and externally using cross-validation and the validation datasets. The root mean square error of prediction (RMSEP) is computed to estimate the error in predicting the measured values of a known sample, while the root mean square error of cross-validation (RMSECV) estimates the error in predicting the values of a calibration sample. The models are also tested by R^2 (goodness of fit) and Q^2 (goodness of prediction) values. R^2 gives the amount of variance explained by the model, and Q^2 gives the amount of variance predicted by the model. Both PLS models required only two LVs to compress the spectral data variables and capture the variance in the data, while giving good predictions with high linearity ($R^2 > 0.99$, $Q^2 > 0.97$). The high accuracy is highlighted by the levels of the RMSEP and RMSECV that show a lower order of magnitude for mass fraction errors than the mass fraction values of the calibration samples (see the Appendix B Table B1).

Table 4.1: Results of PLS calibration models for UV and CD spectral data acquired in the 200 to 260 nm range describing the accuracy in the composition prediction. Results are the number of latent variables (LVs) required, the root mean square error of prediction (RMSEP), the root mean square error of cross-validation (RMSECV), the goodness of fit R^2, and the goodness of prediction Q^2.

Data	Method	Value predicted	N° of LVs	RMSEP ($\times 10^{-6}$) (g/g)	RMSECV ($\times 10^{-6}$) (g/g)	R^2	Q^2
UV	PLS	x_{S+R}	2	16.3	13.0	0.997	0.977
		x_{S-MA}		14.5	12.0		
CD	PLS	x_{S-R}	2	12.0	1.16	0.998	0.986
		x_{S-MA}		15.4	11.1		

Figure 4.7 shows the predicted values of calibration samples through the calibration models versus their actual values for x_{S+R} (a), x_{S-R} (b), and x_{S-MA} (c, d), to visualize the goodness of fit. It can be observed that the split of samples between validation sets (green triangles) and calibration sets (blue points), performed using the Kennard-Stone algorithm,[73] is uniform in the distribution and therefore representative. The values of x_{S-R} from CD in Figure 4.7b range from positive to negative, representing an excess of S and R in the sample, respectively. Very strong linearity along the diagonal lines in red can be seen in the plots for all samples, meaning that prediction is very close to the actual value. The linearity relates to the RMSEP and RMSECV values that quantify the error on how much samples from the calibration sets and validation sets deviate from the diagonal line, therefore giving an estimation of the average error in a prediction. There is no significant difference between x_{S-MA} predicted from both the UV and CD measurements (Figure 4.7c,d), with the RMSEP and RMSECV values being very similar, thus showing the accuracy and consistency of the models. However, the PLS model with CD data gives the best prediction with the lowest RMSECV and R^2. Therefore, the x_{S-MA} value from CD is always used in calculations for accuracy.

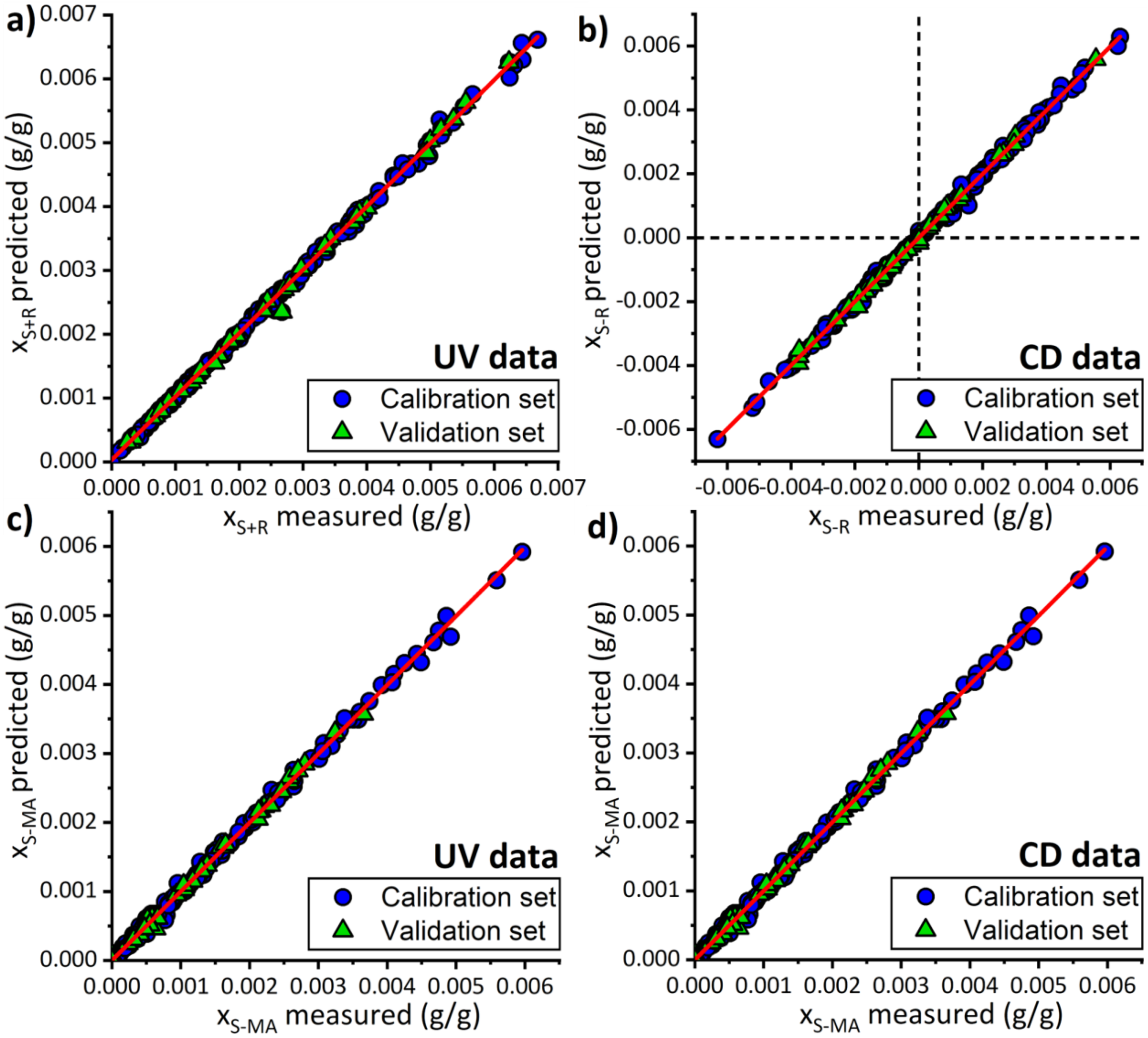

Figure 4.7: Plots for experimental values of calibration samples versus their predicted values through the calibration models for **(a)** Total mass fraction in enantiomers x_{S+R} (UV data). **(b)** Differential enantiomers mass fraction enantiomers x_{S-R} (CD data). **(c)** Mass fraction in S-MA x_{S-MA} (UV data). **(d)** Mass fraction in S-MA x_{S-MA} (CD data).

The UV-CD model predictions are compared with results obtained from the gravimetric method for 28 compositions of different ratios in S and S-MA that were analyzed simultaneously by UV-CD spectroscopy. The percentage error $\delta\ (\%) = \frac{|X-Y|}{Y}$ is used for comparison, with X being the total solubility obtained with the UV-CD model result, and Y the total solubility from the gravimetric method, on the same saturated solution. It shows a mean δ of 2.09% between the two methods on the total solubility, with a standard deviation of 1.47% (see the Appendix B Table B2). Even though gravimetry is not an accurate quantification method, particularly when using a single measure, it relies on a physical measurement and therefore confirms that our multivariate calibration models do not have a bias in their calculations. These validated calibration models allow accurate determination of the mass fractions of unknown solutions in R (x_R), S (x_S), S-MA (x_{S-MA}), and MeCN (x_{MeCN}), and therefore, they are used for computing the phase diagram data.

4.3.2. Isothermal Ternary Phase Diagrams

4.3.2.1. Ternary System of R/S/MeCN

In the R/S/MeCN system, the stable solids consisting of pure R, pure S, and pure racemic compound RS are expected to crystallize at equilibrium. In total, 26 equilibrated solution compositions, with enantiomeric excess (E) values from 0 to 100%, are computed from experimental results. Due to symmetry along racemic compositions in enantiomeric systems, 26 additional points corresponding to negative values of enantiomeric excess (E) are deduced from the mirror projection of the first 26 points. The isothermal ternary phase diagram of R and S in MeCN at 9 °C is plotted in Figure 4.8. Solubility lines correspond to the typical shape of a stable racemic compound in an isothermal ternary system and solid phases in equilibrium are confirmed. This phase diagram is in excellent agreement with previous data obtained with a combination of achiral and chiral chromatography methods (Figure 4.8, beige diamonds).[35]

The eutectic points a and b (Figure 4.8, gray triangles) are obtained with an experimental composition presenting S and RS in stable suspension. These points fit perfectly with the intersection of neighboring solubility curves. Experimental solubility values of pure R, S, and RS solids, with compositions of eutectic points a and b, are compiled in the Appendix B, Table B3. All data point compositions with related solid phases identified at equilibrium used in Figure 4.8 and Figure 4.9 are given in the Appendix B, Table B4. Only the pure enantiomer solubility differs slightly from previous data.[35] However, we note that our value is confirmed through the repetition of four measurements in different saturated solutions of pure S, with UV-CD and the gravimetric method used to compare the model's prediction. Both methods lead to the same value with about 0.5 mg/mL variation (see the Appendix B, Table B5).

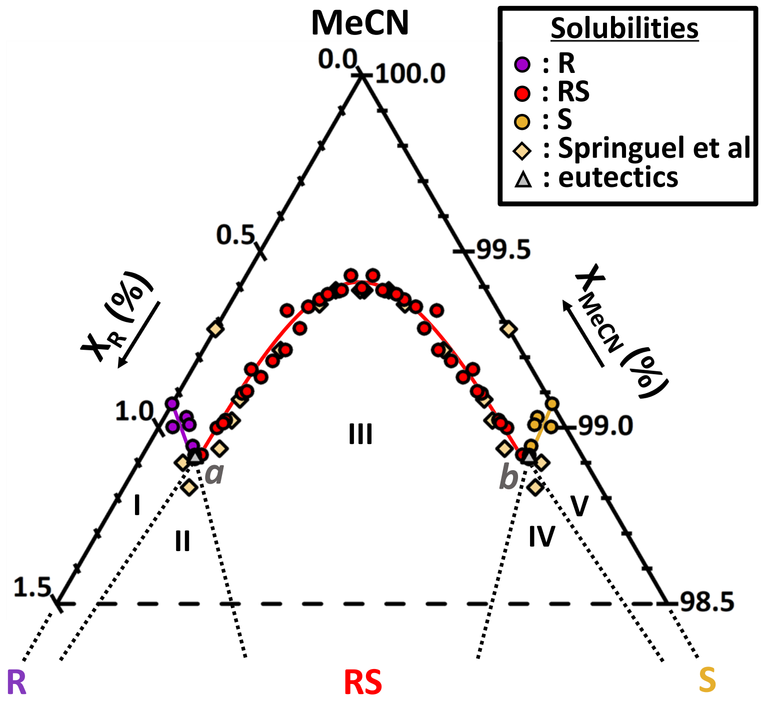

Figure 4.8: Isothermal ternary phase diagram of R and S in MeCN at 9 °C showing a racemic compound system. Regions I, III, and V are, respectively, the stability domains in which an overall composition phase splits into a saturated solution and, respectively, the solid R (purple solubility points), racemic solid RS (red solubility points), and the solid S (yellow solubility points). Regions II and IV are triphasic domains between the racemic compound RS, a solution of eutectic composition (gray triangle) and R

and S, respectively. Above the solubility lines is the single-phase domain of the undersaturated solution. Dotted lines are boundaries between stability domains. Beige diamonds are the solubility points from the Springuel et al. study obtained with achiral and chiral chromatography.[35] Note that the phase diagram is zoomed in to the solvent corner. Data points used for the construction of this diagram are detailed in the Appendix B (Table B4). Eutectic points a and b were measured experimentally with a composition presenting S and RS in stable suspension.

Figure 4.9 represents the experimental mole fractions X_R against X_S of the equilibrium solubility points in the R/S/MeCN system at 9 °C. The solubilities X_R* and X_S* of pure R and S solids are indicated. No significant solubility modification effect is observed for pure R (purple) and pure S (yellow) solid solubility points due to the presence of the other component as X_R and X_S stay relatively constant. The solubility increase for X_R and X_S values at the eutectic points a and b is only 2%. Where the racemic compound RS equilibrates (red points), its solubility $(X_R \times X_S)^*$ shows an important curvature depicting lower X_R values than X_R at the eutectic a, down to a minimal total solubility $(X_R + X_S) = 0.6$ % for pure RS at the intersection with the dashed line indicating the 1:1 stoichiometry between R and S. The solubility of the pure enantiomer in the pure solution is 1.5 times higher than pure RS total solubility in a racemic solution. Maximum total solubilities are reached in eutectic points, where the total solubility is 1.2 times higher than pure R and S and 1.8 times higher than pure RS solubility.

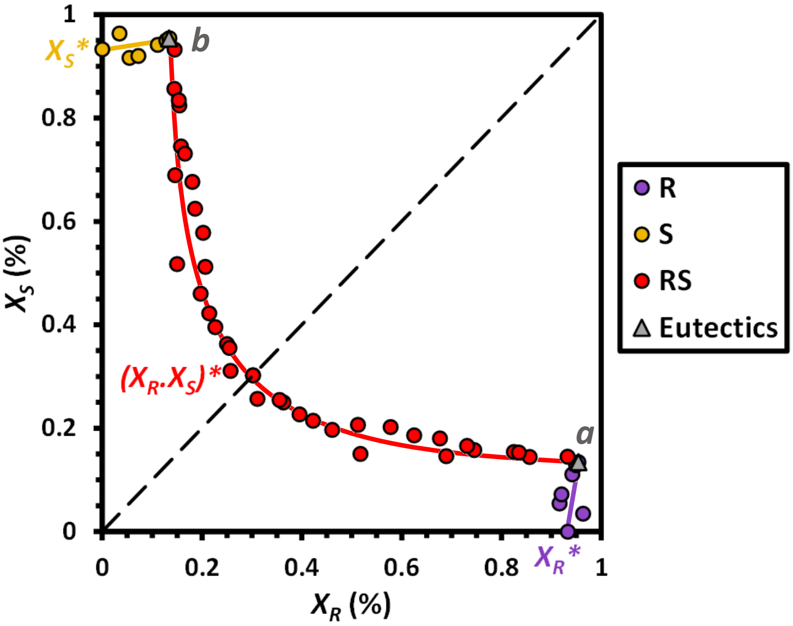

Figure 4.9: Experimental mole fractions X_R against X_S of the solubility points in the R/S/MeCN system at 9 °C. X_R* and X_S* are solubilities of pure components crystals, and $(X_R \times X_S)$* is the solubility of the racemic compound RS. The dashed line indicates 1:1 stoichiometry between R and S.

4.3.2.2. Ternary System between S/S-MA/MeCN

In the S/S-MA/MeCN system, the stable solids consisting of pure S, pure S-MA, and pure 1:1 enantiospecific cocrystal S:S-MA are expected to crystallize at equilibrium. Experimental solubilities are computed from experimental results of 55 equilibrated suspensions of varying ratios between S and S-MA in MeCN. The isothermal ternary phase diagram at 9 °C is plotted in Figure 4.10, zoomed in to the solvent corner. The phase diagram corresponds to a stable 1:1 cocrystal forming system between S and S-MA. As the theoretical line between the 1:1 stoichiometry of the S:S-MA solid phase and the pure solvent MeCN crosses the solubility curve of

S:S-MA (green), the cocrystal exhibits a congruent solubility at 9 °C, meaning that it forms a stable suspension in solutions with the same stoichiometry as the cocrystal.

The eutectic point c is obtained at an experimental composition presenting S and S:S-MA in stable suspension. It fits well with the intersection of neighboring solubility curves. The eutectic point d is estimated at the intersection of converging solubility curves. In Figure 4.10, the phase diagram solubility points and domain shapes differ slightly from previous data and their interpretation with fewer data points on the same system by Springuel et al.,[35] as they suggested the cocrystal to have an incongruent solubility (diamond points). Here, with more data points presented, and an experiment resulting in eutectic solution composition c with S and S-MA solids in suspension, we revaluated the stability domains. A shift can also be observed between some of their solubility data and ours, even in pure component solubilities. We checked the latter through the repetition of four measurements in different saturated solutions of pure S and pure S-MA with the UV-CD model and the gravimetric method that was used when validating the model's predictions by comparison with an external method. It gives consistent values and negligible variations (see the Appendix B, Table B5). Moreover, 28 saturated solutions from our ternary system were validated simultaneously by the gravimetric method (see the Appendix B, Table B2). Therefore, we propose an accurate revaluation of the phase diagram using consistent results. Experimental solubility values of pure S, S-MA, and S:S-MA solids, with compositions of eutectic points c and d, are compiled in the Appendix B, Table B3. All data point compositions with related solid phases identified at equilibrium used in Figure 4.10 and Figure 4.11 are given in the Appendix B, Table B6.

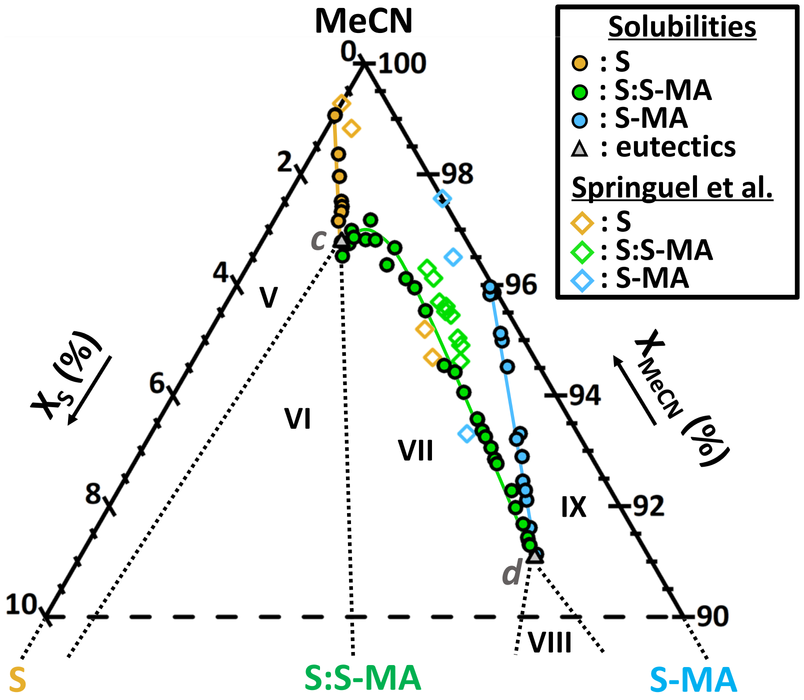

Figure 4.10: Isothermal ternary phase diagram of S and S-MA in MeCN at 9 °C showing an enantiospecific cocrystal system. Regions V, VII, and IX are the stability domains in which an overall composition phase splits into a saturated solution and the solid S (yellow solubility points), the cocrystal S:S-MA (green solubility points), and the solid S-MA (blue solubility points), respectively. Regions VI and VIII are triphasic domains between the cocrystal S:S-MA, a solution of eutectic composition (gray triangle) and S and S-MA, respectively. Above the solubility lines is the single-phase domain of the undersaturated solution. Dotted lines are boundaries between stability domains.

Diamonds are the solubility points from Springuel et al. study obtained with achiral and chiral chromatography.[35] Note that the phase diagram is zoomed in to the solvent corner. Data points used for the construction of this diagram are detailed in the Appendix B (Table B6). Eutectic point c was measured experimentally in a composition presenting S and S:S-MA in stable suspension. Eutectic point d was estimated at the intersection of converging solubility curves.

Figure 4.11 shows the experimental mole fractions X_S against X_{S-MA} of the equilibrium solubility points in the S/S-MA/MeCN system at 9 °C. The solubilities X_S* and X_{S-MA}*of pure S and S-MA solids are indicated. A strong effect on the solubility of pure S solid is observed (yellow) as a function of the concentration of S-MA: the solubility X_S at the eutectic point c is 2.1 times higher than that in the pure solvent. The total solubility at eutectic point c, including the S-MA concentration, is 3.5 times higher than that in the pure solvent. Similarly, pure S-MA solid solubility points (blue) are increased by the presence of S, up to a solubility X_{S-MA} at eutectic point d that is 1.8 times higher than for pure S-MA solubility, while the total solubility is 2.2 times higher than for S-MA in the pure solvent. The solubility $(X_S \times X_{S-MA})^*$ of the S:S-MA cocrystal (green points) decreases as a function of concentration of S and S-MA, from a maximum value at the eutectics, down to a minimum solubility point that is the pure S:S-MA congruent solubility value at the intersection with the dashed line indicating the 1:1 stoichiometry between S and S-MA, for a minimal total solubility $(X_S + X_{S-MA}) = 3.2\,\%$. The solubility of S-MA in pure solvent is 1.3 times higher than the total solubility of S:S-MA, whose X_{S-MA} is divided by 2.5 compared to the pure S-MA solubility. However, the total solubility of pure S:S-MA is 3.4 times higher than pure S, with X_S being 1.7 times the pure S solubility. The possible explanations for the increase in solubility of pure S and pure S-MA solids, with the presence of the other component in solution, are most likely due to favorable intermolecular interactions between components in solution. Nevertheless, solution complexation is also a possible reason as it has been reported to occur for some cocrystal components.[75]

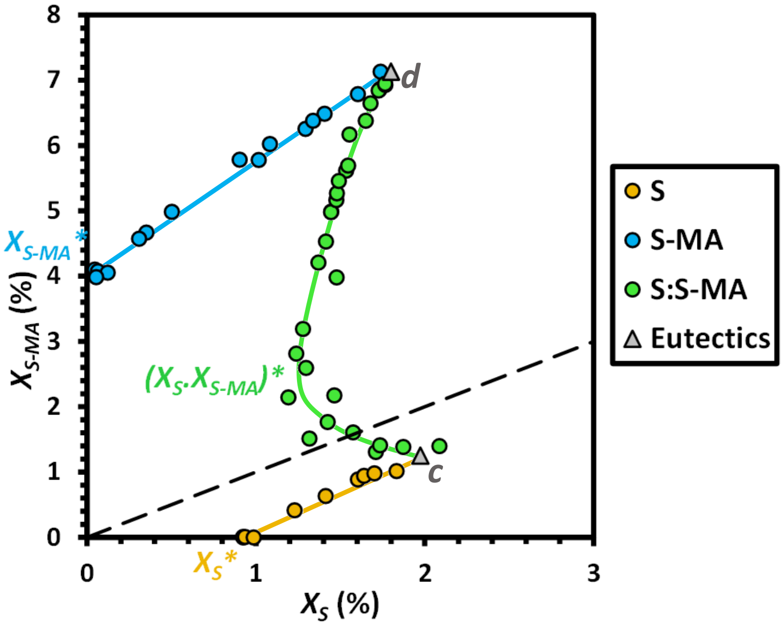

Figure 4.11: Experimental mole fractions X_S against X_{S-MA} of the solubility points in the S/S-MA/MeCN system at 9 °C. X_S* and X_{S-MA}* are pure components crystals solubilities and $(X_S \times X_{S-MA})^*$ is the solubility of the S:S-MA cocrystal. The dashed line indicates 1:1 stoichiometry between S and S-MA.

4.3.2.3. Ternary System between R/S-MA/MeCN

In the R/S-MA/MeCN system, the stable solids consisting of pure R and pure S-MA are expected to crystallize at equilibrium. Experimental solubilities are computed from experimental results of 28 equilibrated suspensions of varying ratios between R and S-MA in MeCN. The isothermal ternary phase diagram at 9 °C is plotted in Figure 4.12, zoomed in to the solvent corner. Contrary to the S/S-MA/MeCN system, no cocrystal forms between R and S-MA as the solubility lines seem to converge to a single eutectic point e and no new solid phase is identified in the experiments. Therefore, it confirms the enantiospecific nature of the S:S-MA cocrystal identified from the Springuel et al. study.[31]

Solubility lines show a strong influence of the components on each other's solubility, with the total solubility increasing sharply in mixtures. The solubility of R is increased more by the concentration of S-MA than the solubility of S in the S/S-MA/MeCN system. This strong increase of the solubility of R with the S-MA concentration, coupled with the absence of cocrystal formation, is causing eutectic point e to be a deep eutectic. This strong affinity between components was already reported in the binary system of R and S-MA,[31] whose binary eutectic temperature of around 32 °C is about 100 °C deeper than the pure R and pure S-MA melting points. Therefore, in the R/S-MA/MeCN ternary system at 9 °C, it induces a small triphasic domain between R, S-MA, and a saturated liquid of eutectic composition e that is at a very high equilibrium concentration. This leads experimentally to a big increase in sample viscosity as solubility increases strongly for compositions close to the eutectic point e, making it difficult to estimate as the solutions are too viscous to be accurately sampled for liquid analysis. Trial experiments to screen eutectic point e are represented in Figure 4.12 by square points, which correspond to five highly concentrated suspensions left at 9 °C for more than 3 weeks, after complete dissolution and seeding with a small amount of R and S-MA solids. For three compositions (blue squares), a very small amount of solid phase crystallizes in the highly viscous liquids. The isolated solid, characterized using XRPD, is pure S-MA despite a low intensity signal because of the small amount of solid recovered. For the two other compositions (white squares), the liquor remains clear with no crystallization happening, it is then assumed they belong to the undersaturated solution domain. These results help to estimate roughly the extension of solubility lines and to define a compositional region in which eutectic point e is positioned. For the system representation and description purposes, the composition of eutectic point e is an approximation. Experimental solubility values of pure R, S-MA, and estimation of eutectic point e are compiled in the Appendix B, Table B3. All data point compositions with related solid phases identified at equilibrium used in Figure 4.12 and Figure 4.13 are given in the Appendix B, Table B7.

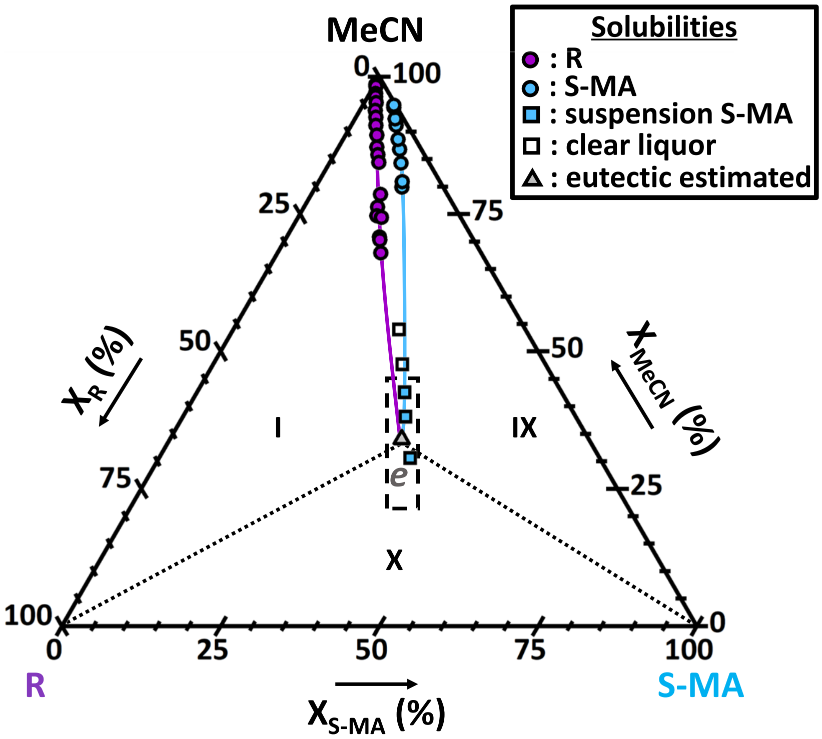

Figure 4.12: Isothermal ternary phase diagram of R and S-MA in MeCN at 9 °C showing a single eutectic equilibrium. Regions I and IX are the stability domains in which an overall composition phase splits into a saturated solution and the solids R (purple solubility points) and S-MA (blue solubility points), respectively. Region X is the triphasic domain between R, S-MA, and a solution of eutectic composition e (gray triangle). Above the solubility lines is the single-phase domain of the undersaturated solution. Dotted lines are boundaries between stability domains. Blue squares correspond to overall compositions of which, due to the high viscosity, only the equilibrated solid could be sampled for XRPD analysis to be identified as S-MA. White squares correspond to sample compositions in which no solid was present after the equilibration period. The dashed box is the region in which eutectic point e is estimated, from the extrapolation of solubility curves and suspensions obtained at blue squares. The center of the box is chosen as the most likely estimation. Data points used for the construction of this diagram are detailed in the Appendix B (Table B7).

Figure 4.13 represents the experimental mole fractions X_R against X_{S-MA} of the equilibrium solubility points in the R/S-MA/MeCN system at 9 °C. The solubilities X_R* and X_{S-MA}*of pure R and S-MA solids are indicated. An important solubility increase effect is observed for the pure R solid solubility points (purple) as X_R values increase due to the increasing presence of S-MA, up to an estimated value of about 32 times higher than pure R solubility at the estimated eutectic point e. The total solubility at eutectic point e is about 70.7 times higher than for pure R in MeCN. Similarly, pure S-MA solid solubility points (blue) are increased by the presence of R, up to a X_{S-MA} value being about 9 times higher than pure S-MA solubility at eutectic point e, whose total solubility is about 16 times higher than for pure S-MA in MeCN. The solubility behavior of the R/S-MA/MeCN system is therefore very different from that of the S/S-MA/MeCN system, with a stronger impact of R solubility with S-MA concentration than it is for S solubility, and no cocrystal forming. This difference will cause a huge asymmetry in the quaternary system. Favorable intermolecular interactions between components in solution could be the reasons why the solubility of pure R and pure S-MA solids increase with the presence of the other component in solution. Another possibility is the occurrence of solution complexation between the components.[75]

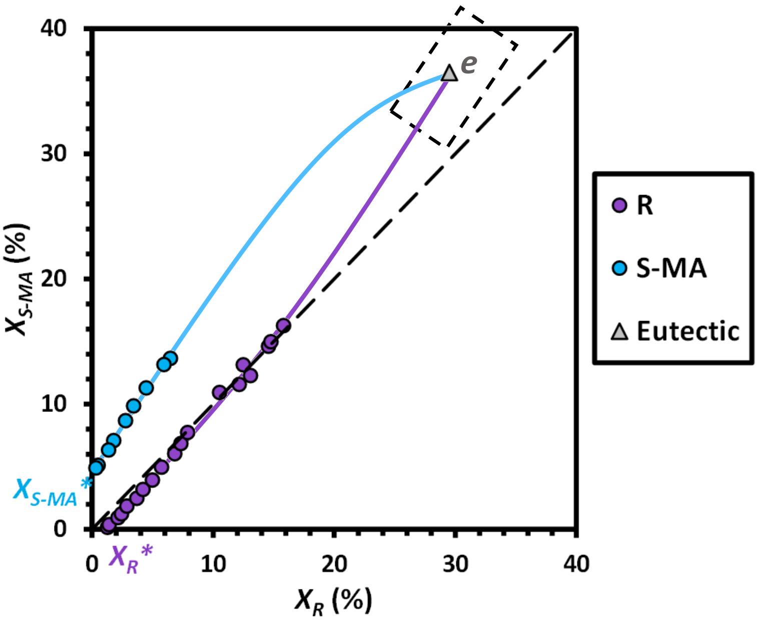

Figure 4.13: Experimental mole fractions X_R against X_{S-MA} of the solubility points in the R/S-MA/MeCN system at 9°C. X_R* and X_{S-MA}* are pure R and S-MA crystals solubilities. The dashed box is the region in which eutectic point *e* is estimated. The dashed line is added as a guide to the eye and indicates 1:1 stoichiometry between S and S-MA.

4.3.3. Quaternary System with R/S/S-MA in MeCN at 9 °C

After investigating the three isothermal ternary phase diagrams that correspond to each face of the quaternary tetrahedron, the full isothermal quaternary phase diagram has been explored using 168 equilibrated quaternary suspensions distributed inside the tetrahedron. In this system, all stable solids from the ternary systems, consisting of pure R, S, S-MA, RS, and S:S-MA are expected to crystallize at equilibrium. As for every phase diagram, quaternary phase diagrams follow the Gibbs phase rule (Equation 4.1),[76] which defines the number of degrees of freedom, *v,* that are independent intensive parameters required to define an equilibrium state. The Gibbs phase rule is expressed as

$$v = C + N - \varphi \qquad \text{Equation 4.1}$$

where C is the number of independent components (in this case $C = 4$), N is the number of intensive parameters that the system depends on (in this case $N = 0$) and φ is the number of phases in equilibrium, giving $v = 4 - \varphi$ for this system.

The maximum total solubility point in this quaternary phase diagram is measured to be about 140 times higher than the minimal total solubility point, making it impossible to clearly represent the full characteristics of the quaternary in the 3D phase diagram. Therefore, a solvent-free projection of solubility surfaces is used in Figure 4.14 (left) to display all experimental points from the quaternary system and related ternary systems. By removing the dependency on the solvent concentration, solubility data can be shown in a two-dimensional plot where points are positioned based on their relative solvent-free molar ratio in dissolved components (R, S, and S-MA). Explanations about how solvent-free projections are performed from phase diagram solubility points are provided in the Appendix B (Figure B3). The points in Figure 4.14 (left) are colored according to the solid phase(s) identified in equilibrium for each saturated solution. The points identified as belonging to biphasic domains ($v = 2$) correspond to a split of an overall composition between a saturated solution and one of the solids R (purple), S (yellow), S-MA (blue), RS (red), or S:S-MA (green). When two solids are identified at equilibrium (light gray), the points belong to a triphasic domain ($v = 1$) of which the measured saturated solution is a eutectic composition, similarly to previously measured eutectics in ternary sections (light gray triangles). A maximum of three solids can be identified as stable in a suspension at equilibrium (dark gray squares), that is therefore part of a quadriphasic domain ($v = 0$) of which the measured saturated solution is the unique possible liquid composition, referred here as a quaternary point.

Figure 4.14 (right) is our interpretation of experimental points in the solvent-free projection. Biphasic domain points cover a region defining a solubility surface, whose color is chosen depending on the related stable solid. These regions have boundaries that are a part of the figure sides corresponding to the solid solubilities in the ternary phase diagrams (black lines) down to a ternary eutectic point (light gray triangle). For example, the solubility surface of pure S (yellow) presents the solubility data from R/S/MeCN and S/S-MA/MeCN ternaries, from pure S solubility to ternary eutectic points b and c. The boundaries between regions are also eutectic lines (dark gray) that link eutectic compositions associated to triphasic domains that equilibrate the two same solids, each being from the neighboring solubility surfaces. The eutectic lines can link a ternary eutectic point with a quaternary point that presents the two same solids at equilibrium. For instance, between ternary eutectic b showing S and RS solids equilibrating in the liquid, and quaternary point f equilibrating S, RS, and S:S-MA in suspension. It can also link two quaternary points presenting the same two solids in their equilibrated suspensions, such as quaternary points f and h both equilibrating RS and S:S-MA among their stable solids. Quaternary points always correspond to the intersection of three eutectic lines, as they represent the solution of unique composition possible in a quadriphasic domain ($v = 0$), saturated in the three stable solids in suspension, according to the Gibbs phase rule.[76] For example, the quaternary point f is the saturated solution corresponding to RS, S, and S:S-MA in stable suspension. It is identified experimentally with a XRPD result presenting the three solids' signatures. We can observe it fits perfectly with the convergence of three eutectic lines equilibrating two of these solids.

The arrows shown in Figure 4.14 (right) are pointing toward the direction of increasing total solubility, to represent the relative quantity of solvent in the saturated solutions based on experiments results. The pure solid phases are always presenting a total solubility lower than the ternary eutectic points they are linked to, therefore with an arrow pointing down to them. The ternary eutectic points themselves have a lower total solubility than the quaternary point they are linked to and, consequently, an arrow directed toward them. For instance, the total solubility of quaternary point f is 3.7 times higher than ternary eutectic point b and 1.3 times higher than ternary eutectic point c. Its solubility in S is the highest of the whole stability domain of S, being 2.3 times higher than pure S solubility. Between, two quaternary points linked, there is no rule regarding the direction of evolution of total solubility. Overall, S/S-MA/MeCN ternary system (S to S-MA axis) exhibits a much lower solubility than the R/S-MA/MeCN one (R to S-MA axis). Figure 4.14 (right) reflects this huge difference by a substantial asymmetry in the quaternary system. All solubility surfaces dive toward compositions close to the estimated eutectic point e, as shown in the direction of the eutectic lines. The lack of experimental data in Figure 4.14 close to eutectic point e is again due to viscous solutions, difficult to equilibrate and sample. Four eutectic lines are converging in this region but the way they meet cannot be determined precisely. However, because of the Gibbs phase rule,[76] it is impossible for four phases to be in equilibrium with one composition in such an isothermal isobaric quaternary system. Therefore, there must exist the two quaternary points, g and h, each being the intersection of three eutectic lines. The compositional zones in which they are expected can be estimated from the extension of the eutectic lines, as represented in Figure 4.14, to compute an approximate solvent-free ratio (see the Appendix B, Table B3). We also know that both total solubilities at g and h are higher than at eutectic point e, which we estimate to be approximately 6 g/mL MeCN. However, it is not possible to know whether g or h has the highest overall solubility, and therefore, the direction of the eutectic line in-between is unknown. Experimental solubility values of all pure solid phases, ternary eutectic points, and quaternary points are compiled in the Appendix B (Table B3). Compositions of all saturated solution points in the quaternary phase diagram can be found in the Appendix B (Table B8).

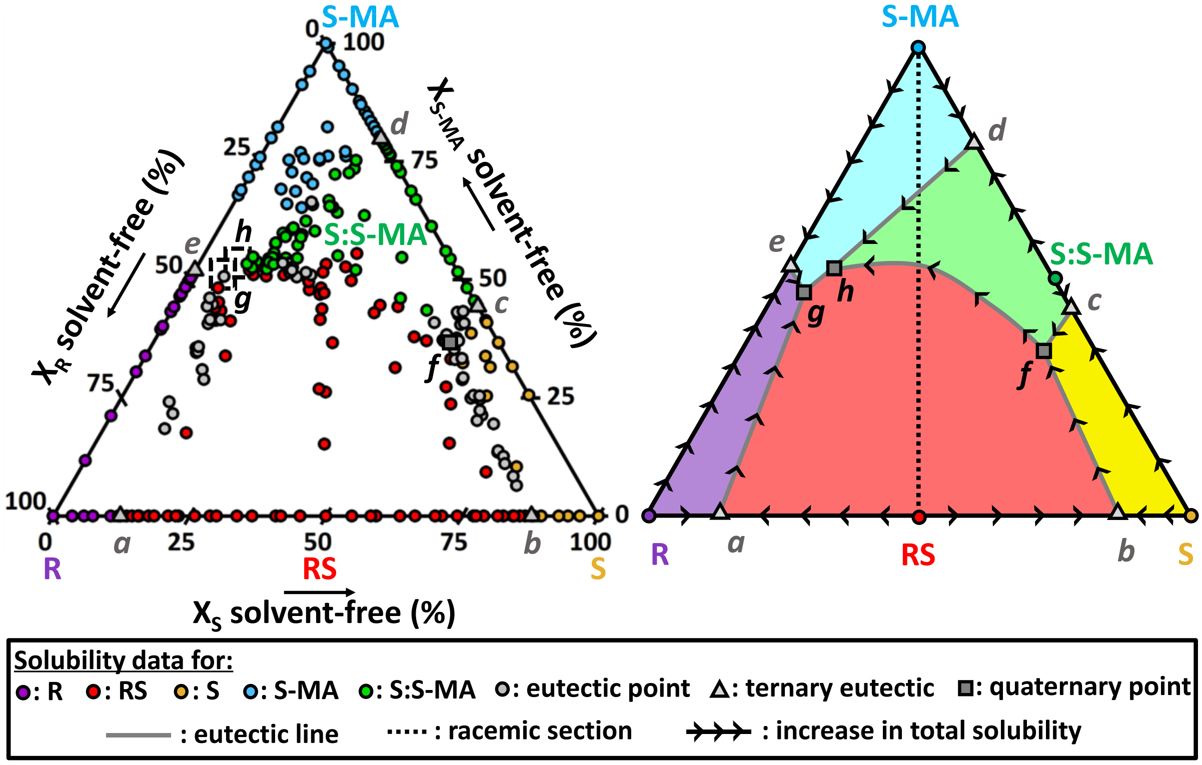

Figure 4.14: Left: projection of experimental results from the equilibration experiments showing the solvent-free solution compositions in the quaternary phase diagram R/S/S-MA/MeCN at 9°C. The colors of the points indicate the solids that are equilibrated with a saturated solution. Dashed boxes are compositional zones in which quaternary points are not measured but expected. All data used in the quaternary phase diagram can be found in the Appendix B (Table B8).
Right: interpretation of results projection into solubility surfaces, eutectic lines, and quaternary points. Arrows point toward the direction of increasing total solubility. The dotted black line represents the racemic section in the quaternary (equimolar ratio between R and S).

Figure 4.15 shows a schematic interpretation of the full quaternary phase diagram as a tetrahedron plot, based on experimental data points plotted in the Appendix B (Figures B4 and B5) for different scales and viewing angles in the tetrahedron. Figure 4.15 is therefore not a representation to scale because of the large variation in total solubility in the full tetrahedron. We can identify the shapes and boundaries of the five biphasic stability domains, highlighting every possible composition that leads to the stable suspension of a pure stable solid (R, S, RS, S-MA, and S:S-MA) in a saturated solution through tie-lines. All possible saturated solutions spread as a solubility surface at the separation with the undersaturated solution domain whose apex is pure

MeCN. Eutectic lines are identified on the intercept of two solubility surfaces and define a line of saturated liquids in both neighboring solid phases stability domains. The triphasic domains, not highlighted here for clarity, correspond to the zone of existence of suspensions following this equilibrium, linking saturated liquids from the eutectic lines to the two pure solids through tie-triangles. At the intersection of three eutectic lines are the quaternary points of unique liquid composition possible for suspension of three solids. The quadriphasic domain, not highlighted here for clarity, is a tetrahedron zone whose apexes are the three pure solids and the quaternary point, defining the existence zone of the suspensions. Inside, the phase compositions are not changing, only the mass balance between them is varying.

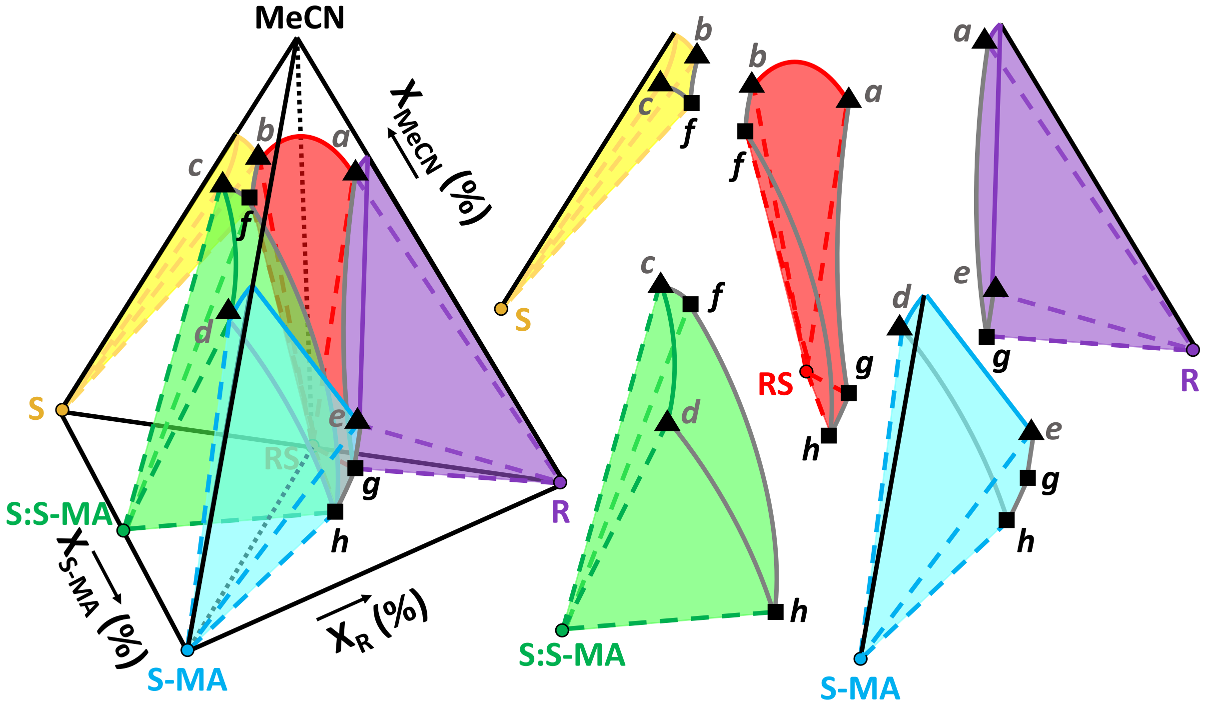

Figure 4.15: Graphical interpretation, not to scale, of the R/S/S-MA/MeCN quaternary phase diagram and the expanded view of biphasic stability domains of pure solid phases with their related colored solubility surface in equilibrium. Black triangles correspond to eutectic points in the ternary systems, and gray lines to eutectic lines originating from them, representing the equilibrium liquid composition lines saturated in two solid phases from adjacent domains. At the intersection of three eutectic lines are quaternary points (black squares) corresponding to the liquid composition saturated in the three neighboring solid phase domains. For clarity, the figure does not highlight triphasic domains (domain of tie-triangles linking eutectic lines to the two solids they are saturated in) and quadriphasic domains (domain whose boundaries are quaternary points linked with their three solids in equilibrium). The black dotted line indicates a cross-section of racemic composition (composition equal in R and S) in the quaternary.

4.4. Discussion

In pure racemic compound systems, such as the ternary system R/S/MeCN, it is impossible to perform crystallization-enhanced chiral separation under stable conditions by starting from a racemic solution. Therefore, crystallization-enhanced chiral resolutions are performed using kinetic processes like preferential crystallization. As stable racemic compound systems occur in 90 to 95% of cases for crystallization equilibria of chiral molecules, it makes chiral resolution complex. Nonetheless, the symmetry in enantiomeric systems can be broken when adding a chiral component, such as S-MA, which can form enantiospecific solids, such as the S:S-MA cocrystal, even in racemic solutions. By determining the R/S/S-MA/MeCN quaternary phase diagram, we show the boundaries and shapes of the stability domains of all stable solids in the system. This leads to the understanding of the relation between overall composition and solid formation. We observe a huge asymmetry in the S/S-MA/MeCN ternary system, forming a stable S:S-MA cocrystal of low solubility, and the R/S-MA/MeCN ternary system highlighting a strong affinity between components in solutions, therefore reaching very highly concentrated solubility points. The consequence for the quaternary system is that the stability domain of S:S-MA is strongly skewed towards the opposite face of the tetrahedron, and therefore extends beyond the racemic composition. Indeed, in both Figure 4.14 and Figure 4.15, we can observe that the racemic composition (Figure 4.14, dotted line) crosses the solubility domains of RS (red), S:S-MA (green), and S-MA (blue). This asymmetry highlights a zone along the racemic cross-section RS/S-MA/MeCN where the S:S-MA cocrystal is accessible for crystallization. A chiral resolution experiment in this zone has the advantage of being in stable conditions as the phase diagram describes thermodynamic equilibrium, with S:S-MA being the only solid present at equilibrium. This was experimentally proved by Springuel et al.[31] To optimize chiral resolution in this zone, the knowledge of the entire quaternary phase diagram is required to define accurately the best working compositions. Based on the quaternary phase diagram data acquired here, it is possible to design process conditions during which the racemic compound RS and the chiral coformer S-MA as input can lead to obtaining only S:S-MA chiral cocrystal as output. Afterward, the cocrystal can be separated into its pure components and thereby the pure levetiracetam API (S), a nootropic drug used as an anticonvulsant to treat epilepsy. Therefore, the knowledge of complex phase diagrams can help in designing alternative chiral separation routes with crystallization for industry.

The need for complex chiral phase diagrams is limited due to the difficulty in quantifying chiral molecules in multicomponent chiral systems. With UV-CD spectroscopy and multivariate calibration models, we have managed to quantify different chiral molecules in solution with great accuracy and are not limited by the increasing number of chiral components. This enlarges the range of methods available for chiral molecule quantification, used here for phase diagram determination, and especially on multicomponent systems such as quaternary systems that were difficult to access until now. The UV-CD spectroscopy method can be extended to even more complex systems, if necessary, with appropriate multivariate calibration models. As multivariate techniques consider the variations in the whole spectrum and not at specific wavelengths, it is possible to take into account accurately the existing interactions in solution. For instance, the occurrence of complexation in solution can induce shifts in the spectra or potential changes in the molar absorptivity coefficient, which can be integrated in the multivariate calibration model. The UV-CD spectroscopy method could also be used for online monitoring of the solution composition during a crystallization process through in situ measurements or solution sampling of the liquid phase concentration and enantiomeric excess. The advantages of the UV-CD method are the absorbance detection of both chiral and achiral molecules, unaffected by the sample temperature, facile method development, and quick analysis. The sample preparation is minimal, requiring only sampling and dilution, and guarantees no possible physical/chemical degradation as it can be the case for other methods like chiral HPLC that introduces new solvents in contact with the sampled analytes. The same multivariate calibration models are needed for quantification of several components, and we prove the high consistency of data obtained through the present study. The limitations of the UV-CD method are the need for the molecules to absorb in the UV region, preferably in a region different from the solvent used. However, these criteria are already a requirement for chiral HPLC methods that use UV spectroscopy in their detectors. UV-CD cannot be applied to UV-sensitive molecules that become modified or degrade under UV light.[77-79] Other chiroptical techniques like vibrational circular dichroism (VCD) or Raman optical activity can be a good alternative to UV-CD,[60] as they present more pronounced spectra that arise from the vibration modes of the bonds, and thus are not limited by chemical degradation and absorption requirements. Both techniques also produce spectra, and therefore offer big possibilities in terms of data analysis with multivariate analysis to build quantification methods for chiral molecules.

4.5. Conclusions

A new multicomponent chiral quantification method using UV-CD spectroscopy and PLS calibration models was created to measure unknown compositions in up to three different chiral components in solution, with two being enantiomers. This method was used to design calibration models covering the R/S/S-MA/MeCN quaternary system. Three accurate ternary phase diagrams were measured, revising previous literature data. Moreover, with the newly possible quaternary composition quantification, the full quaternary phase diagram tetrahedron at 9 °C was proposed for the first time. It shows the equilibria of the two enantiomers forming a racemic compound RS, and the enantiomer S forming an enantiospecific cocrystal S:S-MA with the chiral coformer S-MA. The calibration results show very high accuracy for models in predicting known compositions. They can predict the total mass fraction in enantiomers x_{S+R} with a RMSEP of 16.3×10^{-6} g/g, the differential mass fraction between enantiomers x_{S-R} with a RMSEP of 12.0×10^{-6} g/g, and the mass fraction in S-MA x_{S-MA} with a RMSEP of 15.4×10^{-6} g/g. The obtained phase diagram experimental results prove to be in good agreement with those obtained with other analytical methods such as HPLC and gravimetric analysis. The CD spectroscopy method is promising as it can be extended to wavelengths different from UV to build similar quantification models. Moreover, a higher number of different chiral molecules could be quantified in solution, with the appropriate multivariate calibration models on spectral data. Most chiral pharmaceutical compounds absorb in UV without degrading, and their concentration tends to have an influence on the spectrum, which is detectable by the PLS method in sufficient accuracy. Therefore, the method is potentially applicable to a large range of organic molecules. The accurate description of the quaternary phase diagram underlines a large asymmetry along the racemic composition, which shows the feasibility of a chiral separation process with enantioselective cocrystallization of levetiracetam under stable conditions. This highlights the necessity of complex multicomponent chiral phase diagram determination with precise methods, such as UV-CD spectroscopy and multivariate analysis.

4.6. Associated content

Supporting Information

The Supporting Information related to this chapter is the Appendix B.

Materials, models development data, phase diagrams data.

Data Availability Statement

All data underpinning this publication are openly available from the University of Strathclyde KnowledgeBase at: https://doi.org/10.15129/414d46ee-fe46-4ec0-9cbb-67f29c5efdf6

4.7. Acknowledgments

This research received funding as part of the CORE ITN Project by the European Union's Horizon 2020 Research and Innovation Program under the Marie Skłodowska-Curie grant agreement no. 722456 CORE ITN. The authors thank the EPSRC Centre for Innovative Manufacturing in Continuous Manufacturing and Crystallization (http://www.cmac.ac.uk) for support (EPSRC funding under grant reference: EP/I033459/1). We thank UCB Pharma (Braine-l'Alleud, Belgium) for providing pure levetiracetam, its counter-enantiomer, and racemic compound etiracetam.

4.8. References

(1) Jacques, J.; Collet, A.; Wilen, S. H. *Enantiomers, racemates, and resolutions*; Wiley, 1981.
(2) Nguyen, L. A.; He, H.; Pham-Huy, C. Chiral drugs: an overview. *Int J Biomed Sci* **2006**, *2* (2), 85-100.
(3) Reddy, I. K.; Mehvar, R. *Chirality in drug design and development*; CRC Press, 2004.
(4) Saigo, K.; Sakai, K. Resolution of chiral drugs and drug intermediates by crystallisation. *Chirality in drug research* **2006**, 127-154.
(5) Li, Z. J.; Grant, D. J. Relationship between physical properties and crystal structures of chiral drugs. *J Pharm Sci* **1997**, *86* (10), 1073-1078.
(6) Ariens, E. J. Stereochemistry, a basis for sophisticated nonsense in pharmacokinetics and clinical pharmacology. *Eur J Clin Pharmacol* **1984**, *26* (6), 663-668.
(7) Kenda, B. M.; Matagne, A. C.; Talaga, P. E.; Pasau, P. M.; Differding, E.; Lallemand, B. I.; Frycia, A. M.; Moureau, F. G.; Klitgaard, H. V.; Gillard, M. R.; et al. Discovery of 4-substituted pyrrolidone butanamides as new agents with significant antiepileptic activity. *J Med Chem* **2004**, *47* (3), 530-549.
(8) van der Meijden, M. W.; Leeman, M.; Gelens, E.; Noorduin, W. L.; Meekes, H.; van Enckevort, W. J. P.; Kaptein, B.; Vlieg, E.; Kellogg, R. M. Attrition-Enhanced Deracemization in the Synthesis of Clopidogrel - A Practical Application of a New Discovery. *Organic Process Research & Development* **2009**, *13* (6), 1195-1198.
(9) Suwannasang, K.; Flood, A. E.; Coquerel, G. A Novel Design Approach To Scale Up the Temperature Cycle Enhanced Deracemization Process: Coupled Mixed-Suspension Vessels. *Crystal Growth & Design* **2016**, *16* (11), 6461-6467.
(10) Sheldon, R. A. *Chirotechnology: industrial synthesis of optically active compounds*; CRC press, 1993.
(11) Belletti, G.; Tortora, C.; Mellema, I. D.; Tinnemans, P.; Meekes, H.; Rutjes, F.; Tsogoeva, S. B.; Vlieg, E. Photoracemization-Based Viedma Ripening of a BINOL Derivative. *Chemistry* **2020**, *26* (4), 839-844.
(12) Sakai, K.; Hirayama, N.; Tamura, R. *Novel optical resolution technologies*; Springer, 2007.
(13) Suwannasang, K.; Flood, A. E.; Rougeot, C.; Coquerel, G. Using Programmed Heating–Cooling Cycles with Racemization in Solution for Complete Symmetry Breaking of a Conglomerate Forming System. *Crystal Growth & Design* **2013**, *13* (8), 3498-3504.
(14) Li, W. W.; Spix, L.; de Reus, S. C. A.; Meekes, H.; Kramer, H. J. M.; Vlieg, E.; ter Horst, J. H. Deracemization of a Racemic Compound via Its Conglomerate-Forming Salt Using Temperature Cycling. *Crystal Growth & Design* **2016**, *16* (9), 5563-5570.
(15) Sogutoglu, L. C.; Steendam, R. R.; Meekes, H.; Vlieg, E.; Rutjes, F. P. Viedma ripening: a reliable crystallisation method to reach single chirality. *Chem Soc Rev* **2015**, *44* (19), 6723-6732.

(16) Buol, X.; Caro Garrido, C.; Robeyns, K.; Tumanov, N.; Collard, L.; Wouters, J.; Leyssens, T. Chiral Resolution of Mandelic Acid through Preferential Cocrystallization with Nefiracetam. *Crystal Growth & Design* **2020**, *20* (12), 7979-7988.

(17) Lorenz, H.; Seidel-Morgenstern, A. Processes to separate enantiomers. *Angew Chem Int Ed Engl* **2014**, *53* (5), 1218-1250.

(18) Kellogg, R. M. Practical Stereochemistry. *Acc Chem Res* **2017**, *50* (4), 905-914.

(19) Maggioni, G. M.; Fernández-Ronco, M. P.; van der Meijden, M. W.; Kellogg, R. M.; Mazzotti, M. Solid state deracemisation of two imine-derivatives of phenylglycine derivatives via high-pressure homogenisation and temperature cycles. *CrystEngComm* **2018**, *20* (27), 3828-3838.

(20) Breveglieri, F.; Maggioni, G. M.; Mazzotti, M. Deracemization of NMPA via Temperature Cycles. *Crystal Growth & Design* **2018**, *18* (3), 1873-1881.

(21) Belletti, G.; Meekes, H.; Rutjes, F.; Vlieg, E. Role of Additives during Deracemization Using Temperature Cycling. *Cryst Growth Des* **2018**, *18* (11), 6617-6620.

(22) Levilain, G.; Coquerel, G. Pitfalls and rewards of preferential crystallization. *CrystEngComm* **2010**, *12* (7), 1983-1992.

(23) Harfouche, L. C.; Brandel, C.; Cartigny, Y.; Ter Horst, J. H.; Coquerel, G.; Petit, S. Enabling Direct Preferential Crystallization in a Stable Racemic Compound System. *Mol Pharm* **2019**, *16* (11), 4670-4676.

(24) Kozma, D. *CRC handbook of optical resolutions via diastereomeric salt formation*; Crc Press, 2001.

(25) Marchand, P.; Lefèbvre, L. c.; Querniard, F.; Cardinaël, P.; Perez, G.; Counioux, J.-J.; Coquerel, G. Diastereomeric resolution rationalized by phase diagrams under the actual conditions of the experimental process. *Tetrahedron: Asymmetry* **2004**, *15* (16), 2455-2465.

(26) Lam, W. H.; Ng, K. M. Diastereomeric salt crystallization synthesis for chiral resolution of ibuprofen. *AIChE Journal* **2007**, *53* (2), 429-437.

(27) Harfouche, L. C.; Couvrat, N.; Sanselme, M.; Brandel, C.; Cartigny, Y.; Petit, S.; Coquerel, G. Discovery of New Proxyphylline-Based Chiral Cocrystals: Solid State Landscape and Dehydration Mechanism. *Crystal Growth & Design* **2020**, *20* (6), 3842-3850.

(28) Neurohr, C.; Marchivie, M.; Lecomte, S.; Cartigny, Y.; Couvrat, N.; Sanselme, M.; Subra-Paternault, P. Naproxen–Nicotinamide Cocrystals: Racemic and Conglomerate Structures Generated by CO2 Antisolvent Crystallization. *Crystal Growth & Design* **2015**, *15* (9), 4616-4626.

(29) Wacharine-Antar, S.; Levilain, G.; Dupray, V.; Coquerel, G. Resolution of (±)-Imeglimin-2,4-dichlorophenylacetate Methanol Solvate by Preferential Crystallization. *Organic Process Research & Development* **2010**, *14* (6), 1358-1363.

(30) Guillot, M.; de Meester, J.; Huynen, S.; Collard, L.; Robeyns, K.; Riant, O.; Leyssens, T. Cocrystallization-Induced Spontaneous Deracemization: A General Thermodynamic Approach to Deracemization. *Angew Chem Int Ed Engl* **2020**, *59* (28), 11303-11306.

(31) Springuel, G.; Leyssens, T. Innovative Chiral Resolution Using Enantiospecific Co-Crystallization in Solution. *Crystal Growth & Design* **2012**, *12* (7), 3374-3378.

(32) Harmsen, B.; Leyssens, T. Dual-Drug Chiral Resolution: Enantiospecific Cocrystallization of (S)-Ibuprofen Using Levetiracetam. *Crystal Growth & Design* **2017**, *18* (1), 441-448.

(33) Harmsen, B.; Leyssens, T. Enabling Enantiopurity: Combining Racemization and Dual-Drug Co-crystal Resolution. *Crystal Growth & Design* **2018**, *18* (6), 3654-3660.

(34) Springuel, G.; Robeyns, K.; Norberg, B.; Wouters, J.; Leyssens, T. Cocrystal Formation between Chiral Compounds: How Cocrystals Differ from Salts. *Crystal Growth & Design* **2014**, *14* (8), 3996-4004.
(35) Springuel, G.; Collard, L.; Leyssens, T. Ternary and quaternary phase diagrams: key tools for chiral resolution through solution cocrystallization. *CrystEngComm* **2013**, *15* (39), 7951-7958.
(36) Mullin, J. W. *Crystallization*; Elsevier, 2001.
(37) Coquerel, G. Crystallization of molecular systems from solution: phase diagrams, supersaturation and other basic concepts. *Chem Soc Rev* **2014**, *43* (7), 2286-2300.
(38) Cascella, F.; Seidel-Morgenstern, A.; Lorenz, H. Exploiting Ternary Solubility Phase Diagrams for Resolution of Enantiomers: An Instructive Example. *Chemical Engineering & Technology* **2020**, *43* (2), 329-336.
(39) Brandel, C.; Amharar, Y.; Rollinger, J. M.; Griesser, U. J.; Cartigny, Y.; Petit, S.; Coquerel, G. Impact of molecular flexibility on double polymorphism, solid solutions and chiral discrimination during crystallization of diprophylline enantiomers. *Mol Pharm* **2013**, *10* (10), 3850-3861.
(40) Lorenz, H.; Seidel-Morgenstern, A. Binary and ternary phase diagrams of two enantiomers in solvent systems. *Thermochimica Acta* **2002**, *382* (1-2), 129-142.
(41) Polenske, D.; Lorenz, H. Solubility and Metastable Zone Width of the Methionine Enantiomers and Their Mixtures in Water. *Journal of Chemical & Engineering Data* **2009**, *54* (8), 2277-2280.
(42) Leyssens, T.; ter Horst, J. H. 9. Solution co-crystallisation and its applications. In *Multi-Component Crystals*, De Gruyter, 2017; pp 205-236.
(43) Song, L.; Leng, F.; Robeyns, K.; Leyssens, T. Quaternary phase diagrams as a tool for ionic cocrystallization: the case of a solid solution between a racemic and enantiopure ionic cocrystal. *CrystEngComm* **2020**, *22* (14), 2537-2542.
(44) Zhou, F.; Shemchuk, O.; Charpentier, M. D.; Matheys, C.; Collard, L.; Ter Horst, J. H.; Leyssens, T. Simultaneous Chiral Resolution of Two Racemic Compounds by Preferential Cocrystallization*. *Angew Chem Int Ed Engl* **2021**, *60* (37), 20264-20268.
(45) Buol, X.; Robeyns, K.; Caro Garrido, C.; Tumanov, N.; Collard, L.; Wouters, J.; Leyssens, T. Improving Nefiracetam Dissolution and Solubility Behavior Using a Cocrystallization Approach. *Pharmaceutics* **2020**, *12* (7),
(46) Alvarez Rodrigo, A.; Lorenz, H.; Seidel-Morgenstern, A. Online monitoring of preferential crystallization of enantiomers. *Chirality* **2004**, *16* (8), 499-508.
(47) Hughes, D.; Carreira, E.; Yamamoto, H. Comprehensive Chirality. *Carreira, EM* **2012**,
(48) Gawley, R. E.; Aubé, J. *Principles of asymmetric synthesis*; Elsevier, 2012.
(49) Hanna, G. M. Determination of enantiomeric composition of ibuprofen in bulk drug by proton nuclear magnetic resonance spectroscopy with a chiral lanthanide chelate. *J Pharm Biomed Anal* **1997**, *15* (12), 1805-1811.
(50) Oketani, R.; Marin, F.; Tinnemans, P.; Hoquante, M.; Laurent, A.; Brandel, C.; Cardinael, P.; Meekes, H.; Vlieg, E.; Geerts, Y.; et al. Deracemization in a Complex Quaternary System with a Second-Order Asymmetric Transformation by Using Phase Diagram Studies. *Chemistry* **2019**, *25* (61), 13890-13898.
(51) Buol, X.; Robeyns, K.; Caro Garrido, C.; Tumanov, N.; Collard, L.; Wouters, J.; Leyssens, T. Improving Nefiracetam Dissolution and Solubility Behavior Using a Cocrystallization Approach. *Pharmaceutics* **2020**, *12* (7), 653.

(52) Hegade, R. S.; De Beer, M.; Lynen, F. Chiral stationary phase optimized selectivity liquid chromatography: A strategy for the separation of chiral isomers. *J Chromatogr A* **2017**, *1515*, 109-117.

(53) Berova, N.; Polavarapu, P. L.; Nakanishi, K.; Woody, R. W. *Comprehensive chiroptical spectroscopy: applications in stereochemical analysis of synthetic compounds, natural products, and biomolecules*; John Wiley & Sons, 2012.

(54) Berova, N.; Nakanishi, K.; Woody, R. W. *Circular dichroism: principles and applications*; John Wiley & Sons, 2000.

(55) Polavarapu, P. L. *Chiroptical spectroscopy: fundamentals and applications*; Crc Press, 2016.

(56) Liu, M.; Chen, L.; Tian, T.; Zhang, Z.; Li, X. Identification and Quantitation of Enantiomers by Capillary Electrophoresis and Circular Dichroism Independent of Single Enantiomer Standard. *Anal Chem* **2019**, *91* (21), 13803-13809.

(57) Luo, Y.; Wu, L.; Yang, B.; Jin, Y.; Zheng, K.; He, Z. A novel potential primary method for quantification of enantiomers by high performance liquid chromatography-circular dichroism. *Sci Rep* **2018**, *8* (1), 7390.

(58) Nieto, S.; Dragna, J. M.; Anslyn, E. V. A facile CD protocol for rapid determination of enantiomeric excess and concentration of chiral primary amines. *Chemistry* **2010**, *16* (1), 227.

(59) Jo, H. H.; Lin, C. Y.; Anslyn, E. V. Rapid optical methods for enantiomeric excess analysis: from enantioselective indicator displacement assays to exciton-coupled circular dichroism. *Acc Chem Res* **2014**, *47* (7), 2212-2221.

(60) Berova, N.; Polavarapu, P. L.; Nakanishi, K.; Woody, R. W. *Comprehensive Chiroptical Spectroscopy: Instrumentation, Methodologies, and Theoretical Simulations*; John Wiley & Sons, 2011.

(61) Bakeev, K. A. *Process analytical technology: spectroscopic tools and implementation strategies for the chemical and pharmaceutical industries*; John Wiley & Sons, 2010.

(62) Simone, E.; Saleemi, A. N.; Nagy, Z. K. Application of quantitative Raman spectroscopy for the monitoring of polymorphic transformation in crystallization processes using a good calibration practice procedure. *Chemical Engineering Research and Design* **2014**, *92* (4), 594-611.

(63) Morais, C. L. M.; Santos, M. C. D.; Lima, K. M. G.; Martin, F. L. Improving data splitting for classification applications in spectrochemical analyses employing a random-mutation Kennard-Stone algorithm approach. *Bioinformatics* **2019**, *35* (24), 5257-5263.

(64) Winning, H.; Larsen, F. H.; Bro, R.; Engelsen, S. B. Quantitative analysis of NMR spectra with chemometrics. *J Magn Reson* **2008**, *190* (1), 26-32.

(65) Brereton, R. G. *Chemometrics: data driven extraction for science*; John Wiley & Sons, 2018.

(66) Swinehart, D. F. The beer-lambert law. *Journal of chemical education* **1962**, *39* (7), 333.

(67) Adams, M. J. *Chemometrics in analytical spectroscopy*; Royal Society of Chemistry, 2004.

(68) Mower, M. P.; Blackmond, D. G. In-Situ Monitoring of Enantiomeric Excess During a Catalytic Kinetic Resolution. *ACS Catalysis* **2018**, *8* (7), 5977-5982.

(69) Bro, R. Multivariate calibration: what is in chemometrics for the analytical chemist? *Analytica Chimica Acta* **2003**, *500* (1-2), 185-194.

(70) Haenlein, M.; Kaplan, A. M. A beginner's guide to partial least squares analysis. *Understanding statistics* **2004**, *3* (4), 283-297.

(71) Savitzky, A.; Golay, M. J. E. Smoothing and Differentiation of Data by Simplified Least Squares Procedures. *Analytical Chemistry* **2002**, *36* (8), 1627-1639.

(72) Alexandris, N.; Gupta, S.; Koutsias, N. Remote sensing of burned areas via PCA, Part 1; centering, scaling and EVD vs SVD. *Open geospatial data, software and standards* **2017**, *2* (1), 1-11.

(73) Galvao, R. K.; Araujo, M. C.; Jose, G. E.; Pontes, M. J.; Silva, E. C.; Saldanha, T. C. A method for calibration and validation subset partitioning. *Talanta* **2005**, *67* (4), 736-740.

(74) Frank, L. E.; Friedman, J. H. A statistical view of some chemometrics regression tools. *Technometrics* **1993**, *35* (2), 109-135.

(75) Nehm, S. J.; Rodríguez-Spong, B.; Rodríguez-Hornedo, N. Phase Solubility Diagrams of Cocrystals Are Explained by Solubility Product and Solution Complexation. *Crystal Growth & Design* **2005**, *6* (2), 592-600.

(76) Ricci, J. E. *phase rule and heterogeneous equilibrium*; 1951.

(77) Wypych, G. *Handbook of UV degradation and stabilization*; Elsevier, 2020.

(78) Wang, W. L.; Zhang, X.; Wu, Q. Y.; Du, Y.; Hu, H. Y. Degradation of natural organic matter by UV/chlorine oxidation: Molecular decomposition, formation of oxidation byproducts and cytotoxicity. *Water Res* **2017**, *124*, 251-258.

(79) Zayat, M.; Garcia-Parejo, P.; Levy, D. Preventing UV-light damage of light sensitive materials using a highly protective UV-absorbing coating. *Chem Soc Rev* **2007**, *36* (8), 1270-1281.

Chapter 5 - Enantioselective Cocrystallization and Enantiomer Recovery Guidelines from Phase Diagram Information

Maxime D. Charpentier[1], Russell Miller[1,2], Karen Johnston[2], Joop H. ter Horst[1,3]

1. EPSRC Centre for Innovative Manufacturing in Continuous Manufacturing and Crystallization (CMAC), Strathclyde Institute of Pharmacy and Biomedical Sciences (SIPBS), University of Strathclyde

2. Department of Chemical and Process Engineering, University of Strathclyde, James Weir Building, 75 Montrose Street, Glasgow G1 1XJ, U.K.

3. Univ Rouen Normandie, Laboratoire Sciences et Méthodes Séparatives (SMS), UR 3233, F-76000 Rouen, France

Abstract

Enantiopure cocrystals are very useful to enable separation processes for chiral molecules, particularly when racemic mixtures crystallize as a stable racemic compound. However, the related multicomponent thermodynamic systems are complex to work with and require a substantial amount of data to build robust phase diagrams. This study aims to provide detailed guidelines related to the use of complex phase diagrams and chiral resolution with cocrystallization, with the view to design optimized processes. Based on the full quaternary system measured in acetonitrile for the chiral drug levetiracetam, its counter-enantiomer, and the chiral coformer S-mandelic with which levetiracetam forms an enantiospecific cocrystal, an enantioselective cocrystallization process is designed by selection of the ideal working composition for levetiracetam recovery. The process design is validated with experiments that underline the operating conditions. Additionally, the possibilities of enantiomer and coformer recovery from the cocrystal are investigated by solvent-mediated transformation based on phase diagram, which highlights optimization potential through the selection of best conditions. Experimental protocols are also proposed to screen for recovery possibilities by solvent-mediated transformation in new solvent systems. This work illustrates the advantages of enantioselective cocrystallization for enantiomers separation and the benefits of using cocrystals for complete recycling of the materials used during the process.

5.1. Introduction

Chiral molecule separation is a major research area in the pharmaceutical industry, with more than 50% of marketed drugs being chiral.[1] Opposite-enantiomers present the same physical properties,[2] such as melting point and solubility, but interact differently with chiral receptors in the human body, which induces a different biological response. While one enantiomer has a desired therapeutic effect, its opposite-enantiomer can be inactive or produce unwanted side effects.[3-8] Moreover, an inactive opposite-enantiomer in a racemic drug can be considered as an impurity representing up to 50% of the formulation, which presents economic consequences.[9] Therefore, the manufacture of chiral active pharmaceutical ingredients (APIs) is regulated to prefer enantiopure drugs,[10] including Keppra, a nootropic drug used as an anticonvulsant to treat epilepsy, whose API is (S)-2-(2-oxopyrrolidin-1-yl)butanamide, known commonly as levetiracetam.[11]

Enantiopure APIs can be obtained from asymmetric syntheses by using enantiopure precursors selected from the chiral pool, chiral auxiliaries, or asymmetric catalysis.[12-16] However, these technologies tend to be expensive.[17] When non-stereoselective syntheses are used, racemic mixtures are obtained and must be separated with an additional chiral resolution technology, such as chiral chromatography or crystallization.[17-19] Crystallization is generally preferred at industrial scale as it is relatively inexpensive compared to chiral chromatography.[20, 21] Resolution processes with preferential crystallization, temperature-cycling deracemization or Viedma ripening, are effective but generally only applicable if enantiomers from a racemic mixture crystallize separately to form a conglomerate,[2] which occurs in 5-10% of cases.[22-32] In 90-95% of cases, racemic mixtures crystallize as racemic crystals[2] making enantiomer separation difficult, with processes relying on kinetics.[33, 34] However, multicomponent crystal engineering with an additional molecule can prompt different crystallization equilibria.[35, 36] The formation of diastereomeric salts, which have different physical properties, is the most popular method but is limited by the necessity of an API to be ionizable to form a salt with a chiral base or acid.[28] Cocrystallization with a coformer molecule offers an excellent solution that is applicable to non-ionizable APIs, as cocrystals form through strong intermolecular interactions like hydrogen bonds, that are universal.[37-39]

Cocrystals are the result of the association in a crystal of two or more distinct neutral molecules that are solids at ambient conditions,[40-43] and relevant technologies now exist for cocrystal prediction and screening.[44-46] In the last decades, cocrystals have become widely used to modify the physicochemical and biological properties of API crystals,[40, 47-52] but can also be used as a separation technology.[53] For instance, a conglomerate of enantiopure cocrystals can sometimes be obtained using an achiral coformer to enable chiral resolution techniques.[54, 55] However, if the coformer is chiral, it always generates a resolution possibility, with a diastereomeric pair of enantiopure cocrystals, or an enantiospecific cocrystal,[35, 36, 56-60] and contrary to salts, cocrystals show more often enantiospecificity.[61] Enantioselective cocrystallization is reported for levetiracetam, that forms an enantiospecific cocrystal with (S)-mandelic acid,[56] (S)-ibuprofen,[62] (2S,3S)-tartaric acid,[63] and five halogenated mandelic acid derivatives.[64] Therefore, levetiracetam is often used as a model compound to develop chiral resolution processes with enantioselective cocrystallization in solution, while being an example of a molecule that cannot form salts easily.

Levetiracetam can be used as a resolution agent to separate racemic mixtures,[62, 64] but is more commonly the target API separated from its racemic compound etiracetam.[56, 65, 66] Springuel and Leyssens propose an enantioselective cocrystallization process of levetiracetam with (S)-mandelic acid in acetonitrile, and report a resolution yield of 14.7 % at 9°C and 69.6 % at -10 °C.[56] However, these results were obtained from trial and error compositions as the phase diagram of the corresponding system was not known. Recently, we published in Chapter 4[67] the full quaternary phase diagram at 9°C (Figure 5.1) between levetiracetam (S), its counter-enantiomer (R), (S)-mandelic acid (S-MA) and acetonitrile (MeCN). Figure 5.1 shows the results for stability domains of pure solid phases, represented in a tetrahedron plot (left) and a solvent-free projection of solubility surfaces (right). Explanations about solvent-free projections are provided in the Appendix C, Figure C1. We reported that due to the formation of the enantiospecific cocrystal S:S-MA between S and S-MA, the system shows a significant asymmetry in the solubility surfaces. Consequently, some compositions from the racemic section (dotted line) permit the chiral resolution of the racemic compound RS by designing enantioselective cocrystallization processes where only the S:S-MA cocrystal is stable at equilibrium. Therefore, in this study we propose some guidelines to use the knowledge of our quaternary phase diagram data to design an enantioselective cocrystallization process with an optimized chiral resolution yield. As phase diagrams relate thermodynamic equilibria, such an isolation process of the enantiospecific levetiracetam cocrystal in solution is robust under scale-up conditions.[68]

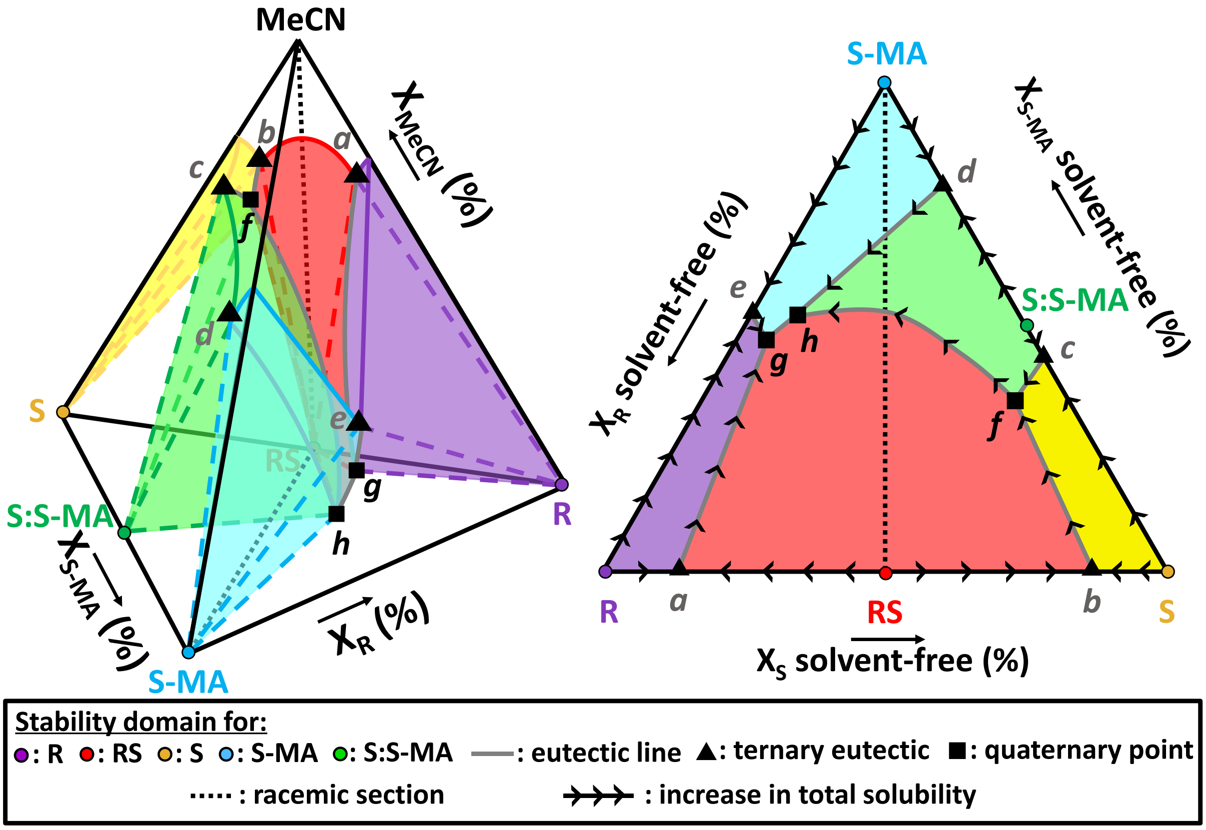

Figure 5.1: Quaternary phase diagram figures from Chapter 4[67] of levetiracetam (S), its counter-enantiomer (R), the coformer (S)-mandelic acid (S-MA) and the solvent acetonitrile (MeCN) at 9°C. The stability domains of pure solid phases are represented in a tetrahedron plot (left) and a solvent-free projection of solubility surfaces (right). Under specific racemic conditions, there is a composition region in which the chiral cocrystal is stable.

To complete the chiral separation, the enantiopure cocrystal must be separated into its pure components in an additional step of enantiomer recovery. Cocrystal deconstruction is a recent research topic, but it has similarities with salt deconstruction generally done with recrystallization. However, while salts require recrystallization with another acid or base and form an unwanted conjugated waste salt, the regeneration of an API from a cocrystal involves neutral molecules only, which prevents the production of waste.[69-71] This favors cocrystallization over salt-formation for isolation processes, and gives possibilities of recycling of the pure coformer for reuse, which is advantageous for process economics. Nevertheless, the in-situ recovery of an API from its cocrystal by recrystallization requires conditions to crystallize the API only, based on property differences between the API and the coformer.[72, 73] For instance, sublimation in vacuum or thermal degradation methods use the differences in melting point or vapor pressure but only work for specific systems. However, the API and coformer solubilities are always affected differently by the solvent, and thereby solvent-based recrystallization methods appear universal. In aqueous solutions, a pH modification can be used to affect differently the cocrystal component solubilities.[74] Working with a two immiscible solvent system can also lead to liquid-liquid separation with one solvent extracting the API and the other the coformer, that can later be crystallized separately.[73] In this study, we are interested in a solvent-mediated transformation.[73]

In this method, the isolated cocrystal is placed in a solvent that gives conditions for converting the cocrystal into a pure solid API in suspension, while dissolving the coformer in the solvent. This technique is often done by trial and error through washing steps, and we aim to discuss the conditions for optimizing it, based on phase diagram information. Moreover, the levetiracetam recovery from its cocrystal has not been studied yet.

By using levetiracetam as a model system in this study, we aim to propose guidelines to optimize the design of the enantioselective cocrystallization process of levetiracetam from its racemic compound with (S)-mandelic acid reported by Springuel and Leyssens,[56] by using the acquired full quaternary phase diagram in Chapter 4.[67] We combine this process with a solvent-mediated transformation step that permits the recovery of pure levetiracetam from its cocrystal. Phase diagram information can be used to understand the importance of solvent selection, and to propose guidelines to identify conditions optimizing the enantiomer recovery.

5.2. Experimental Section

(S)-2-(2-oxopyrrolidin-1-yl)butanamide (levetiracetam, Acros Organics) (**S**), (S)-mandelic acid (≥ 99%, Sigma-Aldrich) (**S-MA**), and acetonitrile (HPLC grade, 100%, VWR Chemicals) (**MeCN**) were used as received. The racemic compound **RS** (etiracetam) was prepared from a racemization reaction of 100.81 g of S, using as a racemizing agent 1.59 g (0.05 eq.) of sodium methoxide MeONa (98%, Alfa Aesar), in 100 mL of MeOH (methanol, ≥ 99.8%, Fisher Scientific) kept at reflux under continuous stirring for 24 h.[59] After cooling to room temperature, the RS form II crystallized spontaneously, and the compound was washed three times with 20 mL of cold MeOH after filtration. To obtain the RS form I, the stable form below 30 °C, the solid was fully dissolved in a minimal amount of MeOH, and then the solution was slowly evaporated at room temperature.[75] The 1:1 cocrystal phase of S and (S)-mandelic acid (**S:S-MA**) was prepared from a solution of 15 mL of MeCN with 5.55 g of S and 6.03 g of S-MA dissolved at 45 °C and crystallized at 9 °C for 24 h before filtration of the suspension, based on ternary phase diagram S/S-MA/MeCN data from Chapter 4.[67] The recovered solid was washed three times with 20 mL of MeCN at about -10 °C.

5.2.1. X-ray Powder Diffraction

XRPD analyses were performed using a Bruker D2 Phaser diffractometer with Bragg-Brentano reflection θ/θ geometry from a Ni filtered Cu source radiation (1.541 Å) with an operating voltage of 30 kV, current 10 mA and 0.2 mm anti-divergence slit. A scanning range of 2θ values from 4° to 35° was applied with a 0.017° step and a step time of 1 s.

5.2.2. Ultraviolet-Circular Dichroism Spectroscopy

Dried solids were dissolved in MeCN, and their R, S, and S-MA compositions were determined with UV-CD spectroscopy using a Chirascan-Plus spectrometer from Applied Photophysics, constantly purged with a nitrogen flow. The solutions were diluted to fall into the calibration range, set from 0.5 to 5 mg/ml of total concentration in dissolved components for this system (conditions found in Chapter 4[67]). The solution samples were analyzed in a Hellma quartz cell with a 0.1 mm path length. Both UV and CD spectra were collected with a 0.5 nm step and 1 s per point in the 200-260 nm range. The background of pure MeCN was measured and automatically subtracted from the spectra using the instrument software. The data was collected using Chirascan Pro data V4.4.2.0 and the data analysis was done using Origin Pro 2017 and PLS_toolbox 4.0 from Eigenvector research Inc. The spectra of both UV and CD were pre-processed with a first derivative baseline correction followed by a Savitzky-Golay smoothing[76] of the second order polynomial with five window points and mean centering.[77] The mass fractions for R (x_R), S (x_S) and S-MA (x_{S-MA}), were computed from the same partial least squares (PLS) calibration model as used for quaternary phase diagram determination in Chapter 4.[67]

5.2.3. Solubility Measurements

Solubility curves were determined using recently purchased solvents with purities higher than 99% by determining the saturation temperatures T_{sat} of suspensions with known compositions. The samples in 2 mL vials, stirred at 700 rpm, were measured using Crystal16 (Technobis) equipment. The following temperature profile was used: dissolution at 60 °C for 30 min followed by 3 cycles of cooling to -5 °C (-0.5 °C/min) and heating to 60 °C (0.3 °C/min), with isothermal periods of 90 min at -5 °C and 30 min at 60 °C. The clear point temperature in each cycle was identified during the heating ramps as the temperature at which the light transmission passing through a sample reached 100%. The 100% value is calibrated to be a clear solution with a tuning step after the dissolution step. The average of the 3 clear point temperatures was taken as the saturation temperature T_{sat} of the sample. The saturation temperatures were fitted with the Van 't Hoff equation (Equation 5.1), allowing the estimation of any solubility of a pure component in the observed temperature range by using heat of fusion ΔH^f, and melting temperature T_m as fitting parameters.

$$\ln(X^*) = -\frac{\Delta H^f}{R}\left(\frac{1}{T} - \frac{1}{T_m}\right) \qquad \text{Equation 5.1}$$

X^*: solubility (mol fraction); T: temperature (K); R: universal gas constant (8.314 J.mol^{-1}.K^{-1}).

5.2.4. Phase Diagram Point Measurement with the Equilibration Method

Experimental compositions were equilibrated at 5 °C to equilibrate saturated liquids in 2 mL sealed vials. After dissolution, they were cooled down to 5 °C and seeded with stable solid phases, to form stable suspensions. All vials were sealed and stored isothermally at 5 °C under stirring, using Polar Bear Plus apparatus (Cambridge Reactor Design). The compositions were left to equilibrate for 14 days. After filtration of the suspensions the saturated solution and solid compositions were separately determined. The saturated liquid phases were sampled as filtrated solutions using a syringe with a filter. After they were weighed, they were left for full evaporation and weighed again, and the dried solid compositions were quantified using the UV-CD spectroscopy method detailed in section 5.2.2. The sample weights and the UV-CD quantification enabled the compositions of the saturated liquids to be determined. The solid phases in equilibrium with the saturated liquids were analyzed by XRPD.

5.2.5. Raman Spectroscopy in Suspensions with Solvent Addition

Solid phase identification in suspensions was performed with Raman spectroscopy. In this way the complete conversion of the cocrystal S:S-MA to pure levetiracetam S could be monitored. Raman signals were measured regularly during progressive addition of a solvent to the pure cocrystal. Experiments were done under stirring in acetone at a controlled temperature of 5 °C, using the Polar Bear Plus apparatus (Cambridge Reactor Design). For a mass of S:S-MA, $m_{S:S-MA}$, in a vial, at most 30 mL solvent was added in steps of 1 or 2 mL after an initial step of a minimal amount of 5 mL solvent addition. Raman spectra were collected 15 min after each addition, a time considered sufficient for equilibration of the compositions, given the small change and the purpose of detection of a solid phase change. Raman spectra were collected from the top of open vials, which were stirred vigorously to allow a representative Raman measurement of the samples. Contactless in situ measurements were performed using Kaiser Optical Systems RXN2 spectrometer with a PhAT probe (250 mm spacer and 6 mm optic) at 785 nm laser excitation. The spectra were captured with adapted exposure times because of the changes in the compositions and the distance between the probe and the suspension. All raw spectra files were treated using Origin Pro 2021 and normalized from the intensity of the acetone peak (788 cm^{-1}) for comparison. Raman signals were used calibration-free to detect complete S:S-MA dissolution rather than absolute quantities, by focusing on characteristic Raman shifts of only the S:S-MA solid (293 cm^{-1} and 751 cm^{-1}).

5.2.6. Phase Diagram Computation Methods in Barycentric Systems

The mass balance of experimental processes is related to phase diagrams through the lever rule. It is a proportionality rule that links the mass fraction of liquid and solid phases in a biphasic domain with the distance ratio between the composition points on a phase diagram tie-line.[78] Mathematical methods are applied[79, 80] in mass phase diagrams to make accurate computations of points' coordinates, distances between points, line equations, and intersections between two lines.

Through the case of a ternary phase diagram, it can be defined as a barycentric triangle (ABC) system whose coordinates variables are mass fraction x_A, x_B and x_C. The apexes are A ($x_A = 1$, $x_B = 0$, $x_C = 0$), B $(0, 1, 0)$ and C $(0, 0, 1)$. The corresponding side lengths opposite the apexes are thus defined as $a = BC$, $b = CA$ and $c = AB$. Note that a ternary diagram is an equilateral triangle and therefore $a = b = c$. In the lever rule application, the ratio of the distances between points is of interest and not the absolute distances value. Consequently, the side lengths are arbitrary, and we chose a value of 1 for simplicity.

Given two points P $(x_{A(1)}, x_{B(1)}, x_{C(1)})$ and Q $(x_{A(2)}, x_{B(2)}, x_{C(2)})$ in barycentric coordinates, we can define $u = x_{A(1)} - x_{A(2)}$, $v = x_{B(1)} - x_{B(2)}$ and $w = x_{C(1)} - x_{C(2)}$. The distance d_{PQ} between P and Q is:

$$d_{PQ} = \sqrt[2]{-a^2vw - b^2wu - c^2uv} \qquad \text{Equation 5.2}$$

Three points P_i $(x_{A(i)}, x_{B(i)}, x_{C(i)})$ with $i = 1, 2, 3$ can be consider colinear only if equation 5.3 is satisfied:

$$\begin{vmatrix} x_{A(1)} & x_{B(1)} & x_{C(1)} \\ x_{A(2)} & x_{B(2)} & x_{C(2)} \\ x_{A(3)} & x_{B(3)} & x_{C(3)} \end{vmatrix} = 0 \qquad \text{Equation 5.3}$$

By knowing the coordinates of two points lying on a same line, and their distance with a third one of unknown coordinates, also belonging to that line, it is possible to find its coordinates that satisfy both equations 5.2 and 5.3. Therefore, by defining two sets of colinear points in the ternary phase diagram, we calculate the coordinates of the intersection between these two lines by demanding that the third, unknown point, fulfils equation 5.3 for both sets of experimental points. The intersection point coordinates are thus $x_{A(1)}$, $x_{B(1)}$ and $x_{C(1)}$ from equation 5.3.

5.3. Results

5.3.1. Development of Enantioselective Cocrystallization Process

The experimental quaternary phase diagram data acquired previously in Chapter 4[67] can be used to design a chiral resolution process through enantioselective cocrystallization of the S:S-MA cocrystal. The quaternary phase diagram R/S/S-MA/MeCN at 9 °C in Figure 5.1 (right) shows that the stability domain of pure enantiospecific cocrystal S:S-MA (the green domain) intercepts the racemic composition plane RS/S-MA/MeCN (triangle delimited with dashed lines). Such racemic working compositions ω in the enantiospecific cocrystal domain, can be prepared by using specific amounts of the racemic compound RS and the coformer S-MA in the solvent MeCN (Figure 5.2). After complete dissolution by heating, to obtain a solution of R, S, and S-MA, cocrystallization can happen under stable conditions by seeding with S:S-MA while cooling down the composition to 9 °C. Another possible crystallization pathway is to prepare a suspension at 9 °C and wait for the solvent-mediated transformation towards the pure stable S:S-MA cocrystal. In all cases, a composition ω equilibrates as a suspension of pure S:S-MA crystals, which can be isolated by solid-liquid separation. In parallel, the filtrated liquid can be separated to recycle the leftovers of the coformer and the enantiomers for reuse. In this section, we use the phase diagram data to select the starting conditions that maximize the theoretical resolution yield, and we determine the operating conditions leading to a successful enantioselective cocrystallization process.

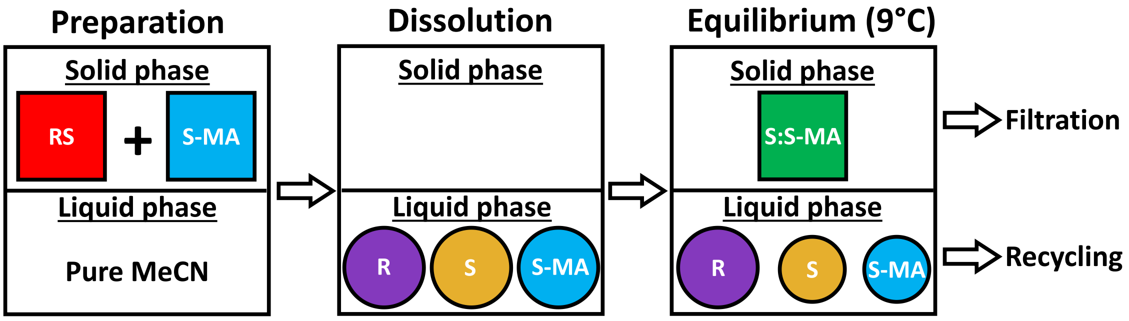

Figure 5.2: Schematic of the evolution of a working composition ω during the enantioselective cocrystallization process. The condition for such process is that the racemic composition ω belongs to the biphasic stability domain of S:S-MA in the quaternary phase diagram.

5.3.1.1. Yield Optimization by Selection of Working Composition

To define the range of possible working compositions ω allowing successful enantioselective cocrystallization processes, we need to determine the intersection surface between the stability domain of S:S-MA and the section of racemic composition defined by the plane RS/S-MA/MeCN in the quaternary. For our model system the racemic section is schematically represented in Figure 5.3 (right), based on interpretation of experimental phase diagram data in mass fractions from Chapter 4[67] (see the Appendix C Figure C2 and Table C1). It shows that the racemic section cuts the stability domain of S:S-MA in a zone delimited by three points A, B and C. A is a point from the eutectic line dh, which also is part of the domain of S-MA. Therefore, point A is a eutectic composition of a triphasic domain in which both S:S-MA and S-MA solids equilibrate with the solution A. Similarly, B is the eutectic composition of a triphasic domain equilibrating S:S-MA and RS solids as it is positioned on the eutectic line fh. Finally, the point C is positioned on the line linking pure S:S-MA point (σ) with the quaternary point h, and the σh line is the boundary with the quadriphasic domain equilibrating S-MA, RS and S:S-MA with a solution of composition h. The point C also connects both triphasic domains mentioned. Each compositional point on the intersection surface ABC will equilibrate towards a suspension of S:S-MA co-crystals in a solution with a composition on the surface ABh and will thus result in a successful enantioselective cocrystallization.

The quaternary point h is at the vertex point from the S:S-MA stability domain and presents the saturated liquid the most highly enriched in R. This indicates point C is the theoretical suspension composition that leads to the maximum yield of cocrystallization, giving at equilibrium the highest quantity of S:S-MA that can be expected from a racemic composition and therefore the highest quantity of S that can be recovered from initial RS inserted. Unfortunately, working with a suspension of composition C is not possible for the present model system as point C is not known precisely due to the composition of quaternary point h not being found experimentally (Chapter 4[67]). In practice, working with the exact composition C would present a risk of entering other stability domains because of experimental imprecision, as the point is positioned at the boundary of four stability domains (see Figure 5.3). For these reasons, a different working composition ω is chosen here. The latter equilibrates pure S:S-MA solid (at point σ) on a tie-line with the saturated solution of composition λ. Composition ω is selected based on λ being the saturated liquid in equilibrium with S:S-MA from the measured quaternary phase diagram that is the most highly enriched in R and therefore the furthest from racemic composition (see experimental data in the Appendix C Figure C2). It is also close to our estimation of point C with maximum yield.

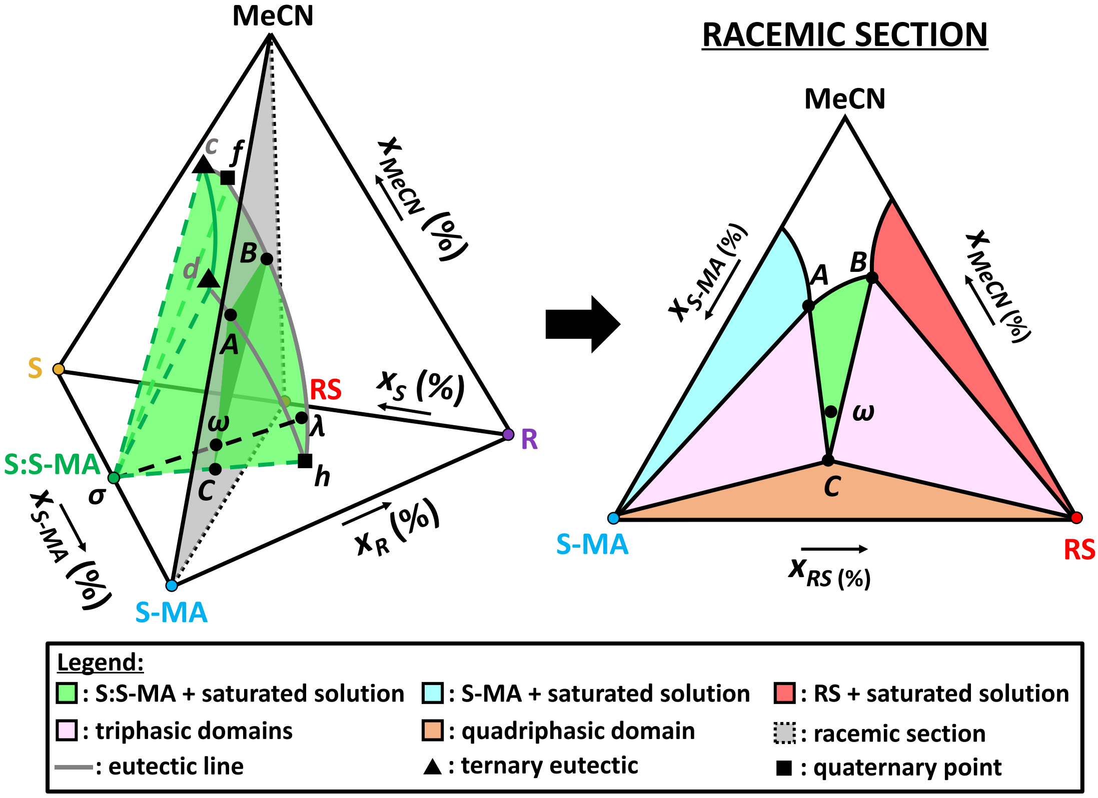

Figure 5.3: Left: isothermal quaternary phase diagram R/S/S-MA/MeCN showing only the domain of S:S-MA solid in equilibrium with a saturated solution. The quaternary phase diagram is fully represented in Figure 5.1. The racemic section cuts the borders of the stability domain of the cocrystal S:S-MA (green) at points A, B and C, defining a region where racemic suspensions equilibrate to pure cocrystal S:S-MA with a saturated solution. The point ω, chosen as the working composition in the present study, is obtained from mixing pure RS, pure S-MA and MeCN. Point ω equilibrates by separating over the black dashed tie-line $\lambda\sigma$ into liquid composition λ and solid composition σ (pure

S:S-MA). The total equilibrium mass of each phase can be computed by mass balance equations. Right: Isoplethal section at racemic composition, represented by the plane S-MA/RS/MeCN in the quaternary phase diagram.

The coordinates of experimental points used for the process we design are determined with the experimental phase diagram data (Appendix C Figure C2) for σ ($x_R = 0\%$, $x_S = 52.80\%$, $x_{S-MA} = 47.20\%$, $x_{MeCN} = 0\%$), ω ($x_R = 21.12\%$, $x_S = 21.12\%$, $x_{S-MA} = 42.28\%$, $x_{MeCN} = 15.48\%$), and λ ($x_R = 31.22\%$, $x_S = 7.30\%$, $x_{S-MA} = 39.37\%$, $x_{MeCN} = 22.11\%$). The equilibrated mass $m_{S:S-MA}^{eq}$ of S:S-MA solid that can crystallize at equilibrium can be deduced with the mass balance from m_{ω}^{total}, the total mass of the suspension of composition ω, by using the lever rule with $d_{\omega\lambda}$ and $d_{\sigma\lambda}$ being the distances between respectively the two points omega-lambda and sigma-lambda such as:

$$m_{S:S-MA}^{eq} = m_{\omega}^{total} \times \frac{d_{\omega\lambda}}{d_{\sigma\lambda}} = m_{\omega}^{total} \times 0.2046 \qquad \text{Equation 5.4}$$

From the experimental mass of solid, m_{solid}^{exp} , recovered from filtration at the end of the process, we can define the yield of crystallization Y (%) such as:

$$Y(\%) = \frac{m_{solid}^{exp}}{m_{S:S-MA}^{eq}} \times 100 \qquad \text{Equation 5.5}$$

The component mass fractions x_R^{solid} (%), x_S^{solid} (%), and x_{S-MA}^{solid} (%) are quantified in the resulting solid with the protocol explained in Section 5.2.2. The quantification of a test sample made with pure S:S-MA has been performed as a reference and resulted in the following quantification by the models: $x_R^{S:S-MA} = -2$ %, $x_S^{S:S-MA} = 55$ %, and $x_{S-MA}^{S:S-MA} = 47$ %. Based on computations from molecular masses, pure S:S-MA solid should give values of $x_R^{S:S-MA} = 0$ %, $x_S^{S:S-MA} = 52.8$ %, and $x_{S-MA}^{S:S-MA} = 47.2$ %. Therefore, we define that an error of quantification of approximately 2% is possible with the models. For that reason, we consider the isolation of the S:S-MA cocrystal at the end of the process to be successful when x_R^{solid} $(\%) = 0 \pm 2$ %. If the obtained solid is assumed to be pure S:S-MA, we can compute the mass of S in the obtained solid m_S^{solid} such as:

$$m_S^{solid} = m_{solid}^{exp} \times x_S^{S:S-MA} = m_{solid}^{exp} \times 0.528 \qquad \text{Equation 5.6}$$

Knowing the initial mass of RS at composition ω , m_{RS}^{ω}, the mass of S that is inserted in the system at composition ω, m_S^{ω}, can be deduced such as:

$$m_S^{\omega} = \frac{m_{RS}^{\omega}}{2} \qquad \text{Equation 5.7}$$

Therefore, we can compute the resolution yield R (%), being the recovery percentage of S from initial RS amount by the chiral resolution process with enantioselective cocrystallization:

$$R\ (\%) = \frac{m_S^{solid}}{m_S^{\omega}} \times 100 \qquad \text{Equation 5.8}$$

By combining equations 5.4, 5.6 and 5.7 for an arbitrary value of m_{ω}^{total}, we calculate the theoretical resolution yield R (%) for our chosen working composition ω to be of 51%.

5.3.1.2. Process Development and Optimization of Operating Conditions

In total, six batches were performed with the view to identifying operating conditions that optimize the cocrystallization process and the recovery of S through S:S-MA isolation at composition ω. Overall compositions were prepared as close as possible to the theoretical composition ω, as highlighted by the experimental masses used for batches ω_1 to ω_6 that are presented in the Appendix C, Table C2. Preliminary experiments help to identify the complete dissolution of composition ω above 50 °C, and therefore a temperature of 55 °C is chosen to ensure an easy and complete dissolution for 30 minutes under stirring. When fully dissolved, the volume V of the overall composition is of about 20 mL. Cooling to 9 °C is performed using Polar Bear Plus apparatus (Cambridge Reactor Design) with a ramp of 1 hour and a stirring of 1000 rpm. When reaching temperatures around 40 °C, the composition ω crystallizes spontaneously in the form of a gel, with solid in suspension in a viscous liquor. Seeding trials with a very small amount of pure S:S-MA introduced at 45 °C result in immediate crystallization of the composition, in the same gel form. When performed at 47.5 °C, the seeding leads to slower and progressive crystallization of a homogeneous suspension. Therefore, 47.5 °C is chosen as optimal seeding temperature. When cooling down, the suspensions become more viscous. Regardless of this viscosity increase, stirring ensures movement in the liquor and the equilibration of composition ω at 9 °C into saturated solution λ and pure S:S-MA. After equilibration, the solid is filtrated by vacuum and washed. Different washing protocols were tried depending on the batches, and results are discussed in the Appendix C, Section C3. The protocol retained for successful isolation of pure crystals is washing with $2 \times V\ (20\mathrm{mL})$ of MeCN fractions kept at about -10 °C. This is the protocol performed for batches ω_4, ω_5, and ω_6. After 1 week of drying in oven at 50 °C, the final solid is weighed to measure m_{solid}^{exp}. Nonetheless, regular weighing proves that after 1 day the final mass does not change. XRPD measurements are performed to identify the nature of the crystalline material. The solid composition is quantified, and results assess if the obtained solid is pure S:S-MA or not. If so, the yield of crystallization Y (%) (Equation 5.5) and the resolution yield R (%) (Equation 5.8) are computed.

All batches lead to crystallization of only pure S:S-MA solid, as reported in the XRPD patterns data presented in the Appendix C Figure C3. This confirms that the selection of composition ω is appropriate for chiral resolution with enantioselective cocrystallization. However, for the batches ω_1, ω_2, and ω_3, the washing protocols tried do not result in complete separation of the solids from their liquor (details in the Appendix C Section C3). The presence of remaining liquor is identified in final solid compositions measured in Table 5.1. Moreover, m_{solid}^{exp} measured for batches ω_2 and ω_3 are above $m_{S:S-MA}^{max}$, which is impossible if a pure and dry S:S-MA solid is obtained. Therefore, these batches fail the chiral resolution because of inappropriate washing conditions, so no yield of crystallization Y (%) and resolution yield R (%) are computed. For the batches ω_4, ω_5, and ω_6, the retained washing protocol discussed earlier is used. This strategy is successful to obtain pure S:S-MA crystals separated from the liquor, as highlighted by the completely dried solids and the solid composition measured in Table 5.1. The crystallization yield $Y(\%)$ is higher than 90%, underlining only a small loss of solid during this washing protocol. Different equilibration times were tried for the batches ω_4, ω_5, and ω_6, from 24 hours to about 1 week, and show no difference in the yield of crystallization $Y(\%)$ obtained. Therefore, the minimum time of 24 hours tried for equilibration appears sufficient. This time could possibly be reduced but no additional experiments were performed.

Table 5.1: Characterization parameter results from enantioselective cocrystallization process batches at composition ω. The crystallization yield Y (%) and the resolution yield R (%) are not computed for the batches whose solid composition highlight that pure solid S:S-MA is not completely isolated from its saturated liquor due to washing conditions.

	Crystallization yield			Solid composition			Chiral resolution		
Batch	m_{solid}^{exp} (g)	$m_{S:S-MA}^{eq}$ (g)	Y (%)	x_R^{solid} (%)	x_S^{solid} (%)	x_{S-MA}^{solid} (%)	m_S^{solid} (g)	m_S^{ω} (g)	R (%)
ω_1	3.43	5.19		10	44	45			
ω_2	9.67	5.19		15	42	43			
ω_3	5.84	5.19		4	49	47			
ω_4	4.90	5.19	94	2	51	47	2.49	5.36	46
ω_5	4.68	5.19	90	0	53	47	2.46	5.36	46
ω_6	4.77	5.19	92	2	51	47	2.42	5.36	45

As the batches ω_4, ω_5, and ω_6, lead to pure S:S-MA solid isolation, the resolution yield $R(\%)$ is calculated and results in a value of about 46% for the three batches. This experimental value is a good result comparing to the theoretically possible resolution yield $R(\%)$ of 51%. It proves the success of the designed chiral resolution process with enantioselective cocrystallization and the chosen operating conditions.

5.3.2. Enantiomer Recovery by Solvent-Mediated Transformation

Levetiracetam (S), which is the molecule of interest, needs to be recovered from its isolated cocrystal S:S-MA. To permit the recovery, physical property differences between the two components S and S-MA need to be exploited. Here, we investigate the pure component solubility difference between S and S-MA in solvents to find suitable recovery conditions for a solvent-mediated transformation. The S/S-MA/solvent ternary systems in different solvents at the same temperature T exhibit the same stability domains, but these domains may differ in their compositional ranges due to different non-ideal behavior. This difference in non-ideal behavior as a function of the solvent is reflected in the solvent-dependent pure component solubilities[81-83] of S and S-MA. A solvent change might induce a change in the pure component solubilities from roughly equal to highly different, which has the result that the initially relatively symmetric ternary phase diagram in the new solvent is strongly skewed. It is possible to find solvents in which S is much less soluble than S-MA, which skews the isothermal ternary phase diagrams as illustrated in Figure 5.4. The higher the difference between pure S solubility x_S^T (yellow point) and pure S-MA solubility x_{S-MA}^T (blue point), the more the S:S-MA cocrystal stability domain is skewed towards x_{S-MA}^T. This influences the position of eutectic points in the ternary phase diagram, and in particular the eutectic point labelled E in Figure 5.4, which is associated to the equilibration of pure S and pure S:S-MA in suspension. The closer the eutectic point E is from the binary axis S-MA/solvent, the higher is the amount of pure S that can be retrieved from the deconstruction of cocrystal S:S-MA.

The position of the eutectic points in the ternary phase diagram is also a function of the cocrystal stability relative to the pure component stability.[84] From the equilibrium reaction of the cocrystal S:S-MA dissociating in solution to S and S-MA according to

$$S{:}S - MA_{solid} \rightleftharpoons S_{solution} + S - MA_{solution} \qquad \text{Equation 5.9}$$

the cocrystal solubility can be described at temperature T by the solubility product K_{sp}^{T}

$$K_{sp}^{T} = [S]^{T} \times [S - MA]^{T} \qquad \text{Equation 5.10}$$

where we consider that the activities of cocrystal components are their concentrations $[S]^{T}$ and $[S - MA]^{T}$ at equilibrium. A measure of the cocrystal stability with respect to the pure component solubilities is the ratio Q^{T} between the product of pure component solubilities and the cocrystal solubility product.

$$Q^{T} = \frac{x_{S}^{T} \times x_{S-MA}^{T}}{K_{sp}^{T}} \qquad \text{Equation 5.11}$$

The less soluble the cocrystal, the higher Q^{T} becomes, which indicates a higher relative stability of the cocrystal relative to the pure component stability. Consequently, the higher Q^{T}, the more the eutectic points are likely to be closer to the binary solute/solvent axes, with a wider stability region for the cocrystal represented by region III in Figure 5.4. The interactions in solution can also increase or decrease the solubility of components, and thus influence the shift of the cocrystal stability region in the phase diagram. Therefore, the skew and width of the cocrystal stability region is strongly influenced by temperature and the solvent used.[85] When the solubility strongly differs between components the region can become very narrow or even disappear[86], leading to systems that are ideal to envisage cocrystal deconstruction by solvent-mediated transformation.

In this study, we do not take into account any effect of the presence of a component on the pure component solubility of the other and we focus on the solubility difference Δx^{T}, expressed in mass fraction, between x_{S-MA}^{T} and x_{S}^{T} that we define at a temperature T such as:

$$\Delta x^{T} = x_{S-MA}^{T} - x_{S}^{T} \qquad \text{Equation 5.12}$$

We consider that for high enough Δx^{T}, it leads to skewed cocrystal stability regions that exhibit an incongruent solubility for the S:S-MA cocrystal, meaning that the latter dissolves progressively upon solvent addition, while pure S solid crystallizes and coexists with S:S-MA in suspension, as shown in the phase diagrams in Figure 5.4. Indeed, the solvent addition to pure cocrystal S:S-MA leads to overall compositions following the solvent addition lines (red dashed arrows). Starting from pure S:S-MA, these compositions first enter the triphasic domain (region II), where S:S-MA solid progressively converts to solid S in suspension, while S-MA dissolves in the liquid phase of fixed eutectic composition E. When reaching composition point D, the stability domain I is entered, in which pure S solid is the only stable phase in suspension. Therefore, we define cocrystal deconstruction points D as the compositions on the solvent addition lines that require the minimal amount of solvent to stabilize pure S solid. At these points D, the cocrystal is completely deconstructed and pure S solid can be retrieved from filtration of eutectic liquid E. It would give a mass of pure S, m_{S}^{max}, that is the highest that can be expected in an isothermal ternary system. m_{S}^{max} can be deduced from m_{D}^{total}, the total mass of the overall composition at point D, by using the lever rule with d_{DE} and d_{SE} being the distances between the phase diagram compositions points, such as:

$$m_{S}^{max} = m_{D}^{total} \times \frac{d_{DE}}{d_{SE}} \qquad \text{Equation 5.13}$$

However, pure crystals of S can be obtained from filtration for all overall compositions on solvent addition lines that are in the domain I, such as points F in Figure 5.4. A suspension of composition F equilibrates on the tie-line SL, between pure S solid of composition S, and a saturated liquid of composition L. m_S^F, the mass of pure S that can be retrieved from filtration, can be deduced from m_F^{total}, the mass of the overall composition at point F, by using the lever rule with d_{FL} and d_{SL} being the distances between the phase diagram compositions points, such as:

$$m_S^F = m_F^{total} \times \frac{d_{FL}}{d_{SL}} \qquad \text{Equation 5.14}$$

As the m_S^F obtained from filtration would be inferior to m_S^{max}, we can define the deconstruction yield δ (%) such as:

$$\delta(\%) = \frac{m_S^F}{m_S^{max}} \times 100 \qquad \text{Equation 5.15}$$

Knowing the initial masses to prepare a suspension i, its total mass m_i^{total}, and its mass fraction in S x_S^i, the equivalent mass in S, m_S^{eq}, can be deduced such as:

$$m_S^{eq} = m_i^{total} \times x_S^i \qquad \text{Equation 5.16}$$

Therefore, we can compute the recovery yield ρ (%), being the recovery percentage of S from initial S:S-MA amount by the cocrystal deconstruction with solvent addition, with the obtained experimental mass of S, m_S^{exp}, at the end of the process:

$$\rho\ (\%) = \frac{m_S^{exp}}{m_S^{eq}} \times 100 \qquad \text{Equation 5.17}$$

In a theoretical perfect filtration performed at point D exactly, the maximum recovery yield ρ^{max} (%) in a specific isothermal ternary system can be computed such as:

$$\rho^{max}\ (\%) = \frac{m_S^{max}}{m_S^{eq}} \times 100 \qquad \text{Equation 5.18}$$

In this study, we make the hypothesis that the higher Δx^T is, the higher ρ^{max} (%) can be. The recovery of a molecule of interest from a cocrystal is thus strongly influenced by the selection of the solvent and the working temperature T. Using the S/S-MA system that forms a cocrystal as a model, we propose guidelines to identify suitable solvents and temperatures. We also aim to propose ways to estimate the composition of eutectic point E in the ternary systems, to compute accessible ρ^{max} (%).

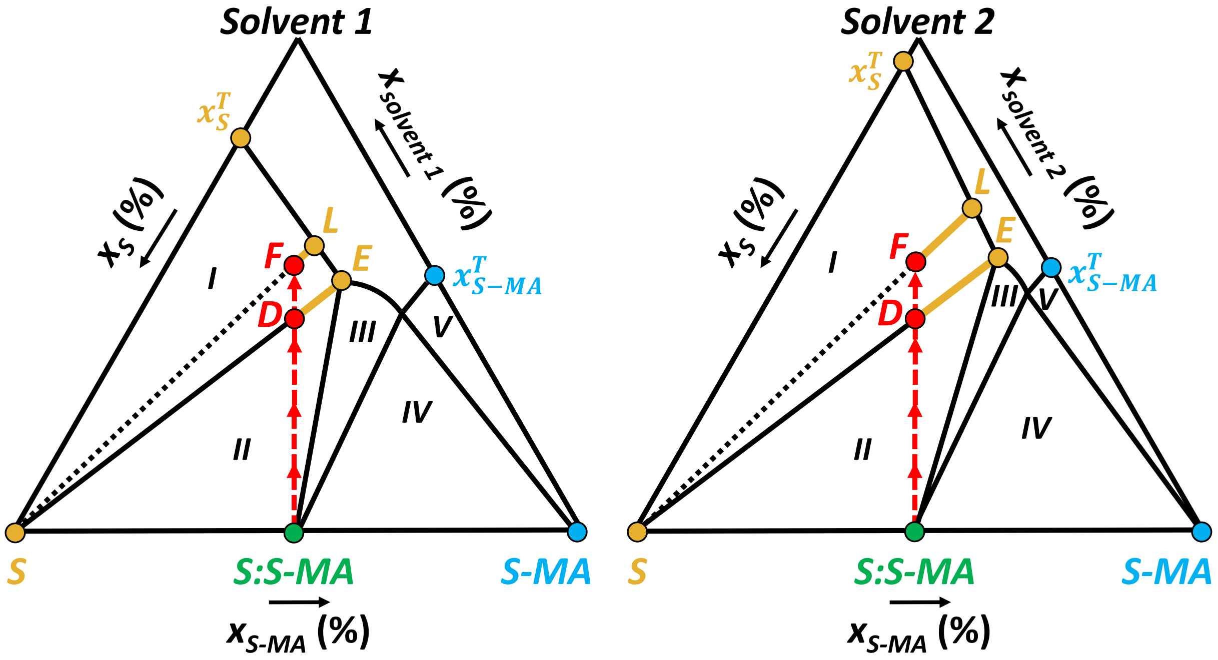

Figure 5.4: Theoretical isothermal ternary phase diagrams, with two different solvents for components S and S-MA forming the enantiospecific cocrystal S:S-MA. Regions I, III and V are stability domains of S, S:S-MA, and S-MA, respectively. Regions II and IV are triphasic domains between S:S-MA, a solution of eutectic composition and respectively S and S-MA. Above the solubility lines is the undersaturated solution domain. x_S^T and x_{S-MA}^T are solubility points of pure S and pure S-MA at temperature T. The red dashed lines correspond to the overall composition pathway when adding solvent to pure S:S-MA. The skew of the phase diagram is strongly related to the difference $\Delta x^T = x_{S-MA}^T - x_S^T$. Deconstruction points *D* (red) correspond to the equilibrium compositions from the solvent addition lines that require the minimal amount of solvent to enter the stability domain of pure S (region I). A suspension at *D* equilibrates into a liquid of eutectic composition *E* and pure S in suspension. Starting from a cocrystal suspension, any point *F* on the red dashed line in the region I equilibrates into a liquid of saturated liquid *L* and pure S in suspension. The equilibrium masses of each phase can be computed by mass balance equations. A highly skewed phase diagram allows the conversion of S:S-MA to S in region II with high yields.

5.3.2.1. Optimization of the Enantiomer Recovery by Solvent and Temperature Selection

For S and S-MA system, finding a solvent in which S is much less soluble than S-MA is necessary to guarantee a high Δx^T. Literature data help to select solvents presenting low solubility for S and high solubility for S-MA. When needed, a quick solvent screening at ambient temperature is performed. Following these preliminary studies, the three solvents: acetone, ethyl acetate, and 1,4-dioxane, are selected because of a high apparent Δx^T at ambient temperature. The solubility curves of S and S-MA in each solvent are measured using the protocol explained in Section 5.2.4. In Figure 5.5, the results are reported as Van 't Hoff plots. The experiment data points are presented in the Appendix C, Table C4, with their associated fitted lines parameters in Table C5.

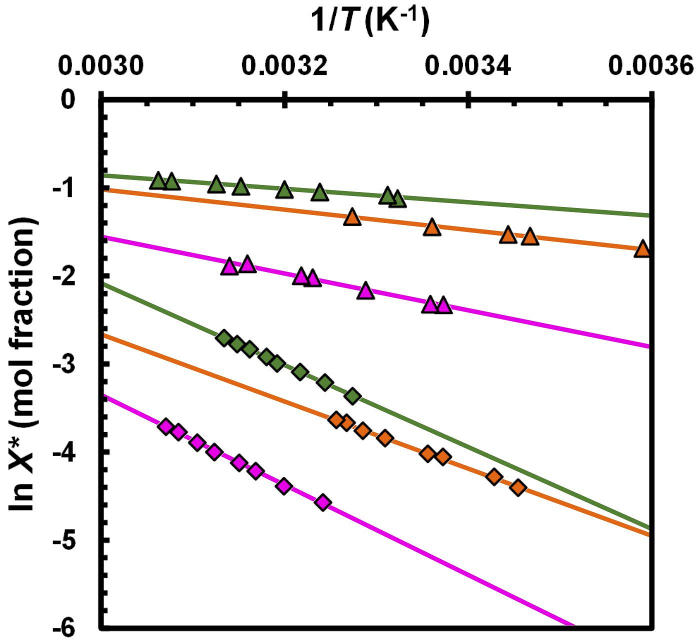

Figure 5.5: Van 't Hoff plots measured for S (diamonds) and S-MA (triangles) in acetone (orange), ethyl acetate (pink) and 1,4-dioxane (dark green).

Using the equations of trend lines from Van 't Hoff plots, the solubility values can be extrapolated at different temperatures, and converted to mass fractions in their respective ternary systems to permit the computation of Δx^{T} as a function of temperature. The results are plotted in Figure 5.6 from 0 to 60 °C, for each solvent, in the limits of their boiling points and freezing points. It highlights the large dependence of Δx^{T} with temperature, strongly increasing with T for ethyl acetate and acetone, but slightly decreasing for 1,4-dioxane. Ethyl acetate presents lower Δx^{T} values than the two other solvents and is less interesting for the design of an enantiomer recovery process. Between 15 to 30 °C, the Δx^{T} for acetone and 1,4-dioxane are similar and close to 0.4. Working with lower temperatures is possible using acetone, which guarantees satisfactory Δx^{T} values around 0.35. Temperatures higher than 25 °C with acetone seem more appropriate for Δx^{T} but with a boiling point of 56 °C and a high vapor pressure, acetone would be too volatile to design a process. With its freezing point of 12 °C, 1,4-dioxane does not allow access to low temperatures, but its boiling point of 101 °C and lower vapor pressure present less evaporation issues and the possibility to work with higher temperatures despite a slightly decreasing Δx^{T}. However, it is more difficult to dry from a filtrated solid, more expensive solvent, and is carcinogenic, making it incompatible with an industrial process design. As a result, acetone is preferred. As experiments for the estimation of compositions require working with small volumes and open reactors, a low temperature is preferred for accuracy, to prevent solvent evaporation.

5 °C is chosen as the working temperature T as it is the lowest temperature accessible with Polar Bear apparatus for equilibration experiments. For acetone at 5 °C, we compute $x_{S-MA}^{5°C} = 0.3698$ and $x_{S}^{5°C} = 0.0209$, therefore $\Delta x^{5°C} = 0.3489$, which is satisfactory enough to expect an important deconstruction with a high R^{max} (%). For ethyl acetate at 5 °C, $x_{S-MA}^{5°C} = 0.1007$ and $x_{S}^{5°C} = 0.0032$, making $\Delta x^{5°C} = 0.0975$, therefore much lower than acetone one. By performing deconstruction experiments in both solvent systems at 5 °C, we aim to verify that the higher Δx^{T} is, the higher ρ^{max} (%) can be.

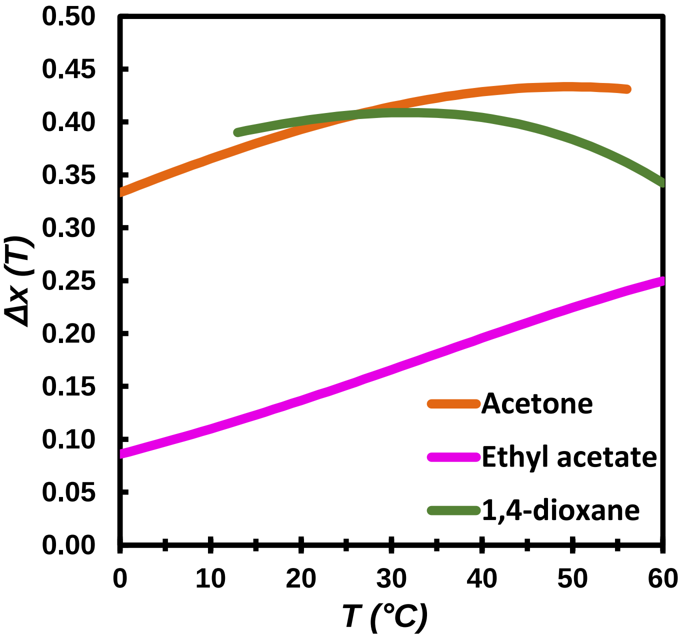

Figure 5.6: Δx^T as a function of temperature, computed with S and S-MA solubilities in acetone (orange), ethyl acetate (pink), and 1,4-dioxane (dark green), from Van 't Hoff plots extrapolation.

5.3.2.2. Eutectic Points $\boldsymbol{E}$ Estimation from Equilibrated Suspensions

Knowing the precise location of the eutectic point E in an isothermal ternary system is ideal to design an optimized enantiomer recovery process by solvent-mediated transformation. Nonetheless, knowing the full phase diagram is not required as only finding the coordinates of point E is necessary. The latter helps to deduce the deconstruction point D, at the intersection between the SE segment and the solvent addition line for the pure cocrystal (see Figure 5.4). Experimental suspensions in the S and S:S-MA triphasic domain for acetone and ethyl acetate systems were prepared to estimate points E at 5 °C using the equilibration method detailed in section 5.2.4. For each system, five samples give consistent results for the measured saturated liquid that equilibrate S and S:S-MA in suspension while being clustered in the ternary phase diagrams plots, therefore being identified as points E. The obtained compositions are summarized in the Appendix C Table C6. For both acetone and ethyl acetate systems, the experimental compositions of the $n = 5$ saturated liquids i in mass fraction percentage (x_S^i, x_{S-MA}^i, $x_{solvent}^i$) are averaged to obtain a centroid of composition E (x_S, x_{S-MA}, $x_{solvent}$). The standard deviation σ in Euclidean distance of all points from the centroid is computed with the equation:

$$\sigma = \sqrt{\frac{\sum_{i=1}^{n}\left(\left(x_S - x_S^i\right)^2 + \left(x_{S-MA} - x_{S-MA}^i\right)^2 + \left(x_{solvent} - x_{solvent}^i\right)^2\right)}{n}} \qquad \text{Equation 5.19}$$

At 5°C, we obtain in the acetone system, E_{ace} ($x_S = 6.13\ \%$, $x_{S-MA} = 9.45\ \%$, $x_{acetone} = 84.42\ \%$) with $\sigma = 0.41\ \%$, while in ethyl acetate we obtain E_{EtOAc} ($x_S = 1.37\ \%$, $x_{S-MA} = 1.67\ \%$, $x_{ethyl\ acetate} = 96.96\ \%$) with $\sigma = 0.26\ \%$. Both σ values highlight an accurate estimation of eutectic points E, whose centroids are represented in Figure 5.7 as a superimposition of both solvent phase diagrams, zoomed in on the solvent corner. From the coordinates of points E and pure solid S, we can compute SE line equations. Similarly, the solvent addition line equation (dashed red) is measured, as it links pure cocrystal coordinates to pure solvent coordinates. At the intersection of both lines, we calculate with the mathematical methods described in section 5.2.6, the deconstruction points D coordinates (Figure 5.7, red). At 5 °C, we compute for acetone, D_{ace} ($x_S = 10.10\ \%$, $x_{S-MA} = 9.05\ \%$, $x_{acetone} = 80.85\ \%$) and for ethyl acetate, D_{EtOAc} ($x_S = 1.82\ \%$, $x_{S-MA} = 1.63\ \%$, $x_{ethyl\,acetate} = 96.55\ \%$). As represented in Figure 5.7, the point E in acetone is much further from point D, than in ethyl acetate. The lengths of segments d_{DE} and d_{SE} are computed for each system by the mathematical methods described in section 5.2.6. From the lever rule equation at point D (Equation 5.13) and the x_S^D value at D, we can adapt the ρ^{max} calculation formula (Equation 5.18) such as:

$$\rho^{max}\ (\%) = \frac{m_S^{max}}{m_S^{eq}} \times 100 = \frac{m_D^{total} \times \frac{d_{DE}}{d_{SE}}}{m_D^{total} \times x_S^D} \times 100 = \frac{d_{DE}}{d_{SE} \times x_S^D} \times 100 \qquad \text{Equation 5.20}$$

We compute for acetone at 5 °C, a $\rho^{max} = 41.87\%$, and for ethyl acetate at 5 °C, a $\rho^{max} = 24.23\%$. With a $\Delta x^{5°C}$ about 3.6 times higher for acetone than ethyl acetate, the estimated ρ^{max} value for acetone is about 1.7 times higher. This confirms the influence of Δx^T on the ρ^{max} and the importance of temperature and solvent selection for the enantiomer recovery. Despite a supposedly small $\Delta x^{5°C} = 0.0975$, the skew in the experimental phase diagram is still important enough to allow the recovery of 24.23% of pure S introduced originally in the system. With a relatively high $\Delta x^{5°C} = 0.3489$ for acetone, this recovery of pure S elevates to 41.87%. Nonetheless, estimation of eutectic points E and deconstruction points D is a success and requires low number of experiments to find out the accessible ρ^{max} in a defined solvent at a working temperature when knowing the solubility curves of the pure components. The disadvantage of this method is that equilibration experiments can take time and require the prior development of an accurate quantification method of the components to measure phase diagram compositions.

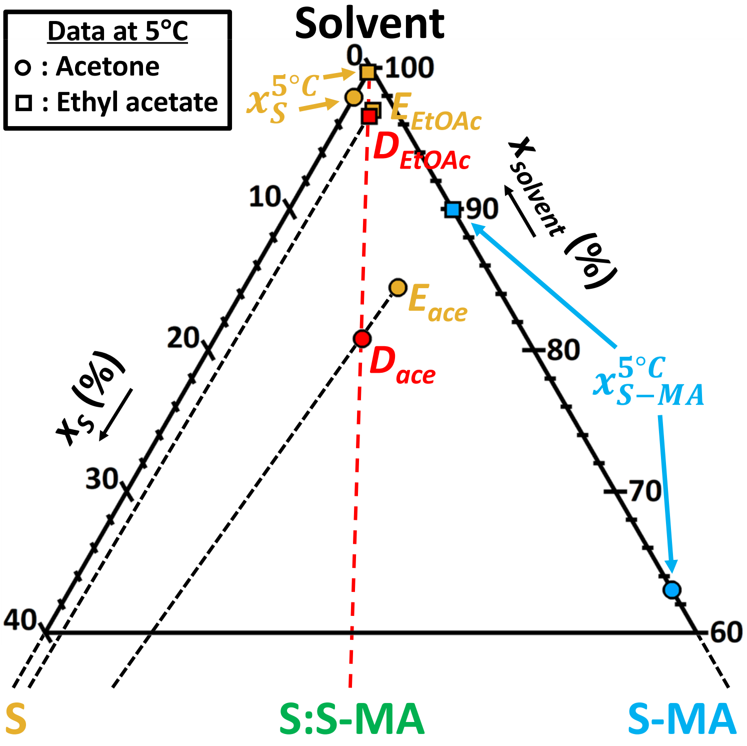

Figure 5.7: Zoom in on the solvent corner of the superimposition of isothermal phase diagrams S/S-MA/solvent data in acetone (circles) and ethyl acetate (squares). $x_S^{5°C}$ and $x_{S-MA}^{5°C}$ are respectively the solubility values of pure solids S and S-MA at 5 °C. The eutectic point E locations are computed from the average of five saturated liquid compositions equilibrating S and S:S-MA. From the intersection between SE line equations (dash-dotted) and solvent addition line equations (red dashed), the deconstruction points D are computed.

5.3.2.3. Detection of Deconstruction Point D with Online Raman Spectroscopy

The estimation of eutectic points E requires preliminary phase diagram studies that can be time consuming. However, there is another way to estimate the compositions of points E and D and therefore ρ^{max}. Looking at Figure 5.4, the point E can be estimated at the intersection of the pure S solid solubility curve with the extension of SD line if the coordinates of point D are known. Taking this into consideration, we propose a protocol to identify the composition at point D while estimating the trend of the solubility curve. In recent work, Svoboda et al.[87] use Raman spectroscopy to screen for ternary phase diagram boundaries in cocrystal systems. By performing solution additions, the suspensions' overall compositions move on a composition line, and the dissolution or crystallization of solids are detected with online Raman spectroscopy. Here, we apply this method for the detection of deconstruction point D, by performing solvent addition on pure cocrystal S:S-MA. Following the solvent addition line (Figure 5.4, red line), we first identify S and S:S-MA in suspension, until reaching the deconstruction point D, where S:S-MA completely dissolves, leaving only pure S solid in suspension. The experimental protocol for identification of the complete S:S-MA dissolution with Raman spectroscopy is detailed in section 5.2.5. Beyond point D, solvent additions are still performed to ensure the obtention of a suspension stabilizing pure S solid, and therefore positioned in Figure 5.4 region I. This suspension of composition F and known mass m_F^{total}, is filtrated and the mass of the recovered solid, m_S^F, is weighed. The solid is assessed to be pure S, from XRPD analysis (section 5.2.1) and component quantification with UV-CD spectroscopy (section 5.2.2). By knowing m_S^F and m_F, the lever rule at point F (Equation 5.14) is adapted knowing that:

$$d_{SL} = d_{SF} + d_{FL} \qquad \text{Equation 5.21}$$

to obtain:

$$d_{FL} = \frac{\frac{m_S^F}{m_F^{total}} \times d_{SF}}{1 - \frac{m_S^F}{m_F^{total}}} \qquad \text{Equation 5.22}$$

Therefore, the length d_{FL} is known from experimental compositions, and with the equation of the SF line, we compute the coordinates of point L in the phase diagram with mathematical methods detailed in section 5.2.6. By making the hypothesis that the influence of S-MA concentration on the solubility of pure S is constant, the solubility curve is thus a line going through pure S solubility point x_S^T and point L (see Figure 5.4)., The intersection of this line with the extension of the SD line is computed to obtain an estimate of the eutectic composition E, that we name E' for comparison with composition E, measured in the previous section.

This protocol is performed in acetone at 5 °C, by using 2.8061 g of S:S-MA cocrystal. The two Raman shifts 293 cm^{-1}, and 751 cm^{-1} are chosen to identify the dissolution of S:S-MA as function of acetone addition. The compositions relevant for identification of point D are selected and represented in Figure 5.8 in the corresponding phase diagram at 5 °C (a), and the appropriate Raman shifts from the spectra are shown for these compositions (b). The coordinates of overall compositions are summarized in the Appendix C, Table C7. The detection of point D' presents some uncertainty as the volume additions performed shift the overall composition through steps. However, the spectra confirm the absence of S:S-MA in the suspension after composition 5, that is assumed to be the deconstruction point D' ($x_S = 9.65$ %, $x_{S-MA} = 8.62$ %, $x_{acetone} = 81.73$ %). Indeed, it shows no more absorption at 293 cm^{-1} and 751 cm^{-1}, with flatten curves that stay the same until the composition 7, where the suspension is filtrated. 0.496 g of filtrated solid is obtained and is confirmed to be pure S, with a quantified purity of 99.5 $\pm$ 2 %. Therefore, the point L ($x_S = 3.81$ %, $x_{S-MA} = 5.13$ %, $x_{acetone} = 91.06$ %) is computed, and the point E' ($x_S = 4.83$ %, $x_{S-MA} = 9.01$ %, $x_{acetone} = 86.16$ %) is estimated.

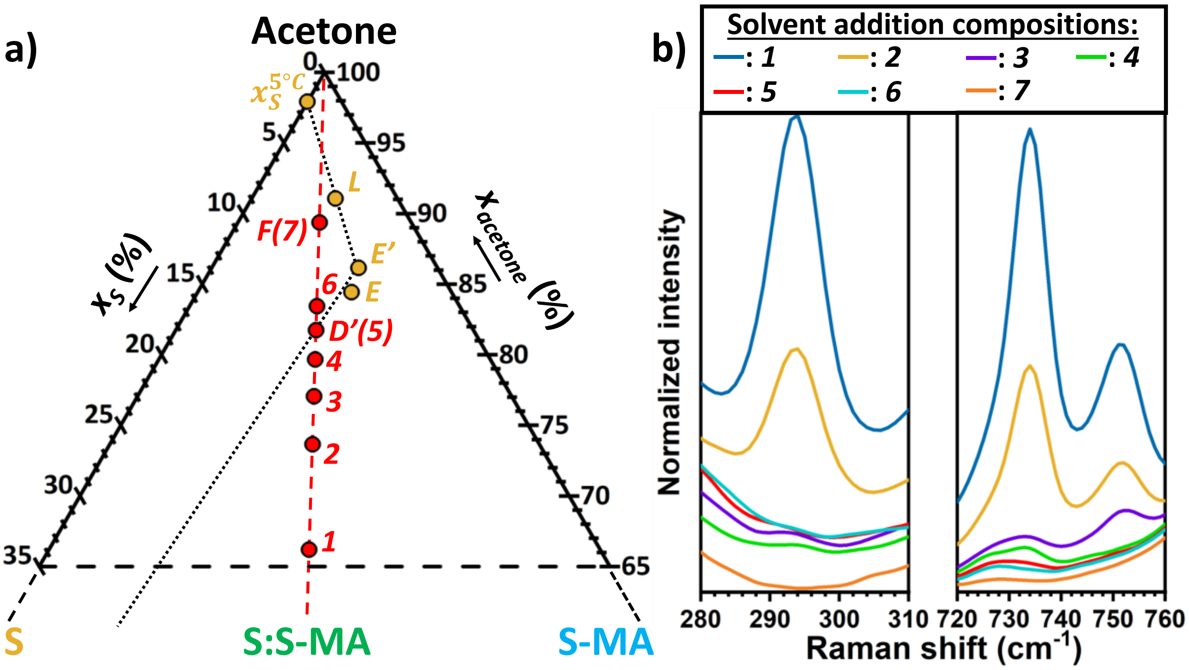

Figure 5.8: Estimation of the deconstruction point D' in acetone at 5 °C from solvent addition experiments and Raman spectra acquisition. The eutectic point E' is estimated by computation of the intersection between the pure S solubility line and the solvent addition line SD'. **a)** Equilibrated suspensions compositions (red), labelled by a number, along the solvent-addition line starting from the cocrystal (red dashed line) represented in the ternary phase diagram. **b)** experimental Raman shifts characteristic of the S:S-MA dissolution, as function of acetone addition in the different compositions with their associated numbers.

In Figure 5.8, we can compare the position of estimated E' with the measured E from the equilibration experiments. There is a slight shift due to the uncertainty in the determination of point D' and the assumption that the solubility curve of pure S is a straight line. However, the estimation is not far from reality and this protocol to screen for deconstruction conditions of a cocrystal is successful in acetone at 5°C.

5.4. Discussion

The knowledge of the full quaternary phase diagram determined in Chapter 4[67] leads to the successful optimization of an enantioselective cocrystallization process to isolate pure S:S-MA chiral cocrystal. This confirms the relevance of phase diagram data for process design. The resolution yield *R(%)* at 9°C is about 46% and is consistent in 3 experiments, which is a substantial improvement from the previously reported resolution yield *R(%)* value of 14.7% by Springuel et al.[56] from trial-and-error suspensions at 9°C in the same system. However, they also report a maximum resolution yield *R(%)* value of 69.6% at -10°C from trial-and-error suspensions compositions. This indicates that the knowledge of the isothermal quaternary phase diagram at -10°C could be even more interesting as it would allow the development of a process leading to a potentially very high value of resolution yield *R(%)*. It also highlights the necessity to develop screening tools permitting to easily determine the optimal working temperature and solvent for quaternary chiral systems designed for chiral resolution, before investigating them in detail. Indeed, quaternary phase diagrams are time consuming to realize, but knowledge of them is necessary when working with asymmetric systems, for instance two enantiomers and a chiral coformer in a solvent. The resolution by formation of diastereomeric or enantiospecific cocrystals is a hot topic and knowing the experimental conditions that could lead to the highest potential asymmetry for isolation of an enantiopure cocrystal is key before long and tedious phase diagram measurements. The value of 46% we obtain for resolution yield $R(\%)$ at 9 °C is satisfactory, but it means that about 54% of levetiracetam (S) is lost in the liquid phase, making this process not viable for industrial purposes. Moreover, working with viscous compositions of high suspension density as is the case in this study, would be incompatible with an industrial scale-up, as it presents stirring and washing constraints. However, this work of enantioselective cocrystallization serves as a case study and the guidelines provided through this example are generalized in Figure 5.9 (step 1) for application to other resolution systems presenting asymmetry in a quaternary phase diagram, such as diastereomeric and enantiospecific cocrystals/salts/solvates. Starting from a racemic compound RS, the working composition ω can be prepared from experimental phase diagram data, with the appropriate amount of chiral coformer K and crystallization solvent O_1. The working composition ω is selected to equilibrate under optimal conditions the stable chiral cocrystal S:K in suspension, which contains the enantiomer of interest, here S. Then, pure S:K can be isolated from solid-liquid separation and the enantiomer S can be recovered from the cocrystal.

The results for the enantiomer recovery by solvent-mediated transformation also highlight the importance of the phase diagrams and the operating conditions when designing such processes. By optimizing parameters such as working temperature and solvent selection, we compute a maximum recovery yield $\rho(\%)$ of 41.9% possible in acetone at 5 °C. This gives prospects for cocrystal deconstruction research to further understand how to recover APIs from their cocrystals, whether they are chiral or not. Our recovery yield $\rho(\%)$ is quite low to be satisfactory for industrial application, as it means 58.1% of levetiracetam (S) remains in the liquid phase when deconstructing the cocrystal at optimal point in this system. Therefore, scaling-up such process by acetone addition at 5 °C does not seem suitable. Nonetheless, the experimental conditions we tried were not at the maximum Δx^T, which is a function of the asymmetry in the phase diagram and thus influences the recovery yield $\rho(\%)$. Systems in which $\Delta x^T > 0.5$ could give high ρ^{max} (%) values above 50 or even 60%. Even higher Δx^T could be envisaged if the molecule of interest and the coformer are very different chemically, making solvents to be a perfect antisolvent for the molecule of interest while showing a very high solubility for the coformer. With the large pool of existing solvents, appropriate deconstruction solvent systems can always be found with a thorough solvent screening, making cocrystal deconstruction by solvent-mediated transformation viable. Moreover, we successfully propose two screening methods to find the deconstruction points D permitting to design enantiomer recovery protocols leading to recovery yield $\rho(\%)$ as close as possible to the maximum value ρ^{max} (%). This works offers prospects and the guidelines provided in this example are generalized in Figure 5.9 (step 2) for all applications of cocrystal deconstructions involving solvents. To the theoretical cocrystal S:K, an optimal amount of deconstruction solvent O_2, chosen from phase diagram information, can be added so that the solid encounters a solvent-mediated transformation towards pure S crystals, while K dissolves in the liquid phase. Then, pure S can be isolated from solid-liquid separation.

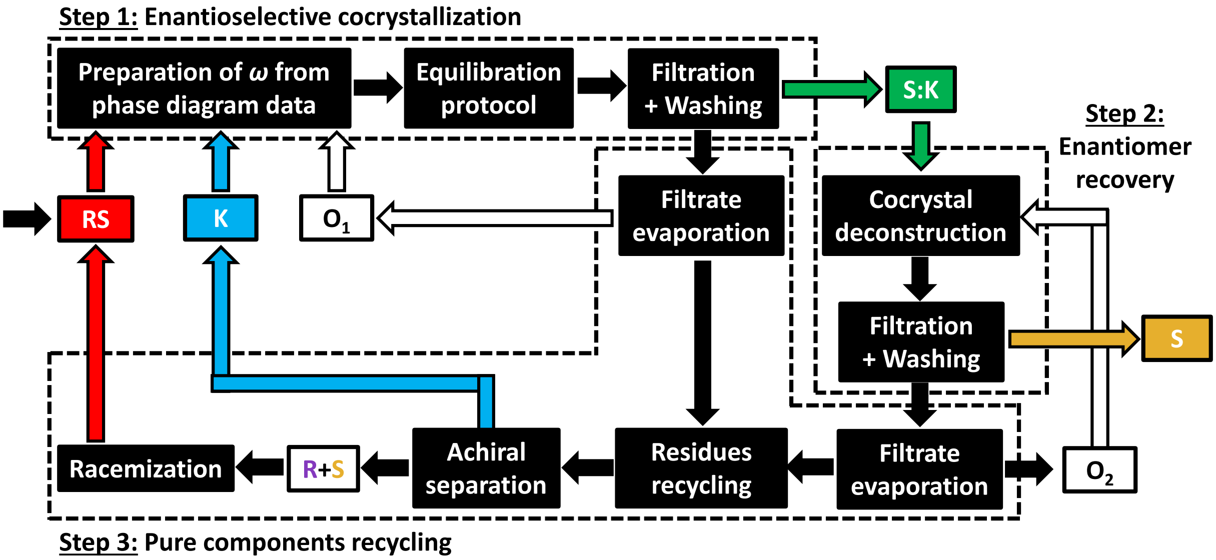

Figure 5.9: Proposed method for the complete chiral separation of a chiral API S. The optimal working composition ω is prepared with the racemic compound RS, the chiral coformer K, and the crystallization solvent O_1, using quaternary phase diagram data. Following an enantioselective cocrystallization process, the chiral cocrystal of S:K is isolated (step 1). Then, a cocrystal deconstruction process, for instance via solvent-mediated transformation, is applied to recover pure S, based on ternary phase diagram data of the preferred enantiomer S, the chiral coformer K and the solvent O_2 (step 2). To minimize losses, the pure components can be recycled (step 3) after each filtration step through the evaporation of the filtrates, and the capture of solvents for reusage. The residues from all evaporated filtrates can be mixed, and by using achiral separation methods such as chromatography or liquid-liquid extraction, the chiral coformer can be recovered and reused from remaining liquids to the preferred enantiomer cocrystals. Moreover, the enantiomers leftovers can be racemized and recrystallized as the racemic compound RS, to cycle the chiral resolution.

The combination of the enantioselective cocrystallization in MeCN at 9°C (resolution yield $R = 46\%$) with the enantiomer recovery by solvent-mediated transformation with minimal amount of acetone at 5°C (recovery yield $\rho = 41.9\%$) would result to a recovery yield $\rho(\%)$ of 19.4 % of the initial S (levetiracetam) contained in its racemic compound RS. Although the experiments show that the preferred enantiomer is successfully obtained, this yield is low, and new conditions should be found to enhance the results. However, as represented in Figure 5.9 (step 3), the combined processes can be cycled without materials loss through pure components recycling, which is an advantage. Indeed, after solid-liquid separations to recover the solid phases of interest, the filtrates can be evaporated, and the solvents captured to be reused in their process step. Contrary to salts, no waste solids are formed during any of the processes as the residues obtained from evaporated filtrates can be recycled as well. By using achiral separation methods, such as chromatography or liquid-liquid extraction, the coformer can be separated from the enantiomers, and regenerated for further use. Moreover, the enantiomer mixtures can be racemized with a racemizing agent, as it is the case for levetiracetam (see Section 5.2), and then crystallized in the form of their racemic compound. The latter can be recycled in the process loop, to cycle the chiral resolution.

5.5. Conclusions

This study provides detailed guidelines related to the exploitation of complex phase diagrams and the separation of chiral molecules with cocrystallization, for efficient processes design. Through the quaternary phase diagram of the two enantiomers and a chiral coformer in a solvent, an enantioselective cocrystallization process was designed to optimize the chiral resolution of levetiracetam from its racemic compound, with the coformer S-mandelic acid, in acetonitrile at 9 °C. An experimental resolution yield $R(\%)$ of 46% recovery percentage of initial S from its RS amount input could be obtained successfully in three experiments by isolation of pure S:S-MA cocrystals under stable conditions, for a theoretical one of 51%. This enhances the results reported in literature for the same system. Additionally, a pure enantiomer recovery process from the cocrystal was designed by solvent-mediated transformation. The theory behind such process was explored, and the selection of optimal conditions was discussed to propose a maximum recovery yield ρ $(\%)$ of 41.9% of initial S from its S:S-MA amount, by isolation of pure S crystals under stable conditions using acetone at 5 °C. Moreover, two successful screening protocols, for the identification of eutectic points and the determination of deconstruction points, were designed. The first protocol uses equilibration experiments to directly find the eutectic composition, and the second uses Raman spectroscopy to detect the complete cocrystal deconstruction. Finally, the unique advantage of cocrystals for separation is highlighted, with their ability to propose complete recycling of the materials during the processes, as no waste is generated.

5.6. Associated content

Supporting Information

The Supporting Information related to this chapter is the Appendix C.

Solvent-free projection in a quaternary phase diagram, quaternary phase diagram data in mass fraction, enantioselective cocrystallization batches results, solubility measurements results, eutectic points E estimations with equilibration method, detection of deconstruction point D with online Raman spectroscopy.

5.7. Acknowledgments

This research received funding as part of the CORE ITN Project by the European Union's Horizon 2020 Research and Innovation Program under the Marie Skłodowska-Curie grant agreement no. 722456 CORE ITN. The authors thank the EPSRC Centre for Innovative Manufacturing in Continuous Manufacturing and Crystallization (http://www.cmac.ac.uk) for support (EPSRC funding under grant reference: EP/I033459/1).

5.8. References

(1) Li, Z. J.; Grant, D. J. Relationship between physical properties and crystal structures of chiral drugs. *Journal of Pharmaceutical Sciences* **1997**, *86* (10), 1073-1078.
(2) Jacques, J.; Collet, A.; Wilen, S. H. *Enantiomers, racemates, and resolutions*; Wiley, 1981.
(3) Nguyen, L. A.; He, H.; Pham-Huy, C. Chiral drugs: an overview. *Int J Biomed Sci* **2006**, *2* (2), 85-100.
(4) Fabro, S.; Smith, R. L.; Williams, R. T. Toxicity and teratogenicity of optical isomers of thalidomide. *Nature* **1967**, *215* (5098), 296.
(5) Reddy, I. K.; Mehvar, R. *Chirality in drug design and development*; CRC Press, 2004.

(6) Saigo, K.; Sakai, K. Resolution of chiral drugs and drug intermediates by crystallisation. *Chirality in drug research* **2006**, 127-154.

(7) Li, Z. J.; Grant, D. J. Relationship between physical properties and crystal structures of chiral drugs. *J Pharm Sci* **1997**, *86* (10), 1073-1078.

(8) Kuusela, E.; Raekallio, M.; Anttila, M.; Falck, I.; Molsa, S.; Vainio, O. Clinical effects and pharmacokinetics of medetomidine and its enantiomers in dogs. *J Vet Pharmacol Ther* **2000**, *23* (1), 15-20.

(9) Ariens, E. J. Stereochemistry, a basis for sophisticated nonsense in pharmacokinetics and clinical pharmacology. *Eur J Clin Pharmacol* **1984**, *26* (6), 663-668.

(10) Solano, D. M.; Hoyos, P.; Hernáiz, M.; Alcántara, A.; Sánchez-Montero, J. Industrial biotransformations in the synthesis of building blocks leading to enantiopure drugs. *Bioresource technology* **2012**, *115*, 196-207.

(11) Kenda, B. M.; Matagne, A. C.; Talaga, P. E.; Pasau, P. M.; Differding, E.; Lallemand, B. I.; Frycia, A. M.; Moureau, F. G.; Klitgaard, H. V.; Gillard, M. R.; et al. Discovery of 4-substituted pyrrolidone butanamides as new agents with significant antiepileptic activity. *J Med Chem* **2004**, *47* (3), 530-549.

(12) Savile, C. K.; Janey, J. M.; Mundorff, E. C.; Moore, J. C.; Tam, S.; Jarvis, W. R.; Colbeck, J. C.; Krebber, A.; Fleitz, F. J.; Brands, J.; et al. Biocatalytic asymmetric synthesis of chiral amines from ketones applied to sitagliptin manufacture. *Science* **2010**, *329* (5989), 305-309.

(13) Blaser, H. U. The chiral pool as a source of enantioselective catalysts and auxiliaries. *Chemical reviews* **1992**, *92* (5), 935-952.

(14) Masamune, S.; Choy, W.; Petersen, J. S.; Sita, L. R. Double asymmetric synthesis and a new strategy for stereochemical control in organic synthesis. *Angewandte Chemie International Edition in English* **1985**, *24* (1), 1-30.

(15) Ager, D. J.; Prakash, I.; Schaad, D. R. 1, 2-Amino alcohols and their heterocyclic derivatives as chiral auxiliaries in asymmetric synthesis. *Chemical Reviews* **1996**, *96* (2), 835-876.

(16) Noyori, R. Asymmetric catalysis: science and opportunities (Nobel lecture). *Angew Chem Int Ed Engl* **2002**, *41* (12), 2008-2022.

(17) Caner, H.; Groner, E.; Levy, L.; Agranat, I. Trends in the development of chiral drugs. *Drug Discov Today* **2004**, *9* (3), 105-110.

(18) Sheldon, R. A. *Chirotechnology: industrial synthesis of optically active compounds*; CRC press, 1993.

(19) Beesley, T. E.; Scott, R. P. *Chiral chromatography*; John Wiley & Sons, 1999.

(20) van der Meijden, M. W.; Leeman, M.; Gelens, E.; Noorduin, W. L.; Meekes, H.; van Enckevort, W. J. P.; Kaptein, B.; Vlieg, E.; Kellogg, R. M. Attrition-Enhanced Deracemization in the Synthesis of Clopidogrel - A Practical Application of a New Discovery. *Organic Process Research & Development* **2009**, *13* (6), 1195-1198.

(21) Suwannasang, K.; Flood, A. E.; Coquerel, G. A Novel Design Approach To Scale Up the Temperature Cycle Enhanced Deracemization Process: Coupled Mixed-Suspension Vessels. *Crystal Growth & Design* **2016**, *16* (11), 6461-6467.

(22) Belletti, G.; Tortora, C.; Mellema, I. D.; Tinnemans, P.; Meekes, H.; Rutjes, F.; Tsogoeva, S. B.; Vlieg, E. Photoracemization-Based Viedma Ripening of a BINOL Derivative. *Chemistry* **2020**, *26* (4), 839-844.

(23) Sakai, K.; Hirayama, N.; Tamura, R. *Novel optical resolution technologies*; Springer, 2007.

(24) Suwannasang, K.; Flood, A. E.; Rougeot, C.; Coquerel, G. Using Programmed Heating–Cooling Cycles with Racemization in Solution for Complete Symmetry Breaking of a Conglomerate Forming System. *Crystal Growth & Design* **2013**, *13* (8), 3498-3504.

(25) Li, W. W.; Spix, L.; de Reus, S. C. A.; Meekes, H.; Kramer, H. J. M.; Vlieg, E.; ter Horst, J. H. Deracemization of a Racemic Compound via Its Conglomerate-Forming Salt Using Temperature Cycling. *Crystal Growth & Design* **2016**, *16* (9), 5563-5570.
(26) Sogutoglu, L. C.; Steendam, R. R.; Meekes, H.; Vlieg, E.; Rutjes, F. P. Viedma ripening: a reliable crystallisation method to reach single chirality. *Chem Soc Rev* **2015**, *44* (19), 6723-6732.
(27) Buol, X.; Caro Garrido, C.; Robeyns, K.; Tumanov, N.; Collard, L.; Wouters, J.; Leyssens, T. Chiral Resolution of Mandelic Acid through Preferential Cocrystallization with Nefiracetam. *Crystal Growth & Design* **2020**, *20* (12), 7979-7988.
(28) Lorenz, H.; Seidel-Morgenstern, A. Processes to separate enantiomers. *Angew Chem Int Ed Engl* **2014**, *53* (5), 1218-1250.
(29) Kellogg, R. M. Practical Stereochemistry. *Acc Chem Res* **2017**, *50* (4), 905-914.
(30) Maggioni, G. M.; Fernández-Ronco, M. P.; van der Meijden, M. W.; Kellogg, R. M.; Mazzotti, M. Solid state deracemisation of two imine-derivatives of phenylglycine derivatives via high-pressure homogenisation and temperature cycles. *CrystEngComm* **2018**, *20* (27), 3828-3838.
(31) Breveglieri, F.; Maggioni, G. M.; Mazzotti, M. Deracemization of NMPA via Temperature Cycles. *Crystal Growth & Design* **2018**, *18* (3), 1873-1881.
(32) Belletti, G.; Meekes, H.; Rutjes, F.; Vlieg, E. Role of Additives during Deracemization Using Temperature Cycling. *Cryst Growth Des* **2018**, *18* (11), 6617-6620.
(33) Levilain, G.; Coquerel, G. Pitfalls and rewards of preferential crystallization. *CrystEngComm* **2010**, *12* (7), 1983-1992.
(34) Harfouche, L. C.; Brandel, C.; Cartigny, Y.; Ter Horst, J. H.; Coquerel, G.; Petit, S. Enabling Direct Preferential Crystallization in a Stable Racemic Compound System. *Mol Pharm* **2019**, *16* (11), 4670-4676.
(35) Harmsen, B.; Leyssens, T. Enabling Enantiopurity: Combining Racemization and Dual-Drug Co-crystal Resolution. *Crystal Growth & Design* **2018**, *18* (6), 3654-3660.
(36) Guillot, M.; de Meester, J.; Huynen, S.; Collard, L.; Robeyns, K.; Riant, O.; Leyssens, T. Cocrystallization-Induced Spontaneous Deracemization: A General Thermodynamic Approach to Deracemization. *Angew Chem Int Ed Engl* **2020**, *59* (28), 11303-11306.
(37) Wouters, J.; Quéré, L. *Pharmaceutical salts and co-crystals*; Royal Society of Chemistry, 2011.
(38) Bond, A. D. What is a co-crystal? *CrystEngComm* **2007**, *9* (9), 833-834.
(39) Alhalaweh, A.; George, S.; Basavoju, S.; Childs, S. L.; Rizvi, S. A. A.; Velaga, S. P. Pharmaceutical cocrystals of nitrofurantoin: screening, characterization and crystal structure analysis. *CrystEngComm* **2012**, *14* (15), 5078-5088.
(40) Almarsson, Ö.; Zaworotko, M. J. Crystal engineering of the composition of pharmaceutical phases. Do pharmaceutical co-crystals represent a new path to improved medicines? *Chemical communications* **2004**, (17), 1889-1896.
(41) Aakeröy, C. B.; Salmon, D. J. Building co-crystals with molecular sense and supramolecular sensibility. *CrystEngComm* **2005**, *7*, 439-448.
(42) Aitipamula, S.; Banerjee, R.; Bansal, A. K.; Biradha, K.; Cheney, M. L.; Choudhury, A. R.; Desiraju, G. R.; Dikundwar, A. G.; Dubey, R.; Duggirala, N. Polymorphs, salts, and cocrystals: what's in a name? *Crystal growth & design* **2012**, *12* (5), 2147-2152.
(43) Grothe, E.; Meekes, H.; Vlieg, E.; Ter Horst, J.; de Gelder, R. d. Solvates, salts, and cocrystals: a proposal for a feasible classification system. *Crystal Growth & Design* **2016**, *16* (6), 3237-3243.

(44) Devogelaer, J. J.; Charpentier, M. D.; Tijink, A.; Dupray, V.; Coquerel, G.; Johnston, K.; Meekes, H.; Tinnemans, P.; Vlieg, E.; Ter Horst, J. H.; et al. Cocrystals of Praziquantel: Discovery by Network-Based Link Prediction. *Cryst Growth Des* **2021**, *21* (6), 3428-3437.
(45) Charpentier, M. D.; Devogelaer, J. J.; Tijink, A.; Meekes, H.; Tinnemans, P.; Vlieg, E.; de Gelder, R.; Johnston, K.; Ter Horst, J. H. Comparing and Quantifying the Efficiency of Cocrystal Screening Methods for Praziquantel. *Cryst Growth Des* **2022**, *22* (9), 5511-5525.
(46) Li, W.; De Groen, M.; Kramer, H. J.; De Gelder, R.; Tinnemans, P.; Meekes, H.; Ter Horst, J. H. Screening approach for identifying cocrystal types and resolution opportunities in complex chiral multicomponent systems. *Crystal Growth & Design* **2020**, *21* (1), 112-124.
(47) Shefter, E.; Higuchi, T. Dissolution Behavior of Crystalline Solvated and Nonsolvated Forms of Some Pharmaceuticals. *J Pharm Sci* **1963**, *52* (8), 781-791.
(48) Shevchenko, A.; Miroshnyk, I.; Pietila, L. O.; Haarala, J.; Salmia, J.; Sinervo, K.; Mirza, S.; van Veen, B.; Kolehmainen, E.; Nonappa; et al. Diversity in Itraconazole Cocrystals with Aliphatic Dicarboxylic Acids of Varying Chain Length. *Crystal Growth & Design* **2013**, *13* (11), 4877-4884.
(49) Lin, Y.; Yang, H.; Yang, C.; Wang, J. Preparation, characterization, and evaluation of dipfluzine-benzoic acid co-crystals with improved physicochemical properties. *Pharm Res* **2014**, *31* (3), 566-578.
(50) Remenar, J. F.; Morissette, S. L.; Peterson, M. L.; Moulton, B.; MacPhee, J. M.; Guzman, H. R.; Almarsson, O. Crystal engineering of novel cocrystals of a triazole drug with 1,4-dicarboxylic acids. *J Am Chem Soc* **2003**, *125* (28), 8456-8457.
(51) Schultheiss, N.; Newman, A. Pharmaceutical Cocrystals and Their Physicochemical Properties. *Cryst Growth Des* **2009**, *9* (6), 2950-2967.
(52) Friscic, T.; Jones, W. Benefits of cocrystallisation in pharmaceutical materials science: an update. *J Pharm Pharmacol* **2010**, *62* (11), 1547-1559.
(53) Urbanus, J.; Roelands, C. P. M.; Verdoes, D.; Jansens, P. J.; ter Horst, J. H. Co-Crystallization as a Separation Technology: Controlling Product Concentrations by Co-Crystals. *Crystal Growth & Design* **2010**, *10* (3), 1171-1179.
(54) Harfouche, L. C.; Couvrat, N.; Sanselme, M.; Brandel, C.; Cartigny, Y.; Petit, S.; Coquerel, G. Discovery of New Proxyphylline-Based Chiral Cocrystals: Solid State Landscape and Dehydration Mechanism. *Crystal Growth & Design* **2020**, *20* (6), 3842-3850.
(55) Neurohr, C.; Marchivie, M.; Lecomte, S.; Cartigny, Y.; Couvrat, N.; Sanselme, M.; Subra-Paternault, P. Naproxen–Nicotinamide Cocrystals: Racemic and Conglomerate Structures Generated by CO2 Antisolvent Crystallization. *Crystal Growth & Design* **2015**, *15* (9), 4616-4626.
(56) Springuel, G.; Leyssens, T. Innovative chiral resolution using enantiospecific co-crystallization in solution. *Crystal growth & design* **2012**, *12* (7), 3374-3378.
(57) Harmsen, B.; Leyssens, T. Dual-Drug Chiral Resolution: Enantiospecific Cocrystallization of (S)-Ibuprofen Using Levetiracetam. *Crystal Growth & Design* **2017**, *18* (1), 441-448.
(58) Springuel, G.; Robeyns, K.; Norberg, B.; Wouters, J.; Leyssens, T. Cocrystal Formation between Chiral Compounds: How Cocrystals Differ from Salts. *Crystal Growth & Design* **2014**, *14* (8), 3996-4004.
(59) Springuel, G.; Collard, L.; Leyssens, T. Ternary and quaternary phase diagrams: key tools for chiral resolution through solution cocrystallization. *Crystengcomm* **2013**, *15* (39), 7951-7958.
(60) Sánchez-Guadarrama, O.; Mendoza-Navarro, F.; Cedillo-Cruz, A.; Jung-Cook, H.; Arenas-García, J. I.; Delgado-Díaz, A.; Herrera-Ruiz, D.; Morales-Rojas, H.; Höpfl, H. Chiral resolution

of RS-praziquantel via diastereomeric co-crystal pair formation with L-malic acid. *Crystal Growth & Design* **2016**, *16* (1), 307-314.

(61) Braga, D.; Casali, L.; Grepioni, F. The Relevance of Crystal Forms in the Pharmaceutical Field: Sword of Damocles or Innovation Tools? *International Journal of Molecular Sciences* **2022**, *23* (16), 9013.

(62) Harmsen, B.; Leyssens, T. Dual-drug chiral resolution: enantiospecific cocrystallization of (s)-ibuprofen using levetiracetam. *Crystal Growth & Design* **2018**, *18* (1), 441-448.

(63) Springuel, G.; Norberg, B.; Robeyns, K.; Wouters, J.; Leyssens, T. Advances in Pharmaceutical Co-crystal Screening: Effective Co-crystal Screening through Structural Resemblance. *Crystal Growth & Design* **2011**, *12* (1), 475-484.

(64) Wang, J.; Peng, Y. Resolution of Halogenated Mandelic Acids through Enantiospecific Co-Crystallization with Levetiracetam. *Molecules* **2021**, *26* (18), 5536.

(65) Nulek, T.; Klaysri, R.; Cedeno, R.; Nalaoh, P.; Bureekaew, S.; Promarak, V.; Flood, A. E. Separation of Etiracetam Enantiomers Using Enantiospecific Cocrystallization with 2-Chloromandelic Acid. *ACS Omega* **2022**,

(66) Zhou, F.; Shemchuk, O.; Charpentier, M. D.; Matheys, C.; Collard, L.; Ter Horst, J. H.; Leyssens, T. Simultaneous chiral resolution of two racemic compounds by preferential cocrystallization. *Angewandte Chemie International Edition* **2021**, *60* (37), 20264-20268.

(67) Charpentier, M. D.; Venkatramanan, R.; Rougeot, C.; Leyssens, T.; Johnston, K.; ter Horst, J. H. Multicomponent Chiral Quantification with Ultraviolet Circular Dichroism Spectroscopy: Ternary and Quaternary Phase Diagrams of Levetiracetam. *Molecular Pharmaceutics* **2023**, *20* (1), 616-629.

(68) Leyssens, T.; ter Horst, J. H. 9. Solution co-crystallisation and its applications. In *Multi-Component Crystals*, De Gruyter, 2017; pp 205-236.

(69) Urbanus, J.; Roelands, C. M.; Verdoes, D.; Jansens, P. J.; ter Horst, J. H. Co-crystallization as a separation technology: controlling product concentrations by co-crystals. *Crystal growth & design* **2010**, *10* (3), 1171-1179.

(70) Roa Engel, C. A.; Straathof, A. J.; Zijlmans, T. W.; van Gulik, W. M.; van der Wielen, L. A. Fumaric acid production by fermentation. *Applied microbiology and biotechnology* **2008**, *78* (3), 379-389.

(71) Urbanus, J.; Roelands, C. M.; Mazurek, J.; Verdoes, D.; ter Horst, J. H. Electrochemically induced co-crystallization for product removal. *CrystEngComm* **2011**, *13* (8), 2817-2819.

(72) Urbanus, J.; Roelands, C.; Verdoes, D.; Ter Horst, J. Intensified crystallization in complex media: Heuristics for crystallization of platform chemicals. *Chemical engineering science* **2012**, *77*, 18-25.

(73) Urbanus, J. Product removal by in-situ crystallization. **2001**,

(74) Bethune, S. J.; Huang, N.; Jayasankar, A.; Rodriguez-Hornedo, N. Understanding and predicting the effect of cocrystal components and pH on cocrystal solubility. *Crystal Growth & Design* **2009**, *9* (9), 3976-3988.

(75) Herman, C.; Vermylen, V.; Norberg, B.; Wouters, J.; Leyssens, T. The importance of screening solid-state phases of a racemic modification of a chiral drug: thermodynamic and structural characterization of solid-state phases of etiracetam. *Acta Crystallogr B Struct Sci Cryst Eng Mater* **2013**, *69* (Pt 4), 371-378.

(76) Savitzky, A.; Golay, M. J. E. Smoothing and Differentiation of Data by Simplified Least Squares Procedures. *Analytical Chemistry* **2002**, *36* (8), 1627-1639.

(77) Alexandris, N.; Gupta, S.; Koutsias, N. Remote sensing of burned areas via PCA, Part 1; centering, scaling and EVD vs SVD. *Open geospatial data, software and standards* **2017**, *2* (1), 1-11.

(78) Ricci, J. E. *phase rule and heterogeneous equilibrium*; 1951.

(79) Grozdev, S.; Dekov, D. Barycentric coordinates: formula sheet. *International Journal of Computer Discovered Mathematics* **2016**, *1* (2), 75-82.

(80) Volenec, V. Metrical relations in barycentric coordinates. *Mathematical Communications* **2003**, *8* (1), 55-68.

(81) Ter Horst, J.; Deij, M.; Cains, P. Discovering new co-crystals. *Crystal Growth & Design* **2009**, *9* (3), 1531-1537.

(82) Chiarella, R. A.; Davey, R. J.; Peterson, M. L. Making Co-CrystalsThe Utility of Ternary Phase Diagrams. *Crystal Growth & Design* **2007**, *7* (7), 1223-1226.

(83) Childs, S. L.; Rodriguez-Hornedo, N.; Reddy, L. S.; Jayasankar, A.; Maheshwari, C.; McCausland, L.; Shipplett, R.; Stahly, B. C. Screening strategies based on solubility and solution composition generate pharmaceutically acceptable cocrystals of carbamazepine. *Crystengcomm* **2008**, *10* (7), 856-864.

(84) Rodríguez-Hornedo, N.; Nehm, S. J.; Seefeldt, K. F.; Pagán-Torres, Y.; Falkiewicz, C. J. Reaction Crystallization of Pharmaceutical Molecular Complexes. *Molecular Pharmaceutics* **2006**, *3* (3), 362-367.

(85) Leyssens, T.; Springuel, G.; Montis, R.; Candoni, N.; Veesler, S. p. Importance of solvent selection for stoichiometrically diverse cocrystal systems: caffeine/maleic acid 1: 1 and 2: 1 cocrystals. *Crystal growth & design* **2012**, *12* (3), 1520-1530.

(86) Ainouz, A.; Authelin, J.-R.; Billot, P.; Lieberman, H. Modeling and prediction of cocrystal phase diagrams. *International journal of pharmaceutics* **2009**, *374* (1-2), 82-89.

(87) Svoboda, V.; Venkatramanan, R.; Jaap, M.; Lue, L.; ter Horst, J. H.; Sefcik, J. Co-crystal Phase Diagram Determination by the Solution Addition Method. *Crystal Growth & Design* **2022**, *22* (5), 3376-3384.

Chapter 6 - Cocrystallization Opportunities for Chiral Resolution of Racemic Compounds

Maxime D. Charpentier[1], Karen Johnston[2], Joop H. ter Horst[1,3]

1. EPSRC Centre for Innovative Manufacturing in Continuous Manufacturing and Crystallization (CMAC), Strathclyde Institute of Pharmacy and Biomedical Sciences (SIPBS), University of Strathclyde

2. Department of Chemical and Process Engineering, University of Strathclyde, James Weir Building, 75 Montrose Street, Glasgow G1 1XJ, U.K.

3. Univ Rouen Normandie, Laboratoire Sciences et Méthodes Séparatives (SMS), UR 3233, F-76000 Rouen, France

Abstract

Chiral resolution by cocrystallization provides a relevant collection of strategies when racemic enantiomer mixtures crystallize as racemic compounds. Nonetheless, the enantiomers can interact in many ways with the coformers, and not all scenarios lead to thermodynamic systems permitting the chiral separation. This study proposes the key points about the cocrystallization of enantiomers that allow to understand the parameters leading to a quick and efficient identification of the optimal resolution strategy. A viable strategy can be developed if in the used system the enantiopure phase is thermodynamically more stable than the racemic compound. Therefore, the relative stability of the racemic compound versus the enantiopure phases is important to consider for the conglomerate screening strategy with achiral coformers, as some racemic structures are difficult to convert into separate chiral ones despite large numbers of new cocrystals screened. When facing such issues, the chiral cocrystallization should be considered by using a chiral coformer instead. However, the coformer selection methods present limitations to suggest chiral molecules, and the increased complexity in the resulting thermodynamic systems can appear as a barrier, which leads to an underrepresentation of chiral cocrystallization as a resolution strategy. Therefore, we structure all possible cocrystallization scenarios for a stable racemic compound system when using achiral molecules, chiral molecules, and racemic mixtures as coformer material. For each scenario identified, we discuss on their assessment from cocrystal screening results, and conclude on the chiral resolution possibilities they present. The guidelines facilitate the design of a chiral resolution by cocrystallization.

6.1. Introduction

Chiral molecules are exempted from symmetry elements, and from each center of dissymmetry emerge enantiomers, that are a pair of non-superimposable mirror-image compounds. Enantiomers exhibit some enantiopure physical and chemical properties that are identical, as melting temperature and solubility, or symmetrical, like their interaction with polarized light.[1] However, in a chiral environment such as the human body, enantiomers present different biological properties because of the asymmetric configuration of biochemical receptors, enzymes or proteins. Only the wanted enantiomer can interact with the targeted receptor to trigger the desired therapeutic effect, while the counter-enantiomer can be inactive, different in its pharmacological activity, or even produce unwanted side effects.[2-7] In addition to toxicity risks, economic consequences emerge from the presence of the counter-enantiomer in a racemic drug that can be considered as an impurity representing up to 50% of the formulation.[8] Over 50% of active pharmaceutical ingredients (APIs) in the pharmaceutical industry are chiral molecules and important problematics have developed around their separation, through a preferred marketing of enantiopure drugs.[9-11] Asymmetric syntheses allow to produce enantiopure APIs,[12-16] but this production route is not always available and tend to be expensive.[17] The achiral syntheses routes lead to racemic mixtures to be separated by methods like chiral chromatography or crystallization, with crystallization being preferred because of more interesting costs.[17-21] Therefore, it is essential to understand the crystallization equilibria involving enantiomers, with the view to apply crystallization-based separation technologies.

The problematic of chiral separation originates from the different equilibria possibilities for a racemic mixture to crystallize. In this study, we focus only on the two most common crystallization scenarios, that are the formation of a racemic compound or a conglomerate.[1] Racemic compounds, which occur in 90-95% of cases, are crystals made of an equimolar association of both enantiomers in the unit-cell. In this case, any of the symmetry operations from crystallography is compatible with the crystallization of a racemic compound, which makes all 230 space groups available.[22] Nonetheless, most racemic compounds exhibit centrosymmetric space groups, which possess elements of inverse symmetry, with 95% of racemic compound structures represented by the space groups $P2_1/c$, $P\overline{1}$, $Pbca$ and $C2/c$.[23] In racemic crystal structures, it can be considered that enantiomers have a greater affinity with their mirror-image than with themselves.[24] The separation of enantiomers is difficult when they crystallize as racemic compounds, as feasible processes rely on kinetics.[25, 26] Conglomerates, which occur in 5-10% of cases, are physical mixtures of separated enantiopure crystals. Among the 230 space groups, only 65 are non-centrosymmetric as they lack reflection and inversion symmetry, and they are the only ones compatible with the crystallization of a pure enantiomer.[27, 28] Statistical studies highlight that 95% of all enantiomers crystallize in only four space groups that are $P2_12_12_1$, $P2_1$, $C2$ and $P1$.[23] The formation of such chiral structures can be considered to be because of enantiomers having a greater affinity with themselves than for the counter-enantiomer. Conglomerates are favorable systems to design chiral resolution processes.[29-39] Therefore, the detection of chiral crystals with appropriate techniques is key for the screening of resolution possibilities.[40] It can be done through phase diagram constructions but it requires a lot of work. Most of time, spectroscopic data are compared between the racemic mixture and the pure enantiomer with techniques such as infrared spectroscopy, Raman spectroscopy, X-ray diffraction, solid-state nuclear magnetic resonance, or terahertz spectroscopy. Furthermore, nonlinear optics methods such as second harmonic generation (SHG) are very convenient to screen for potential conglomerates, as non-centrosymmetric crystals illuminated by laser pulses convert a part of the energy to the generation of the second harmonic.[41] Despite little chances for racemic crystals to occur in non-centrosymmetric space groups, SHG is very promising for automation and quick pre-screening of chiral crystals. However, the reasons why a chiral molecule would crystallize as a racemic compound or a conglomerate, are not yet understood. It constitutes a major topic of research, through the investigation of thermodynamic and crystallographic data, with the view to predict the most likely outcomes for a new chiral molecule.

When a given chiral molecule crystallizes as a racemic compound, different crystallization equilibria must be found to allow the chiral resolution. For instance, the chemical modification of the achiral part of the molecule can prompt new chances to obtain a conglomerate system, though it requires many steps. Another strategy relies on the engineering of multicomponent crystals with an additional molecule, to form salts, solvates or cocrystals.[42, 43] Commonly, diastereomeric salts are formed and separated by exploiting physical properties differences, but it requires the former molecule to be ionizable.[35] On the contrary, cocrystallization and solvate formation are always possible because they rely on intermolecular interactions like hydrogen bonds.[44, 45] Resolution by cocrystal formation has become a major topic because of the emergence of many cocrystal preparation methods that facilitate their prediction and screening.[46-52] As represented schematically in Figure 6.1, using an achiral coformer with a racemic compound can result in the formation of either a racemic cocrystal or a conglomerate of enantiopure cocrystals.[53, 54] However, the outcomes for chiral resolution are more favorable by using a chiral coformer, that can generate a diastereomeric pair of enantiopure cocrystals, or an enantiospecific cocrystal.[42, 43, 55, 56] Nonetheless, this research area is constantly expanding and the cocrystallization scenarios, their occurrence, and the influence of coformer choice, must be investigated to highlight the best resolution opportunities.

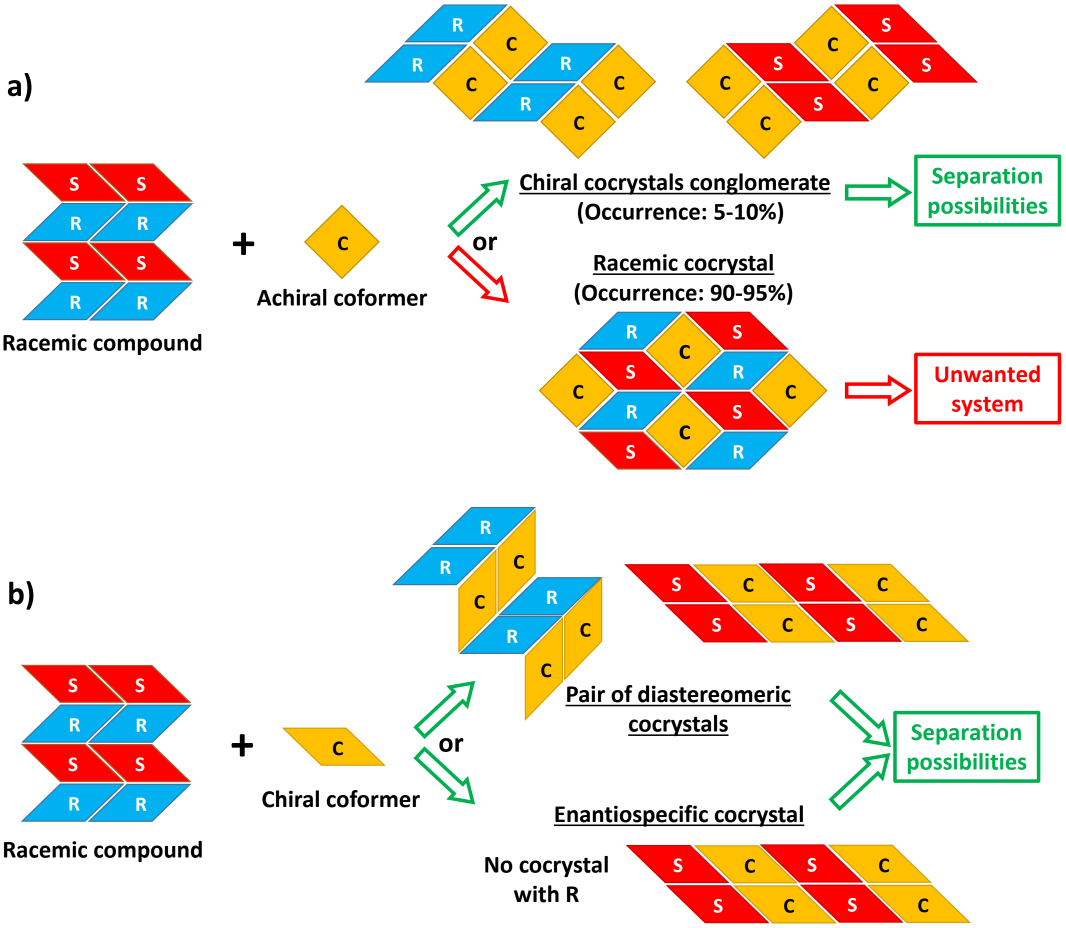

Figure 6.1: Cocrystallization scenarios that lead to resolution opportunities for a racemic compound API using **a)** an achiral coformer **b)** a chiral coformer.

In this chapter, we aim to identify a structured approach to transform racemic compounds into chiral crystals to permit the chiral resolution by cocrystallization. First, we investigate the relative stabilities of racemic compounds through the construction and analysis of a thermal database of chiral systems. Then, we discuss on the importance and limitations of the coformer selection methods, especially for chiral coformers that are less considered in resolution studies. Finally, we review crystallization scenarios that lead to different thermodynamic system outcomes, and we link them with chiral resolution opportunities. By discussing major results from previous chapters, we propose new guidelines for the chiral resolution possibilities of stable racemic compounds with cocrystallization.

6.2. Relative Stability of Racemic Compounds and Conglomerates

A detailed study in 2020 from Rekis on chiral compound structures found in the Cambridge Structural Database (CSD) estimates the occurrence of conglomerates among crystallizing racemic mixtures to be of about 9.5%.[22] However, it is highlighted by Viedma, Coquerel and Cintas, that this number should not always be considered as a statistical chance because of observed trends in conglomerate formation.[40] Indeed, they underline that derivatives of 5-aryl-5-alkyl hydantoins and 4-aryl-triazolyl ketones, as well as *trans*-cinnamate salts of 1-amino-alkan-2-ols, constitute clusters of numerous conglomerates. On the contrary, many conglomerate screening studies for chiral resolution relate of the difficulty to find a conglomerate by formation of chemical derivatives or multicomponent crystals, as most of newly formed crystals are racemic. Furthermore, a statistical analysis by Jacques et al., that required the preparation of more than 500 salts, estimates an occurrence of conglomerates that is 2 to 3 times higher for salts than covalent compounds.[57] All these different variations in conglomerates occurrence, demonstrate that there are reasons that can be understood, about why a chiral molecule would crystallize or not as a conglomerate. In some cases, it can be explained through the comparison of crystal structures, such as for acidic salts of achiral dicarboxylic acids with α-phenylethylamine, for which the presence of hydrogen-bonded chains are identified in the conglomerate, compared to intermolecular hydrogen-bonded dimers in the racemic crystals.[58] Crystal structure prediction tools also help to compute the possible structures for a given chiral system, with the view to estimate which has the lowest lattice energy between the lowest-energy racemic structure and the lowest-energy enantiopure structure.[59] However, structural analyses can be system-dependent and require time-consuming computations, with sometimes uncertain accuracy. Up to now, there are no identified general trends linking molecular and structural data to predict if a new chiral molecule would more likely crystallize as a conglomerate or a racemic compound.

6.2.1. Thermodynamic Data of Chiral Systems

A possibility to identify trends in conglomerate occurrence is to consider the thermodynamic data of chiral systems, such as melting and solubility data, which are also function of how enantiomers are bonding in the structures. Thermal data, like melting temperatures and enthalpies, are the focus of this study, because they are easily accessible with analytical techniques such as Differential Scanning Calorimetry (DSC) or Differential Thermal Analysis (DTA). For a matter of clarity, all data associated to pure enantiomers are expressed in relation to enantiomer R in this study, because of identical thermal data between pure R and S. Consequently, the melting temperature of the pure enantiomer is T_R^f (K), and its melting enthalpy ΔH_R^f (J.mol^{-1}). For mixture of enantiomers, we define a specific composition by its molar fraction x_S in S, as for instance $T_{x_S}^f$, the melting temperature at composition x_S. Therefore, at racemic composition, $x_S = 0.5$, and the melting temperature of the stable racemic mixture is $T_{0.5}^f$and its melting enthalpy $\Delta H_{0.5}^f$. When the racemic mixture crystallizes as a stable racemic compound, $T_{0.5}^f = T_{RS}^f$ and $\Delta H_{0.5}^f = \Delta H_{RS}^f$. The conglomerate between R and S, whether it is stable or metastable, is always characterized as a eutectic crystallization equilibrium at $x_S^{eut} = 0.5$, whose eutectic melting temperature is T_{R+S}^{eut} and its enthalpy ΔH_{R+S}^{eut}. All thermal information is comprised in the binary melting phase diagrams between enantiomers, that are schematically represented in Figure 6.2. In the case of a stable conglomerate (Figure 6.2, left), $T_{0.5}^f = T_{R+S}^{eut}$ is always lower than T_R^f, and solid-liquid stability curves of enantiopure crystals are defined by the simplified Schröder-Van Laar equation[1] (Equation 6.1), with *R* the universal gas constant (8.314 J.mol^{-1}.K^{-1}).

$$\ln(x_S) = \frac{\Delta H_R^f}{R}\left(\frac{1}{T_R^f} - \frac{1}{T_{x_S}^f}\right) \qquad \text{Equation 6.1}$$

In the case of stable racemic compounds, the enantiomers binary systems can be seen as two symmetrical eutectic equilibria between the racemic compound RS and an enantiomer, along the racemic composition (Figure 6.2). The solid-liquid stability curves of the racemic compound RS are here defined by the Prigorine-Defay equation[1] (Equation 6.2). The eutectic invariant information between R and RS, of composition x_S^{eut}, eutectic melting temperature is T_{R+RS}^{eut}, and eutectic melting enthalpy ΔH_{R+RS}^{eut}, can be estimated by equalization of Equation 6.1 and Equation 6.2. Both equations assume the immiscibility in the solid state, and the ideality of mixtures in the liquid state.

$$\ln 4x_S(1 - x_S) = \frac{2\Delta H_{RS}^f}{R}\left(\frac{1}{T_{RS}^f} - \frac{1}{T_{x_S}^f}\right) \qquad \text{Equation 6.2}$$

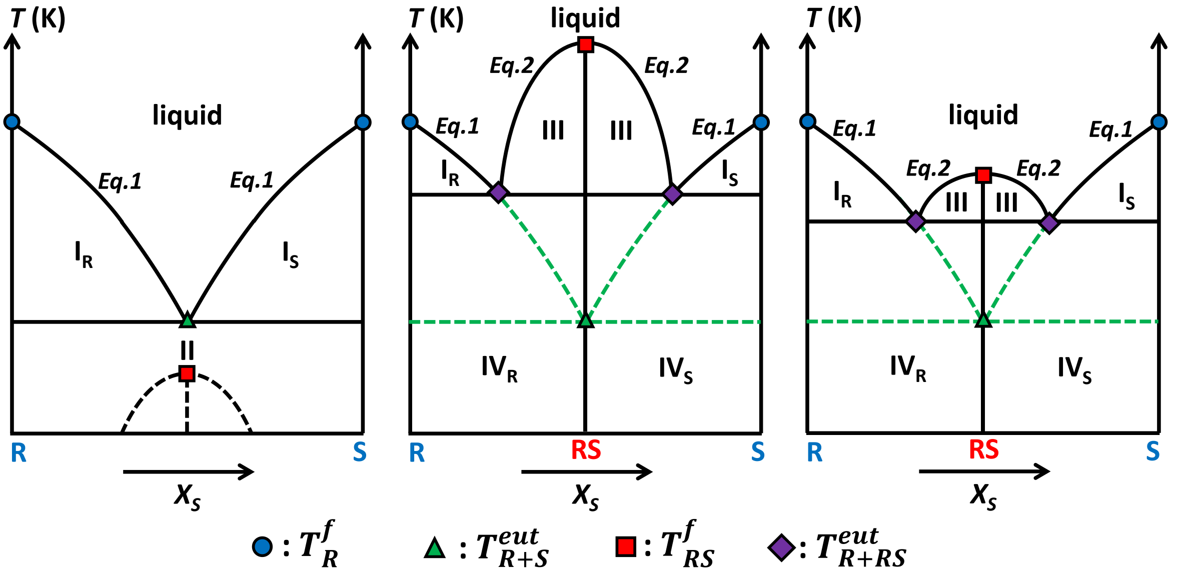

Figure 6.2: Binary melting phase diagrams between enantiomers in the case of a stable conglomerate (left), a stable racemic compound whose melting point is higher than the pure enantiomer crystals (middle), and a stable racemic compound whose melting point is lower than the pure enantiomer crystals. Regions I_R, I_S, and III are the biphasic stability domains in which an overall composition phase splits into a saturated liquid and respectively the solids R, S, and RS. Regions II, IV_R, and IV_S are the biphasic stability domains in which an overall composition phase splits between respectively, R and S solids, R and RS solids, RS and S solids. Metastable equilibria are represented by dashed lines.

The relative stability of the racemic compound structure compared to the enantiopure crystals varies consequently depending on the chiral system. Indeed, T_{RS}^f can be higher than T_R^f (Figure 6.2, middle), lower (Figure 6.2, right), or even identical.[60] Approaches to discuss the relative stability of racemic compounds are often discussed in the literature. Petterson comments on the stability of the racemic compound with the width of its stability zone (Figure 6.2, region IV), arguing that the closer x_S^{eut} is to racemic composition, the less stable it is. The eutectic composition position is often linked to the melting point differences $(T_{RS}^f - T_{R+RS}^{eut})$ or $(T_{RS}^f - T_R^f)$, and Petterson defines an arbitrary criterium i (Equation 6.3) to evaluate the relative stability of racemic compounds. He describes three different cases, with i lower than 0.5 characterizing a small tendency to form a racemic compound, i comprised between 0.5 and 1.5 a moderate stability, and i higher than 1.5 a racemic compound of high stability.[1, 61]

$$i = \frac{T_{RS}^{f} - T_{R+RS}^{eut}}{T_{R}^{f} - T_{R+RS}^{eut}} \qquad \text{Equation 6.3}$$

Leclercq et al. underline the arbitrary aspect of such values but agree on the relevance of such parameter linking the relative stability of racemic compounds with melting temperatures.[62] They highlight that rigorously, the stability of a racemic compound can only be defined by the free energy change ΔG^0 associated with the process of combining the R and S solids to produce the RS solid (Equation 6.4).

$$R_{solid} + S_{solid} \overset{\Delta G^0}{\Longleftrightarrow} RS_{solid} \qquad \text{Equation 6.4}$$

ΔG^0 can be expressed as a function of the enthalpy variation ΔH^0 and entropy variation ΔS^0(Equation 6.5) associated to Equation 6.4. When ΔG^0 is negative, it indicates the racemic compound formation is favored. ΔH^0 and ΔS^0 can be deduced from thermal data, and by experimental application on a wide range of chiral systems, Leclercq et al. report a proportionality link between ΔG^0 and $(T_{RS}^{f} - T_{R}^{f})$.[62]

$$\Delta G^0 = \Delta H^0 - T\Delta S^0 \qquad \text{Equation 6.5}$$

Li et al. confirm this proportionality and estimates that for values of $(T_{RS}^{f} - T_{R}^{f})$ below -30 K, the ΔG^0 values become approximately zero, indicating that the racemic compound and the conglomerate possess similar relative stabilities.[63] Leclercq et al. were also indicating that values of $(T_{0.5}^{f} - T_{R}^{f})$ below -20 K generally correspond to stable conglomerate systems.[62] Despite the thermodynamic approximations made and the arbitrary values, most of thermodynamic studies highlight the apparent link between the crystallization equilibria of a chiral system, and the melting temperatures of its racemic mixture $T_{0.5}^{f}$ and enantiopure crystal T_{R}^{f}. Therefore, we think some trends can be identified by looking at many chiral systems through these easily accessible data.

6.2.2. Generation and Analysis of a Database of Chiral Systems

According to relevant literature articles, a thermodynamic database of chiral systems was created, with the view to analyze a high number of conglomerates and racemic compound systems and compare their relative stabilities. Presented in the Appendix D Table D1, the database lists chiral systems by their IUPAC (International Union of Pure and Applied Chemistry) names, usual names, stable crystallization equilibria (conglomerate or racemic compound), enantiopure melting temperature T_{R}^{f}, stable racemic mixture melting temperature $T_{0.5}^{f}$, enantiopure melting enthalpy ΔH_{R}^{f}, and stable racemic mixture melting enthalpy $\Delta H_{0.5}^{f}$. Additionally, some space groups corresponding to the stable crystals in all systems, were searched by using ConQuest Version 2020.1 in the Cambridge Structural Database (CSD) version 5.41 (2020). The sources for all gathered data are indicated in the Appendix D bibliography. Care was taken to source only the studies providing a precise protocol for the measurement of thermal data with calorimetry techniques. We limited our selection to organic molecules with not many polymorphs to make sure that the acquired data correspond to the stable equilibrium. Additionally, we considered only systems melting at temperatures higher than 273.15K. A few chiral salts, cocrystals and solvates are also included in the database. The creation of this database is still a work in progress and the aim is that it could be continued and exploited in a further computation project.

Up to now, 109 chiral systems are listed, with 22 conglomerates (20%), and 87 racemic compounds (80%). The structural information confirms that most of enantiopure materials listed crystallize in $P2_12_12_1$ and $P2_1$ space groups, and more rarely in $C2$. Regarding the racemic crystals, the space groups are more diverse, but we highlight a high representation of $P2_1/c$. However, not enough structural data are listed to make statistics. In future work, it could be interesting to study the occurrence of some space groups couples between the enantiopure and the racemic. However, such frequencies might be proportional to the high frequency of the space groups mentioned earlier, and therefore not highlight major results. Nonetheless, the many thermal information gathered can allow to draw first conclusions. First, the $(T_{0.5}^f - T_R^f)$ values range from -20.2K to -43.7K for stable conglomerate systems, with an average value of -27.9K, which is in agreement with conclusions from Li et al. and Leclercq et al.[62, 63] Then, we can observe that for conglomerate systems the measured conglomerate melting enthalpy $\Delta H_{0.5}^f$ is always lower or equal to the measured enantiopure melting enthalpy ΔH_R^f, while for racemic compounds 28 systems (32%) exhibit $\Delta H_{0.5}^f$ lower or equal to ΔH_R^f and 59 systems (68%) present $\Delta H_{0.5}^f$ higher than ΔH_R^f. Therefore, it could be interesting for future projects to try to relate the relative stability of racemic compounds with their melting enthalpy difference $(\Delta H_R^f - \Delta H_{0.5}^f)$. Finally, we can confirm the relevance of Schröder-Van Laar equation for the 22 stable conglomerate systems by comparing theoretical $T_{0.5}^f$ computed with Equation 6.1 using enantiopure data, and the experimental $T_{0.5}^f$ found in literature, as summarized in the Appendix D Table D2. On average, the absolute difference between experimental and theoretical values is of 2.01K, with a standard deviation of 2.65K. This indicates most systems are close to ideal melting behavior and Schröder-Van Laar equation can be used appropriately for prediction of $T_{0.5}^f$ that can then be compared to experimental values for identification of a racemic compound relative stability.

With the view to propose a visual representation of relative stabilities of racemic compounds, the experimental melting temperature of enantiopure crystals T_R^f is plotted as a function of the experimental melting temperature of the stable racemic mixture $T_{0.5}^f$ in Figure 6.3 for the generated chiral systems database. The data are represented differently, whether they exhibit a stable conglomerate (green circle) or a stable racemic compound (light red circle). By using the Schröder-Van Laar equation with a series of T_R^f values and a fixed value for the enantiopure melting enthalpy ΔH_R^f, we can represent theoretical Schröder-Van Laar projection lines (black dotted lines). As ΔH_R^f values from the database are distributed between 12.5 and 54.4 kJ/mol, we choose to represent two projection lines for 10 and 55 kJ/mol. Consequently, a zone can be observed in Figure 6.3 between the two projection lines, that includes all stable conglomerate systems. We can observe that 21 stable racemic compounds are also incorporated in this zone, which indicates that these racemic compounds possess relative stabilities that are close to the corresponding conglomerates. Furthermore, the other stable racemic compound systems deviate more or less from this zone, which allows a visual representation of the racemic compound relative stabilities with the further being the more stable. Therefore, it would be interesting in future work to include more data and understand the links between racemic compound relative stabilities and thermal data. With graphical representations such as Figure 6.3, in which different zones of relative stabilities could be identified, it would be relevant to position a new target chiral molecule by quick acquisition of its thermal data and conclude on its stability by comparison with other systems from a large database. Depending on the racemic compound stability of the target molecule, different chiral resolution strategies would be envisaged.

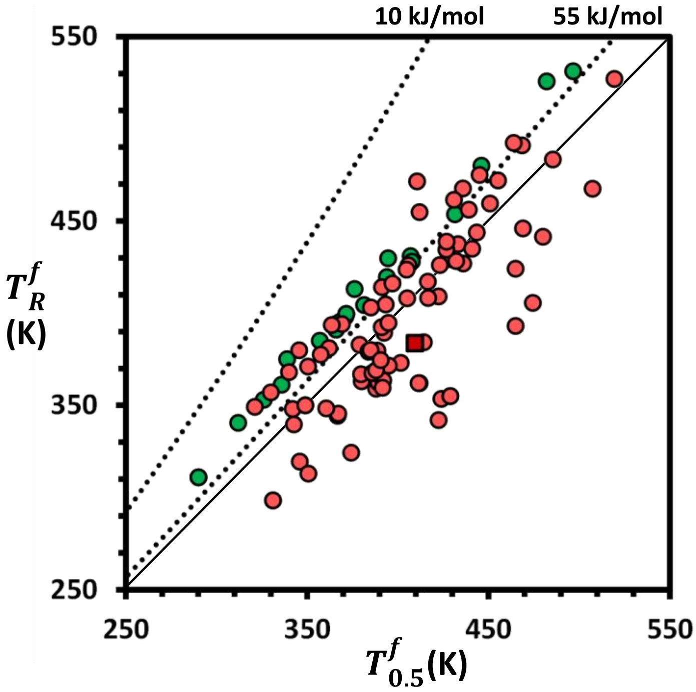

Figure 6.3: Experimental melting temperature of enantiopure crystals T_R^f as a function of the experimental melting temperature of the stable racemic mixture $T_{0.5}^f$ for the generated chiral systems database, whether they exhibit a stable conglomerate (green circle) or a stable racemic compound (light red circle). Theoretical Schröder-Van Laar projections (dotted lines) are plotted using Equation 6.1 for values of enantiopure melting enthalpies ΔH_R^f of 10 kJ/mol and 55 kJ/mol. The data point for Praziquantel (dark red square) is represented for comparison with other racemic compound systems.

6.2.3. Importance of the Racemic Compound Stability for Conglomerate Identification

Praziquantel, the model compound from Chapter 3,[51] is a stable racemic compound forming system and its data point is represented in Figure 6.3 (dark red square). It is positioned among systems far from the conglomerate behavior zone, highlighting a high stability of the racemic compound. Strategies for the chiral separation of this target molecule are often sought with a conglomerate screening, by generation of chemical derivatives, or multicomponent crystals formation with achiral molecules. The motivation relies essentially on the conglomerate statistics, with the logic being that the more some new crystals are identified, the higher is the chance to find a conglomerate allowing chiral resolution. However, we can question ourselves on the relevance of such strategy, given the high relative stability of Praziquantel racemic compound. The results reported from conglomerate screening studies highlight high difficulties to find conglomerates for Praziquantel. For instance, a recent study by Valenti et al. required the screening of up to 30 derivatives of the precursor Praziquanamine, to finally find one conglomerate system that allowed to design a chiral resolution process for Praziquantel.[64] From our cocrystal screening campaign, whose results are presented in Chapter 3,[51] we report 14 new stable cocrystals of Praziquantel, and up to now we have resolved 12 crystal structures that are all racemic crystals. If we combine these results with all multicomponent crystals reported for Praziquantel with achiral molecules in literature,[65-68] it raises this number to about 27 resolved crystal structures that are all racemic. Despite other indications of cocrystal formations whose crystal structures have not been resolved yet and that could potentially be conglomerates, as cocrystals with vanillic acid and 2,4-dihydroxybenzoic acid reported in Chapter 3,[51] Praziquantel shows conglomerate occurrence statistics that are far from the supposedly 5-10% chance. We think that these results correlate with the relatively high stability of Praziquantel racemic compound highlighted in this section. An explanation would be that the interactions between Praziquantel opposite-enantiomers are too favorable in the racemic compound. Therefore, the formation of chemical derivatives by small chemical modifications are not enough to strongly change the nature of intermolecular interactions. Similarly for multicomponent crystals, the newly formed interactions between coformers are not high enough to change the intermolecular interactions nature between enantiomers. For each new derivative or multicomponent crystal, a new point could be positioned in Figure 6.3, that deviates more or less from the Praziquantel racemic compound point. However, the relatively large distance of the former Praziquantel racemic compound point from the conglomerate behavior zone strongly decreases the chances to form new conglomerate systems. It would be interesting to confirm this hypothesis in future projects, through acquisition and comparison of thermal data for cocrystals or chemical derivatives, to observe the points variation in a representation such as Figure 6.3. Similar structures for cocrystals or derivatives would not alter free energy of structure too much and therefore racemic compound still would be favored. One would need to disturb the prevailing patterns substantially to allow new patterns to become dominant which then could be energetically less favorable for racemic compound formation.

6.3. Chirality of the Coformer and Its Limitations

As the conglomerate screening strategy presents limitations in the case of highly stable racemic compounds, we can question ourselves on the relevance of chiral cocrystallization as an alternative to achiral cocrystallization for chiral resolution. For instance, in the case of Praziquantel, Sánchez-Guadarrama et al. report a successful chiral resolution of the racemic compound via diastereomeric cocrystal pair formation with L-malic acid.[69] This result could be achieved with a prior cocrystal screening that required only 4 chiral coformers, from which 3 showed cocrystallization reactivity. Only L-malic cocrystal was used further in this study, which leaves resolution eventualities also for the other cocrystals with L-lactic acid and L-tartaric acid, whose structures are not resolved yet. Additionally, during the Praziquantel cocrystal screening campaign performed in the context of this thesis, we obtained indication of cocrystallization for Praziquantel with (S)-naproxen. This result could not be studied further but it could be used in future projects to design a chiral resolution process. Therefore, chiral cocrystallization for Praziquantel presents way more successful opportunities for chiral resolution than the conglomerate screening results with achiral coformers. This is also the case for levetiracetam, the model compound from Chapters 4 and 5,[70] in which we successfully perform the chiral separation of its racemic compound by enantioselective cocrystallization with the chiral coformer (S)-mandelic acid. Furthermore, many chiral cocrystals are reported in literature for levetiracetam, which gives many choices for the design of chiral separation processes.[55, 71-73] Consequently, the chiral cocrystallization strategy should be favored in many cases to find resolution possibilities. However, it is not the case and conglomerate screening remains the most used strategy. The main reason could be the increased complexity regarding thermodynamics of chiral cocrystal systems, as the latter can require the determination and the use of complicated phase diagrams, as highlighted in Chapters 4 and 5.[70] Nonetheless, chiral cocrystallization is becoming more popular and its understanding is made possible by newcoming studies, comprising the work realized in this thesis. In a close future, the chiral cocrystallization strategy could be considered by a larger public of researchers and industrials.

The underuse of chiral cocrystallization also relies on the current limitations for coformer selection. Most of cocrystal screening studies are still based on trial and error, as the most common strategy is to screen a library of known coformers to find new solid phases. However, this library is essentially constituted of cheap achiral molecules “Generally Recognized as Safe”(GRAS). Another approach for cocrystal design is to select molecules based on their chemical functions to predict interactions and supramolecular synthons with the knowledge of hydrogen bonding from existing cocrystals. Similarly, this strategy does not often include chiral coformers, as achiral coformers are overly represented in existing cocrystals. Moreover, as chiral molecules are often more expensive than achiral ones, they can get discarded for an eventual screening. An emerging strategy for coformer selection is to use cocrystallization predictions tools that use computation from crystallographic data, such as the ones contained in the Cambridge Structural Database (CSD). We can mention the prediction technique used in the Praziquantel cocrystal screening campaign (Chapter 3[51]), which is based on a network approach using data mining techniques and machine learning.[50, 51, 74-76] The principle is that all cocrystals contained in the CSD can be analyzed in the form of a network, which is a collection of coformers, and the links between them the cocrystals. By understanding how coformers relate to each other, link-prediction methods can be applied, which seek and compute possible missing combinations to predict cocrystals. As presented in Chapter 3,[51] the top 30 list of most-likely coformers is constituted of relevant molecules only for cocrystal screening and proved high success for positive cocrystallization reactions. However, the list is constituted of 29 achiral molecules and only 1 chiral compound, which highlights an overrepresentation of achiral molecules in cocrystals from the CSD, and therefore a bias in the prediction tool. When applying a filter to select only the top 30 list of most-likely chiral coformers for Praziquantel, only 16 predicted molecules are actual enantiomers. Indeed, the list also contains diastereomers and meso compounds, which are achiral because of symmetry elements despite presenting chiral centers. Additionally, a few achiral molecules exhibiting atropisomerism are suggested. Because of steric strain, atropisomers can indeed exhibit axial chirality through the hindered rotation of bonds under an energy barrier condition, but they can be complex to use and study, and therefore they are not the type of molecule desired for chiral cocrystallization suggestion in first intention. Furthermore, the atropisomers suggested as coformers for Praziquantel exhibit a complex molecular structure and are mentioned in literature for a specific use far from pharmaceutical sciences. For instance, hexanitrohexaazaisowurtzitane (CL-20) is predicted as a coformer but is used as an explosive and a propellant. Similarly, about half of the 16 suggested enantiomers are specific Active Pharmaceutical Ingredients (APIs), for which the use as a coformer seems unpractical because of availability, complexity, cost, and safety concerns. Such suggestion results prove the limitation of coformer prediction tools in the case of chiral cocrystallization for a chiral resolution use. The records for cocrystals of chiral coformers in the CSD seem to be constituted of a small number of very specific cases, often irrelevant to pharmaceutical purposes, contrary to cocrystals of achiral coformers that are highly represented by pharmaceutical science studies. Therefore, the selection of chiral coformers for chiral cocrystallization presents currently large limitations, mainly due to the selection methods relying on achiral coformer pools, existing cocrystals that are almost all with achiral coformers, and consequently an overrepresentation of the latter in the CSD, which bias the prediction tools that become less efficient. However, many cheap and simple chiral molecules could be used as chiral coformers and the solution would be to popularize resolution opportunities involving chiral cocrystallization. Future studies on chiral cocrystallization are required to establish a pool of chiral coformers, and register more chiral cocrystal entries in the CSD, which would improve their consideration in coformer selection strategies.

6.4. Cocrystallization Scenarios from Stable Racemic Compounds

Cocrystallization can be considered to be a solid-state reaction between solid components, for instance, A and B, to form a stable intermediate solid, here, AB, if the free energy change ΔG^0 associated with the process (Equation 6.6) is negative. However, if the latter is positive, the components remain into separate solids.

$$A_{solid} + B_{solid} \overset{\Delta G^0}{\Longleftrightarrow} AB_{solid} \qquad \text{Equation 6.6}$$

In the case of a chiral system with a coformer material, many cocrystallization scenarios can occur through the formation of stable solids of different natures, stoichiometries, and that can contain one or both enantiomers. Moreover, with a chiral coformer material, the solid-state interactions are no more identical between the enantiomers and the coformer. Therefore, the cocrystal screening outcomes and the chiral resolution possibilities with cocrystallization depend on the thermodynamic relationship between all stable solid phases in the corresponding system. In this section, we aim to review all possible cases at equilibrium for thermodynamic systems presenting a racemic compound and discuss the chiral separation possibilities with coformers, whether they are achiral, chiral or a racemic mixture. For a matter of simplicity, we only consider the cocrystal formation of single stoichiometric cocrystals with an equimolar ratio between coformers. Nonetheless, all mentioned cases can be degenerated to other cocrystal stoichiometries, and to systems presenting several cocrystals in multiple stoichiometries with the coformer.

We choose to represent the cocrystallization scenarios with isothermal subsolidus ternary phase diagrams. These phase diagrams describe the stable equilibria between solid phases only, such as in the case of grinding solid mixtures made of three distinct components. As for every phase diagram, they follow the Gibbs phase rule[77] (Equation 6.7) which defines the number of degrees of freedom, v, that are independent intensive parameters required to define an equilibrium state. In the present case, there are 3 independent components ($c = 3$), the system depends on no intensive parameters ($n = 0$), and it sets the maximum of possible phases φ in equilibrium to 3 as v value cannot be lower than 0.

$$v = c + n - \varphi = 3 - \varphi \qquad \text{Equation 6.7}$$

Racemic compounds and cocrystals are multicomponent crystals, and their existence in a ternary system raises the number of stable solids to more than 3, which implies different stability regions for 3 stable solids coexisting at equilibrium. Consequently, the ternary phase diagram displays multiple 3-solids composition triangles, such as in Figure 6.4, and the lines connecting pure solids (circles) are called quasi-binary sections. In some cases, there are different ways in which the diagram may be divided in 3-solids triangles, and the stable arrangement cannot be predicted from the binary systems.[77] Only solid-state stability studies can permit to conclude on the ternary equilibrium, however quasi-binary sections should never cross each-other to validate the Gibbs phase rule.[78] For example, in Figure 6.4, two arrangements are possible for three 3-solid triangles between the 5 stable solids. Either the AB/C line or the A/BC line is a stable quasi-binary section, but both cannot be. Therefore, this is the visual representation of the stability competition between possible solids, that can in this case be stated by Equation 6.8. If the free energy change ΔG^0 associated with the reaction is positive, the formation of AB and C solids is more stable, and the ternary phase diagram would display the arrangement 1 (Figure 6.4, middle). On the contrary, if the ΔG^0 is negative, the formation of the solids of A and BC is more stable, and the ternary phase diagram would show the arrangement 2 (Figure 6.4, right).

$$AB_{solid} + C_{solid} \overset{\Delta G^0}{\Longleftrightarrow} A_{solid} + BC_{solid} \qquad \text{Equation 6.8}$$

The understanding of the relative stabilities between stable solid phases, and therefore the subsolidus systems, is of great importance. Indeed, each stable quasi-binary section can be considered as an independent binary system, with all tie-lines being in the same plane. Consequently, they validate the Gibbs phase rule in their melting binary phase diagram, and in their ternary phase diagrams if a solvent is introduced. Furthermore, each stable 3-solid triangle leads to a quadriphasic domain in a quaternary phase diagram with a solvent.

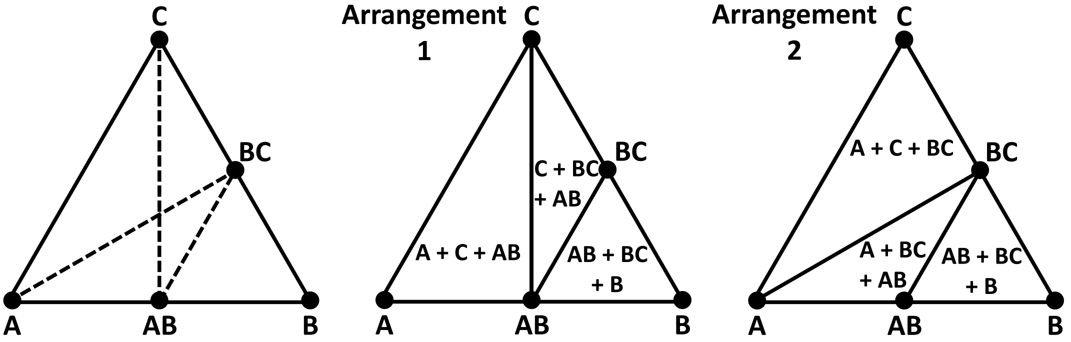

Figure 6.4: Isothermal subsolidus ternary phase diagrams between five stable solid phases (solid black circles), with all possible quasi-binary sections (dashed lines) in the system (left). The sections AB/C and A/BC are in competition for the stable equilibrium, as the Gibbs phase rule states that no more than three solids can equilibrate in composition triangles, which forbids two quasi-binary sections to cross. Based on solid relative stabilities, two arrangements are possible. Either AB and C are more stable (middle) and in equilibrium along a stable quasi-binary section (solid line), or the opposite scenario (right).

6.4.1. Cocrystallization with an Achiral Coformer

A pure enantiomer can form a stable cocrystal with an achiral coformer C (Equation 6.9). The cocrystallization reaction is identical for both enantiomers, and so is the ΔG^0 associated to the reaction. Therefore, either both enantiomers would cocrystallize with the coformer C to form symmetrical cocrystals RC and SC, or not cocrystallize.

$$R_{solid} + C_{solid} \overset{\Delta G^0}{\Longleftrightarrow} RC_{solid} \qquad \text{Equation 6.9}$$

Similarly, the stable racemic compound RS can cocrystallize or not with the coformer C to form a racemic cocrystal RSC (Equation 6.10).

$$RS_{solid} + C_{solid} \overset{\Delta G^0}{\Longleftrightarrow} RSC_{solid} \qquad \text{Equation 6.10}$$

When no racemic cocrystal RSC is stable, but the pure enantiomers show a positive cocrystallization reactivity, the racemic compound RS would dissociate or not, into the symmetrical cocrystal pair RC and SC (Equation 6.11).

$$RS_{solid} + C_{solid} \overset{\Delta G^0}{\Longleftrightarrow} RC_{solid} + SC_{solid} \qquad \text{Equation 6.11}$$

Based on all possible cocrystallization reactions and the thermodynamic relationships between the solids, we represent all scenarios that can be encountered with a racemic compound RS and an achiral coformer C, in Figure 6.5, as isothermal subsolidus ternary phase diagrams. We comment on how each scenario can be identified from cocrystal screening results, with a new XRPD pattern in a solid mixture containing the target molecules and the coformer, compared to the XRPD references of the pure enantiomer, the racemic compound RS and the achiral coformer C. In these scenarios, the chiral solids that crystallize in non-centrosymmetric space groups, are represented by green circles, while the achiral solids, that can crystallize in any space group but are in most cases in centrosymmetric structures, are represented by red circles. Therefore, we consider that despite a risk of false positives in some rare cases, a chiral crystal detection technique such as Second Harmonic Generation (SHG) would also be relevant in identifying all scenarios. We assume that any solid mixture belonging to a quasi-binary section, or a 3-solid triangle, that presents at least one chiral crystal (green circle), would show a positive signal. For every scenario, we indicate if they are favorable thermodynamic systems for chiral resolution (green tick), or not (red cross).

When no cocrystal exists (Figure 6.5a), the cocrystal screening would be negative with both pure enantiomer and the racemic mixture. This scenario presents no interest for chiral resolution, as the only possibility stays the design of a preferential crystallization process in the stable racemic compound R/S binary system,[25, 26] which is not advantageous. The same issue is encountered when there is no stable enantiopure cocrystal but a racemic one is screened positively (Figure 6.5b). Though, the latter scenario can be identified and discarded by a negative signal in chiral crystal detection for any screened composition from the RS/C section.

When no racemic cocrystal exists but enantiopure ones do, both screening with enantiopure and racemic mixture can be positive, and both can have a positive signal in chiral crystal detection (Figure 6.5c). This scenario is favorable for chiral resolution, as both symmetrical cocrystals are linked in a quasi-binary section that is a conglomerate equilibrium. Therefore, the pure symmetrical cocrystals can be synthesized by mixing the corresponding amount of racemic compound and coformer corresponding to the cocrystal stoichiometry. Then, the resulting system is considered as an independent conglomerate, in which one of the chiral cocrystal can be separated kinetically with preferential crystallization, or under stable conditions with a deracemization technique if the system can racemize with a racemizing agent, such as Viedma ripening, temperature cycling, or second-order asymmetric transformation.[29-39, 79] However, if the screening with the racemic mixture is negative, it means that the racemic compound is more stable than the symmetrical cocrystals (Figure 6.5d), and it prevents such chiral separation processes to be designed.

When the cocrystal screening by working with the racemic mixture is positive but presents a negative signal with the chiral crystal detection technique, it means a racemic cocrystal is also stable (Figure 6.5e,f). Two 3-solid triangle arrangements are possible, whether the enantiopure cocrystals are more stable than the racemic one (Figure 6.5e), or the opposite (Figure 6.5f). Nonetheless, both scenarios lead to the same unfavorable result regarding the chiral resolution possibilities. In the case of the enantiopure cocrystals having the same stoichiometry as the racemic one, as it is represented here, the quasi-binary section between the enantiopure cocrystals can be considered as an independent stable racemic cocrystal binary system RC/SC. In some rare cases, this system could be exploited to design a preferential crystallization process. The latter could be more interesting than designing one in the R/S binary system if the relative stability of the racemic cocrystal versus the enantiopure cocrystals is lower than the racemic compound one versus the pure enantiomers. Nonetheless, such possibility should not be considered in first intention for the identification of a favorable chiral resolution scenario, and it would not be possible if the enantiopure cocrystals do not have the same stoichiometry as the racemic one.

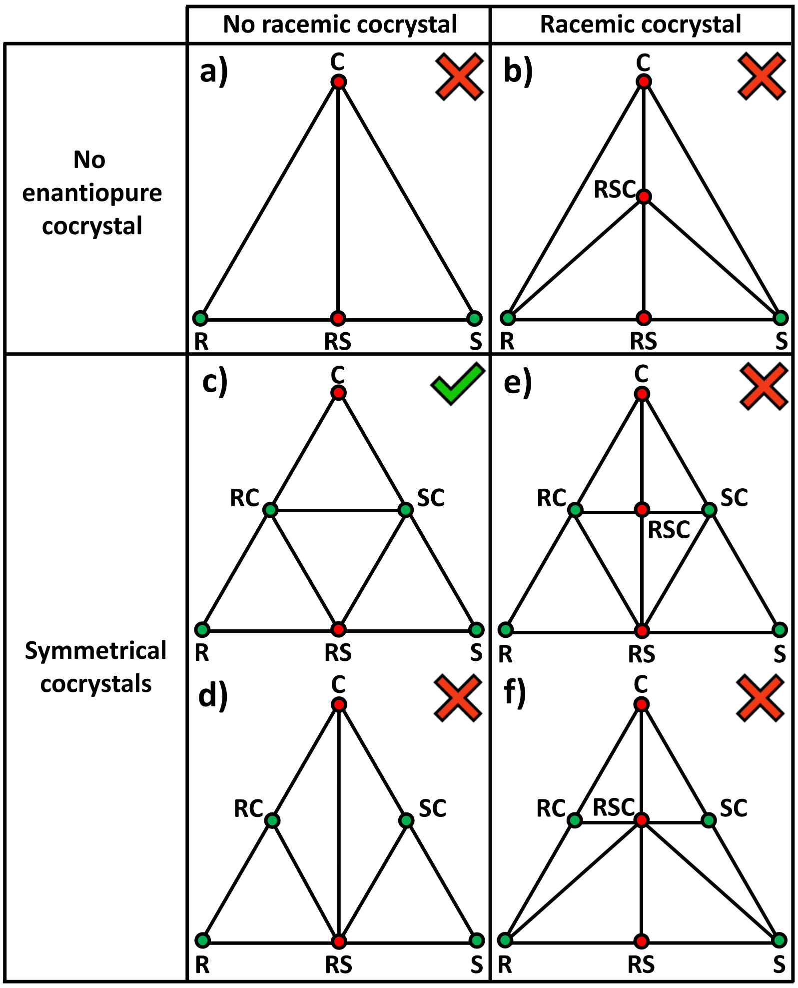

Figure 6.5: All possible cases of cocrystallization, represented as isothermal subsolidus ternary phase diagrams, that can be encountered between a racemic compound RS forming system and an achiral coformer C. Solid solutions are not considered. The presence of chiral crystals (green circles) can be detected in solid mixtures by a non-centrosymmetry detection technique, while other crystals (red circles) are in most cases centrosymmetric. The system favorable for chiral resolution (green tick) is distinguished from the non-favorable ones (red cross).

Through the description of all these scenarios, we put in evidence that there is no interest to use cocrystal screening methods by working with a pure enantiomer and an achiral coformer, as it can be the case in some protocols reported in screening studies. Indeed, the existence of symmetrical enantiopure cocrystals is not a guarantee of chiral separation possibilities, because they can be less stable than the racemic compound (Figure 6.5d), or a racemic cocrystal can also exist and prevent the separation (Figure 6.5e,f). Therefore, a screening with the racemic mixture would always be mandatory to assess the thermodynamic scenario accurately. Moreover, performing the cocrystal screening methods by using only the racemic compound and the coformer gives all necessary information about the existing cocrystals and the chiral resolution possibilities. Any screened composition from the racemic section RS/C would identify a positive cocrystallization with a new XRPD pattern. The only favorable system for resolution, that is the symmetrical cocrystals conglomerate scenario (Figure 6.5c) is the only one that would result in a positive chiral crystal detection with SHG. If such technique is not available, single-crystals can be grown, also by using the racemic compound and the coformer, and the newly found structure can be resolved to identify a chiral space group or not. This is the protocol we used in the Praziquantel cocrystal screening campaign, presented in Chapter 3,[51] and it was successful to eliminate the racemic cocrystal forming systems. Furthermore, it is cheaper to work only with the racemic compound during the cocrystal screening, while saving some time.

6.4.2. Cocrystallization with a Chiral Coformer

A pure enantiomer can form a stable cocrystal with a chiral coformer C^* if the free energy change ΔG^0 associated with the process (Equation 6.12) is negative. However, if the latter is positive, both molecules will remain into separate solids. Because of the chirality of the coformer, the cocrystallization reaction and the ΔG^0 associated are different for both enantiomers. It is possible that none cocrystallize, or only one cocrystallizes leading to an enantiospecific cocrystal, or else both cocrystallize and it leads to a diastereomeric cocrystal pair RC^* and SC^*.

$$R_{solid} + C^*_{solid} \overset{\Delta G^0}{\Longleftrightarrow} RC^*_{solid} \qquad \text{Equation 6.12}$$

We did not find any reported case of a racemic cocrystal RSC^* formed from a racemic compound RS and a chiral coformer C^* (Equation 6.13), but there are no thermodynamic or crystallographic reasons that would prevent the existence of such structures.

$$RS_{solid} + C^*_{solid} \overset{\Delta G^0}{\Longleftrightarrow} RCS^*_{solid} \qquad \text{Equation 6.13}$$

Consequently, in the case of no racemic cocrystal RSC^* existing, mixing the racemic compound RS with the chiral coformer C^* would lead or not to its dissociation into the diastereomeric cocrystal pair RC^* and $SC*$ if both enantiomers cocrystallize (Equation 6.14), or else dissociate or not into one pure enantiomer and one enantiospecific cocrystal if there is enantiospecificity for the coformer (Equation 6.15).

$$RS_{solid} + C^*_{solid} \overset{\Delta G^0}{\Longleftrightarrow} RC^*_{solid} + SC^*_{solid} \qquad \text{Equation 6.14}$$

$$RS_{solid} + C^*_{solid} \overset{\Delta G^0}{\Longleftrightarrow} R_{solid} + SC^*_{solid} \qquad \text{Equation 6.15}$$

Based on all possible cocrystallization reactions and the thermodynamic relationships between the solids, we represent all scenarios that can be encountered with a racemic compound RS and a chiral coformer C^*, in Figure 6.6, as isothermal subsolidus ternary phase diagrams. We comment on how each scenario can be identified from the results of cocrystal screening and chiral crystal detection, and we indicate if the scenarios are favorable for chiral resolution (green tick), or not (red cross). For thermodynamic scenarios of Figure 6.6a-f, the identified possibilities are the same as with an achiral coformer C (Figure 6.5a-f). However, when both enantiomers crystallize into enantiopure cocrystals (Figure 6.6c-f), the crystals are no longer symmetrical and present different physical properties. Therefore, in the case of a favorable chiral resolution system with no racemic cocrystal existing and the enantiopure cocrystals being more stable than the racemic compound (Figure 6.6c), the diastereomeric cocrystals are linked in a quasi-binary section that is not symmetrical, contrary to symmetrical cocrystals conglomerate with an achiral coformer (Figure 6.5c). Consequently, the diastereomeric cocrystals can be synthesized by mixing the corresponding amount of racemic compound and coformer corresponding to the cocrystal stoichiometry. Then, the resulting system is considered as an independent binary system, in which the cocrystal with the highest stability (i.e., with the highest melting or lowest solubility) can be separated under stable conditions at the racemic composition, like for diastereomeric salts.[69, 80] Moreover, if the system can racemize with a racemizing agent, a cocrystallization-induced spontaneous deracemization process can be designed to improve consequently the yield.[43, 81]

In the case of an existing racemic cocrystal with the same stoichiometry as the enantiopure ones (Figure 6.6e,f), the quasi-binary section between the enantiopure cocrystals can also be considered as an independent binary system that is not symmetrical. In some rare cases, we could imagine that the latter could be exploitable for chiral resolution if a solvent presents solubilities of the cocrystalline phases so different that it would skew consequently the ternary phase diagram. In the same way that we performed a solvent-mediated transformation in Chapter 5 to deconstruct a cocrystal into a pure enantiomer, we could imagine such similar transformation of the racemic cocrystal RSC^* into one of the enantiopure cocrystal under the appropriate conditions. Nonetheless, it would be unlikely to find a system of cocrystals that presents such differences in stability, especially as the latter are formed from similar molecular interactions. Therefore, such scenario does not seem favorable for chiral resolution and should not be considered in first intention.

In addition to the similar cocrystallization scenarios identified with achiral coformers (Figure 6.5a-f) and chiral coformers (Figure 6.6a-f), the use of a chiral coformer generates 4 new possible cases because of the ability of the chiral coformer to be enantioselective (Figure 6.6g-j). When no racemic cocrystal exists but an enantiospecific one does, the cocrystal screening can be positive for only one the enantiomers and for the racemic mixture (Figure 6.6g), but can also be negative for the racemic mixture if the racemic compound is more stable than the enantiospecific cocrystal (Figure 6.6h). The first scenario (Figure 6.6g) is ideal for designing a chiral separation process as we did for levetiracetam with (S)-mandelic acid in Chapters 4 and 5.[70] Indeed, it depicts a high stability of the enantiospecific cocrystal in the system, and with an important asymmetry in overall solubilities, the latter can be isolated from the racemic composition by enantioselective cocrystallization. Furthermore, it can also be coupled with racemization in solution to enhance consequently the yield. However, the second scenario (Figure 6.6h) underlines a high stability of the racemic compound and the coformer, compared to the enantiospecific cocrystal, and this system would be unlikely to present such large asymmetry in the overall solubilities to design a resolution process. Another outcome is that the positive screening from the racemic mixture is because of a racemic cocrystal RSC^* (Figure 6.6i,j). Two 3-solid triangle arrangements are possible, whether the enantiospecific cocrystal is more stable than the racemic one (Figure 6.6i), or the opposite (Figure 6.6j). However, both scenarios lead to an impossible chiral resolution. The identification of the favorable chiral resolution scenario (Figure 6.6g) would be performed by observing the same new XRPD pattern in both screenings with the enantiopure and the racemic mixture. On the contrary, the racemic cocrystal scenarios would present different new XRPD patterns for each type of screening. Another possibility is to screen in combination with a chiral crystal detection technique such as SHG. The latter would be positive on any composition from the racemic section RS/C^* of Figure 6.6g, while for Figure 6.6i,j, it would be negative for compositions where the racemic compound is in excess, and positive when the coformer is in excess.

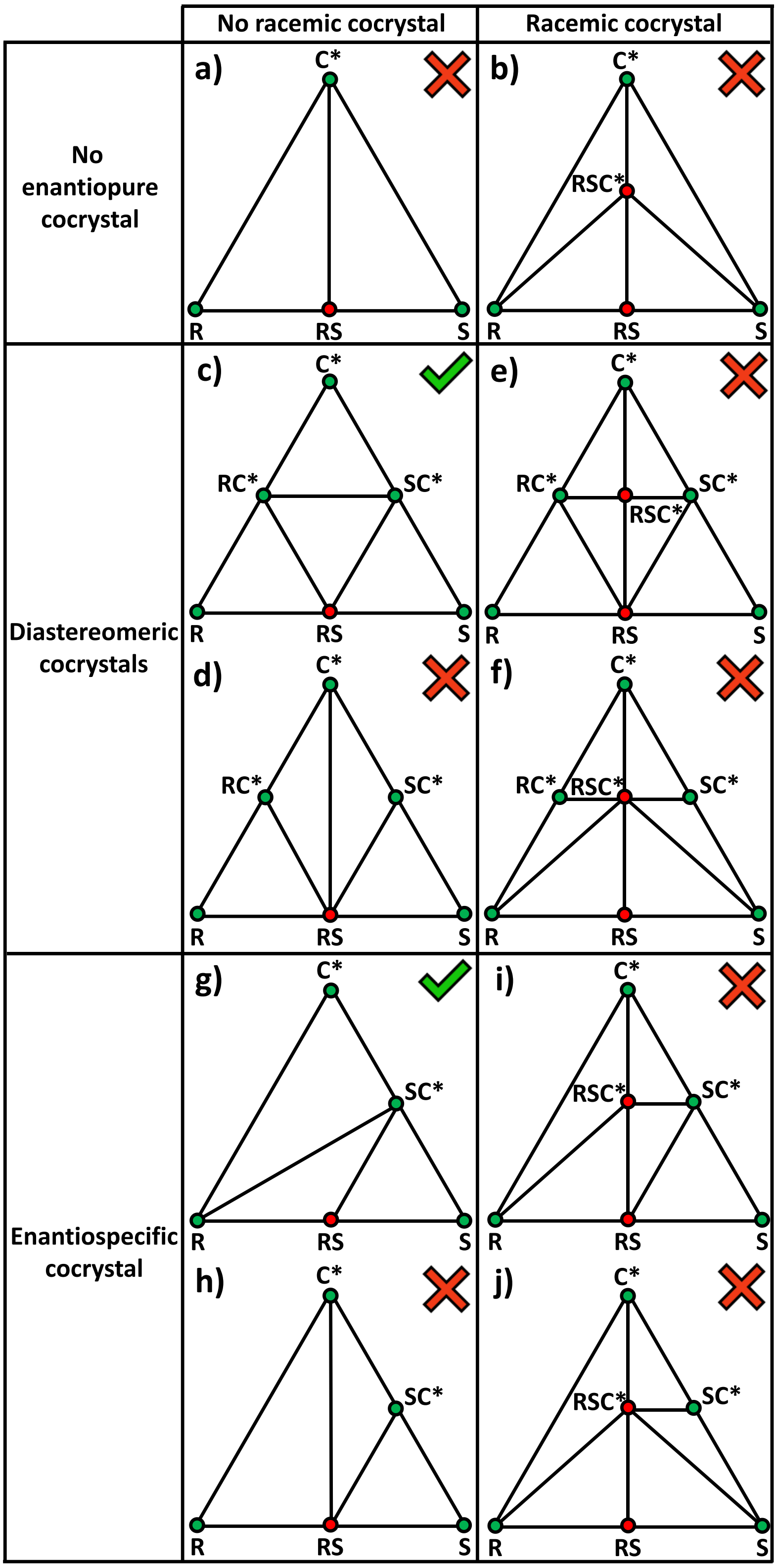

Figure 6.6: All possible cases of cocrystallization, represented as isothermal subsolidus ternary phase diagrams, that can be encountered between a racemic compound RS forming system and a chiral coformer C^*. Solid solutions are not considered. The presence of chiral crystals (green circles) can be detected in solid mixtures by a non-centrosymmetry detection technique, while other crystals (red

circles) are in most cases centrosymmetric. The systems favorable for chiral resolution (green tick) are distinguished from the non-favorable ones (red cross).

Through the description of all these scenarios, we highlight the complexity of using chiral coformers that present more possible cases of cocrystallization, and consequently more thermodynamic relationship possibilities between the stable solids. Therefore, the identification of the corresponding scenario during the cocrystal screening is more difficult than with an achiral coformer. The use of a chiral crystal detection technique is complicated by the chirality of the coformer, which would crystallize on its own in a chiral crystal in some scenarios and give a positive signal. Though, by comparing the new XRPD patterns from the screenings by using the pure enantiomers and the racemic mixture, the corresponding scenario can be identified. It is also possible to screen with the racemic mixture only, by using different mixture ratio between the racemic compound and the chiral coformer. Depending on the chiral nature or not of the phase that is in excess, the corresponding thermodynamic system can be deduced from XRPD and the chiral crystal detection. Nevertheless, more experiments, more time and more material would be required to screen the thermodynamic scenario with a chiral coformer than with an achiral coformer.

However, the scenarios compatible with chiral resolution (Figure 6.6c,g) are more favorable than the chiral resolution outcome from an achiral coformer (Figure 6.5c). Indeed, due to the symmetry breaking, the resulting systems present asymmetry in the solubilities from each side of the racemic composition, and it enhances the yield compared to a symmetrical conglomerate for the same process used. Moreover, it can guarantee to work under stable conditions of crystallization of the targeted cocrystal, as for diastereomeric resolution or the process we designed in Chapter 5 with enantioselective cocrystallization. This is a great asset of cocrystallization with chiral coformers. In addition, each chiral coformer also have a counter-enantiomer that could be used, and that would generate the mirror system. Therefore, if a system screened with a chiral coformer does not present enantiospecificity with the target molecule but with its counter-enantiomer, then the counter-enantiomer of the chiral coformer would present enantiospecificity with the target molecule. Similarly, if a diastereomeric cocrystal system presents a higher solubility for the targeted cocrystal and prevents its isolation, the mirror system by using the counter-enantiomer of the coformer would reverse the situation.

6.4.3. Cocrystallization with a Racemic Mixture

The cocrystallization of a racemic compound RS with a racemic mixture of chiral coformers C^R and C^S is also possible but adds another dimension of complexity. Here, we cannot use isothermal subsolidus quaternary phase diagrams, that would be too numerous and complex because of their three-dimensional representation as tetrahedron plots. Instead, we propose to list and discuss the possible solid-state reactions between all chiral molecules to find out the eventual interests for chiral resolution. First, all chiral molecules can associate, or not, to form a double racemic compound RSC^RC^S (Equation 6.16), but such scenario would block chiral resolution possibilities.

$$RS_{solid} + C^R_{solid} + C^S_{solid} \overset{\Delta G^0}{\Leftrightarrow} RSC^RC^S{}_{solid} \qquad \text{Equation 6.16}$$

Also, the components can associate, or not, into two possible sets of two symmetrical 3-component solids. In one scenario, there is no symmetry breaking for the target racemic compound RS (Equation 6.17), but the enantiomers can also split into distinct crystal structures in a second case (Equation 6.18) that allows chiral separation as the system can be seen as an independent conglomerate.

$$RS_{solid} + C^{R}_{solid} + C^{S}_{solid} \overset{\Delta G^{0}}{\Longleftrightarrow} RSC^{R}{}_{solid} + RSC^{S}{}_{solid} \qquad \text{Equation 6.17}$$

$$RS_{solid} + C^{R}_{solid} + C^{S}_{solid} \overset{\Delta G^{0}}{\Longleftrightarrow} RC^{R}C^{S}{}_{solid} + SC^{R}C^{S}{}_{solid} \qquad \text{Equation 6.18}$$

Otherwise, the enantiomers can form cocrystals, or not, with each of the chiral coformers, and lead to a double pair of diastereomeric cocrystals (Equation 6.19). Such situation could permit a chiral resolution because each solid phase presents different physical properties. However, designing a chiral separation process in such system would be overly complicated compared to doing the same in a single chiral coformer system.

$$RS_{solid} + C^{R}_{solid} + C^{S}_{solid} \overset{\Delta G^{0}}{\Longleftrightarrow} RC^{R}{}_{solid} + RC^{S}{}_{solid} + SC^{R}{}_{solid} + SC^{S}{}_{solid} \qquad \text{Equation 6.19}$$

Finally, there can be symmetrical enantiospecific cocrystallization, with each enantiomer associating with only one of the chiral coformers (Equations 6.20 and 6.21). The formation of such symmetrical cocrystals would lead to a conglomerate, in which the cocrystal of interest can be isolated.

$$RS_{solid} + C^{R}_{solid} + C^{S}_{solid} \overset{\Delta G^{0}}{\Longleftrightarrow} RC^{R}{}_{solid} + SC^{S}{}_{solid} \qquad \text{Equation 6.20}$$

$$RS_{solid} + C^{R}_{solid} + C^{S}_{solid} \overset{\Delta G^{0}}{\Longleftrightarrow} RC^{S}{}_{solid} + SC^{R}{}_{solid} \qquad \text{Equation 6.21}$$

The combination of all these scenarios leads to a high number of possible thermodynamic systems because of the eventual thermodynamic relationships between the existing solids. The description of all cases is of low interest, and we can question ourselves about the interest to use the racemic mixture of a chiral coformer as a cocrystallization material for a target racemic compound. Despite working with the racemic mixture being cheaper than with an enantiopure coformer, the added dimension does not provide additional outcomes for chiral resolution and presents complex conditions of application. However, in some specific cases it can be relevant, as for instance for the simultaneous resolution of two target racemic compounds. In a collaborative work realized during this thesis with Zhou et al.,[82] we report the successful isolation of two chiral target molecules from their racemic compounds, by preferential cocrystallization in a conglomerate of enantiospecific cocrystals (Equations 6.20 and 6.21). With a good yield and a high enantiopurity achieved for both target molecules in a single step, the use of a racemic mixture material for cocrystallization was highly relevant in that situation. The screening of such system can be done by using only one chiral coformer to identify the enantiospecificity, such as in Section 6.4.2. After, a screening with equimolar mixtures of both racemic mixtures permits to check if quaternary or ternary cocrystals exist or not (Equations 6.16-6.18). If the conglomerate of symmetrical enantiospecific cocrystals is the only solid-solid equilibrium, it can be synthesized by mixing the corresponding amount of the two racemic compounds corresponding to the cocrystal stoichiometry. Then, the resulting system is considered as an independent conglomerate, in which one of the chiral cocrystal can be separated kinetically with preferential crystallization, or under stable conditions with a deracemization technique if the system can racemize with a racemizing agent, such as Viedma ripening, temperature cycling, or second-order asymmetric transformation.

6.5. Conclusions

The collection of strategies to transform racemic compounds into chiral crystals by cocrystallization were investigated to provide relevant guidelines for optimal chiral resolution strategy selection. Because of complex mechanisms of solid-state association between enantiomers and coformers, many thermodynamic scenarios were identified, which affects the separation possibilities. While most of cocrystal screening studies rely on trial and error to screen for a high number of cocrystals until finding a favorable resolution system, we highlighted in this study that several parameters strongly influence the effectiveness of the screening procedure and the chiral resolution strategy. Therefore, some key points must be considered to identify the best scenario permitting the resolution of a target compound. First, we underlined the importance of assessing the relative stability of the target racemic compound versus the pure enantiomer crystals, particularly when considering a conglomerate screening with an achiral coformer. Using a database of thermal properties for racemic and enantiopure phases, we linked the chances to transform a racemic compound into a conglomerate with the relative stability of racemic compounds. We concluded that some racemic compounds possess relative stabilities that are only slightly higher than the corresponding conglomerates, and therefore, could be converted more easily to a conglomerate of cocrystals. We also identified that some racemic compounds have a high relative stability, such as Praziquantel, for which it is difficult to find a cocrystal conglomerate, despite many new cocrystals identified. In such situation, we highlighted the limitations of the conglomerate screening strategy, and the relevance of chiral cocrystallization as an alternative to obtain a chiral resolution system by using a chiral coformer. However, chiral cocrystallization is not always considered compared to the conglomerate screening strategy. We estimated that this could be because of a bias in the coformer selection methods, where chiral coformers are less suggested, particularly when using prediction tools that rely on existing cocrystals in which achiral coformers are overrepresented. Moreover, the increased complexity regarding the thermodynamics of chiral cocrystal systems could be a limitation explaining the underrepresentation of such resolution strategy. With the view to clarify all thermodynamic scenario possibilities, we listed all outcomes for cocrystallization and solid phases stabilities in a stable racemic compound system, with an achiral coformer, a chiral coformer, and a racemic mixture of chiral coformers. In each scenario, we discussed their identification from cocrystal screening and chiral crystal detection, and we related them to chiral resolution opportunities. With an achiral coformer, a stable conglomerate of cocrystals is the only system amenable to resolution. The latter can be identified in a single screening of a mixture of racemic compound and coformer, if both cocrystal screening and chiral crystal detection are positive. With a chiral coformer, two scenarios can lead to chiral separation, when either an enantiospecific cocrystal or a diastereomeric pair of cocrystals, are more stable than the racemic compound. The identification of such scenarios requires more screening experiments, either with both enantiopure and racemic mixture, or by screening multiple racemic mixtures coupled with chiral crystal detection. However, these two scenarios always present interesting resolution possibilities because of the asymmetry in the generated systems. With a racemic mixture of chiral coformers, the resolution opportunities become too complex to be considered and do not present an added value. Nonetheless, it can be relevant for the double resolution of two target racemic compounds, that can dissociate into a conglomerate of symmetrical enantiospecific cocrystals.

6.6. Associated content

Supporting Information

The Supporting Information related to this chapter is the Appendix D.

Thermal database of chiral system, and sources for the thermal database.

6.7. Acknowledgments

This research received funding as part of the CORE ITN Project by the European Union's Horizon 2020 Research and Innovation Program under the Marie Skłodowska-Curie grant agreement no. 722456 CORE ITN. The authors thank the EPSRC Centre for Innovative Manufacturing in Continuous Manufacturing and Crystallization (http://www.cmac.ac.uk) for support (EPSRC funding under grant reference: EP/I033459/1).

6.8. References

(1) Jacques, J.; Collet, A.; Wilen, S. H. *Enantiomers, racemates, and resolutions*; Wiley, 1981.
(2) Nguyen, L. A.; He, H.; Pham-Huy, C. Chiral drugs: an overview. *Int J Biomed Sci* **2006**, *2* (2), 85-100.
(3) Fabro, S.; Smith, R. L.; Williams, R. T. Toxicity and teratogenicity of optical isomers of thalidomide. *Nature* **1967**, *215* (5098), 296.
(4) Reddy, I. K.; Mehvar, R. *Chirality in drug design and development*; CRC Press, 2004.
(5) Saigo, K.; Sakai, K. Resolution of chiral drugs and drug intermediates by crystallisation. *Chirality in drug research* **2006**, 127-154.
(6) Li, Z. J.; Grant, D. J. Relationship between physical properties and crystal structures of chiral drugs. *J Pharm Sci* **1997**, *86* (10), 1073-1078.
(7) Kuusela, E.; Raekallio, M.; Anttila, M.; Falck, I.; Molsa, S.; Vainio, O. Clinical effects and pharmacokinetics of medetomidine and its enantiomers in dogs. *J Vet Pharmacol Ther* **2000**, *23* (1), 15-20.
(8) Ariens, E. J. Stereochemistry, a basis for sophisticated nonsense in pharmacokinetics and clinical pharmacology. *Eur J Clin Pharmacol* **1984**, *26* (6), 663-668.
(9) Chen, J.; Sarma, B.; Evans, J. M.; Myerson, A. S. Pharmaceutical crystallization. *Crystal growth & design* **2011**, *11* (4), 887-895.
(10) Li, Z. J.; Grant, D. J. Relationship between physical properties and crystal structures of chiral drugs. *Journal of Pharmaceutical Sciences* **1997**, *86* (10), 1073-1078.
(11) Solano, D. M.; Hoyos, P.; Hernáiz, M.; Alcántara, A.; Sánchez-Montero, J. Industrial biotransformations in the synthesis of building blocks leading to enantiopure drugs. *Bioresource technology* **2012**, *115*, 196-207.
(12) Savile, C. K.; Janey, J. M.; Mundorff, E. C.; Moore, J. C.; Tam, S.; Jarvis, W. R.; Colbeck, J. C.; Krebber, A.; Fleitz, F. J.; Brands, J.; et al. Biocatalytic asymmetric synthesis of chiral amines from ketones applied to sitagliptin manufacture. *Science* **2010**, *329* (5989), 305-309.
(13) Blaser, H. U. The chiral pool as a source of enantioselective catalysts and auxiliaries. *Chemical reviews* **1992**, *92* (5), 935-952.
(14) Masamune, S.; Choy, W.; Petersen, J. S.; Sita, L. R. Double asymmetric synthesis and a new strategy for stereochemical control in organic synthesis. *Angewandte Chemie International Edition in English* **1985**, *24* (1), 1-30.
(15) Ager, D. J.; Prakash, I.; Schaad, D. R. 1, 2-Amino alcohols and their heterocyclic derivatives as chiral auxiliaries in asymmetric synthesis. *Chemical Reviews* **1996**, *96* (2), 835-876.

(16) Noyori, R. Asymmetric catalysis: science and opportunities (Nobel lecture). *Angew Chem Int Ed Engl* **2002**, *41* (12), 2008-2022.
(17) Caner, H.; Groner, E.; Levy, L.; Agranat, I. Trends in the development of chiral drugs. *Drug Discov Today* **2004**, *9* (3), 105-110.
(18) Sheldon, R. A. *Chirotechnology: industrial synthesis of optically active compounds*; CRC press, 1993.
(19) Beesley, T. E.; Scott, R. P. *Chiral chromatography*; John Wiley & Sons, 1999.
(20) van der Meijden, M. W.; Leeman, M.; Gelens, E.; Noorduin, W. L.; Meekes, H.; van Enckevort, W. J. P.; Kaptein, B.; Vlieg, E.; Kellogg, R. M. Attrition-Enhanced Deracemization in the Synthesis of Clopidogrel - A Practical Application of a New Discovery. *Organic Process Research & Development* **2009**, *13* (6), 1195-1198.
(21) Suwannasang, K.; Flood, A. E.; Coquerel, G. A Novel Design Approach To Scale Up the Temperature Cycle Enhanced Deracemization Process: Coupled Mixed-Suspension Vessels. *Crystal Growth & Design* **2016**, *16* (11), 6461-6467.
(22) Rekis, T. Crystallization of chiral molecular compounds: what can be learned from the Cambridge Structural Database? *Acta Crystallographica Section B: Structural Science, Crystal Engineering and Materials* **2020**, *76* (3), 307-315.
(23) Belsky, V. K.; Zorkii, P. M. Distribution of organic homomolecular crystals by chiral types and structural classes. *Acta Crystallographica Section A* **1977**, *33* (6), 1004-1006.
(24) Sögütoglu, L.-C.; Steendam, R. R. E.; Meekes, H.; Vlieg, E.; Rutjes, F. P. J. T. Viedma ripening: a reliable crystallisation method to reach single chirality. *Chemical Society Reviews* **2015**, *44* (19), 6723-6732.
(25) Levilain, G.; Coquerel, G. Pitfalls and rewards of preferential crystallization. *CrystEngComm* **2010**, *12* (7), 1983-1992.
(26) Harfouche, L. C.; Brandel, C.; Cartigny, Y.; Ter Horst, J. H.; Coquerel, G.; Petit, S. Enabling Direct Preferential Crystallization in a Stable Racemic Compound System. *Mol Pharm* **2019**, *16* (11), 4670-4676.
(27) Brock, C. P.; Dunitz, J. D. Towards a Grammar of Crystal Packing. *Chemistry of Materials* **2002**, *6* (8), 1118-1127.
(28) Coquerel, G. Review on the heterogeneous equilibria between condensed phases in binary systems of enantiomers. *Enantiomer* **2000**, *5*, 481-498.
(29) Belletti, G.; Tortora, C.; Mellema, I. D.; Tinnemans, P.; Meekes, H.; Rutjes, F.; Tsogoeva, S. B.; Vlieg, E. Photoracemization-Based Viedma Ripening of a BINOL Derivative. *Chemistry* **2020**, *26* (4), 839-844.
(30) Sakai, K.; Hirayama, N.; Tamura, R. *Novel optical resolution technologies*; Springer, 2007.
(31) Suwannasang, K.; Flood, A. E.; Rougeot, C.; Coquerel, G. Using Programmed Heating–Cooling Cycles with Racemization in Solution for Complete Symmetry Breaking of a Conglomerate Forming System. *Crystal Growth & Design* **2013**, *13* (8), 3498-3504.
(32) Li, W. W.; Spix, L.; de Reus, S. C. A.; Meekes, H.; Kramer, H. J. M.; Vlieg, E.; ter Horst, J. H. Deracemization of a Racemic Compound via Its Conglomerate-Forming Salt Using Temperature Cycling. *Crystal Growth & Design* **2016**, *16* (9), 5563-5570.
(33) Sogutoglu, L. C.; Steendam, R. R.; Meekes, H.; Vlieg, E.; Rutjes, F. P. Viedma ripening: a reliable crystallisation method to reach single chirality. *Chem Soc Rev* **2015**, *44* (19), 6723-6732.
(34) Buol, X.; Caro Garrido, C.; Robeyns, K.; Tumanov, N.; Collard, L.; Wouters, J.; Leyssens, T. Chiral Resolution of Mandelic Acid through Preferential Cocrystallization with Nefiracetam. *Crystal Growth & Design* **2020**, *20* (12), 7979-7988.

(35) Lorenz, H.; Seidel-Morgenstern, A. Processes to separate enantiomers. *Angew Chem Int Ed Engl* **2014**, *53* (5), 1218-1250.
(36) Kellogg, R. M. Practical Stereochemistry. *Acc Chem Res* **2017**, *50* (4), 905-914.
(37) Maggioni, G. M.; Fernández-Ronco, M. P.; van der Meijden, M. W.; Kellogg, R. M.; Mazzotti, M. Solid state deracemisation of two imine-derivatives of phenylglycine derivatives via high-pressure homogenisation and temperature cycles. *CrystEngComm* **2018**, *20* (27), 3828-3838.
(38) Breveglieri, F.; Maggioni, G. M.; Mazzotti, M. Deracemization of NMPA via Temperature Cycles. *Crystal Growth & Design* **2018**, *18* (3), 1873-1881.
(39) Belletti, G.; Meekes, H.; Rutjes, F.; Vlieg, E. Role of Additives during Deracemization Using Temperature Cycling. *Cryst Growth Des* **2018**, *18* (11), 6617-6620.
(40) Viedma, C.; Coquerel, G.; Cintas, P. Crystallization of Chiral Molecules. In *Handbook of Crystal Growth*, Nishinaga, T. Ed.; Elsevier, 2015; pp 951-1002.
(41) Galland, A.; Dupray, V.; Berton, B.; Morin-Grognet, S.; Sanselme, M.; Atmani, H.; Coquerel, G. Spotting conglomerates by second harmonic generation. *Crystal Growth and Design* **2009**, *9* (6), 2713-2718.
(42) Harmsen, B.; Leyssens, T. Enabling enantiopurity: combining racemization and dual-drug co-crystal resolution. *Crystal Growth & Design* **2018**, *18* (6), 3654-3660.
(43) Guillot, M.; de Meester, J.; Huynen, S.; Collard, L.; Robeyns, K.; Riant, O.; Leyssens, T. Cocrystallization-Induced Spontaneous Deracemization: A General Thermodynamic Approach to Deracemization. *Angew Chem Int Ed Engl* **2020**, *59* (28), 11303-11306.
(44) Bond, A. D. What is a co-crystal? *CrystEngComm* **2007**, *9* (9), 833-834.
(45) Alhalaweh, A.; George, S.; Basavoju, S.; Childs, S. L.; Rizvi, S. A. A.; Velaga, S. P. Pharmaceutical cocrystals of nitrofurantoin: screening, characterization and crystal structure analysis. *CrystEngComm* **2012**, *14* (15), 5078-5088.
(46) Trask, A. V.; Jones, W. Crystal engineering of organic cocrystals by the solid-state grinding approach. *Organic Solid State Reactions* **2005**, *254*, 41-70.
(47) Shaikh, R.; Singh, R.; Walker, G. M.; Croker, D. M. Pharmaceutical Cocrystal Drug Products: An Outlook on Product Development. *Trends Pharmacol Sci* **2018**, *39* (12), 1033-1048.
(48) Lin, S. Y. Mechanochemical Approaches to Pharmaceutical Cocrystal Formation and Stability Analysis. *Curr Pharm Des* **2016**, *22* (32), 5001-5018.
(49) Leyssens, T.; ter Horst, J. H. 9. Solution co-crystallisation and its applications. In *Multi-Component Crystals*, De Gruyter, 2017; pp 205-236.
(50) Devogelaer, J. J.; Charpentier, M. D.; Tijink, A.; Dupray, V.; Coquerel, G.; Johnston, K.; Meekes, H.; Tinnemans, P.; Vlieg, E.; Ter Horst, J. H.; et al. Cocrystals of Praziquantel: Discovery by Network-Based Link Prediction. *Cryst Growth Des* **2021**, *21* (6), 3428-3437.
(51) Charpentier, M. D.; Devogelaer, J. J.; Tijink, A.; Meekes, H.; Tinnemans, P.; Vlieg, E.; de Gelder, R.; Johnston, K.; Ter Horst, J. H. Comparing and Quantifying the Efficiency of Cocrystal Screening Methods for Praziquantel. *Cryst Growth Des* **2022**, *22* (9), 5511-5525.
(52) Li, W.; De Groen, M.; Kramer, H. J.; De Gelder, R.; Tinnemans, P.; Meekes, H.; Ter Horst, J. H. Screening approach for identifying cocrystal types and resolution opportunities in complex chiral multicomponent systems. *Crystal Growth & Design* **2020**, *21* (1), 112-124.
(53) Harfouche, L. C.; Couvrat, N.; Sanselme, M.; Brandel, C.; Cartigny, Y.; Petit, S.; Coquerel, G. Discovery of New Proxyphylline-Based Chiral Cocrystals: Solid State Landscape and Dehydration Mechanism. *Crystal Growth & Design* **2020**, *20* (6), 3842-3850.
(54) Neurohr, C.; Marchivie, M.; Lecomte, S.; Cartigny, Y.; Couvrat, N.; Sanselme, M.; Subra-Paternault, P. Naproxen–Nicotinamide Cocrystals: Racemic and Conglomerate Structures

Generated by CO2 Antisolvent Crystallization. *Crystal Growth & Design* **2015**, *15* (9), 4616-4626.

(55) Springuel, G.; Leyssens, T. Innovative Chiral Resolution Using Enantiospecific Co-Crystallization in Solution. *Crystal Growth & Design* **2012**, *12* (7), 3374-3378.

(56) Harmsen, B.; Leyssens, T. Dual-Drug Chiral Resolution: Enantiospecific Cocrystallization of (S)-Ibuprofen Using Levetiracetam. *Crystal Growth & Design* **2017**, *18* (1), 441-448.

(57) Jacques, J.; Leclercq, M.; Brienne, M.-J. La formation de sels augmente-t-elle la fréquence des dédoublements spontanés? *Tetrahedron* **1981**, *37* (9), 1727-1733.

(58) Böcskei, Z.; Kassai, C.; Simon, K.; Fogassy, E.; Kozma, D. Racemic compound formation–conglomerate formation. Part 3. Investigation of the acidic salts of α-phenylethylamine by achiral dicarboxylic acids. Optical resolution by preferential crystallization and a structural study of (R)-α-phenylethylammonium hydrogen itaconate. *Journal of the Chemical Society, Perkin Transactions 2* **1996**, (7), 1511-1515.

(59) Gourlay, M. D.; Kendrick, J.; Leusen, F. J. Rationalization of racemate resolution: Predicting spontaneous resolution through crystal structure prediction. *Crystal growth & design* **2007**, *7* (1), 56-63.

(60) Dwivedi, S. K.; Sattari, S.; Jamali, F.; Mitchell, A. G. Ibuprofen racemate and enantiomers: Phase diagram, solubility and thermodynamic studies. *International Journal of Pharmaceutics* **1992**, *87* (1), 95-104.

(61) Polenske, D.; Lorenz, H.; Seidel-Morgenstern, A. The binary phase diagram of propranolol hydrochloride and crystallization-based enantioseparation. *J Pharm Sci* **2010**, *99* (4), 1762-1773.

(62) Leclercq, M.; Collet, A.; Jacques, J. Etude des melanges d'antipodes optiques—XII: mesure de la stabilite des racemiques vrais. *Tetrahedron* **1976**, *32* (7), 821-828.

(63) Li, Z. J.; Zell, M. T.; Munson, E. J.; Grant, D. J. Characterization of racemic species of chiral drugs using thermal analysis, thermodynamic calculation, and structural studies. *J Pharm Sci* **1999**, *88* (3), 337-346.

(64) Valenti, G.; Tinnemans, P.; Baglai, I.; Noorduin, W. L.; Kaptein, B.; Leeman, M.; Ter Horst, J. H.; Kellogg, R. M. Combining Incompatible Processes for Deracemization of a Praziquantel Derivative under Flow Conditions. *Angew Chem Int Ed Engl* **2021**, *60* (10), 5279-5282.

(65) Espinosa-Lara, J. C.; Guzman-Villanueva, D.; Arenas-García, J. I.; Herrera-Ruiz, D.; Rivera-Islas, J.; Román-Bravo, P.; Morales-Rojas, H.; Höpfl, H. Cocrystals of Active Pharmaceutical Ingredients—Praziquantel in Combination with Oxalic, Malonic, Succinic, Maleic, Fumaric, Glutaric, Adipic, And Pimelic Acids. *Crystal Growth & Design* **2012**, *13* (1), 169-185.

(66) Zanolla, D.; Hasa, D.; Arhangelskis, M.; Schneider-Rauber, G.; Chierotti, M. R.; Keiser, J.; Voinovich, D.; Jones, W.; Perissutti, B. Mechanochemical Formation of Racemic Praziquantel Hemihydrate with Improved Biopharmaceutical Properties. *Pharmaceutics* **2020**, *12* (3), 289.

(67) Yang, D.; Cao, J.; Heng, T.; Xing, C.; Yang, S.; Zhang, L.; Lu, Y.; Du, G. Theoretical Calculation and Structural Analysis of the Cocrystals of Three Flavonols with Praziquantel. *Crystal Growth & Design* **2021**, *21* (4), 2292-2300.

(68) Liu, Q.; Yang, D.; Chen, T.; Zhang, B.; Xing, C.; Zhang, L.; Lu, Y.; Du, G. Insights into the Solubility and Structural Features of Four Praziquantel Cocrystals. *Crystal Growth & Design* **2021**, *21* (11), 6321-6331.

(69) Sánchez-Guadarrama, O.; Mendoza-Navarro, F.; Cedillo-Cruz, A.; Jung-Cook, H.; Arenas-García, J. I.; Delgado-Díaz, A.; Herrera-Ruiz, D.; Morales-Rojas, H.; Höpfl, H. Chiral Resolution of RS-Praziquantel via Diastereomeric Co-Crystal Pair Formation with l-Malic Acid. *Crystal Growth & Design* **2015**, *16* (1), 307-314.

(70) Charpentier, M. D.; Venkatramanan, R.; Rougeot, C.; Leyssens, T.; Johnston, K.; ter Horst, J. H. Multicomponent Chiral Quantification with Ultraviolet Circular Dichroism Spectroscopy: Ternary and Quaternary Phase Diagrams of Levetiracetam. *Molecular Pharmaceutics* **2023**, *20* (1), 616-629.

(71) Harmsen, B.; Leyssens, T. Dual-drug chiral resolution: enantiospecific cocrystallization of (s)-ibuprofen using levetiracetam. *Crystal Growth & Design* **2018**, *18* (1), 441-448.

(72) Springuel, G.; Norberg, B.; Robeyns, K.; Wouters, J.; Leyssens, T. Advances in Pharmaceutical Co-crystal Screening: Effective Co-crystal Screening through Structural Resemblance. *Crystal Growth & Design* **2011**, *12* (1), 475-484.

(73) Wang, J.; Peng, Y. Resolution of Halogenated Mandelic Acids through Enantiospecific Co-Crystallization with Levetiracetam. *Molecules* **2021**, *26* (18), 5536.

(74) Devogelaer, J.-J.; Brugman, S. J. T.; Meekes, H.; Tinnemans, P.; Vlieg, E.; de Gelder, R. Cocrystal design by network-based link prediction. *CrystEngComm* **2019**, *21* (44), 6875-6885.

(75) Devogelaer, J. J.; Meekes, H.; Vlieg, E.; de Gelder, R. Cocrystals in the Cambridge Structural Database: a network approach. *Acta Crystallogr B Struct Sci Cryst Eng Mater* **2019**, *75* (Pt 3), 371-383.

(76) Devogelaer, J. J.; Meekes, H.; Tinnemans, P.; Vlieg, E.; de Gelder, R. Co-crystal Prediction by Artificial Neural Networks*. *Angew Chem Int Ed Engl* **2020**, *59* (48), 21711-21718.

(77) Ricci, J. E. *phase rule and heterogeneous equilibrium*; 1951.

(78) McHale, A. E. *Phase diagrams and ceramic processes*; Springer Science & Business Media, 2012.

(79) Oketani, R.; Hoquante, M.; Brandel, C.; Cardinael, P.; Coquerel, G. Resolution of an Atropisomeric Naphthamide by Second-Order Asymmetric Transformation: A Highly Productive Technique. *Organic Process Research & Development* **2019**, *23* (6), 1197-1203.

(80) Songsermsawad, S.; Nalaoh, P.; Promarak, V.; Flood, A. E. Chiral Resolution of RS-Baclofen via a Novel Chiral Cocrystal of R-Baclofen and L-Mandelic Acid. *Crystal Growth & Design* **2022**, *22* (4), 2441-2451.

(81) Guillot, M.; de Meester, J.; Collard, L.; Riant, O.; Leyssens, T. Co-Crystallization-Induced Spontaneous Deracemization: An Optimization Study. *Organic Process Research & Development* **2021**, *25* (4), 884-891.

(82) Zhou, F.; Shemchuk, O.; Charpentier, M. D.; Matheys, C.; Collard, L.; Ter Horst, J. H.; Leyssens, T. Simultaneous Chiral Resolution of Two Racemic Compounds by Preferential Cocrystallization*. *Angew Chem Int Ed Engl* **2021**, *60* (37), 20264-20268.

Chapter 7 - Conclusions and Outlook

The main aim of this thesis was to investigate the challenges related to the thermodynamic characterization and understanding of multicomponent chiral systems, with the view to apply chiral resolution strategies of racemic compounds with cocrystallization. Therefore, a variety of novel analytical techniques and optimization of existing methods were demonstrated in order to enhance the screening of new cocrystals, quantify complex chiral systems, perform cocrystallization resolution processes leading to pure enantiomer recovery, and decide on the most adapted strategy for the chiral resolution of stable racemic compounds with cocrystallization.

In Chapter 3, the detection of new cocrystals was studied through the investigation of results obtained during a campaign aiming to find a conglomerate of cocrystals permitting the resolution of the racemic compound of praziquantel (PZQ). Four cocrystal screening methods were applied to screen PZQ with a total of 30 coformers, which were selected based on a link prediction algorithm using data mining of the Cambridge Structural Database (CSD). From this screening campaign, we reported a total of 17 new cocrystals, with 14 showing stability, and 12 new structures were resolved and registered in the CSD. By defining quantified comparison parameters based on our results, we reviewed thoroughly the efficiencies of the cocrystal screening methods used: liquid-assisted grinding (LAG), solvent evaporation (SE), saturation temperature measurements of coformer mixtures (STM), and a novel thermal technique based on binary eutectic temperature differences (EUT). LAG highlighted the best results, with the largest screenable coformers fraction and the highest number of cocrystals found that are suspected to be stable, even though amorphous phases are obtained in a few cases. SE showed numerous limitations due to its solvent dependence and its lack of crystallization control. Less coformers were screenable with SE, and a lower number of cocrystals suspected to be stable was identified, while highlighting a risk of obtaining metastable phases and missing existing cocrystals. STM method presented similar results as LAG, despite slightly less coformers that were screenable, but a similar number of cocrystals suspected to be stable was detected, which reveals a tendency to identify multiple cocrystals per successful coformers. However, STM was less convenient than LAG and SE because of time and material required with solvent screening and solubility curve measurements. Despite the innovative concept of EUT, investigations using this method were stopped due to thermal degradation and difficulties in reaching equilibrium. Nevertheless, we highlighted that EUT method could be tried as an interesting alternative for thermodynamic systems that lack a suitable solvent. In summary, we advised LAG method for a quick and efficient screening route and STM for a slower route that provides relevant solubility data useful for future screenings, single-crystal growth, and eventual future cocrystal production in larger scale. Despite all positive cocrystal screening results, a suitable resolution system for PZQ was not found during this campaign, which would require additional screening results as future work, but it also raises the question of the efficiency of the conglomerate screening strategy with achiral coformers. Nonetheless, this work contributed in proving the efficiency of coformer prediction algorithms, while generating relevant conclusions on the optimization of cocrystal screening method selection. Finally, we proposed a new way to compare cocrystal screening methods with quantified parameters, and we think this could be transposed to other studies in the future.

In Chapter 4, the issue of chiral quantification in complex multicomponent systems was investigated by demonstrating successfully a new multicomponent chiral quantification method using ultraviolet circular dichroism (UV-CD) spectroscopy coupled with multivariate partial least square (PLS) models for data analysis. This method was created to measure unknown compositions in up to three different chiral components in solution, with two being enantiomers. It was applied on the model quaternary system of levetiracetam enantiomer (S), its counter-enantiomer (R), the chiral coformer (S)-mandelic acid (S-MA), and the solvent acetonitrile (MeCN). The designed calibration models showed very high accuracy in predicting known compositions for every possible ratio between components in the R/S/S-MA/MeCN quaternary system. The total mass fraction in enantiomers x_{S+R} could be predicted from the UV spectral data, while the differential mass fraction between enantiomers x_{S-R} could be obtained from the CD spectral data, which lead to the computation of the corresponding enantiomeric excess values. The mass fraction in S-MA x_{S-MA} could be predicted from both types of spectra, which gave identical prediction result. The mass fraction in MeCN x_{MeCN} could be deduced to obtain the complete quantification of quaternary compositions. This new approach for multicomponent chiral quantification with CD proved to be relevant to characterize complex chiral systems. It is a promising method that can be applied to different wavelengths to build similar quantification models in future work, by using for instance infrared (IR) light with vibrational circular dichroism (VCD) or Raman optical activity techniques. Moreover, a higher number of different chiral molecules could be quantified in solution, with the appropriate multivariate calibration models on spectral data. Indeed, the accuracy and capability of the prediction models are meant to evolve with the progress in data analysis science, and different tools could be envisaged to extract the quantification information from spectral data, for instance in machine learning and other artificial intelligence technologies. Different molecular systems should be tried in the future to gather more knowledge on this method with lots of potential, while identifying new applications that would require the quantification of complex multicomponent chiral systems. In our work, this UV-CD quantification method was used to understand the solid-liquid equilibria in the R/S/S-MA/MeCN quaternary system, with the view to identify the conditions permitting a chiral separation process with cocrystallization. By using the PLS models, we were able to determine accurately the full quaternary phase diagram at 9°C for the first time, while revising previous literature data about three related ternary phase diagrams. The generated phase diagrams helped to describe completely the equilibria of the two enantiomers forming a racemic compound RS, and the enantiomer S forming an enantiospecific cocrystal S:S-MA with the chiral coformer S-MA. The quaternary phase diagram underlined a large asymmetry along the racemic composition, which showed the feasibility of a chiral separation process with enantioselective cocrystallization of levetiracetam (S) under stable conditions.

Consequently, the information and the data from Chapter 4 were utilized in Chapter 5 to design an enantioselective cocrystallization process to recover levetiracetam (S) from its racemic compound RS through the isolation of the enantiospecific cocrystal S:S-MA. We used the acquired R/S/S-MA/MeCN quaternary phase diagram at 9°C as a model system to provide detailed guidelines for the design of optimal chiral separation processes with cocrystallization by using complex phase diagrams. In three repetitions of the optimised process we designed, we were able to obtain an experimental resolution yield $R(\%)$ of 46% recovery percentage of the initial S from its RS amount input, in the form of isolated pure S:S-MA cocrystals under stable conditions, for a theoretical yield of 51%. Additionally, this process was combined with a solvent-mediated transformation step that we designed to permit the retrieval of pure levetiracetam (S) from its S:S-MA cocrystal. The theory behind the pure enantiomer recovery process was also discussed with phase diagram guidelines we provided to advise on the selection of optimal conditions. In the model system we explored, we proposed a process leading to a maximum recovery yield ρ (%) of 41.9% of initial S from its S:S-MA amount, by the isolation of pure S crystals under stable conditions using acetone at 5 °C. Moreover, two successful screening protocols were designed for the identification of eutectic solutions points and the determination of cocrystal deconstruction points in ternary phase diagrams. The first protocol was based on equilibration experiments to directly find the eutectic composition, and the second was using Raman spectroscopy to detect the complete cocrystal deconstruction during solvent addition. Throughout this work, we demonstrated the efficiency of complex multicomponent chiral phase diagrams and their importance for the design of chiral separation processes, while providing guidelines helping to use them. We confirmed the relevance of the chiral cocrystallization strategy with chiral coformers in enantiomeric separation processes, as they permit to isolate a pure enantiomer under stable conditions with great efficacy. Finally, the advantage of using cocrystals for separation was underlined through their ability to be deconstructed to recover the molecule of interest, while permitting the recycling of all used materials during the processes for further use. In future work, other chiral systems should be separated with these technologies and optimized with the provided guidelines to select the best experimental parameters in order to enhance the possible resolution yields. In the case of levetiracetam separation, we were limited by time and material, but we highlighted that the resolution yields we obtained can be greatly enhanced by using different solvents and different working temperatures in future experiments. By coupling the provided knowledge with chemical engineering expertise, we believe that chiral resolution processes by enantioselective cocrystallization coupled with enantiomer recovery could be significantly optimized in future work. It could become a cheap resolution tool with great efficacy for development at larger scale and be compatible with green chemistry through the recycling potential of the technology.

Finally, in Chapter 6, we used the information from Chapters 3 to 5 and from literature to provide a guideline for the identification of the best scenarios permitting the resolution of a target racemic compound. Therefore, we discussed the collection of strategies available for the chiral resolution of stable racemic compounds with cocrystallization, and we highlighted the parameters that must be considered for optimal chiral resolution strategy selection. We underlined as a first key point the importance of assessing the relative stability of a racemic compound versus its pure enantiomer crystals, particularly when considering a conglomerate screening with an achiral coformer. Indeed, by using a database of thermal properties for racemic and enantiopure phases, we linked the chances to transform a racemic compound into a conglomerate of chiral crystals with the relative stability of racemic compounds. We concluded that some racemic compounds possess relative stabilities that are only slightly higher than the corresponding conglomerates, and therefore, could be converted more easily to a conglomerate by achiral cocrystallization or chemical modification. We also identified that some racemic compounds have a high relative stability, such as PZQ, the model compound of Chapter 3, for which it appears difficult to find a cocrystal conglomerate, despite many new cocrystals identified. We concluded on the limitations of the conglomerate screening strategy when the relative stability of the target racemic compound is high. Therefore, as a second key point, we highlighted the relevance of chiral cocrystallization with chiral coformers to be a good alternative to find more easily a resolution system. However, we discussed the current limitations regarding this technology. We underlined the bias of coformer selection methods that suggest inaccurately chiral coformers, and particularly the prediction tools that rely on existing cocrystals in which achiral coformers are overrepresented. Moreover, we discussed the increased complexity regarding the thermodynamics of systems with a chiral coformer, which could be responsible of an underrepresentation of this resolution strategy. Nonetheless, we hope that the work provided in this thesis would help to make it more accessible. As a third key point, we underlined that the chiral resolution possibilities are function of the solid phases present in the thermodynamic system, but also of their relative stability. With the view to clarify all thermodynamic scenario possibilities, we listed all outcomes for cocrystallization and solid phases stabilities in a stable racemic compound system, with an achiral coformer, a chiral coformer, and a racemic mixture of chiral coformers. In each scenario, we discussed their identification from cocrystal screening and chiral crystal detection, and we related them to chiral resolution opportunities. With an achiral coformer, a stable conglomerate of cocrystals is the only system amenable to resolution. The latter can be identified in a single screening of a mixture of racemic compound and coformer, if both cocrystal screening and chiral crystal detection are positive. With a chiral coformer, two scenarios can lead to chiral separation, when either an enantiospecific cocrystal or a diastereomeric pair of cocrystals, are more stable than the racemic compound. The identification of such scenarios requires more screening experiments, either with both enantiopure and racemic mixture, or by screening multiple racemic mixtures coupled with chiral crystal detection. However, these two scenarios always present interesting resolution possibilities because of the asymmetry in the generated systems. With a racemic mixture of chiral coformers, the resolution opportunities become too complex to be considered and do not present an added value. Nonetheless, it can be relevant for the double resolution of two target racemic compounds, that can dissociate into a conglomerate of symmetrical enantiospecific cocrystals. In future work, we hope that these key parameters will help for cocrystal screening studies to find chiral resolution systems with the appropriate screening procedure and the optimal separation strategy.

The work carried out in this thesis has provided new relevant tools and deepened the knowledge about thermodynamics in chiral cocrystal systems. These advancements contribute to facilitate the characterization of complex chiral systems, and to optimize the chiral resolution of stable racemic compounds with cocrystallization technology. All the results presented offer great opportunities to continue to solve the challenges of enantiomeric separation through the selection of the most relevant strategies. With the further development of the presented methodologies, it is hoped that significant improvements can be achieved to identify more easily new cocrystals and their separation possibilities, to improve the accuracy in multicomponent chiral quantification, to enhance the resolution yields of chiral separation processes while reducing their costs, and to comprehend more efficiently how to design optimal chiral resolution strategies.

Appendix A - Supporting Information of Chapter 3

Supporting Information of Chapter 3: "Comparing and Quantifying the Efficiency of Cocrystal Screening Methods for Praziquantel"

Maxime D. Charpentier[1], Jan-Joris Devogelaer[2], Arnoud Tijink[2], Hugo Meekes[2], Paul Tinnemans[2], Elias Vlieg[2], René de Gelder[2], Karen Johnston[3], Joop H. ter Horst[1,4]

1. EPSRC Centre for Innovative Manufacturing in Continuous Manufacturing and Crystallization (CMAC), University of Strathclyde, Technology and Innovation Centre, 99 George Street, Glasgow G1 1RD, U.K.

2. Radboud University, Institute for Molecules and Materials, Heyendaalseweg 135, 6525AJ Nijmegen, The Netherlands

3. Department of Chemical and Process Engineering, University of Strathclyde, James Weir Building, 75 Montrose Street, Glasgow G1 1XJ, U.K.

4. Univ Rouen Normandie, Laboratoire Sciences et Méthodes Séparatives (SMS), UR 3233, F-76000 Rouen, France

Table of contents

A1 – Materials

This section is an overview of the coformers list used for the cocrystal screening, with their molecular structures (Figure A1), the suppliers and purities of materials used for LAG and SE methods (Table A1) and the ones used for STM and EUT methods (Table A2).

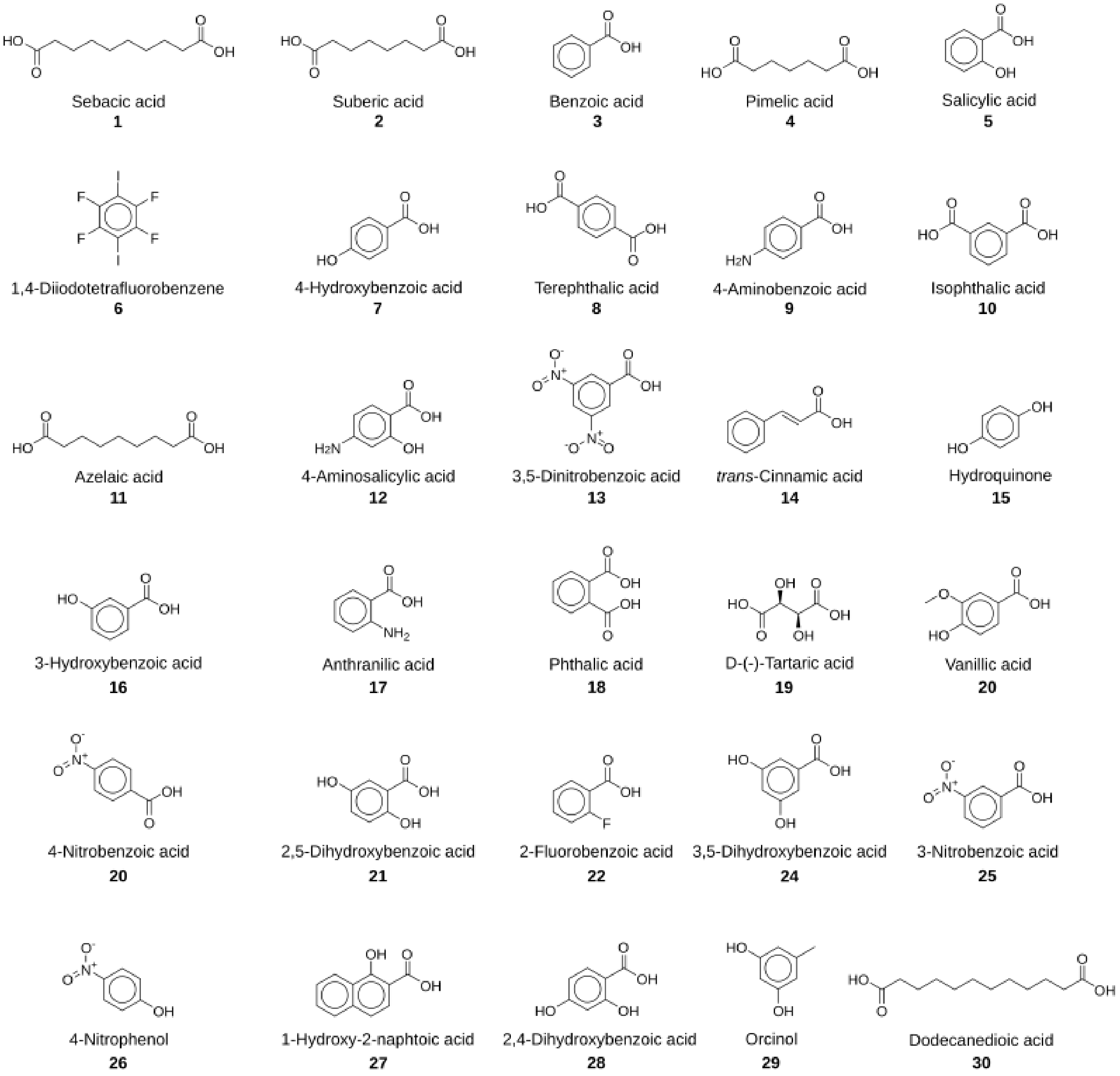

Figure A1: The thirty coformers screened experimentally for cocrystallization. Reprinted with permission from Crystal Growth & Design 2021 21 (6), 3428-3437. Copyright 2021 American Chemical Society.

Table A1: Coformers used for LAG and SE experiments with their CAS-number, chemical supplier, and purity. Reprinted with permission from Crystal Growth & Design 2021 21 (6), 3428-3437. Copyright 2021 American Chemical Society.

Rank	Coformer	CAS	Supplier	Purity
1	Sebacic acid	111-20-6	Acros Organics	98%
2	Suberic acid	505-48-6	Aldrich	98%
3	Benzoic acid	65-85-0	Sigma-Aldrich	≥ 99.5%
4	Pimelic acid	111-16-0	Sigma-Aldrich	98%
5	Salicylic acid	69-72-7	Alfa-Aesar	99%
6	1,4-Diiodotetrafluorobenzene	392-57-4	Merck	98%
7	4-Hydroxybenzoic acid	99-96-7	Fluka	≥ 99.8%
8	Terephthalic acid	100-21-0	Acros organics	≥ 99%
9	4-Aminobenzoic acid	150-13-0	Sigma-Aldrich	≥ 99%
10	Isophthalic acid	121-91-5	Aldrich	99%
11	Azelaic acid	123-99-9	Sigma-Aldrich	98%
12	4-Aminosalicylic acid	65-49-6	TCI Chemicals	≥ 98%
13	3,5-Dinitrobenzoic acid	99-34-3	Aldrich	97%
14	trans-Cinnamic acid	140-10-3	TCI Chemicals	> 98%
15	Hydroquinone	123-31-9	Merck	> 99%
16	3-Hydroxybenzoic acid	99-06-9	Aldrich	99%
17	Anthranilic acid	118-92-3	Sigma-Aldrich	> 98%
18	Phthalic acid	88-99-3	Merck	≥ 99.5%
19	D-(-)-Tartaric acid	147-71-7	Alfa-Aesar	99%
20	Vanillic acid	121-34-6	Sigma-Aldrich	≥ 97%
21	4-Nitrobenzoic acid	62-23-7	Fluorochem	99%
22	2,5-Dihydroxybenzoic acid	490-79-9	Fluorochem	99%
23	2-Fluorobenzoic acid	456-22-4	Merck	97%
24	3,5-Dihydroxybenzoic acid	99-10-5	Fluorochem	recryst. from MeCN
25	3-Nitrobenzoic acid	121-92-6	Sigma-Aldrich	99%
26	4-Nitrophenol	100-02-7	Acros Organics	99%
27	1-Hydroxy-2-naphtoic acid	86-48-6	Aldrich	≥ 97%
28	2,4-Dihydroxybenzoic acid	89-86-1	Aldrich	97%
29	Orcinol	504-15-4	Sigma-Aldrich	97%
30	Dodecanedioic acid	693-23-2	Acros Organics	99%

Table A2: Coformers used for STM and EUT experiments with their CAS-number, chemical supplier, and purity.

Rank	**Coformer**	**CAS**	**Supplier**	**Purity**
1	Sebacic acid	111-20-6	Sigma-Aldrich	99%
2	Suberic acid	505-48-6	Sigma-Aldrich	98%
3	Benzoic acid	65-85-0	Sigma-Aldrich	≥ 99.5%
4	Pimelic acid	111-16-0	Sigma-Aldrich	98%
5	Salicylic acid	69-72-7	Sigma-Aldrich	≥ 99%
6	1,4-Diiodotetrafluorobenzene	392-57-4	Sigma-Aldrich	98%
7	4-Hydroxybenzoic acid	99-96-7	Sigma-Aldrich	≥ 99%
8	Terephthalic acid	100-21-0	Sigma-Aldrich	98%
9	4-Aminobenzoic acid	150-13-0	Sigma-Aldrich	≥ 99%
10	Isophthalic acid	121-91-5	Sigma-Aldrich	99%
11	Azelaic acid	123-99-9	Sigma-Aldrich	98%
12	4-Aminosalicylic acid	65-49-6	Sigma-Aldrich	99%
13	3,5-Dinitrobenzoic acid	99-34-3	Sigma-Aldrich	99%
14	trans-Cinnamic acid	140-10-3	Sigma-Aldrich	99%
15	Hydroquinone	123-31-9	Sigma-Aldrich	≥ 99.5%
16	3-Hydroxybenzoic acid	99-06-9	Sigma-Aldrich	99%
17	Anthranilic acid	118-92-3	Sigma-Aldrich	≥ 99.5%
18	Phthalic acid	88-99-3	Sigma-Aldrich	≥ 99.5%
19	D-(-)-Tartaric acid	147-71-7	Sigma-Aldrich	99%
20	Vanillic acid	121-34-6	Sigma-Aldrich	≥ 97%
21	4-Nitrobenzoic acid	62-23-7	Sigma-Aldrich	98%
22	2,5-Dihydroxybenzoic acid	490-79-9	Sigma-Aldrich	98%
23	2-Fluorobenzoic acid	456-22-4	Sigma-Aldrich	97%
24	3,5-Dihydroxybenzoic acid	99-10-5	Sigma-Aldrich	97%
25	3-Nitrobenzoic acid	121-92-6	Sigma-Aldrich	99%
26	4-Nitrophenol	100-02-7	Sigma-Aldrich	≥ 99%
27	1-Hydroxy-2-naphtoic acid	86-48-6	Sigma-Aldrich	99%
28	2,4-Dihydroxybenzoic acid	89-86-1	Sigma-Aldrich	97%
29	Orcinol	504-15-4	Sigma-Aldrich	97%
30	Dodecanedioic acid	693-23-2	Sigma-Aldrich	99%

A2 – Experimental Conditions and XRPD Results for LAG, SE, and STM Methods

This section is an overview of the experimental conditions used for LAG, SE, and STM (Table A3) and the corresponding XRPD patterns obtained in cases where new patterns emerged (Figures A2 to A16).

Table A3: Solvents used for the LAG, SE and STM screening methods. The stoichiometric ratios in parentheses are expressed as 'mol coformer per mol of PZQ' for the STM method. For LAG and SE, this ratio is always equal to 1.
'-[i]': symbol used when coformers present solubility issues in all solvents tried.
Adapted with permission from Crystal Growth & Design 2021 21 (6), 3428-3437. Copyright *2021* American Chemical Society.

Rank	Coformer	Solvent LAG	Solvent SE	Solvent STM (Ratio $mol_{coformer}$ per mol_{PZQ})	XRPD Figure associated
1	Sebacic acid	MeOH, EtOH	MeOH, EtOH, iPrOH	EtOH (1.4), AcOEt (0.3)	
2	Suberic acid	MeOH, EtOH	MeOH, EtOH	EtOH (2.1)	
3	Benzoic acid	EtOH	EtOH	EtOH (13.3), MeCN (3.3), AcOEt (12.9)	
4	Pimelic acid	MeCN	MeCN	MeCN (0.7), AcOEt (2.4)	A2
5	Salicylic acid	EtOH	EtOH	EtOH (10.6), MeCN (2.2), AcOEt (9.2)	A3
6	1,4-Diiodotetrafluorobenzene	MeCN	MeCN	EtOH (5)	A4
7	4-Hydroxybenzoic acid	MeCN	MeCN	EtOH (8.3), MeCN (0.9)	A5
8	Terephthalic acid	MeCN	-[i]	-[i]	
9	4-Aminobenzoic acid	MeCN	MeCN	EtOH (3.3), MeCN (1.5), AcOEt (3.4)	
10	Isophthalic acid	MeCN	-[i]	-[i]	
11	Azelaic acid	EtOH	EtOH	EtOH (4.1), AcOEt (0.8)	
12	4-Aminosalicylic acid	MeCN	MeCN	MeCN (0.4)	A6
13	3,5-Dinitrobenzoic acid	MeCN	MeCN	MeCN (0.9)	A7
14	trans-Cinnamic acid	MeCN	MeCN	EtOH (5.4), MeCN (1.4), AcOEt (5.5)	
15	Hydroquinone	MeCN	MeCN	MeCN (3.6)	A8
16	3-Hydroxybenzoic acid	EtOH	EtOH	EtOH (7.7 and 3.9), MeCN (0.9 and 0.8), AcOEt (4.2 and 3.4)	
17	Anthranilic acid	MeCN, MeOH	MeCN, MeOH	EtOH (6.2), MeCN (3), AcOEt (8.7)	
18	Phthalic acid	MeCN	-[i]	-[i]	
19	D-(-)-Tartaric acid	MeCN	MeCN	-[i]	
20	Vanillic acid	EtOH, MeCN	EtOH, MeCN	EtOH (2), MeCN (0.2), AcOEt (0.6)	A9, A10
21	4-Nitrobenzoic acid	MeCN	MeCN	EtOH (0.6), AcOEt (0.6)	
22	2,5-Dihydroxybenzoic acid	Acetone, MeCN	Acetone, MeCN	EtOH (9 and 4.5), MeCN (1.4), AcOEt (4.1)	A11, A12

Table A3 (continued). Adapted with permission from Crystal Growth & Design 2021 21 (6), 3428-3437. Copyright *2021* American Chemical Society.

Rank	**Coformer**	**Solvent LAG**	**Solvent SE**	**Solvent STM (Ratio $\text{mol}_{\text{coformer}}$ per mol_{PZQ})**	**XRPD Figure associated**
23	2-Fluorobenzoic acid	EtOH	EtOH	EtOH (17.4), MeCN (5.3), AcOEt (12.8)	
24	3,5-Dihydroxybenzoic acid	MeCN	MeCN	MeCN (0.7)	A13
25	3-Nitrobenzoic acid	EtOH	EtOH	MeCN (3.6), AcOEt (9.7)	
26	4-Nitrophenol	EtOH, MeCN	EtOH	EtOH (32.1)	
27	1-Hydroxy-2-naphtoic acid	MeCN	MeCN	AcOEt (0.6)	
28	2,4-Dihydroxybenzoic acid	MeCN	MeCN	EtOH (8.1), MeCN (1), AcOEt (5.7 and 4.3)	A14, A15
29	Orcinol	EtOH, MeCN	EtOH, MeCN	-[i]	A16
30	Dodecanedioic acid	MeCN	EtOH	EtOH (0.9)	

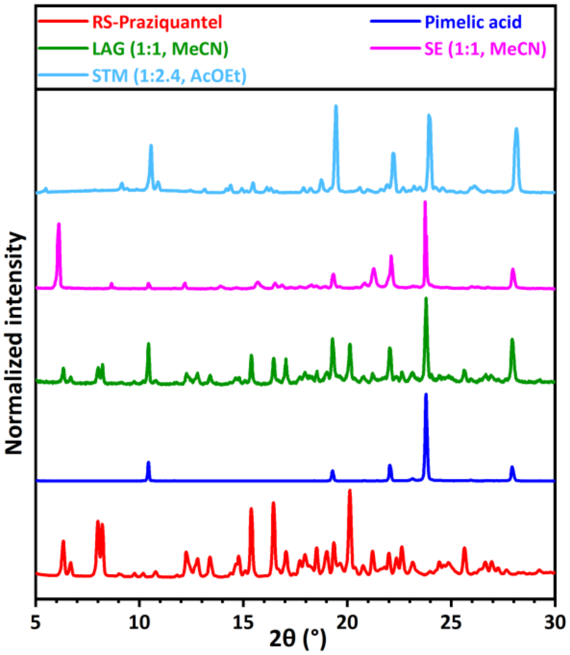

Figure A2: XRPD patterns for RS-PZQ, pimelic acid and solid phases obtained from their mixtures after LAG, SE and STM (with corresponding solvent and molar ratio between coformer and PZQ $M_{PZQ/cof}$). New peaks are identified for SE (structure could not be resolved), while LAG and STM resulted in a physical mixtures of the coformers.

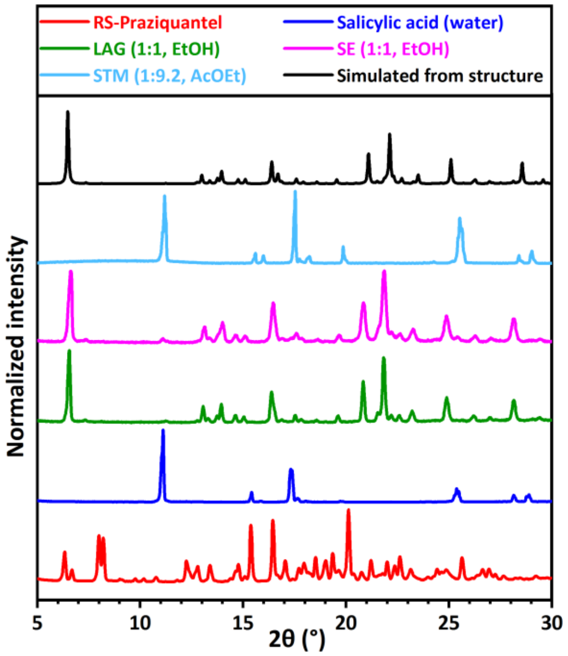

Figure A3: XRPD patterns for RS-PZQ, salicylic acid and solid phases obtained from their mixtures after LAG, SE and STM (with corresponding solvent and molar ratio between coformer and PZQ $M_{PZQ/cof}$). The simulated powder pattern from resolved cocrystal hydrate (CCDC 2054486) is added for comparison. This new pattern is identified for LAG and SE while STM resulted in a physical mixture in solvents tried.

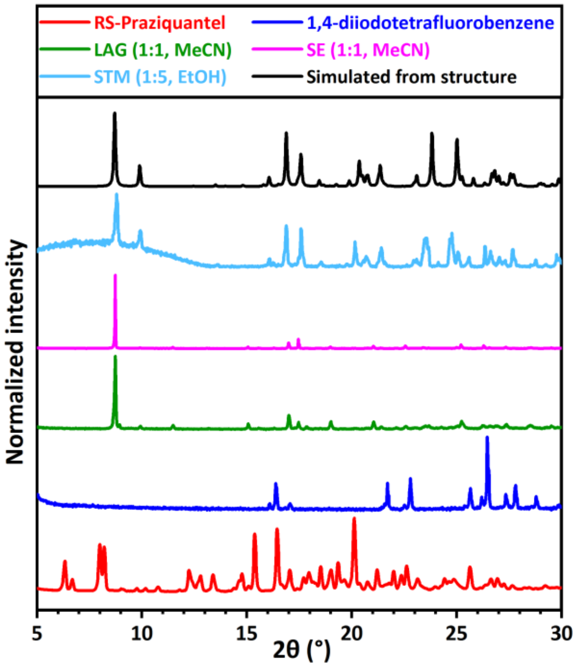

Figure A4: XRPD patterns for RS-PZQ, 1,4-diiodotetrafluorobenzene and solid phases obtained from their mixtures after LAG, SE and STM (with corresponding solvent and molar ratio between coformer and PZQ $M_{PZQ/cof}$). The simulated powder pattern from resolved cocrystal (CCDC 2054495) is added for comparison. This new pattern is identified for LAG, SE and STM.

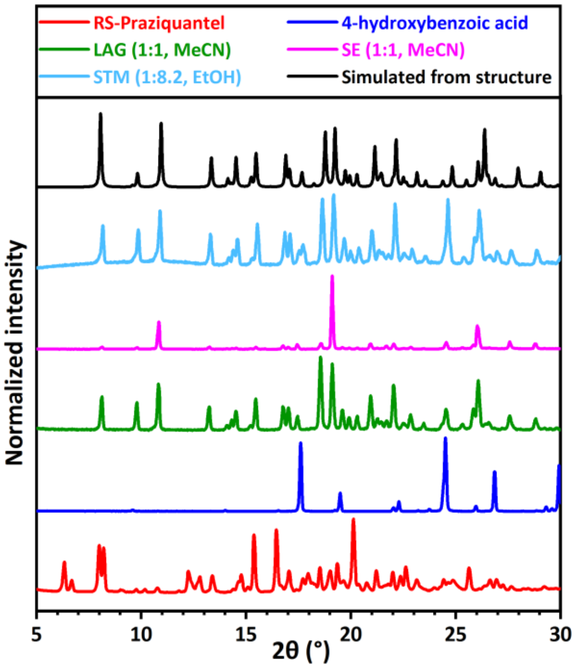

Figure A5: XRPD patterns for RS-PZQ, 4-hydroxybenzoic acid and solid phases obtained from their mixtures after LAG, SE and STM (with corresponding solvent and molar ratio between coformer and PZQ $M_{PZQ/cof}$). The simulated powder pattern from resolved cocrystal (CCDC 2054492) is added for comparison. This new pattern is identified for LAG, SE and STM.

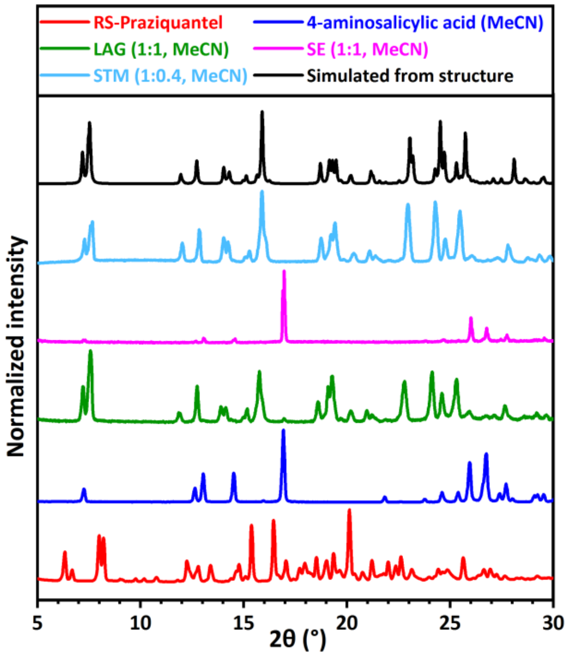

Figure A6: XRPD patterns for RS-PZQ, 4-aminosalicylic acid and solid phases obtained from their mixtures after LAG, SE and STM (with corresponding solvent and molar ratio between coformer and PZQ $M_{PZQ/cof}$). The simulated powder pattern from resolved cocrystal solvate (CCDC 2054493) is added for comparison. This new pattern is identified for LAG and STM, but not SE.

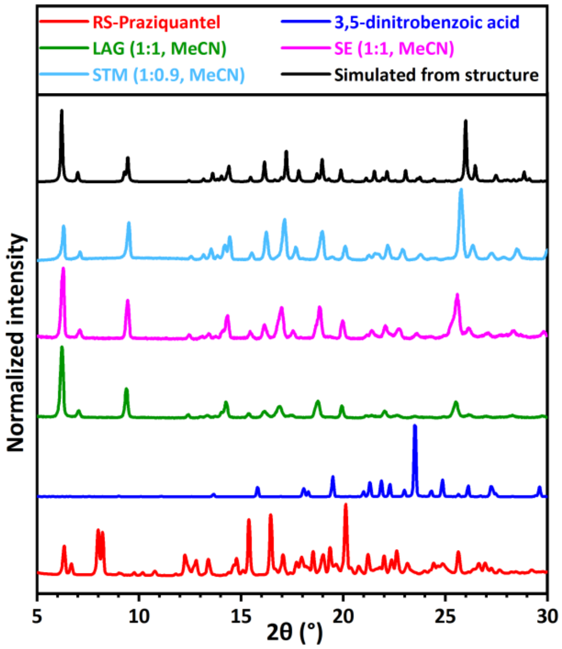

Figure A7: XRPD patterns for RS-PZQ, 3,5-dinitrobenzoic acid and solid phases obtained from their mixtures after LAG, SE and STM (with corresponding solvent and molar ratio between coformer and PZQ $M_{PZQ/cof}$). The simulated powder pattern from resolved cocrystal (CCDC 2054491) is added for comparison. This new pattern is identified for LAG, SE and STM.

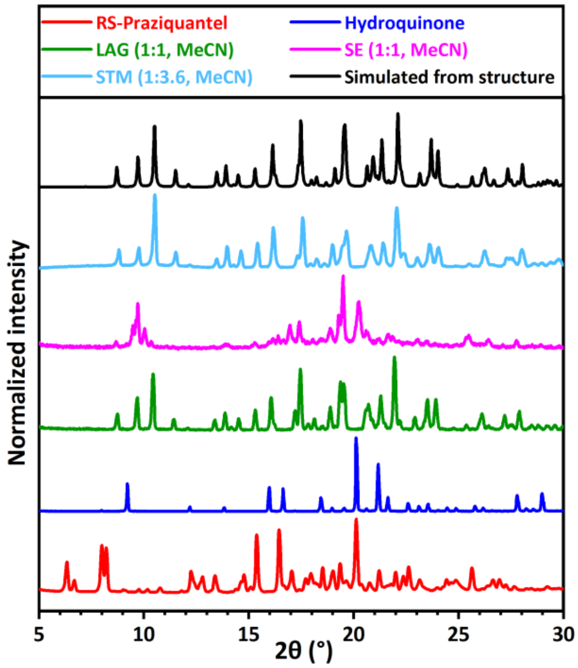

Figure A8: XRPD patterns for RS-PZQ, hydroquinone and solid phases obtained from their mixtures after LAG, SE and STM (with corresponding solvent and molar ratio between coformer and PZQ $M_{PZQ/cof}$). The simulated powder pattern from resolved cocrystal (CCDC 2054497) is added for comparison. This new pattern is identified for LAG and STM. SE presents a different new pattern (structure not resolved)

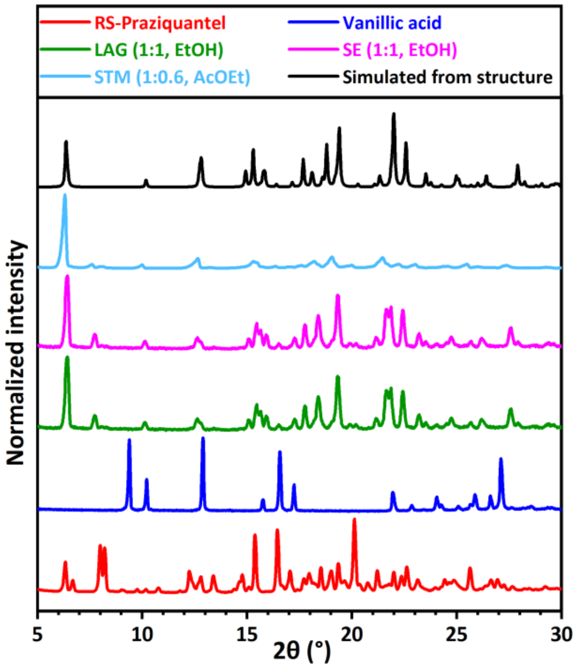

Figure A9: XRPD patterns for RS-PZQ, vanillic acid and solid phases obtained from their mixtures after LAG, SE and STM (with corresponding solvent and molar ratio between coformer and PZQ $M_{PZQ/cof}$). The simulated powder pattern from resolved cocrystal (CCDC 2054490) is added for comparison. This new pattern is identified for LAG, SE and STM.

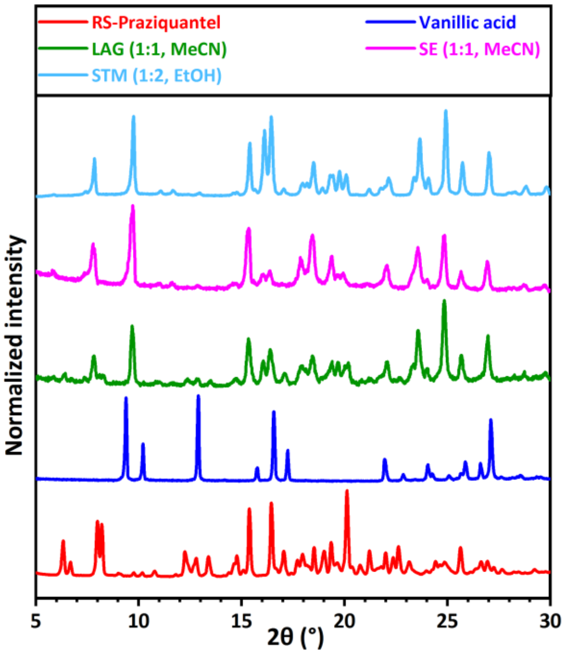

Figure A10: XRPD patterns for RS-PZQ, vanillic acid and solid phases obtained from their mixtures after LAG, SE and STM (with corresponding solvent and molar ratio molar ratio between coformer and PZQ $M_{PZQ/cof}$). A new pattern is identified for LAG, SE and STM. It differs from the resolved cocrystal (CCDC 2054490) (in Figure A8) also obtained with vanillic acid in other solvents.

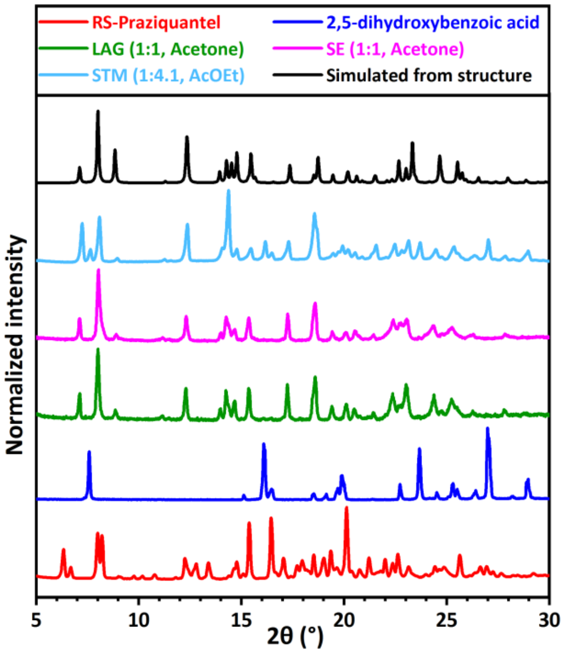

Figure A11: XRPD patterns for RS-PZQ, 2,5-dihydroxybenzoic acid and solid phases obtained from their mixtures after LAG, SE and STM (with corresponding solvent and molar ratio molar ratio between coformer and PZQ $M_{PZQ/cof}$). The simulated powder pattern from resolved cocrystal (CCDC 2054489) is added for comparison. This new pattern is identified for LAG, SE and STM.

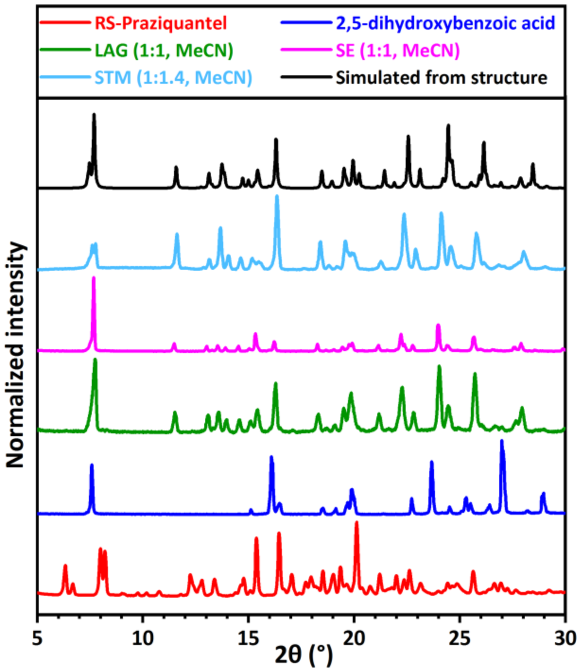

Figure A12: XRPD patterns for RS-PZQ, 2,5-dihydroxybenzoic acid and solid phases obtained from their mixtures after LAG, SE and STM (with corresponding solvent and molar ratio between coformer and PZQ $M_{PZQ/cof}$). The simulated powder pattern from resolved cocrystal solvate (CCDC 2054487) is added for comparison. This new pattern is identified for LAG, SE and STM.

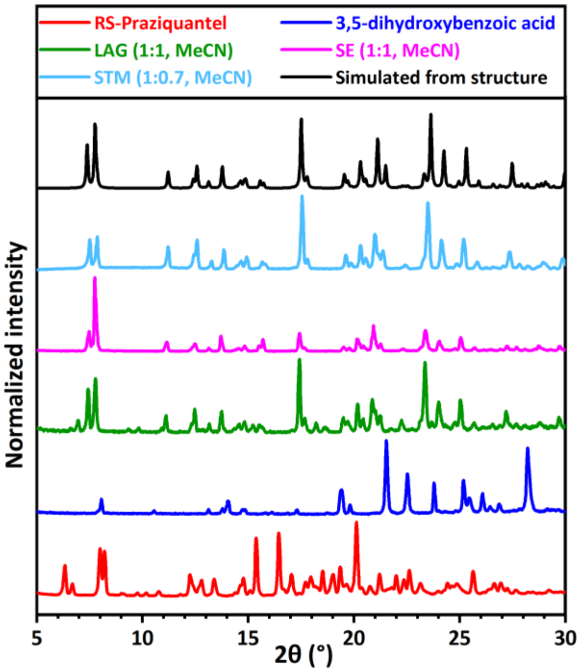

Figure A13: XRPD patterns for RS-PZQ, 3,5-dihydroxybenzoic acid and solid phases obtained from their mixtures after LAG, SE and STM (with corresponding solvent and molar ratio between coformer and PZQ $M_{PZQ/cof}$). The simulated powder pattern from resolved cocrystal solvate (CCDC 2054496) is added for comparison. This new pattern is identified for LAG, SE and STM.

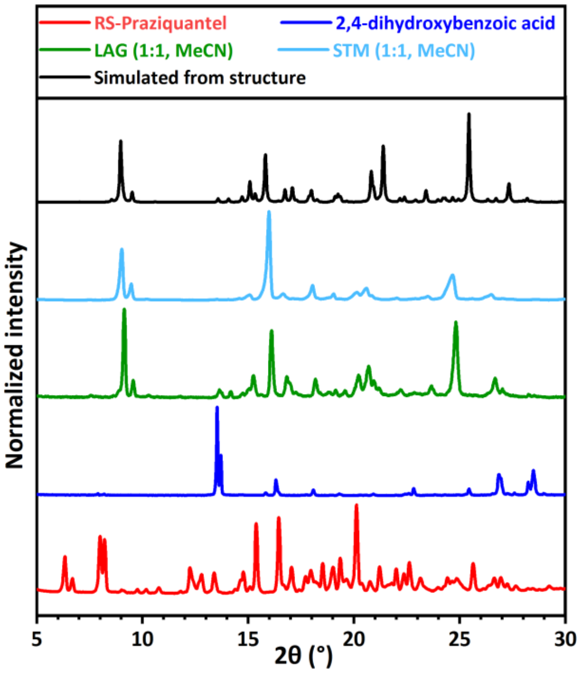

Figure A14: XRPD patterns for RS-PZQ, 2,4-dihydroxybenzoic acid and solid phases obtained from their mixtures after LAG and STM (with corresponding solvent and molar ratio between coformer and PZQ $M_{PZQ/cof}$). The simulated powder pattern from resolved cocrystal (CCDC 2054494) is added for comparison. This new pattern is identified for LAG and STM.

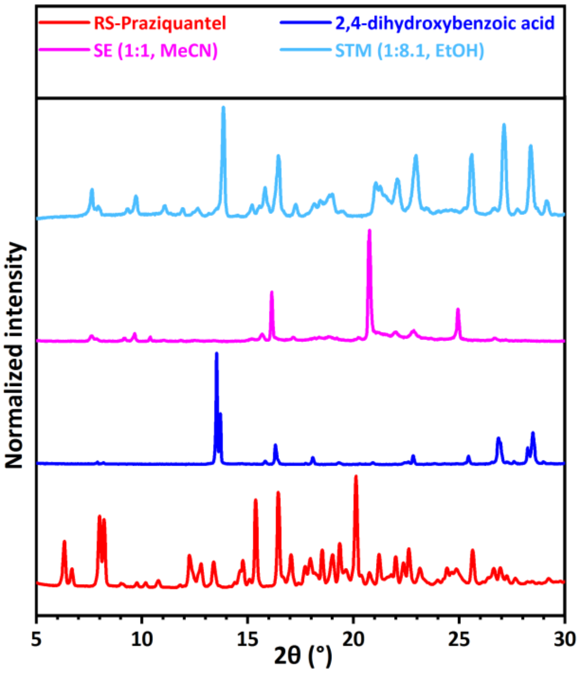

Figure A15: XRPD patterns for RS-PZQ, 2,4-dihydroxybenzoic acid and solid phases obtained from their mixtures after SE and STM (with corresponding solvent and molar ratio between coformer and PZQ $M_{PZQ/cof}$). New different patterns are identified for SE and STM. They differ from the resolved cocrystal (CCDC 2054494) (in Figure A14) also obtained with 2,4-dihydroxybenzoic in other conditions.

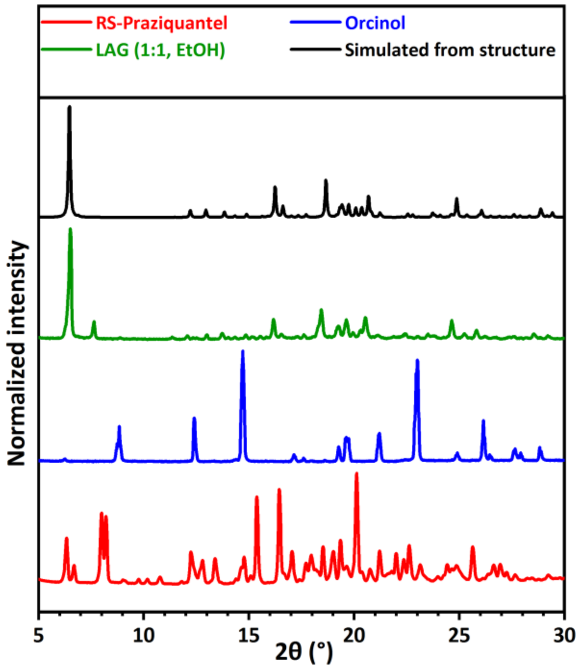

Figure A16: XRPD patterns for RS-PZQ, orcinol and solid phase obtained from a mixtures after LAG (with corresponding solvent and molar ratio between coformer and PZQ $M_{PZQ/cof}$). The simulated powder pattern from resolved cocrystal (CCDC 2054488) is added for comparison.

A3 – Experimental Solubility Results for STM Screening Method

This section presents the experimental temperature-solubility measurements data for RS-PZQ and pure coformers (Tables A4 to A29) and their associated Van ‘t Hoff plots (Figures A17 to A42) in ethanol (EtOH), acetonitrile (MeCN) and ethyl acetate (AcOEt). Table A30 summarizes STM method results with the ternary compositions screened and temperature differences *ΔT* measured for all coformers in solvents tried between reference temperature T_r and average experimental saturation temperature T_{sat}.

$$\ln(x^*) = -\frac{\Delta H^f}{R}\left(\frac{1}{T} - \frac{1}{T_m}\right)$$ Van ’t Hoff equation

x^*: solubility (molar fraction); ΔH^f: fusion enthalpy (J.mol^{-1}); T_m: melting temperature of the compound (K); T: temperature (K); R: universal gas constant equal to 8.314 J.mol^{-1}.K^{-1}

<u>Praziquantel (*RS*-PZQ)</u>

Table A4: RS-PZQ solubilities with Crystal16.

	Molar fraction x	Average T_{sat} (K)
EtOH	0.00825	289.15
	0.01106	296.05
	0.01511	301.92
	0.01823	304.95
	0.02156	307.88
	0.02506	310.48
	0.03036	313.52
	0.03598	316.55
MeCN	0.01234	297.25
	0.01609	303.12
	0.01877	306.25
	0.02271	310.78
	0.02537	313.05
	0.02879	315.28
	0.03370	318.18
	0.03806	320.75
AcOEt	0.1370	296.78
	0.1740	303.88
	0.2197	310.58
	0.2519	313.35
	0.3026	319.45
	0.3283	321.38
	0.3739	324.58
	0.4056	325.38

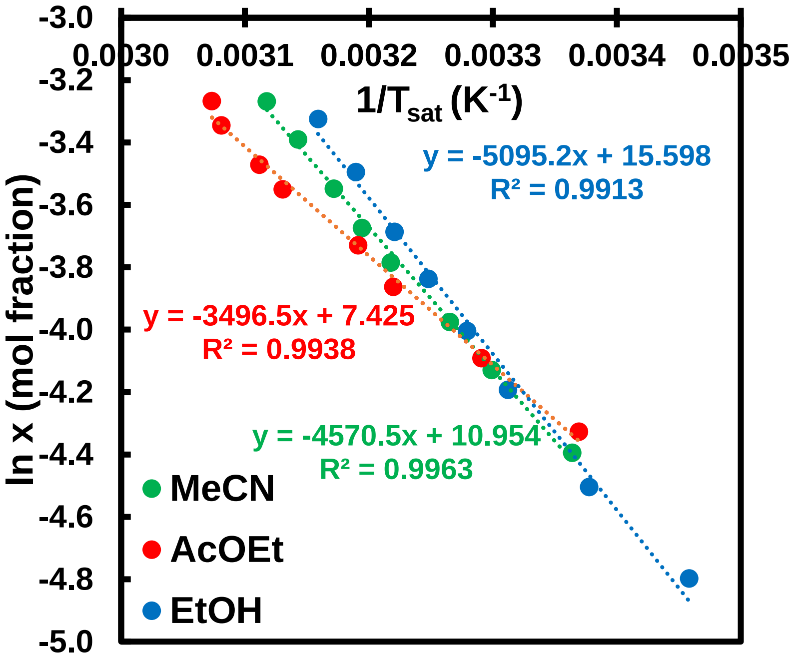

Figure A17: Van ’t Hoff plots for RS-PZQ.

Sebacic acid (**1**)

Table A5: Sebacic acid solubilities with Crystal16.

	Molar fraction x	Average T_{sat} (K)
EtOH	0.03163	309.32
	0.04626	317.38
	0.05679	322.05
	0.06796	326.58
	0.02169	301.68
AcOEt	0.00356	315.25
	0.00438	317.82
	0.00537	319.98
	0.00139	296.78
	0.00180	301.05
	0.00224	305.48

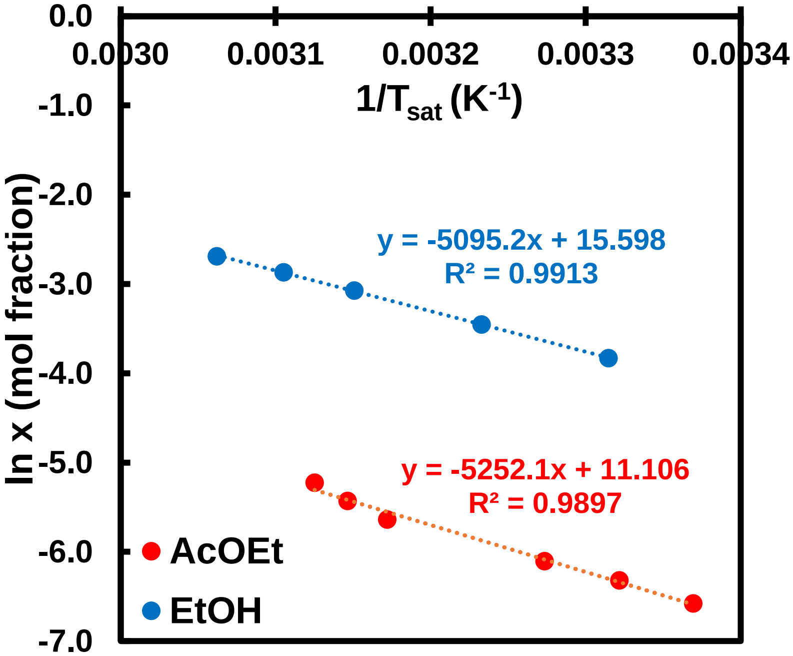

Figure A18: Van ’t Hoff plots for sebacic acid.

Suberic acid (**2**)

Table A6: Suberic acid solubilities with Crystal16.

	Molar fraction x	Average T_{sat} (K)
EtOH	0.02919	299.22
	0.04384	309.12
	0.05640	315.92
	0.03887	305.65

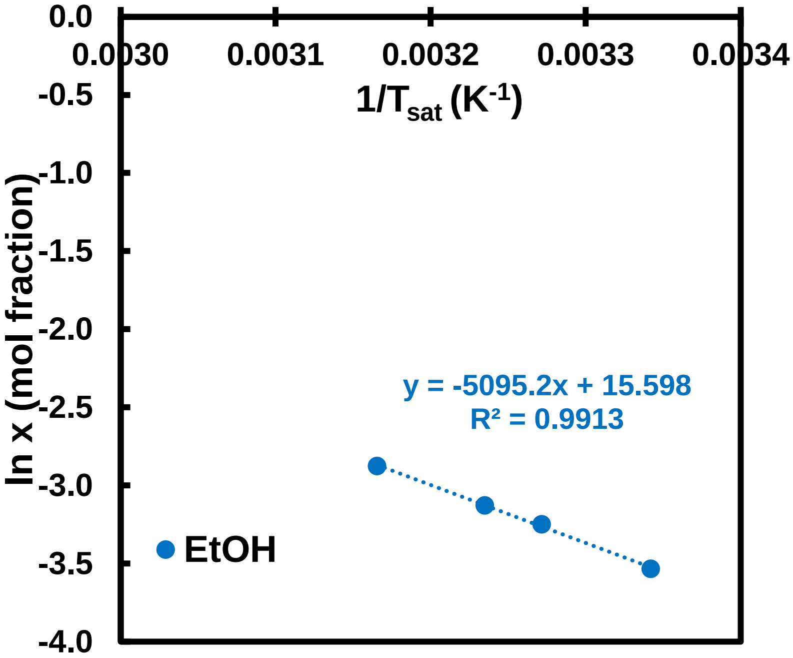

Figure A19: Van ’t Hoff plot for suberic acid.

Benzoic acid (**3**)

Table A7: Benzoic acid solubilities with Crystal16.

	Molar fraction x	Average T_{sat} (K)
EtOH	0.14250	287.88
	0.16241	294.95
	0.18061	300.68
	0.19945	308.15
	0.21627	312.92
	0.23651	316.05
MeCN	0.03697	290.62
	0.04574	296.68
	0.05180	299.98
	0.06041	304.65
	0.07022	309.18
AcOEt	0.08590	294.58
	0.09826	299.85
	0.10996	304.45
	0.11754	307.42

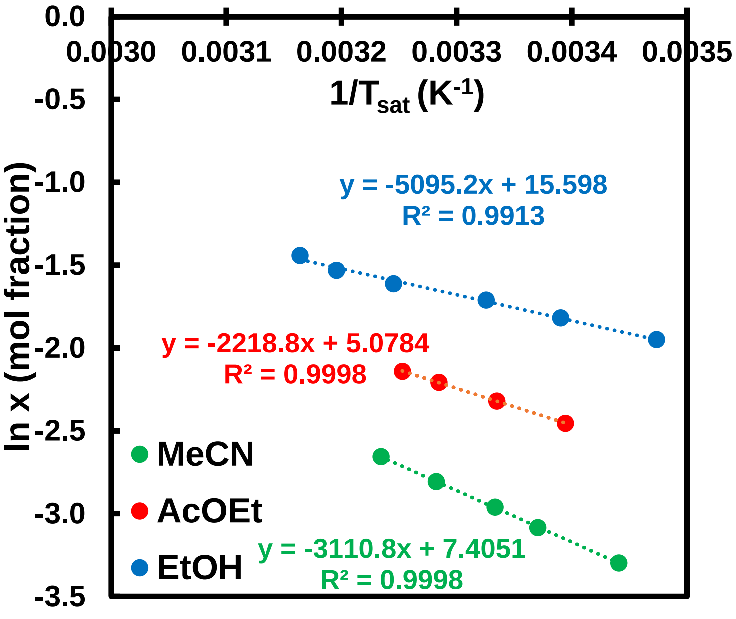

Figure A20: Van 't Hoff plots for benzoic acid.

Pimelic acid (**4**)

Table A8: Pimelic acid solubilities with Crystal16.

	Molar fraction x	Average T_{sat} (K)
MeCN	0.01957	308.62
	0.02999	314.15
	0.04210	318.98
	0.05619	323.25
	0.00979	298.72
	0.01266	302.55
	0.01508	305.05
AcOEt	0.02286	307.52
	0.02750	310.78
	0.03027	312.18
	0.02061	304.72
	0.02379	307.75

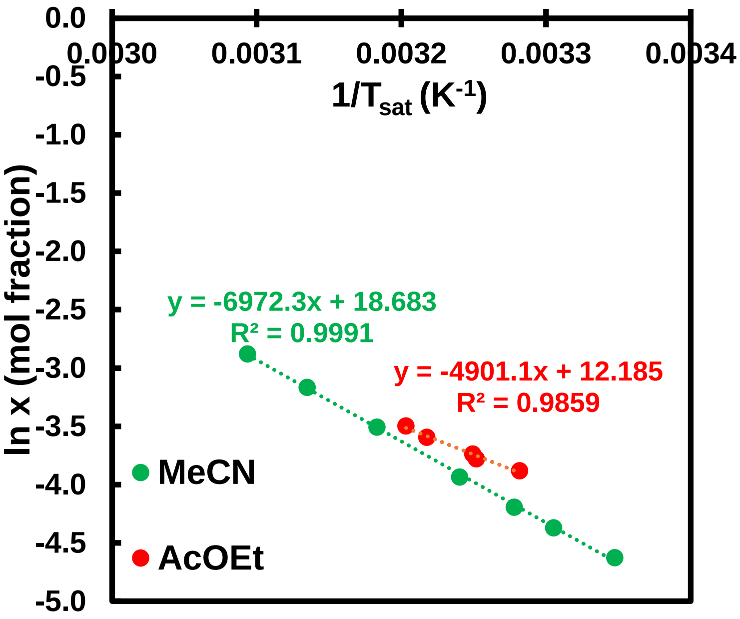

Figure A21: Van 't Hoff plots for pimelic acid.

Salicylic acid (**5**)

Table A9: Salicylic acid solubilities with Crystal16.

	Molar fraction x	Average T_{sat} (K)
EtOH	0.12098	286.65
	0.15694	303.38
	0.14560	299.58
	0.17904	312.82
	0.19251	320.02
	0.20828	326.02
MeCN	0.04238	306.48
	0.05062	311.48
	0.05605	314.60
	0.06332	317.02
	0.02647	291.58
	0.03132	296.98
	0.03795	303.55
	0.07017	323.52
AcOEt	0.07077	294.72
	0.08518	306.05
	0.10858	322.32

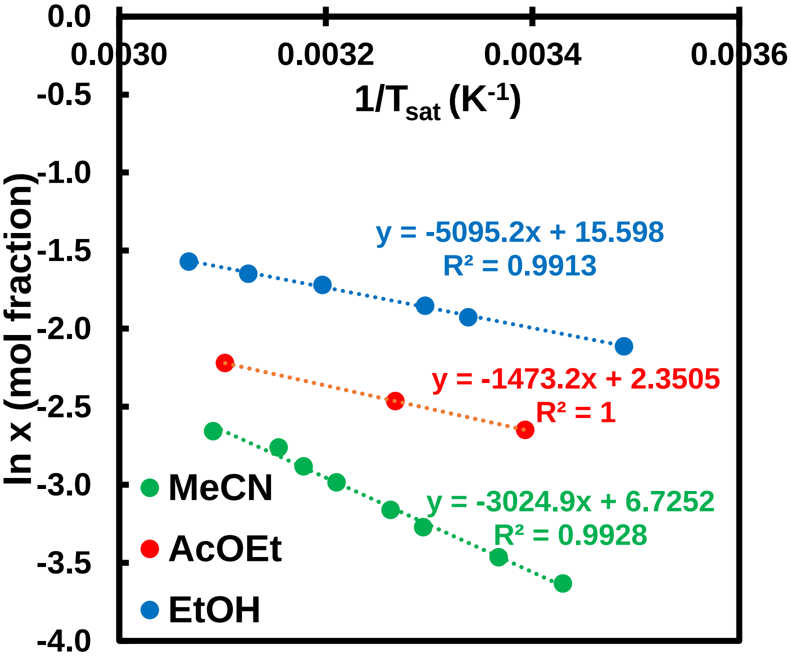

Figure A22: Van 't Hoff plots for salicylic acid.

1,4-Diiodotetrafluorobenzene (**6**)

Table A10: 1,4-Diiodotetrafluorobenzene solubilities with Crystal16.

	Molar fraction x	Average T_{sat} (K)
EtOH	0.07043	297.80
	0.08175	305.38
	0.09557	312.48
	0.07846	303.62
	0.11166	319.42

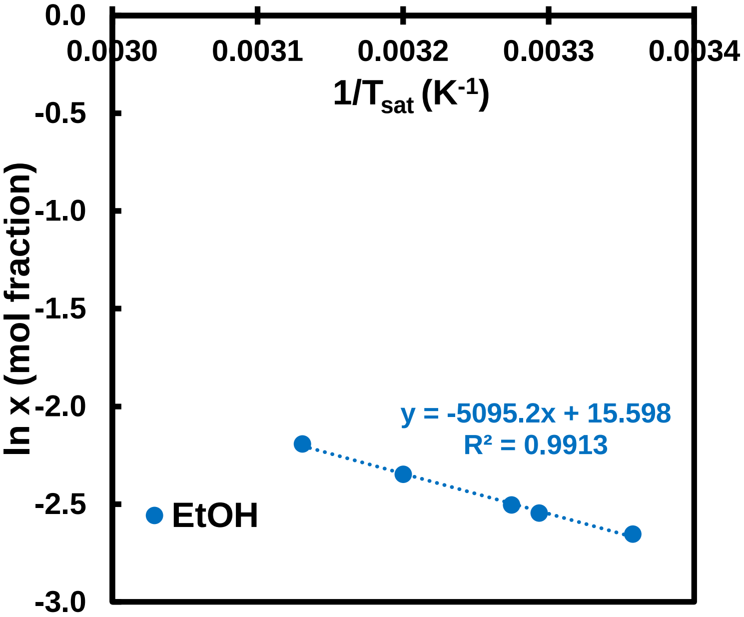

Figure A23: Van 't Hoff plot for 1,4-diiodotetrafluorobenzene.

4-Hydroxybenzoic acid (**7**)

Table A11: 4-Hydroxybenzoic solubilities with Crystal16.

	Molar fraction x	Average T_{sat} (K)
EtOH	0.12369	296.45
	0.13577	309.15
	0.14859	319.22
	0.12389	296.88
	0.12869	301.92
	0.15166	323.32
MeCN	0.01581	298.55
	0.01877	304.38
	0.02170	309.02
	0.02391	312.52

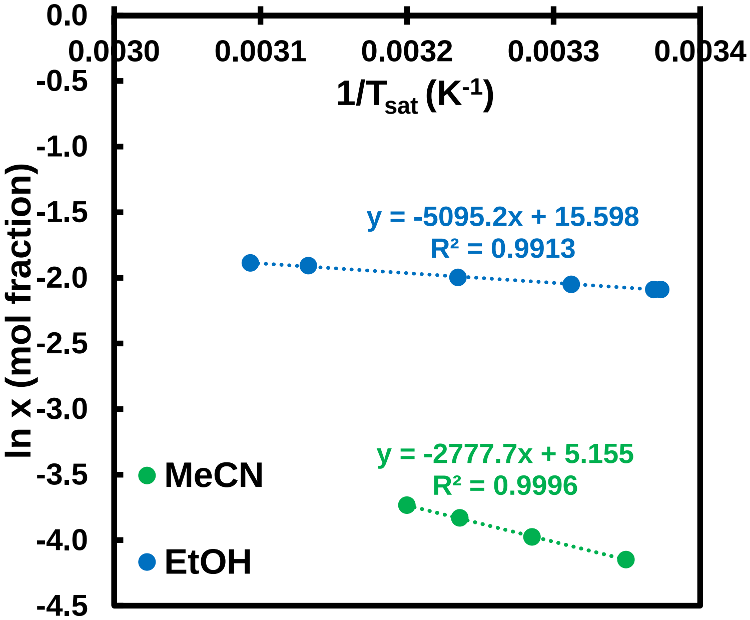

Figure A24: Van 't Hoff plots for 4-hydroxybenzoic acid.

4-aminobenzoic acid (**9**)

Table A12: 4-aminobenzoic acid solubilities with Crystal16.

	Molar fraction x	Average T_{sat} (K)
EtOH	0.04672	295.12
	0.06511	314.02
	0.08930	327.55
	0.05931	310.25
	0.07762	323.45
MeCN	0.03040	306.78
	0.03548	311.35
	0.04367	315.22
	0.02094	294.42
	0.02385	299.22
	0.02892	305.88
AcOEt	0.02539	285.15
	0.02997	300.92
	0.03353	309.85
	0.03850	317.45

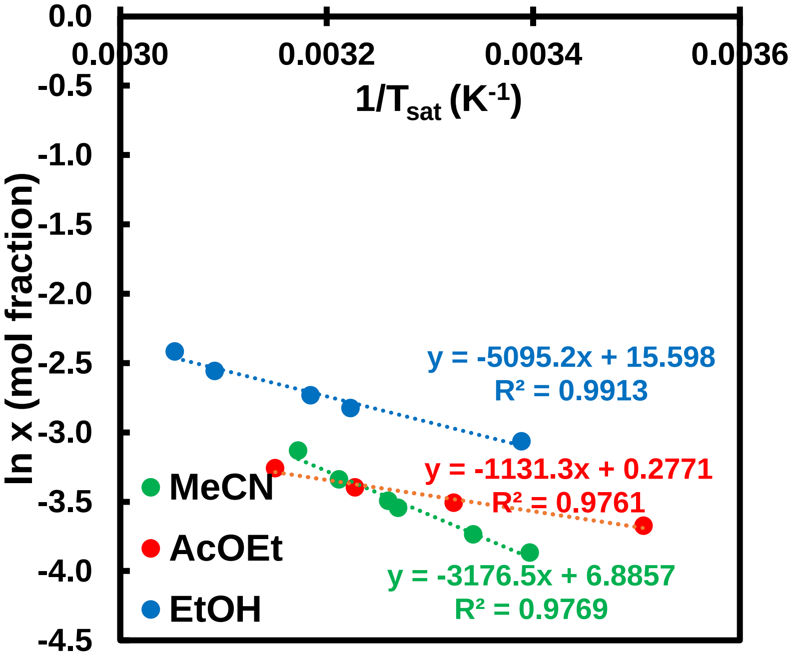

Figure A25: Van 't Hoff plots for 4-aminobenzoic acid.

Azelaic acid (**11**)

Table A13: Azelaic acid solubilities with Crystal16.

	Molar fraction x	Average T_{sat} (K)
EtOH	0.04803	294.58
	0.06705	302.18
	0.08730	311.22
	0.10216	317.38
AcOEt	0.00353	293.82
	0.00479	299.82
	0.00681	305.25
	0.00838	308.88

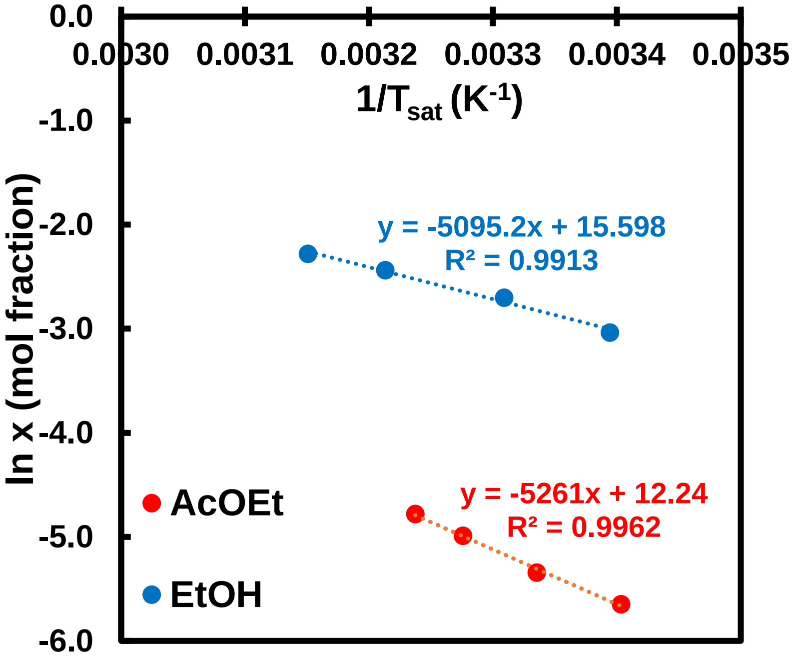

Figure A26: Van 't Hoff plots for azelaic acid.

4-Aminosalicylic acid (**12**)

Table A14: 4-Aminosalicylic acid solubilities with Crystal 16.

	Molar fraction x	Average T_{sat} (K)
MeCN	0.00824	311.02
	0.01064	320.08
	0.01270	329.15
	0.00532	294.22
	0.00690	304.52

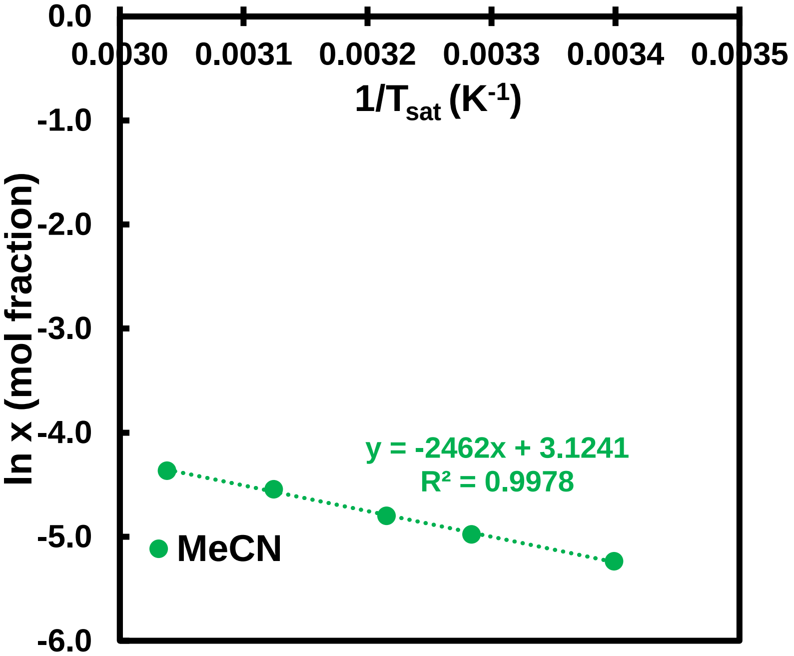

Figure A27: Van 't Hoff plots for 4-aminosalicylic acid.

3,5-dinitrobenzoic acid (**13**)

Table A15: 3,5-dinitrobenzoic acid solubilities with Crystal 16.

	Molar fraction x	Average T_{sat} (K)
MeCN	0.01662	304.55
	0.02308	315.85
	0.02787	322.38
	0.03295	328.52
	0.01124	291.55
	0.01400	298.48

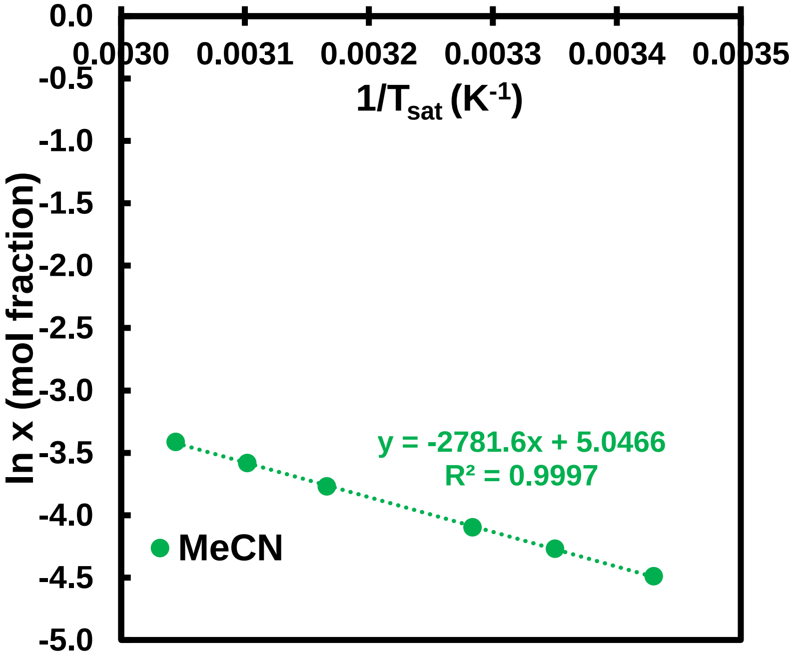

Figure A28: Van 't Hoff plots for 3,5-dinitrobenzoic acid.

trans-cinnamic acid (**14**)

Table A16: trans-cinnamic acid solubilities with Crystal16.

	Molar fraction x	Average T_{sat} (K)
EtOH	0.09441	307.55
	0.11460	320.15
	0.12712	323.62
	0.14219	330.32
MeCN	0.02600	304.58
	0.03285	310.65
	0.04132	316.05
	0.05008	320.05
	0.01819	296.18
	0.02275	301.78
AcOEt	0.03625	293.88
	0.04746	303.65
	0.05413	308.12
	0.06260	313.38

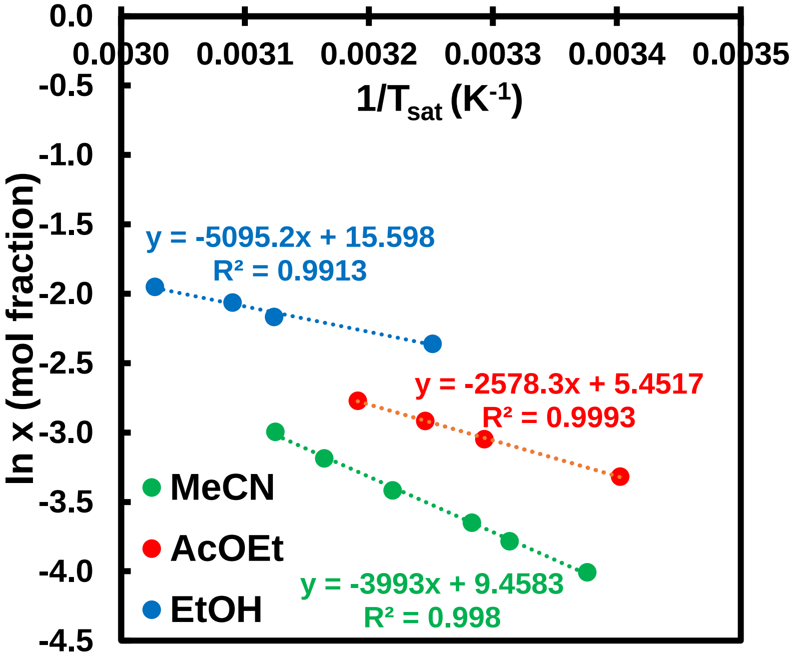

Figure A29: Van 't Hoff plots for trans-cinnamic acid.

Hydroquinone (**15**)

Table A17: Hydroquinone solubilities with Crystal 16.

	Molar fraction x	Average T_{sat} (K)
MeCN	0.06815	305.65
	0.08702	314.58
	0.10673	321.72
	0.12058	326.65
	0.05215	296.15
	0.03856	286.48

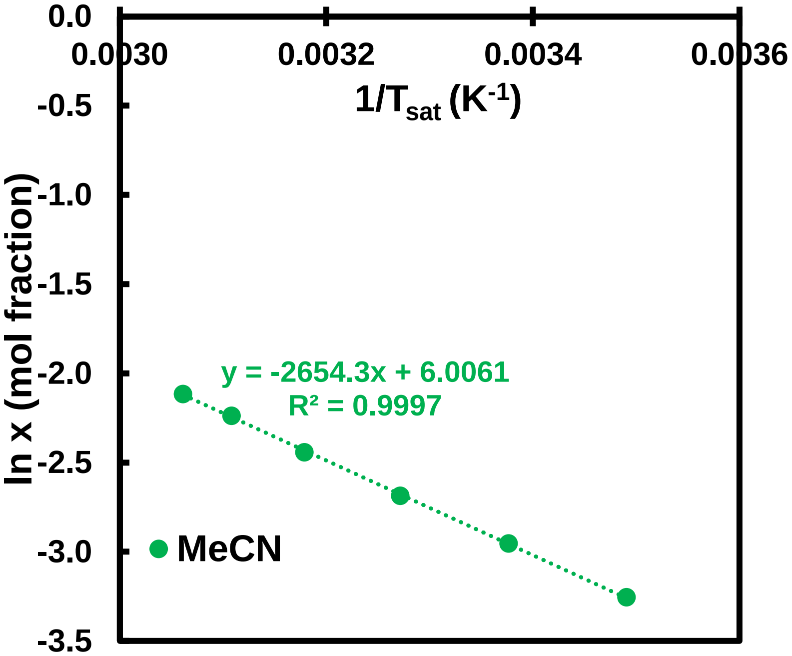

Figure A30: Van 't Hoff plots for hydroquinone.

3-hydroxybenzoic acid (**16**)

Table A18: 3-hydroxybenzoic acid solubilities with Crystal16.

	Molar fraction x	Average T_{sat} (K)
EtOH	0.11816	305.18
	0.14358	324.15
	0.11243	298.32
	0.12885	312.85
	0.13652	318.32
MeCN	0.01422	294.75
	0.01699	300.68
	0.01985	305.58
	0.02214	309.62
AcOEt	0.03386	296.87
	0.04548	314.55
	0.03857	303.18
	0.04221	308.28
	0.04867	317.43

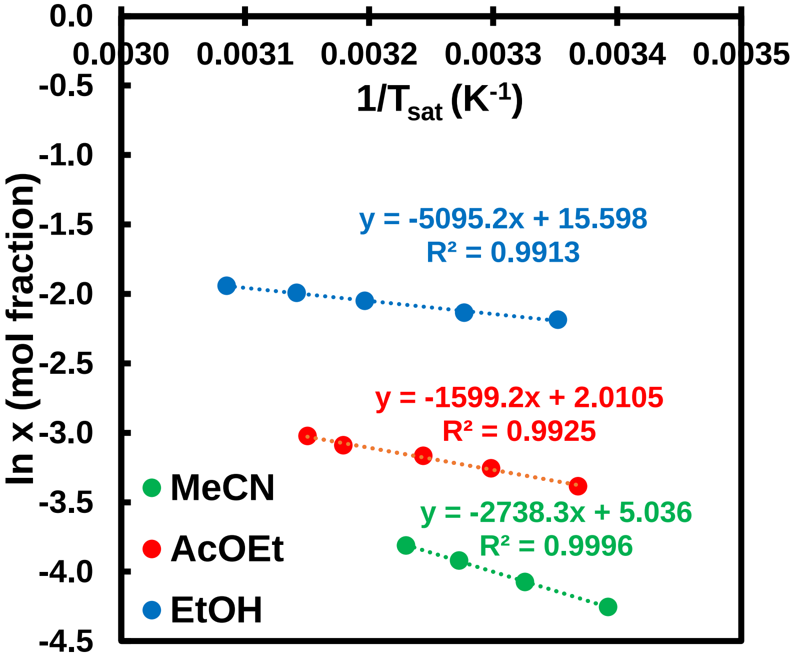

Figure A31: Van 't Hoff plots for 3-hydroxybenzoic acid.

Anthranilic acid (**17**)

Table A19: Anthranilic acid solubilities with Crystal16.

	Molar fraction x	Average T_{sat} (K)
EtOH	0.07297	287.58
	0.10451	305.45
	0.13092	316.45
	0.15430	324.62
MeCN	0.04539	299.92
	0.07768	314.08
	0.10263	322.68
	0.11930	328.95
AcOEt	0.05304	280.38
	0.06991	296.68
	0.08854	310.18
	0.10011	317.58

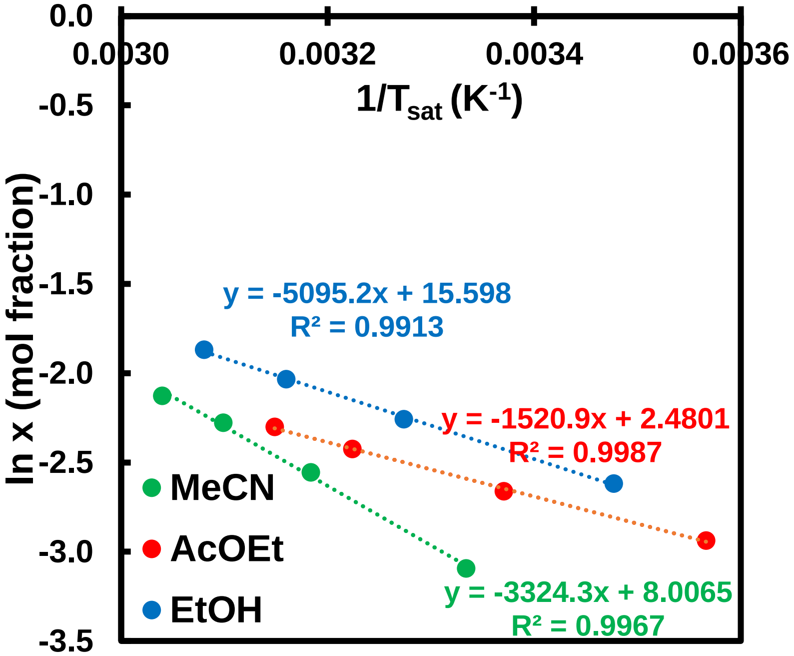

Figure A32: Van 't Hoff plots for anthranilic acid.

Vanillic acid (**20**)

Table A20: Vanillic acid solubilities with Crystal16.

	Molar fraction x	Average T_{sat} (K)
EtOH	0.03420	302.95
	0.04180	314.02
	0.04893	322.05
	0.03406	303.95
	0.03854	310.78
MeCN	0.00610	315.19
	0.00700	319.24
	0.00820	324.31
	0.00925	328.52
AcOEt	0.00628	298.91
	0.00753	307.94
	0.00843	314.34
	0.00935	318.97

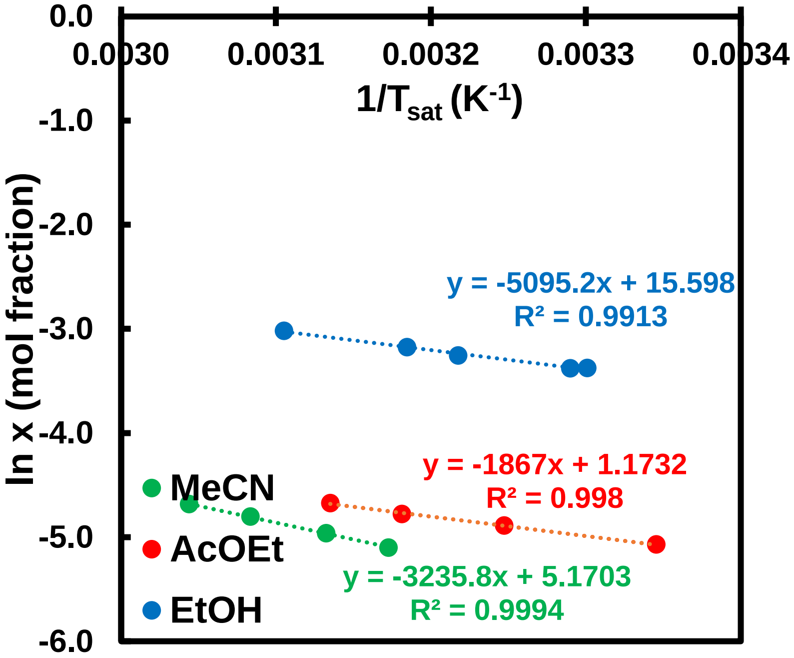

Figure A33: Van 't Hoff plots for vanillic acid.

4-nitrobenzoic acid (**21**)

Table A21: 4-nitrobenzoic acid solubilities with Crystal16.

	Molar fraction x	Average T_{sat} (K)
EtOH	0.00792	295.98
	0.01030	303.88
	0.01268	309.12
	0.01494	313.32
	0.01875	318.92
AcOEt	0.00508	301.62
	0.00596	307.45
	0.00731	315.28
	0.00859	321.82

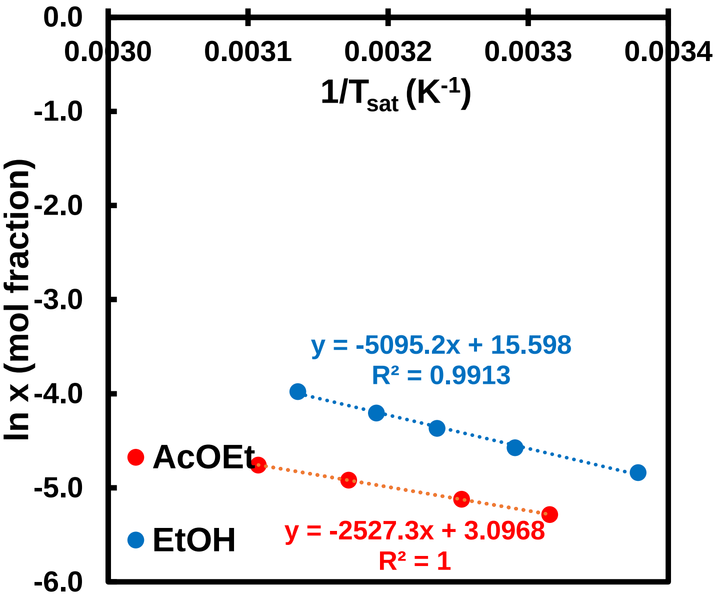

Figure A34: Van 't Hoff plots for 4-nitrobenzoic acid.

2,5-dihydroxybenzoic acid (**22**)

Table A22: 2,5-dihydroxybenzoic acid solubilities with Crystal16.

	Molar fraction x	Average T_{sat} (K)
EtOH	0.12645	284.88
	0.13976	297.55
	0.15176	316.65
	0.16106	324.15
	0.14059	309.35
	0.14593	314.55
	0.15436	321.35
	0.16044	325.75
MeCN	0.03037	309.98
	0.03766	319.38
	0.04502	327.85
	0.02700	305.62
	0.02940	308.92
	0.03065	310.85
	0.03573	317.88
AcOEt	0.05745	314.73
	0.06571	331.01
	0.05365	309.53
	0.05601	314.29
	0.05996	321.71
	0.06207	325.44

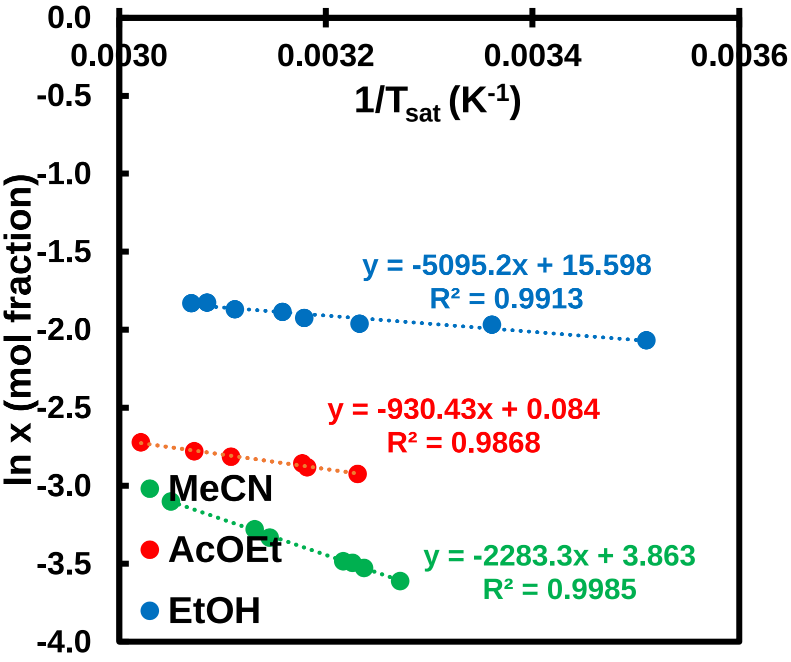

Figure A35: Van 't Hoff plots for 2,5-dihydroxybenzoic acid.

2-fluorobenzoic acid (**23**)

Table A23: 2-fluorobenzoic acid solubilities with Crystal16.

	Molar fraction x	Average T_{sat} (K)
EtOH	0.21026	297.98
	0.25579	310.25
	0.31040	323.98
	0.33159	326.42
MeCN	0.06421	294.32
	0.08018	300.75
	0.09646	306.18
	0.10800	309.72
AcOEt	0.13149	311.15
	0.14624	315.88
	0.15638	318.95
	0.16940	322.78
	0.09759	298.05
	0.11411	305.28

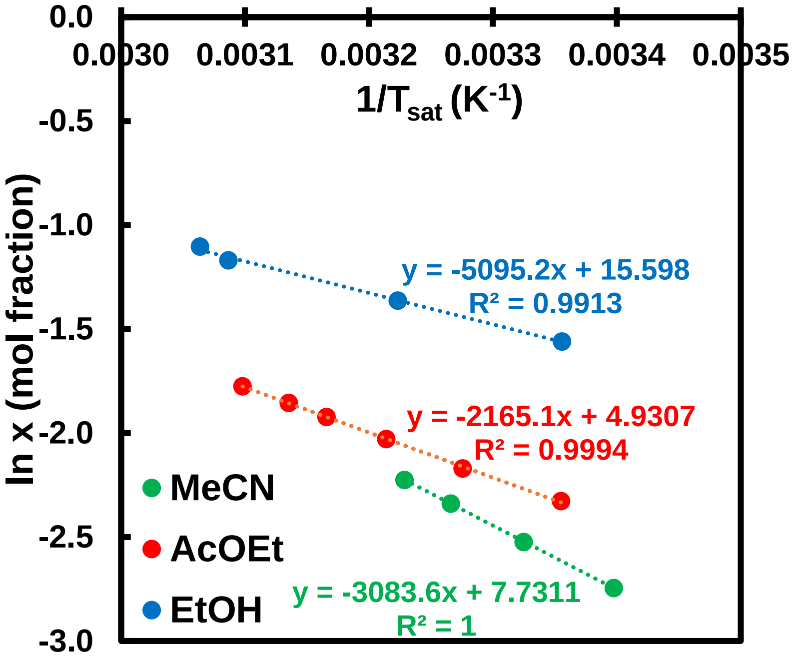

Figure A36: Van 't Hoff plots for 2-fluorobenzoic acid.

3,5-Dihydroxybenzoic acid (**24**)

Table A24: 3,5-dihydroxybenzoic acid solubilities with Crystal 16.

	Molar fraction x	Average T_{sat} (K)
MeCN	0.01455	309.75
	0.01843	316.45
	0.02408	323.98
	0.02860	328.58
	0.00669	287.05
	0.00914	296.88
	0.01194	303.65

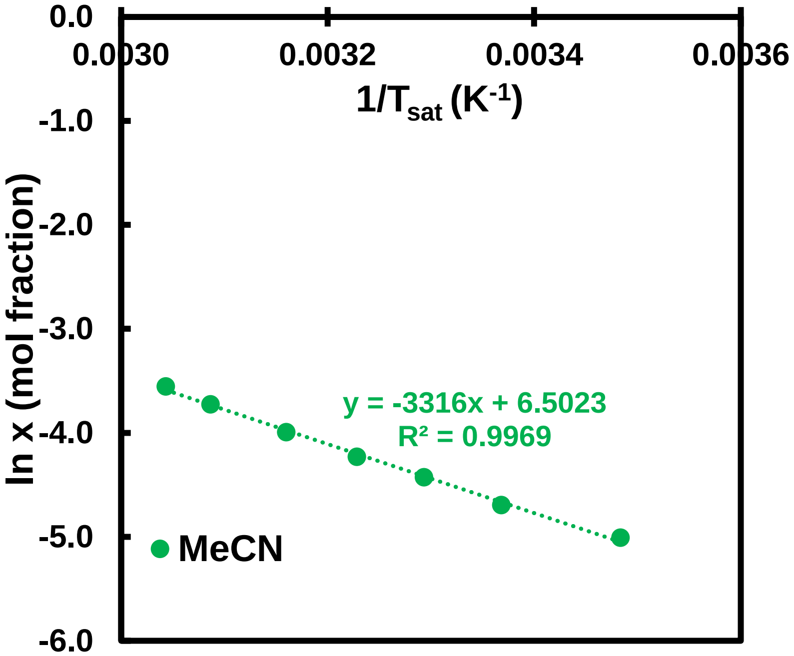

Figure A37: Van 't Hoff plots for 3,5-dihydroxybenzoic acid.

3-nitrobenzoic acid (**25**)

Table A25: 3-nitrobenzoic acid solubilities with Crystal16.

	Molar fraction x	Average T_{sat} (K)
MeCN	0.05277	298.95
	0.07554	308.78
	0.10244	314.15
	0.12569	320.85
	0.08768	313.45
	0.06196	303.42
	0.06965	306.58
AcOEt	0.08701	304.95
	0.09869	311.05
	0.12141	323.55

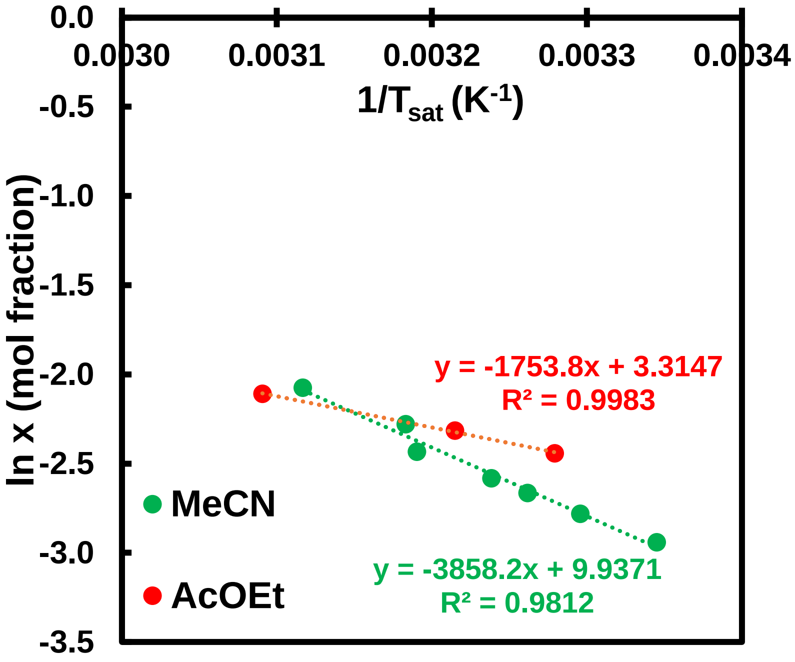

Figure A38: Van 't Hoff plots for 3-nitrobenzoic acid.

4-nitrophenol (**26**)

Table A26: 4-nitrophenol solubilities with Crystal16.

	Molar fraction x	Average T_{sat} (K)
EtOH	0.32995	296.05
	0.40186	321.60
	0.37231	312.38
	0.39650	320.38
AcOEt	0.27923	302.12
	0.29343	308.12
	0.31332	315.45
	0.33093	321.22

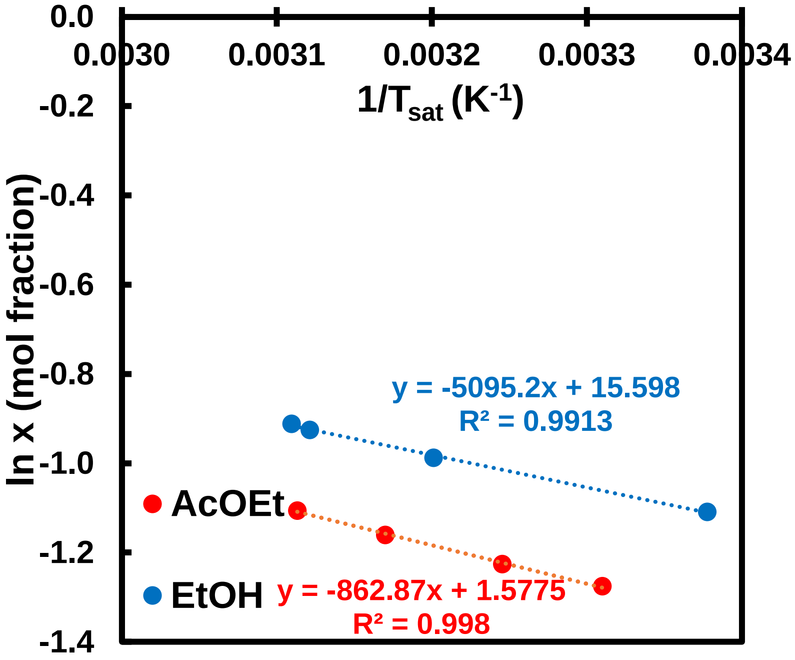

Figure A39: Van 't Hoff plots for 4-nitrophenol.

1-hydroxy-2-naphtoic acid (**27**)

Table A27: 1-hydroxy-2-naphtoic acid solubilities with Crystal 16.

	Molar fraction x	Average T_{sat} (K)
AcOEt	0.02221	315.28
	0.02592	322.95
	0.02895	331.95
	0.01765	302.88
	0.02010	309.25
	0.02069	311.38

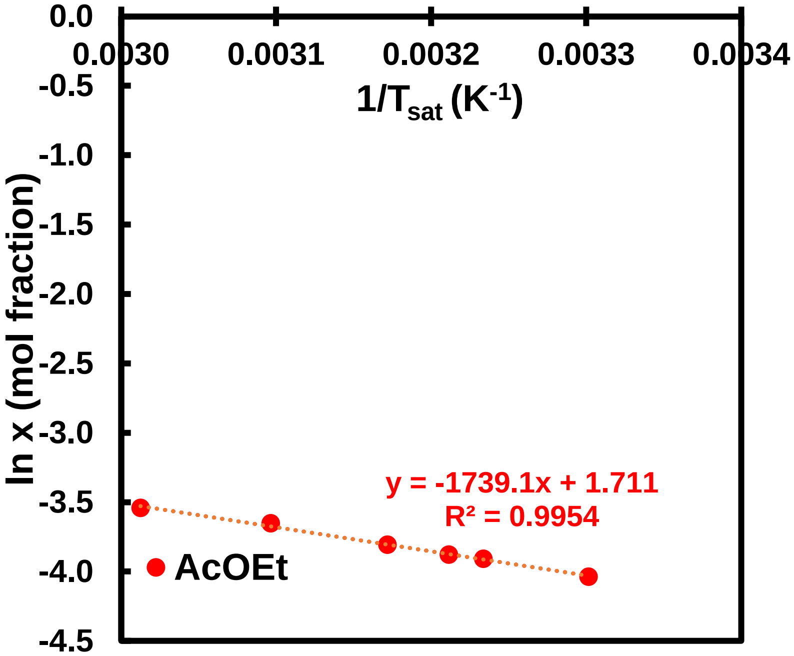

Figure A40: Van 't Hoff plots for 1-hydroxy-2-naphtoic acid.

2,4-dihydroxybenzoic acid (**28**)

Table A28: 2,4-dihydroxybenzoic acid solubilities with Crystal16.

	Molar fraction x	Average T_{sat} (K)
EtOH	0.11936	297.42
	0.14665	326.75
	0.12966	309.58
	0.14095	320.42
	0.15231	332.22
MeCN	0.03089	311.29
	0.03680	319.19
	0.04397	326.57
	0.04891	329.67
AcOEt	0.06524	328.34
	0.06844	330.90
	0.05774	308.44
	0.06127	318.69

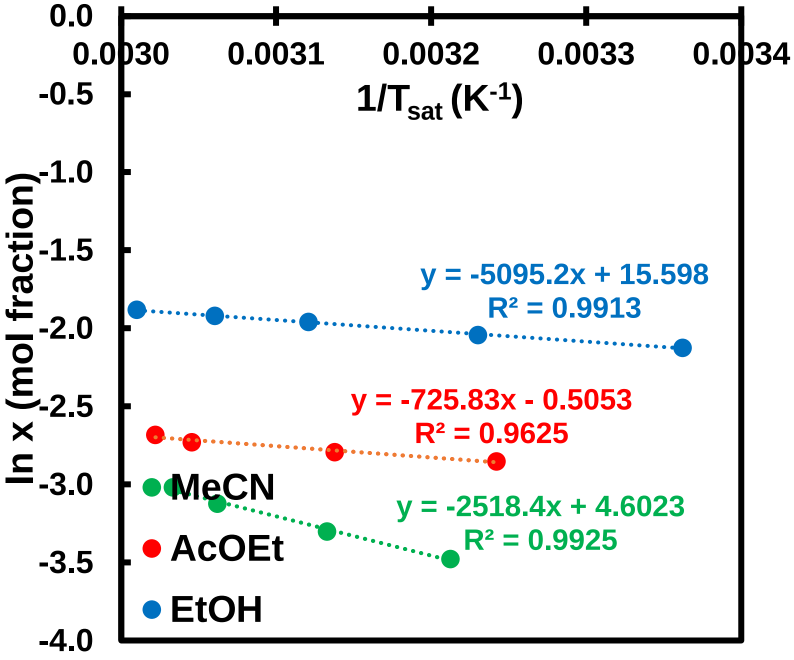

Figure A41: Van 't Hoff plots for 2,4-dihydroxybenzoic acid.

Orcinol (**29**)

Solubility measurements of orcinol in EtOH, MeCN and AcOEt were not possible as any mixture in these solvents lead to the formation of a viscous liquor for which crystallization never occurred when cooling. A possible explanation for this phenomenon is the relatively low melting point of that compound (109°C) and a suspected eutectic equilibrium whose temperature would be too low to induce supersaturation high enough when cooling.

Dodecanedioic acid (**30**)

Table A29: Dodecanedioic acid solubilities with Crystal 16.

	Molar fraction x	Average T_{sat} (K)
EtOH	0.00644	289.38
	0.00856	293.72
	0.00968	295.75
	0.01118	297.72
	0.01782	305.52
	0.02422	310.85
	0.03141	315.42

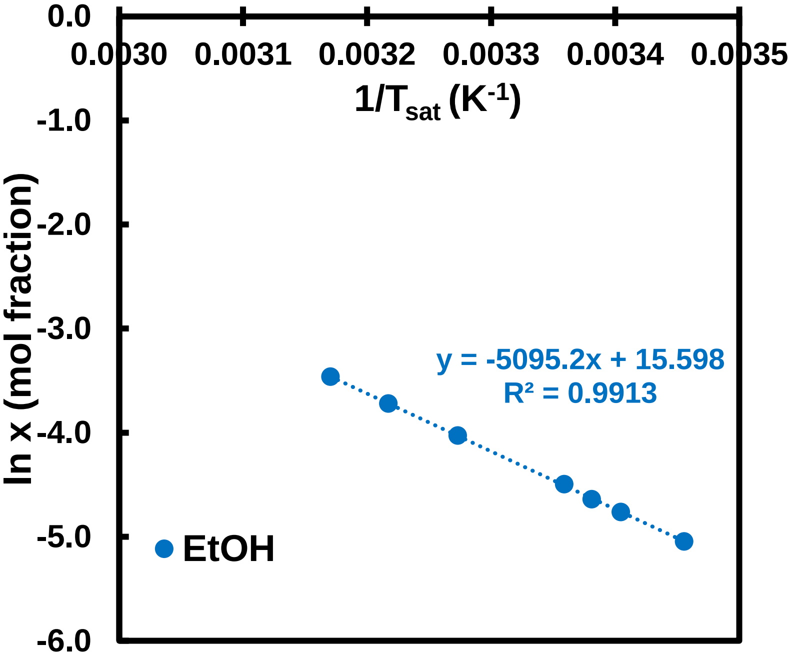

Figure A42: Van 't Hoff plots for dodecanedioic acid.

Table A30: Ternary compositions and saturation temperatures results screened by the STM method. 'T_r' is the highest value of theoretical saturation temperature computed from pure components Van 't Hoff plots and 'T_{sat}' is the average of three experimental measurements of saturation temperature. ([i]: positive hits for which screening was not performed in all three solvents as a cocrystal was found in one ; [ii]: false positive that could be due to overall solubility lowered by unfavourable interactions)

Rank	Coformer	Solvent	Concentration RS-PZQ (mol/L)	Concentration coformer (mol/L)	Ratio $M_{PZQ:cof}$ in solution (mol_{cof} per mol_{PZQ})	Theoretical T_r (K)	Experimental average T_{sat} (K)	ΔT (= $T_{sat} - T_r$)
1	Sebacic acid	EtOH	0.2891	0.4114	1.42	303.19	298.15	**-5.04**
		MeCN	Coformer insoluble					
		AcOEt	0.2082	0.0548	0.26	309.16	303.55	**-5.61**
2	Suberic acid	EtOH	0.2878	0.5995	2.08	302.56	296.72	**-5.84**
		MeCN	Coformer insoluble					
		AcOEt	Poor affinity between coformer and solvent					
3	Benzoic acid	EtOH	0.2866	3.8135	13.30	302.43	307.18	4.75 [ii]
		MeCN	0.3255	1.0633	3.27	303.86	290.55	**-13.31**
		AcOEt	0.2129	2.7418	12.88	309.29	304.15	**-5.14**
4	Pimelic acid	EtOH	Solubility measurements not consistent					
		MeCN	0.3180	0.2384	0.75	303.65	289.52	**-14.13**
		AcOEt	0.2147	0.5055	2.36	309.11	302.58	**-6.53**
5	Salicylic acid	EtOH	0.2882	3.0522	10.59	302.53	291.15	**-11.38**
		MeCN	0.3259	0.7060	2.17	304.04	**Never crystallized upon cooling**	
		AcOEt	0.2077	1.9180	9.24	344.13	299.45	**-9.49**
6	1,4-Diiodotetrafluorobenzene[i]	EtOH	0.2856	1.4377	5.03	302.54	**Crystallized when mixed: never dissolved**	
7	4-Hydroxybenzoic acid[i]	EtOH	0.3203	2.6470	8.26	306.35	326.45	**20.1**
		MeCN	0.4089	0.3789	0.93	309.32	**Crystallized when mixed: never dissolved**	
8	Terephthalic acid	Coformer insoluble in all solvents tried: could not be screened with STM method						
9	4-Aminobenzoic acid	EtOH	0.2868	0.9609	3.35	302.64	280.58	**-22.06**
		MeCN	0.4091	0.5914	1.45	309.05	284.88	**-24.17**
		AcOEt	0.2062	0.6976	3.38	310.20	**Never crystallized upon cooling**	
10	Isophthalic acid	Coformer insoluble in all solvents tried: could not be screened with STM method						
11	Azelaic acid	EtOH	0.2895	1.1863	4.10	302.61	297.92	**-4.69**
		MeCN	Solubility measurements not consistent					
		AcOEt	0.2181	0.1644	0.75	309.53	298.52	**-11.01**
12	4-Aminosalicylic acid[i]	EtOH	Suspected degradation behaviour (solubility reducing over time)					
		MeCN	0.3237	0.1219	0.38	305.15	312.30	**7.15**
13	3,5-Dinitrobenzoic acid[i]	EtOH	System forming too dense crystals to be stirred					
		MeCN	0.3168	0.2834	0.89	303.75	326.72	**22.97**
14	trans-Cinnamic acid	EtOH	0.2949	1.5796	5.36	302.94	294.78	**-8.16**
		MeCN	0.3130	0.4353	1.39	303.68	288.72	**-14.97**
		AcOEt	0.2095	1.1415	5.45	308.74	302.05	**-6.69**

15	Hydroquinone[i]	EtOH	Degradation (solutions turning pink over time)					
		MeCN	0.3203	1.1689	3.65	303.54	317.75	**14.21**
16	3-Hydroxybenzoic acid	EtOH	0.2943 / 0.7009	2.2718 / 2.7447	7.72 / 3.92	303.02 / 319.97	**Never crystallized upon cooling**	
		MeCN	0.4110 / 0.6536	0.3862 / 0.5023	0.94 / 0.77	309.68 / 319.00	**Never crystallized upon cooling**	
		AcOEt	0.2073 / 0.2997	0.8648 / 1.0318	4.17 / 3.44	309.11 / 319.57	**Never crystallized upon cooling**	
17	Anthranilic acid	EtOH	0.3115	1.9452	6.25	303.93	**Never crystallized upon cooling**	
		MeCN	0.3150	0.9416	2.99	303.47	**Never crystallized upon cooling**	
		AcOEt	0.2158	1.8857	8.74	309.55	299.98	**-9.57**
18	Phthalic acid	Coformer insoluble in all solvents tried: could not be screened with STM method						
19	D-(-)-Tartaric acid	Solubility issues in all solvents tried						
20	Vanillic acid	EtOH	0.2913	0.5971	2.05	303.07	313.14	**10.07**
		MeCN	0.6628	0.1155	0.17	318.58	312.44	**-6.14**
		AcOEt	0.3057	0.1854	0.61	319.56	325.13	**5.56**
21	4-Nitrobenzoic acid	EtOH	0.2977	0.1783	0.60	303.21	300.41	**-2.80**
		MeCN	Coformer insoluble					
		AcOEt	0.2095	0.1223	0.58	309.00	**Never crystallized upon cooling**	
22	2,5-Dihydroxybenzoic acid	EtOH	0.6903	3.1355	4.54	320.84	275.05	**-45.79**
		MeCN	0.3220	0.4548	1.41	304.09	**Crystallized when mixed: never dissolved**	
		AcOEt	0.2987	1.2287	4.11	319.35	329.22	**9.87**
23	2-Fluorobenzoic acid	EtOH	0.2894	5.0500	17.45	302.76	298.28	**-4.48**
		MeCN	0.3130	1.6474	5.26	303.54	294.55	**-8.99**
		AcOEt	0.2182	2.7947	12.81	309.55	303.22	**-6.33**
24	3,5-Dihydroxybenzoic acid[i]	EtOH	Solubility measurements not consistent					
		MeCN	0.3079	0.2041	0.66	303.18	329.85	**26.67**
25	3-Nitrobenzoic acid	EtOH	Solubility measurements not consistent					
		MeCN	0.3119	1.1336	3.64	303.57	287.35	**-16.22**
		AcOEt	0.2117	2.0492	9.68	309.22	298.75	**-10.47**
26	4-Nitrophenol	EtOH	0.2685	8.6263	32.13	301.26	292.98	**-8.28**
		MeCN	Solubility too high and solubility measurements not consistent					
		AcOEt	0.2176	9.0790	41.65	316.36	312.55	**-3.81**
27	1-Hydroxy-2-naphtoic acid	EtOH	Suspected degradation (colour changes over time)					
		MeCN	Coformer insoluble					
		AcOEt	0.2147	0.1383	0.64	309.12	**Never crystallized upon cooling**	

28	2,4-Dihydroxybenzoic acid	EtOH	0.2899	2.3608	8.14	302.63	332.07	**29.43**
		MeCN	0.6625	0.6590	0.99	319.17	**Crystallized when mixed: never dissolved**	
		AcOEt	0.2166 / 0.3025	1.2401 / 1.3074	5.72 / 4.32	313.47 / 320.33	**Crystallized when mixed: never dissolved**	
29	Orcinol	Mixture of orcinol with any solvent forms of an undersaturated viscous liquor: no crystallization possible						
30	Dodecanedioic acid	EtOH	0.2920	0.2684	0.92	303.10	300.08	**-3.02**
		MeCN	Coformer insoluble					
		AcOEt	Poor affinity between coformer and solvent					

A4 – Thermograms Related to EUT Method Results

This section presents thermograms results obtained by DSC through EUT method trials, with RS-PZQ issues regarding crystallization from the melt (Figure A43), example of coformers showing sought-after thermal behaviour for the use of EUT method (Figure A44) and difficulty in reaching equilibrium from melt crystallization with coformers physical mixtures (Figures A45 and A46).

Praziquantel (*RS*-PZQ)

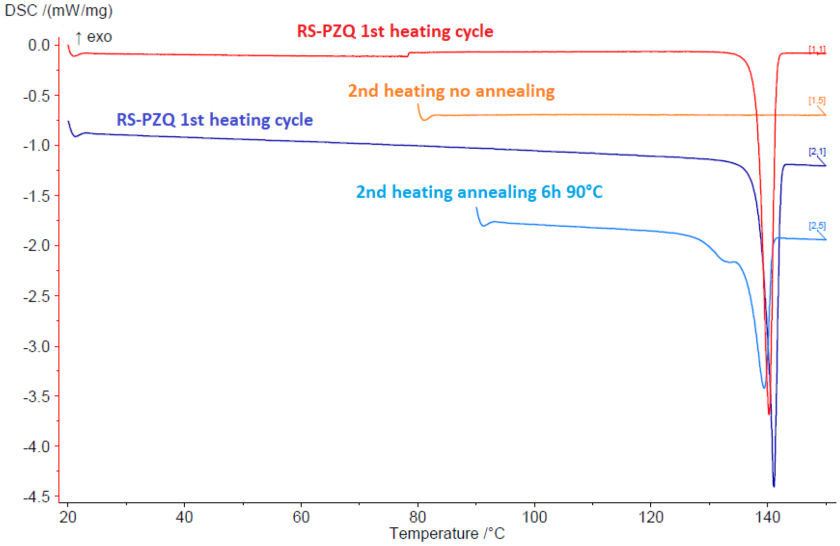

Figure A43: Comparison between two pure RS-PZQ samples heated a first time until melting and a second time after: no annealing (no crystallization from the melt occurring, in orange) and with a 6 h annealing at 90 °C (evidence of an impurity starting to appear due to degradation, in light blue)

Selection of coformers not degrading with temperature

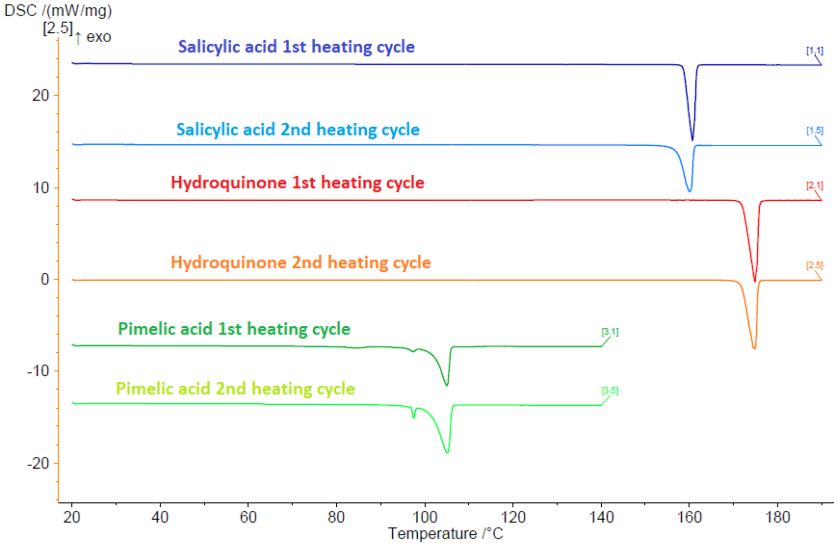

Figure A44: Thermograms obtained for a selection of coformers crystallizing back to their stable equilibrium from the melt (first and second heating cycles identical)

Screening on 10/90 and 90/10 PZQ/Hydroquinone physical mixtures

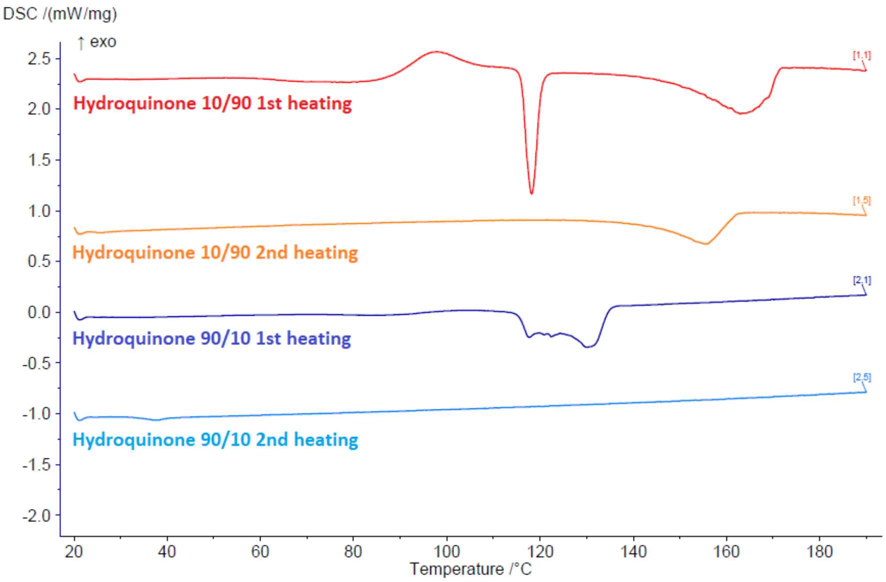

Figure A45: Thermograms during screening of 10/90 and 90/10 PZQ/Hydroquinone physical mixtures (two heating cycles, no annealing)

Screening on 10/90 and 90/10 PZQ/Pimelic acid physical mixtures

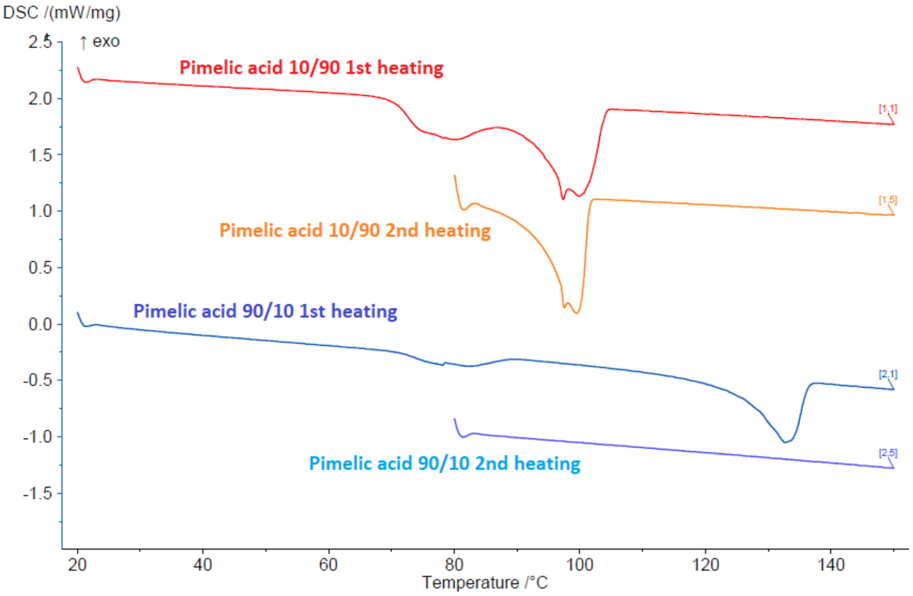

Figure A46: Thermograms during screening of 10/90 and 90/10 PZQ/Pimelic acid physical mixtures (two heating cycles, annealing 80 °C 30 min)

Appendix B - Supporting Information of Chapter 4

Supporting Information of Chapter 4: “Multicomponent Chiral Quantification with Ultraviolet Circular Dichroism Spectroscopy: Ternary and Quaternary Phase Diagrams of Levetiracetam”

Maxime D. Charpentier[1], Raghunath Venkatramanan[1], Céline Rougeot[2], Tom Leyssens[3], Karen Johnston[4], Joop H. ter Horst[1,5]

1. EPSRC Centre for Innovative Manufacturing in Continuous Manufacturing and Crystallization (CMAC), University of Strathclyde, Technology and Innovation Centre, 99 George Street, Glasgow G1 1RD, U.K.

2. UCB Pharma SA, chemin du Foriest, 1420 Braine-L’Alleud, Belgium

3. Institute of Condensed Matter and Nanosciences, UCLouvain, Place L. Pasteur 1, Belgium.

4. Department of Chemical and Process Engineering, University of Strathclyde, James Weir Building, 75 Montrose Street, Glasgow G1 1XJ, U.K.

5. Univ Rouen Normandie, Laboratoire Sciences et Méthodes Séparatives (SMS), UR 3233, F-76000 Rouen, France

Table of contents

B1 – Materials

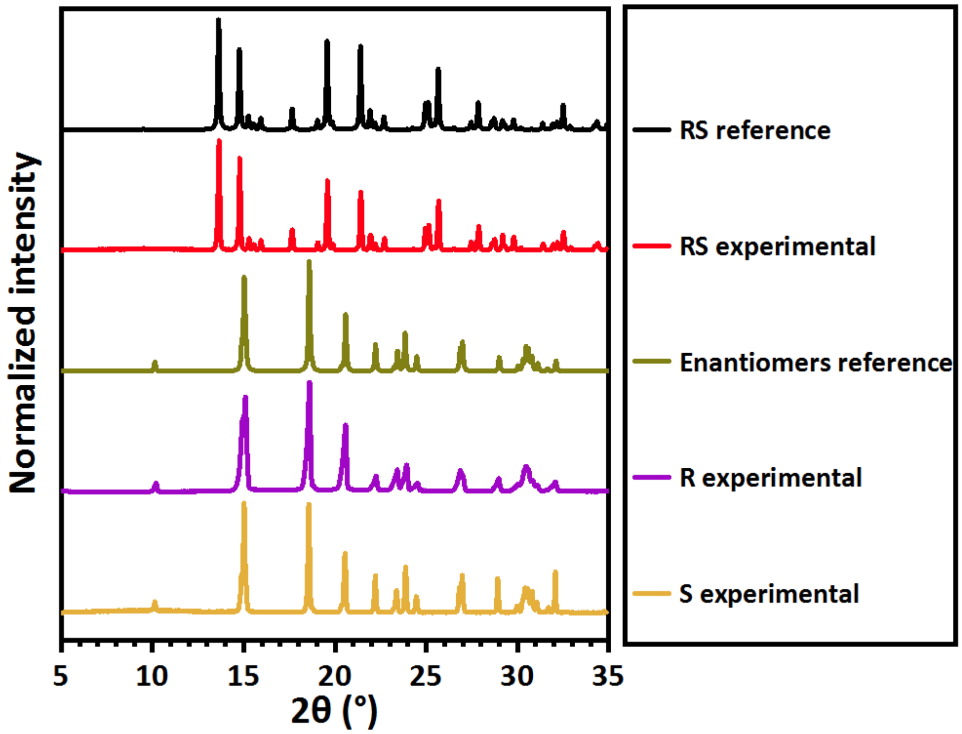

Figure B7: Experimental and reference XRPD patterns for solids of both enantiomers, and racemic compound RS.

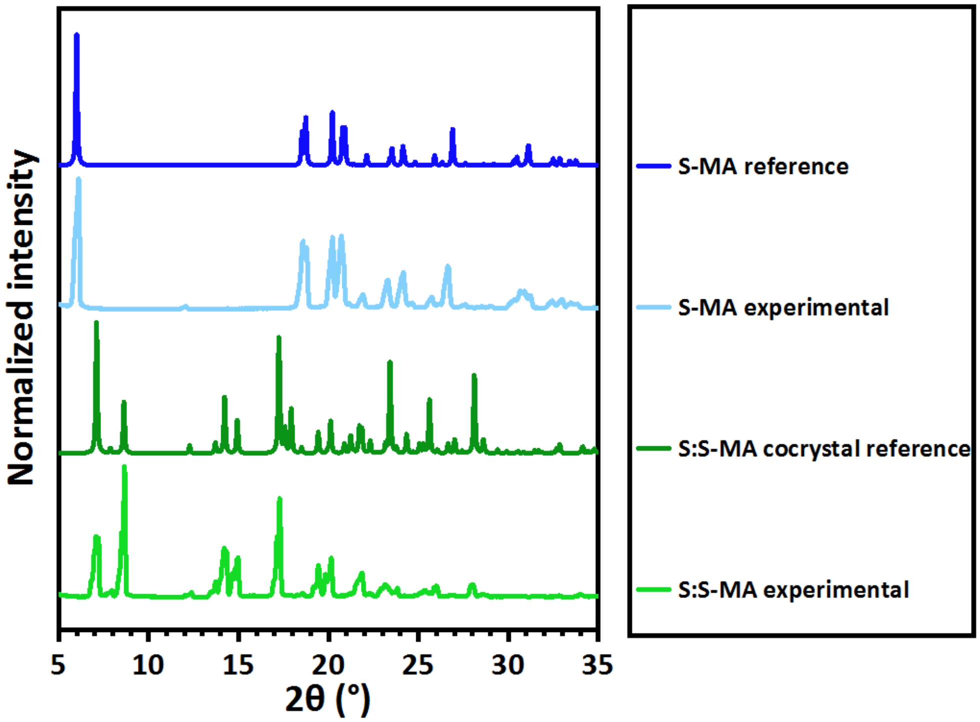

Figure B8: Experimental and reference XRPD patterns for solids of S:S-MA cocrystal and S-MA.

B2 – Multivariate Calibration Model Development Data

B2.1 – Mass Fractions of Calibration Samples Used

Table B2: Components mass fractions of calibration samples prepared in MeCN used for the calibration model.

Section	x_R	x_S	$x_{S\text{-}MA}$
Ternary R/S/MeCN	0	0.001266	0
	0	0.002657	0
	0	0.003947	0
	0	0.005210	0
	0	0.006307	0
	0.000115	0.001126	0
	0.000226	0.002213	0
	0.000348	0.003403	0
	0.000464	0.004538	0
	0.000580	0.005668	0
	0.000243	0.000990	0
	0.000492	0.001999	0
	0.000740	0.003008	0
	0.000985	0.004007	0
	0.001230	0.005004	0
	0.000381	0.000897	0
	0.000764	0.001801	0
	0.001150	0.002710	0
	0.001533	0.003612	0
	0.001915	0.004513	0
	0.000518	0.000813	0
	0.001038	0.001629	0
	0.001557	0.002444	0
	0.002080	0.003265	0
	0.002598	0.004078	0
	0.000636	0.000636	0
	0.001286	0.001286	0
	0.001931	0.001931	0
	0.002578	0.002578	0
	0.003219	0.003219	0
	0.001266	0	0
	0.002657	0	0
	0.003947	0	0
	0.005210	0	0
	0.006307	0	0
	0.001126	0.000115	0
	0.002213	0.000226	0

	0.003403	0.000348	0
	0.004538	0.000464	0
	0.005668	0.000580	0
	0.000990	0.000243	0
	0.001999	0.000492	0
	0.003008	0.000740	0
	0.004007	0.000985	0
	0.005004	0.001230	0
	0.000897	0.000381	0
	0.001801	0.000764	0
	0.002710	0.001150	0
	0.003612	0.001533	0
	0.004513	0.001915	0
	0.000813	0.000518	0
	0.001629	0.001038	0
	0.002444	0.001557	0
	0.003265	0.002080	0
	0.004078	0.002598	0
Ternary S/SMA/MeCN	0	0	0.001197
	0	0	0.002379
	0	0	0.003604
	0	0	0.004751
	0	0	0.005964
	0	0.000296	0.000936
	0	0.000608	0.001922
	0	0.000917	0.002900
	0	0.001238	0.003916
	0	0.001555	0.004918
	0	0.000460	0.000808
	0	0.000924	0.001625
	0	0.001395	0.002452
	0	0.001859	0.003268
	0	0.002334	0.004103
	0	0.000743	0.000527
	0	0.001490	0.001057
	0	0.002220	0.001575
	0	0.002982	0.002115
	0	0.003721	0.002640
	0	0.000942	0.000261
	0	0.001941	0.000537
	0	0.002900	0.000802
	0	0.003832	0.001060
	0	0.004807	0.001329

	0	0.001248	0
	0	0.002465	0
	0	0.003723	0
	0	0.004978	0
	0	0.006244	0
	0	0.000180	0.001131
	0	0.000352	0.002214
	0	0.000527	0.003310
	0	0.000704	0.004427
	0	0.000889	0.005590
	0	0.000355	0.000903
	0	0.000713	0.001817
	0	0.001041	0.002652
	0	0.001405	0.003579
	0	0.001763	0.004490
	0	0.000684	0.000616
	0	0.001371	0.001235
	0	0.002046	0.001842
	0	0.002734	0.002461
	0	0.003426	0.003084
	0	0.000893	0.000465
	0	0.001759	0.000916
	0	0.002650	0.001381
	0	0.003553	0.001852
	0	0.004457	0.002323
	0	0.001100	0.000126
	0	0.002206	0.000252
	0	0.003314	0.000379
	0	0.004422	0.000506
	0	0.005550	0.000635
Ternary R/SMA/MeCN	0.000136	0	0.001150
	0.000276	0	0.002330
	0.000416	0	0.003507
	0.000554	0	0.004668
	0.000242	0	0.001049
	0.000490	0	0.002124
	0.000737	0	0.003193
	0.000982	0	0.004254
	0.000354	0	0.000844
	0.000716	0	0.001710
	0.001080	0	0.002579
	0.001440	0	0.003436
	0.000522	0	0.000742

	0.001054	0	0.001499
	0.001587	0	0.002256
	0.002113	0	0.003005
	0.000655	0	0.000649
	0.001316	0	0.001303
	0.001960	0	0.001942
	0.002645	0	0.002620
	0.000663	0	0.000429
	0.001335	0	0.000864
	0.002004	0	0.001296
	0.002676	0	0.001731
	0.003344	0	0.002163
	0.000755	0	0.000319
	0.001523	0	0.000643
	0.002285	0	0.000965
	0.003055	0	0.001290
	0.003813	0	0.001610
	0.000831	0	0.000200
	0.001673	0	0.000403
	0.002518	0	0.000607
	0.003356	0	0.000808
	0.004191	0	0.001010
	0.000942	0	0.000115
	0.001884	0	0.000229
	0.002822	0	0.000344
	0.003764	0	0.000458
	0.004703	0	0.000573
Quaternary	0.000492	0.000492	0.000495
	0.000978	0.000978	0.000984
	0.001467	0.001467	0.001476
	0.001950	0.001950	0.001962
	0.000330	0.000330	0.000944
	0.000656	0.000656	0.001874
	0.000981	0.000981	0.002803
	0.001309	0.001309	0.003739
	0.000149	0.000149	0.001218
	0.000297	0.000297	0.002422
	0.000448	0.000448	0.003646
	0.000597	0.000597	0.004859
	0.000678	0.000678	0.000296
	0.001340	0.001340	0.000585
	0.002019	0.002019	0.000881
	0.002682	0.002682	0.001171

	0.000322	0.000970	0.000327
	0.000646	0.001945	0.000656
	0.000985	0.002965	0.001000
	0.001290	0.003884	0.001310
	0.000128	0.000971	0.000154
	0.000257	0.001948	0.000308
	0.000384	0.002911	0.000460
	0.000515	0.003908	0.000618
	0.000642	0.004874	0.000771
	0.000165	0.000830	0.000321
	0.000329	0.001649	0.000639
	0.000491	0.002464	0.000954
	0.000656	0.003292	0.001275
	0.000820	0.004117	0.001595
	0.000123	0.000577	0.000521
	0.000244	0.001148	0.001037
	0.000369	0.001737	0.001569
	0.000495	0.002328	0.002102
	0.000621	0.002922	0.002638
	0.000116	0.000330	0.000794
	0.000234	0.000664	0.001599
	0.000352	0.001001	0.002411
	0.000474	0.001347	0.003242
	0.000595	0.001691	0.004072
	0.000258	0.000522	0.000519
	0.000506	0.001024	0.001018
	0.000760	0.001539	0.001530
	0.001020	0.002064	0.002052
	0.001284	0.002599	0.002584
	0.000442	0.000713	0.000195
	0.000868	0.001400	0.000383
	0.001312	0.002115	0.000579
	0.001746	0.002815	0.000771
	0.002168	0.003495	0.000957
	0.000657	0.000235	0.000218
	0.001320	0.000472	0.000439
	0.001989	0.000711	0.000662
	0.002651	0.000947	0.000882
	0.003310	0.001183	0.001101
	0.000860	0.000113	0.000103
	0.001723	0.000227	0.000206
	0.002594	0.000342	0.000310
	0.003467	0.000457	0.000414

	0.004321	0.000570	0.000516
	0.000680	0.000105	0.000298
	0.001373	0.000213	0.000601
	0.002060	0.000319	0.000902
	0.002750	0.000426	0.001205
	0.003433	0.000532	0.001504
	0.000490	0.000144	0.000475
	0.000989	0.000289	0.000959
	0.001488	0.000436	0.001443
	0.001981	0.000580	0.001921
	0.002474	0.000724	0.002399
	0.000362	0.000098	0.000672
	0.000725	0.000197	0.001347
	0.001092	0.000297	0.002029
	0.001455	0.000396	0.002703
	0.001817	0.000494	0.003375
	0.000448	0.000216	0.000424
	0.000901	0.000435	0.000852
	0.001350	0.000652	0.001276
	0.001803	0.000871	0.001705
	0.002250	0.001087	0.002128
	0.000663	0.000360	0.000110
	0.001338	0.000726	0.000223
	0.002007	0.001090	0.000334
	0.002677	0.001453	0.000445
	0.003343	0.001814	0.000556
	0.000621	0.000207	0.000269
	0.001260	0.000420	0.000546
	0.001891	0.000630	0.000820
	0.002525	0.000842	0.001095
	0.003151	0.001050	0.001366
	0.000825	0.000100	0.000100
	0.001657	0.000201	0.000201
	0.002487	0.000301	0.000301
	0.003320	0.000402	0.000402
	0.004137	0.000501	0.000501
	0.000638	0.000125	0.000314
	0.001279	0.000251	0.000630
	0.001922	0.000377	0.000946
	0.002569	0.000505	0.001264
	0.003207	0.000630	0.001578
	0.000484	0.000106	0.000457
	0.000975	0.000212	0.000920

	0.001463	0.000319	0.001380
	0.001955	0.000426	0.001845
	0.002437	0.000531	0.002298
	0.000308	0.000093	0.000611
	0.000618	0.000187	0.001224
	0.000930	0.000281	0.001842
	0.001240	0.000374	0.002456
	0.001547	0.000467	0.003065
	0.000389	0.000194	0.000405
	0.000787	0.000392	0.000818
	0.001189	0.000592	0.001236
	0.001586	0.000790	0.001650
	0.001980	0.000987	0.002059
	0.000640	0.000349	0.000094
	0.001269	0.000693	0.000187
	0.001922	0.001049	0.000282
	0.002560	0.001397	0.000376
	0.003197	0.001744	0.000470

B2.2 – Models Validation by Comparing Results with Gravimetric Method

Table B2: Comparison of results obtained from UV-CD calibration method and gravimetry on the same 28 solutions of varying compositions in S and S-MA. The percentage error $\delta\ (\%) = \frac{|X-Y|}{Y}$ is used, with X being the total solubility obtained with UV-CD models result, and Y the total solubility from gravimetric method, on the same saturated solution.

Mass fraction total solid X (UV-CD)	Mass fraction total solid Y (Gravimetry)	Percentage Error δ (%)
0.037	0.037	0.294
0.038	0.038	0.198
0.040	0.039	0.361
0.138	0.133	3.528
0.139	0.137	1.912
0.135	0.132	2.168
0.213	0.214	0.459
0.224	0.227	1.261
0.216	0.214	0.567
0.236	0.234	0.725
0.245	0.241	1.583
0.240	0.236	1.982
0.258	0.254	1.444
0.270	0.288	6.368
0.099	0.095	4.283
0.105	0.101	3.634
0.117	0.114	2.463
0.110	0.107	2.341
0.125	0.123	2.206
0.118	0.116	1.599
0.114	0.113	0.861
0.114	0.111	2.636
0.114	0.112	2.136
0.128	0.122	4.468
0.118	0.121	2.507
0.135	0.13	3.881
0.140	0.136	2.507
0.152	0.152	0.192
Average percentage error δ		**2.091**
Standard deviation		**1.472**

B3 – Phase Diagrams Data

Table B3: Solubilities of pure solid phases, eutectic points in ternary sections and quaternary points from the quaternary system R/S/S-MA/MeCN results at 9°C. Pure R, S and S-MA solubilities are the average of four compositions points. Pure RS and pure S:S-MA solubilities are computed from extrapolation of solubility curves. Points a, b and c were found experimentally. Points d, e and f were estimated from intersection of neighbouring solubility curves or surfaces. Points g and h could not be determined because of very high viscosity of saturated solutions in the region they belong, therefore only a roughly estimated compositional region is proposed.

Solubility at 9°C	Molar fraction X in dissolved components (%mol)	Mass concentration (mg/mL MeCN)
Pure R and S	**R/S:** 0.933	**R/S:** 30.7
Pure RS	**R:** 0.302 **S:** 0.302 **Total:** 0.604	**R:** 9.9 **S:** 9.9 **Total:** 19.8
Pure S-MA (average)	**S-MA:** 4.054	**S-MA:** 123.2
Pure S:S-MA	**S:** 1.591 **S-MA:** 1.591 **Total:** 3.182	**S:** 53.6 **S-MA:** 47.9 **Total:** 101.5
Eutectic point ***a*** (equilibrium with R and RS)	**R:** 0.954 **S:** 0.134 **Total:** 1.088	**R:** 31.4 **S:** 4.4 **Total:** 35.8
Eutectic point ***b*** (equilibrium with RS and S)	**R:** 0.134 **S:** 0.954 **Total:** 1.088	**R:** 4.4 **S:** 31.4 **Total:** 35.8
Eutectic point ***c*** (equilibrium with S and S:S-MA)	**S:** 1.974 **S-MA:** 1.253 **Total:** 3.227	**S:** 66.5 **S-MA:** 37.7 **Total:** 102.2
Eutectic point ***d*** (equilibrium with S:S-MA and S-MA)	**S:** 1.799 **S-MA:** 7.132 **Total:** 8.931	**S:** 64.4 **S-MA:** 228.2 **Total:** 292.6
Eutectic point ***e*** (equilibrium with R and S-MA)	**R:** 29.5 **S-MA:** 36.5 **Total:** 66.0	**R:** 2827.7 **S-MA:** 3127.4 **Total:** 5955.1
Quaternary point ***f*** (equilibrium with S, RS and S:S-MA)	**R:** 0.356 **S:** 2.176 **S-MA:** 1.513 **Total:** 4.045	**R:** 12.1 **S:** 73.9 **S-MA:** 45.9 **Total:** 131.9

Quaternary point ***g*** (equilibrium with R, RS and S-MA)	**Solvent-free ratio** **R:** 38.1% **S:** 8.1% **S-MA:** 53.8%	Total solubility > 6000 mg/mL MeCN
Quaternary point ***h*** (equilibrium with RS, S-MA and S:S-MA)	**Solvent-free ratio** **R:** 43.0% **S:** 6.0% **S-MA:** 51.0%	Total solubility > 6000 mg/mL MeCN

B3.1 – Isothermal Ternary System Between Enantiomers R and S

Table B4: Data used for the ternary phase diagram R/S/MeCN at 9°C.

Model prediction from UV-CD			**Dilution**	**Final liquid composition (molar fraction)**			**Solid**
x_{S+R} of diluted solution	x_{S-R} of diluted solution	Enantiomeric excess E of diluted solution (%)	Dilution ratio	X_R (%)	X_S (%)	X_{MeCN} (%)	Solid phase(s) in suspension (XRPD)
0.00336	0.00336	100.00	10.667	0.000	0.889	99.111	S
0.00333	0.00310	93.07	12.045	0.035	0.964	99.002	S
0.00369	0.00328	88.78	10.573	0.054	0.916	99.029	S
0.00375	0.00320	85.41	10.643	0.072	0.920	99.008	S
0.00380	0.00300	78.94	11.104	0.111	0.942	98.947	S
0.00396	0.00302	76.16	10.915	0.129	0.950	98.922	S
0.00385	0.00290	75.33	11.335	0.134	0.954	98.911	S + RS
0.00396	0.00289	73.08	10.913	0.145	0.933	98.922	RS
0.00372	0.00265	71.14	10.813	0.144	0.857	98.999	RS
0.00351	0.00240	68.49	11.213	0.154	0.825	99.021	RS
0.00360	0.00248	68.98	11.040	0.153	0.835	99.012	RS
0.00287	0.00187	65.08	12.698	0.158	0.745	99.097	RS
0.00261	0.00170	65.09	12.930	0.146	0.689	99.165	RS
0.00331	0.00209	63.05	10.922	0.166	0.731	99.103	RS
0.00281	0.00163	57.92	12.332	0.180	0.677	99.143	RS
0.00287	0.00155	54.11	11.431	0.186	0.625	99.189	RS
0.00234	0.00129	55.02	11.603	0.150	0.518	99.332	RS
0.00255	0.00123	48.17	12.401	0.202	0.578	99.220	RS
0.00257	0.00109	42.52	11.329	0.207	0.512	99.281	RS
0.00240	0.00096	40.10	11.116	0.197	0.460	99.343	RS
0.00230	0.00075	32.68	11.276	0.214	0.422	99.363	RS
0.00232	0.00063	27.11	10.926	0.227	0.395	99.378	RS
0.00218	0.00040	18.42	11.430	0.250	0.363	99.387	RS
0.00229	0.00038	16.50	10.825	0.255	0.355	99.390	RS
0.00191	0.00018	9.50	12.109	0.257	0.311	99.432	RS
0.00212	0	0	11.614	0.302	0.302	99.396	RS

The 26 other points corresponding to excess of R were deducted from mirror projection due to symmetry along racemic compositions in enantiomeric systems

Table B5: Comparison of four solubility values variation for pure R and S solubilities and S-MA with UV-CD spectroscopy and gravimetry methods.

	UV-CD spectroscopy		**Gravimetry**
	X (% mol)	**Concentration (mg/mL)**	
Pure R and S	0.889	29.218	-
	0.924	30.383	30.438
	0.935	30.756	30.981
	0.986	32.457	32.207
Average	**0.933**	**30.703**	**31.209**
Standard deviation	0.035	1.161	0.734
Pure S-MA	4.103	124.699	-
	4.076	123.861	121.052
	4.054	123.251	124.604
	3.985	120.961	119.771
Average	**4.054**	**123.193**	**121.809**
Standard deviation	0.044	1.387	2.044

B3.2 – Isothermal Ternary System Between Enantiomer S and S-SMA

Table B6: Data used for the ternary phase diagram S/S-MA/MeCN at 9°C.

Model prediction from UV-CD		**Dilution**	**Final liquid composition (molar fraction)**			**Solid**
x_S in diluted solution	$x_{S\text{-}MA}$ in diluted solution	Dilution ratio	X_S (%)	$X_{S\text{-}MA}$ (%)	X_{MeCN} (%)	Solid phase(s) in suspension (XRPD)
0.00403	0.00000	9.237	0.924	0.000	99.083	S
0.00405	0.00122	11.974	1.229	0.414	98.357	S
0.00462	0.00185	11.946	1.412	0.633	97.954	S
0.00295	0.00146	20.953	1.603	0.887	97.509	S
0.00307	0.00158	20.601	1.641	0.944	97.415	S
0.00172	0.00000	21.678	0.924	0.000	99.071	S
0.00173	0.00000	21.764	0.935	0.000	99.060	S
0.00186	0.00000	21.381	0.986	0.000	99.018	S
0.00096	0.00050	67.722	1.701	0.983	97.316	S
0.00105	0.00052	66.641	1.833	1.016	97.152	S
0.00043	0.00378	42.511	0.502	4.984	94.514	S-MA
0.00028	0.00331	45.989	0.351	4.667	94.982	S-MA
0.00019	0.00256	58.420	0.307	4.575	95.118	S-MA

0.00003	0.00216	63.399	0.045	4.103	95.853	S-MA
0.00004	0.00212	63.946	0.063	4.076	95.861	S-MA
0.00006	0.00173	78.056	0.121	4.054	95.825	S-MA
0.00003	0.00204	65.176	0.053	3.984	95.962	S-MA
0.00054	0.00307	59.035	0.903	5.786	93.311	S-MA
0.00064	0.00316	58.974	1.082	6.026	92.892	S-MA
0.00059	0.00299	60.309	1.016	5.778	93.206	S-MA
0.00097	0.00420	45.585	1.293	6.257	92.449	S-MA
0.00074	0.00303	64.972	1.405	6.486	92.109	S-MA
0.00074	0.00315	61.701	1.338	6.379	92.283	S-MA
0.00105	0.00396	51.485	1.603	6.786	91.611	S-MA
0.00098	0.00359	59.026	1.739	7.132	91.130	S-MA
0.00101	0.00104	49.702	1.317	1.512	97.171	S:S-MA
0.00101	0.00244	52.329	1.477	3.981	94.542	S:S-MA
0.00078	0.00215	62.629	1.369	4.207	94.423	S:S-MA
0.00088	0.00253	56.878	1.414	4.530	94.055	S:S-MA
0.00106	0.00327	47.867	1.446	4.990	93.564	S:S-MA
0.00120	0.00371	42.160	1.444	4.980	93.576	S:S-MA
0.00110	0.00345	46.829	1.476	5.164	93.360	S:S-MA
0.00090	0.00287	57.190	1.479	5.271	93.250	S:S-MA
0.00114	0.00372	46.580	1.534	5.617	92.849	S:S-MA
0.00119	0.00423	44.496	1.554	6.169	92.278	S:S-MA
0.00119	0.00422	47.378	1.678	6.646	91.676	S:S-MA
0.00102	0.00360	56.960	1.733	6.864	91.403	S:S-MA
0.00119	0.00421	48.618	1.726	6.842	91.432	S:S-MA
0.00100	0.00352	58.655	1.766	6.930	91.304	S:S-MA
0.00129	0.00454	45.573	1.764	6.947	91.289	S:S-MA
0.00109	0.00358	49.021	1.545	5.694	92.761	S:S-MA
0.00112	0.00367	46.113	1.491	5.456	93.053	S:S-MA
0.00116	0.00401	48.195	1.650	6.380	91.970	S:S-MA
0.00130	0.00089	49.903	1.710	1.309	96.981	S:S-MA
0.00125	0.00075	62.757	2.086	1.397	96.516	S:S-MA
0.00104	0.00069	67.882	1.872	1.386	96.741	S:S-MA
0.00102	0.00074	64.592	1.735	1.409	96.855	S:S-MA
0.00087	0.00079	68.930	1.575	1.608	96.817	S:S-MA
0.00085	0.00094	63.791	1.425	1.768	96.807	S:S-MA
0.00081	0.00107	68.101	1.464	2.174	96.361	S:S-MA
0.00073	0.00117	61.931	1.191	2.142	96.666	S:S-MA
0.00092	0.00165	52.348	1.297	2.596	96.107	S:S-MA
0.00077	0.00156	60.033	1.239	2.816	95.946	S:S-MA
0.00080	0.00178	58.983	1.279	3.190	95.532	S:S-MA
0.00117	0.00066	63.977	1.974	1.253	96.773	S + S:S-MA

B3.3 – Isothermal Ternary System Between Enantiomer R and S-MA

Table B7: Data used for the ternary phase diagram R/S-MA/MeCN at 9°C.

Model prediction from UV-CD		**Dilution**	**Final liquid composition (molar fraction)**			**Solid**
x_R in diluted solution	$x_{S\text{-}MA}$ in diluted solution	Dilution ratio	X_R (%)	$X_{S\text{-}MA}$ (%)	X_{MeCN} (%)	Solid phase(s) in suspension (XRPD)
0.00094	0.00011	53.036	1.262	0.168	98.571	R
0.00109	0.00026	51.026	1.411	0.379	98.211	R
0.00091	0.00036	89.046	2.133	0.935	96.932	R
0.00103	0.00047	87.759	2.424	1.240	96.336	R
0.00124	0.00072	83.848	2.860	1.865	95.274	R
0.00079	0.00048	163.125	3.695	2.477	93.827	R
0.00130	0.00088	110.166	4.209	3.199	92.592	R
0.00122	0.00086	133.803	4.968	3.940	91.092	R
0.00101	0.00079	178.077	5.719	4.967	89.313	R
0.00133	0.00106	153.884	6.825	6.054	87.121	R
0.00150	0.00125	143.384	7.332	6.861	85.808	R
0.00117	0.00103	190.982	7.878	7.737	84.385	R
0.00125	0.00116	214.444	10.525	10.937	78.537	R
0.00128	0.00109	231.981	12.150	11.580	76.270	R
0.00126	0.00106	246.714	13.073	12.280	74.647	R
0.00151	0.00142	196.486	12.486	13.146	74.368	R
0.00155	0.00139	210.004	14.561	14.624	70.815	R
0.00150	0.00138	225.100	15.800	16.276	67.925	R
0.00142	0.00129	229.829	14.755	14.985	70.260	R
0.00078	0.00147	218.602	6.469	13.668	79.862	S-MA
0.00068	0.00135	234.158	5.934	13.177	80.889	S-MA
0.00071	0.00161	180.174	4.469	11.307	84.224	S-MA
0.00083	0.00214	124.180	3.413	9.862	86.726	S-MA
0.00053	0.00149	163.260	2.760	8.686	88.554	S-MA
0.00062	0.00222	95.137	1.777	7.096	91.127	S-MA
0.00050	0.00207	93.682	1.363	6.344	92.294	S-MA
0.00029	0.00275	59.964	0.491	5.127	94.382	S-MA
0.00017	0.00242	65.795	0.308	4.911	94.781	S-MA
			Suspension composition			
			19.914	26.145	53.942	No solid
			22.539	29.862	47.599	No solid
			24.740	32.748	42.511	S-MA
			26.783	35.136	38.080	S-MA
			29.847	39.608	30.545	S-MA

B3.4 – Quaternary Phase Diagram R/S/S-MA/MeCN

Table B8: Data used for the quaternary phase diagram R/S/S-MA/MeCN at 9°C (inside of the tetrahedron).

Model prediction from UV-CD			**Dilution**	**Final liquid composition (molar fraction)**				**Solubility surface projection (molar fraction)**			**Solid phase(s) in suspension (XRPD)**
x_R in diluted solution	x_S in diluted solution	$x_{S\text{-}MA}$ in diluted solution	Dilution ratio	X_R (%)	X_S (%)	$X_{S\text{-}MA}$ (%)	X_{MeCN} (%)	X_S (%)	$X_{S\text{-}MA}$ (%)	X_R (%)	XRPD
0.00087	0.00087	0.00177	48.943	1.171	1.174	2.675	94.980	23.386	53.281	23.334	RS
0.00055	0.00052	0.00102	70.578	1.045	1.002	2.179	95.774	23.706	51.572	24.723	RS
0.00041	0.00038	0.00066	76.957	0.828	0.773	1.493	96.906	24.983	48.256	26.761	RS
0.00062	0.00057	0.00094	42.213	0.679	0.625	1.152	97.544	25.458	46.895	27.647	RS
0.00046	0.00050	0.00050	42.664	0.498	0.538	0.599	98.365	32.895	36.643	30.462	RS
0.00020	0.00116	0.00050	46.746	0.237	1.402	0.676	97.685	60.564	29.215	10.221	S+RS
0.00020	0.00120	0.00042	40.499	0.212	1.241	0.483	98.065	64.121	24.932	10.948	S+RS
0.00020	0.00125	0.00044	38.312	0.194	1.224	0.485	98.098	64.332	25.488	10.181	S+RS
0.00018	0.00131	0.00045	37.799	0.177	1.267	0.491	98.064	65.477	25.381	9.141	S+RS
0.00026	0.00154	0.00080	39.679	0.274	1.602	0.927	97.198	57.169	33.065	9.766	S+RS
0.00027	0.00169	0.00095	38.027	0.268	1.692	1.068	96.972	55.871	35.275	8.854	S+RS
0.00021	0.00144	0.00074	43.277	0.234	1.632	0.932	97.201	58.321	33.307	8.372	S+RS
0.00020	0.00122	0.00077	62.745	0.336	2.050	1.455	96.159	53.376	37.875	8.748	S+RS
0.00021	0.00131	0.00081	55.686	0.310	1.947	1.347	96.397	54.032	37.377	8.591	S+RS
0.00022	0.00135	0.00088	53.674	0.317	1.942	1.408	96.333	52.964	38.385	8.651	S:S-MA+S
0.00018	0.00093	0.00069	74.849	0.364	1.860	1.539	96.237	49.426	40.895	9.678	S:S-MA+RS
0.00020	0.00110	0.00068	68.658	0.377	2.023	1.411	96.190	53.092	37.023	9.885	S:S-MA
0.00016	0.00119	0.00073	63.320	0.264	2.019	1.379	96.338	55.140	37.658	7.201	S:S-MA
0.00029	0.00089	0.00090	65.956	0.515	1.575	1.785	96.125	40.648	46.059	13.293	S:S-MA
0.00021	0.00099	0.00082	64.593	0.355	1.704	1.587	96.355	46.744	43.521	9.735	S:S-MA
0.00071	0.00090	0.00259	59.571	1.259	1.589	5.118	92.034	19.944	64.247	15.809	S:S-MA
0.00041	0.00093	0.00210	59.825	0.700	1.589	4.000	93.711	25.275	63.601	11.123	S:S-MA
0.00035	0.00081	0.00289	65.234	0.691	1.590	6.315	91.404	18.502	73.458	8.040	S:S-MA

0.00040	0.00106	0.00398	54.905	0.688	1.799	7.561	89.952	17.909	75.247	6.844	S:S-MA
0.00038	0.00041	0.00330	57.816	0.649	0.691	6.227	92.434	9.131	82.297	8.572	S-MA
0.00064	0.00068	0.00377	60.716	1.211	1.295	7.999	89.494	12.328	76.140	11.531	S-MA
0.00090	0.00096	0.00333	65.173	1.882	2.005	7.809	88.305	17.143	66.769	16.088	S:S-MA
0.00150	0.00122	0.00369	48.852	2.303	1.877	6.336	89.484	17.847	60.253	21.900	S:S-MA
0.00024	0.00094	0.00033	39.949	0.238	0.951	0.369	98.443	61.046	23.689	15.265	RS
0.00022	0.00140	0.00039	38.838	0.221	1.395	0.437	97.947	67.927	21.304	10.768	S+RS
0.00024	0.00132	0.00035	38.104	0.231	1.286	0.383	98.100	67.666	20.158	12.177	S+RS
0.00020	0.00129	0.00038	40.246	0.209	1.322	0.440	98.028	67.071	22.328	10.601	S+RS
0.00020	0.00140	0.00047	36.829	0.188	1.321	0.495	97.995	65.905	24.699	9.396	S
0.00032	0.00132	0.00055	43.854	0.370	1.510	0.705	97.415	58.421	27.269	14.310	RS
0.00034	0.00110	0.00079	39.231	0.349	1.110	0.890	97.651	47.265	37.885	14.850	RS
0.00028	0.00160	0.00068	38.293	0.278	1.595	0.759	97.368	60.604	28.837	10.559	RS
0.00024	0.00163	0.00080	40.602	0.256	1.735	0.953	97.057	58.935	32.374	8.691	S
0.00042	0.00160	0.00106	35.765	0.394	1.506	1.118	96.982	49.913	37.030	13.057	RS
0.00029	0.00180	0.00112	44.681	0.356	2.176	1.513	95.955	53.799	37.400	8.802	S+RS
0.00062	0.00131	0.00139	40.116	0.667	1.412	1.672	96.249	37.645	44.577	17.778	RS
0.00041	0.00217	0.00137	36.006	0.394	2.110	1.487	96.009	52.871	37.252	9.876	RS
0.00026	0.00200	0.00119	39.848	0.274	2.147	1.426	96.153	55.807	37.064	7.129	S:S-MA+S
0.00034	0.00095	0.00091	63.642	0.581	1.626	1.753	96.040	41.070	44.258	14.671	RS
0.00034	0.00188	0.00116	41.019	0.371	2.075	1.427	96.127	53.574	36.851	9.575	S:S-MA+RS
0.00065	0.00094	0.00141	52.943	0.937	1.364	2.284	95.415	29.749	49.808	20.444	RS
0.00034	0.00057	0.00101	65.902	0.594	0.999	1.988	96.419	27.906	55.507	16.587	RS
0.00078	0.00106	0.00184	52.099	1.146	1.560	3.012	94.282	27.285	52.674	20.041	RS
0.00068	0.00108	0.00171	55.322	1.061	1.689	2.983	94.267	29.461	52.038	18.502	S:S-MA
0.00024	0.00102	0.00136	53.308	0.348	1.457	2.181	96.015	36.563	54.714	8.723	S:S-MA
0.00094	0.00114	0.00227	49.959	1.344	1.631	3.647	93.379	24.628	55.080	20.292	S:S-MA
0.00092	0.00106	0.00334	51.472	1.432	1.654	5.816	91.098	18.582	65.330	16.088	S:S-MA
0.00057	0.00108	0.00389	43.588	0.725	1.377	5.562	92.337	17.968	72.575	9.457	S:S-MA
0.00112	0.00122	0.00398	49.605	1.742	1.896	6.928	89.434	17.948	65.565	16.487	S:S-MA
0.00077	0.00098	0.00408	53.499	1.285	1.644	7.643	89.428	15.546	72.297	12.157	S:S-MA

0.00057	0.00107	0.00468	51.981	0.937	1.777	8.657	88.628	15.630	76.126	8.244	S-MA
0.00054	0.00102	0.00469	47.279	0.780	1.491	7.641	90.087	15.043	77.085	7.872	S-MA
0.00028	0.00012	0.00117	139.523	1.109	0.472	5.273	93.145	6.892	76.927	16.181	S-MA
0.00045	0.00013	0.00158	141.129	1.971	0.575	7.755	89.699	5.581	75.285	19.133	S-MA
0.00037	0.00018	0.00152	146.910	1.673	0.837	7.773	89.717	8.141	75.587	16.272	S-MA
0.00072	0.00027	0.00237	112.468	2.714	1.015	9.967	86.304	7.412	72.772	19.817	S-MA
0.00039	0.00024	0.00142	181.283	2.359	1.430	9.535	86.675	10.734	71.560	17.706	S-MA
0.00058	0.00018	0.00153	189.884	3.945	1.205	11.554	83.296	7.214	69.170	23.616	S-MA
0.00050	0.00024	0.00145	197.506	3.517	1.672	11.368	83.444	10.096	68.663	21.241	S-MA
0.00047	0.00033	0.00169	170.410	2.784	1.999	11.301	83.915	12.431	70.260	17.309	S-MA
0.00079	0.00032	0.00193	184.459	6.030	2.456	16.468	75.046	9.843	65.994	24.163	S-MA
0.00060	0.00036	0.00162	223.500	5.683	3.373	16.999	73.945	12.945	65.242	21.813	S-MA
0.00046	0.00031	0.00115	257.884	4.582	3.097	12.746	79.576	15.162	62.404	22.434	S:S-MA
0.00084	0.00033	0.00142	252.583	9.991	3.924	18.901	67.184	11.958	57.596	30.447	S:S-MA
0.00097	0.00042	0.00186	188.424	8.122	3.544	17.382	70.952	12.199	59.840	27.962	S:S-MA
0.00097	0.00050	0.00202	157.046	6.177	3.195	14.408	76.220	13.436	60.589	25.975	S:S-MA
0.00073	0.00045	0.00141	169.992	4.461	2.736	9.650	83.153	16.242	57.281	26.478	S:S-MA
0.00110	0.00044	0.00172	190.280	9.336	3.735	16.402	70.527	12.673	55.650	31.677	S:S-MA
0.00098	0.00039	0.00168	195.249	8.317	3.272	15.876	72.534	11.915	57.804	30.281	S:S-MA
0.00079	0.00037	0.00151	193.166	5.986	2.813	12.718	78.483	13.074	59.109	27.818	S:S-MA
0.00056	0.00036	0.00121	211.423	4.250	2.744	10.307	82.698	15.862	59.575	24.563	S:S-MA
0.00123	0.00039	0.00162	189.678	10.394	3.252	15.297	71.056	11.237	52.852	35.911	RS
0.00098	0.00036	0.00144	214.768	9.137	3.376	14.960	72.527	12.287	54.455	33.258	S:S-MA
0.00105	0.00042	0.00158	190.103	8.416	3.356	14.221	74.007	12.913	54.709	32.379	S:S-MA
0.00086	0.00044	0.00140	163.365	5.079	2.591	9.221	83.109	15.338	54.595	30.067	S:S-MA
0.00069	0.00038	0.00111	162.698	3.695	2.035	6.598	87.671	16.506	53.521	29.973	S:S-MA
0.00150	0.00032	0.00169	145.224	8.476	1.818	10.671	79.036	8.672	50.899	40.429	No solid
0.00145	0.00041	0.00187	121.134	6.392	1.797	9.197	82.615	10.334	52.901	36.765	RS
0.00090	0.00040	0.00137	155.469	4.861	2.185	8.282	84.672	14.253	54.033	31.714	RS
0.00062	0.00034	0.00099	165.274	3.276	1.778	5.808	89.138	16.371	53.471	30.159	S:S-MA+RS
0.00045	0.00045	0.00014	39.876	0.448	0.442	0.160	98.950	42.131	15.194	42.674	RS

0.00038	0.00038	0.00024	53.510	0.509	0.508	0.361	98.622	36.854	26.195	36.951	RS
0.00051	0.00047	0.00032	45.035	0.574	0.536	0.407	98.483	35.312	26.854	37.834	RS
0.00063	0.00059	0.00077	45.195	0.735	0.684	1.010	97.570	28.166	41.575	30.259	RS
0.00057	0.00054	0.00077	48.477	0.714	0.679	1.085	97.521	27.403	43.779	28.818	RS
0.00068	0.00066	0.00107	46.267	0.827	0.808	1.460	96.905	26.099	47.170	26.732	RS
0.00027	0.00089	0.00019	44.731	0.302	1.000	0.237	98.461	64.989	15.377	19.634	RS
0.00020	0.00094	0.00010	47.574	0.242	1.132	0.140	98.485	74.722	9.273	16.005	RS
0.00017	0.00108	0.00017	44.796	0.192	1.224	0.221	98.363	74.761	13.504	11.734	S+RS
0.00017	0.00108	0.00018	45.541	0.192	1.243	0.229	98.336	74.708	13.783	11.509	S+RS
0.00015	0.00107	0.00008	48.212	0.189	1.305	0.103	98.404	81.751	6.431	11.818	S+RS
0.00017	0.00116	0.00017	47.046	0.203	1.390	0.230	98.176	76.237	12.624	11.139	S+RS
0.00015	0.00104	0.00010	45.235	0.170	1.190	0.125	98.515	80.129	8.406	11.465	S+RS
0.00017	0.00110	0.00014	44.706	0.188	1.245	0.178	98.389	77.260	11.076	11.664	S+RS
0.00012	0.00098	0.00011	49.294	0.150	1.218	0.159	98.473	79.770	10.398	9.832	S
0.00015	0.00125	0.00042	45.802	0.173	1.469	0.559	97.800	66.759	25.394	7.847	S
0.00010	0.00149	0.00065	47.349	0.118	1.846	0.903	97.133	64.380	31.500	4.121	S
0.00011	0.00171	0.00083	45.177	0.126	2.043	1.106	96.725	62.379	33.780	3.841	S
0.00012	0.00171	0.00103	47.552	0.153	2.188	1.475	96.183	57.339	38.652	4.009	S
0.00018	0.00132	0.00032	44.499	0.202	1.512	0.415	97.871	71.023	19.491	9.486	S+RS
0.00036	0.00077	0.00046	45.547	0.414	0.899	0.599	98.088	47.026	31.342	21.632	RS
0.00026	0.00138	0.00073	42.597	0.285	1.536	0.906	97.273	56.316	33.215	10.469	RS
0.00046	0.00088	0.00090	45.994	0.555	1.054	1.212	97.179	37.365	42.972	19.663	RS
0.00016	0.00169	0.00112	51.500	0.219	2.363	1.757	95.661	54.454	40.500	5.046	S:S-MA+S
0.00012	0.00160	0.00106	52.515	0.175	2.274	1.687	95.865	54.980	40.794	4.226	S:S-MA+S
0.00015	0.00179	0.00129	49.160	0.200	2.411	1.937	95.452	53.018	42.590	4.392	S:S-MA+S
0.00015	0.00187	0.00137	49.325	0.211	2.537	2.082	95.171	52.527	43.110	4.363	S:S-MA+S
0.00011	0.00185	0.00134	51.247	0.158	2.623	2.121	95.098	53.514	43.273	3.214	S:S-MA+S
0.00104	0.00014	0.00034	54.444	1.458	0.202	0.528	97.812	9.211	24.135	66.654	R+RS
0.00110	0.00018	0.00026	48.083	1.355	0.216	0.355	98.074	11.212	18.452	70.336	R+RS
0.00098	0.00016	0.00028	52.079	1.310	0.216	0.423	98.051	11.108	21.680	67.212	R+RS
0.00090	0.00021	0.00021	48.209	1.095	0.256	0.288	98.360	15.636	17.574	66.790	RS

0.00090	0.00013	0.00051	89.075	2.150	0.322	1.364	96.163	8.396	35.563	56.040	R+RS
0.00060	0.00012	0.00029	108.553	1.714	0.355	0.927	97.004	11.841	30.936	57.223	R+RS
0.00066	0.00015	0.00029	97.926	1.686	0.384	0.842	97.088	13.202	28.903	57.895	R+RS
0.00056	0.00016	0.00033	93.800	1.359	0.388	0.893	97.360	14.684	33.836	51.480	RS
0.00085	0.00013	0.00046	99.596	2.276	0.361	1.392	95.972	8.959	34.552	56.490	R+RS
0.00084	0.00014	0.00047	99.598	2.256	0.367	1.400	95.977	9.120	34.800	56.080	R+RS
0.00099	0.00016	0.00057	82.983	2.216	0.351	1.432	96.001	8.777	35.802	55.421	R+RS
0.00086	0.00022	0.00068	54.739	1.228	0.311	1.081	97.380	11.875	41.265	46.860	RS
0.00080	0.00013	0.00057	132.948	3.011	0.472	2.389	94.128	8.033	40.689	51.278	R+RS
0.00077	0.00016	0.00058	140.770	3.089	0.633	2.640	93.638	9.950	41.496	48.554	R+RS
0.00073	0.00013	0.00054	140.845	2.898	0.535	2.422	94.144	9.144	41.362	49.494	RS
0.00103	0.00015	0.00085	121.991	3.701	0.526	3.430	92.344	6.867	44.794	48.339	R+RS
0.00090	0.00014	0.00066	151.953	4.063	0.641	3.348	91.948	7.965	41.576	50.459	R+RS
0.00106	0.00020	0.00086	119.881	3.774	0.717	3.453	92.057	9.022	43.469	47.509	RS
0.00102	0.00013	0.00081	167.964	5.469	0.672	4.889	88.970	6.096	44.323	49.581	R+RS
0.00091	0.00014	0.00074	183.369	5.339	0.850	4.863	88.948	7.691	44.003	48.306	RS
0.00068	0.00036	0.00097	142.777	2.993	1.560	4.737	90.710	16.791	50.993	32.217	RS
0.00115	0.00014	0.00099	171.902	6.745	0.793	6.451	86.012	5.668	46.115	48.217	R+RS
0.00069	0.00011	0.00059	287.405	6.847	1.125	6.589	85.440	7.724	45.252	47.024	RS
0.00058	0.00022	0.00074	243.135	4.702	1.807	6.704	86.786	13.677	50.736	35.587	RS
0.00115	0.00015	0.00108	184.329	7.575	1.018	8.017	83.390	6.130	48.268	45.602	RS
0.00085	0.00025	0.00103	202.866	6.135	1.811	8.288	83.766	11.153	51.055	37.792	RS
0.00154	0.00021	0.00161	173.935	11.413	1.575	13.348	73.664	5.982	50.683	43.335	R+RS
0.00103	0.00027	0.00126	189.507	7.360	1.937	10.053	80.650	10.012	51.952	38.036	RS
0.00072	0.00057	0.00105	85.093	1.722	1.361	2.829	94.088	23.018	47.854	29.128	RS
0.00071	0.00057	0.00119	84.666	1.720	1.376	3.220	93.684	21.790	50.982	27.228	S:S-MA+RS
0.00078	0.00061	0.00122	95.143	2.202	1.712	3.843	92.243	22.070	49.543	28.387	RS
0.00102	0.00075	0.00168	75.951	2.316	1.713	4.278	91.694	20.620	51.499	27.881	S:S-MA+RS
0.00078	0.00049	0.00136	142.924	3.740	2.338	7.280	86.642	17.500	54.504	27.996	S:S-MA
0.00079	0.00046	0.00124	168.396	4.641	2.740	8.191	84.428	17.594	52.601	29.804	S:S-MA+RS
0.00076	0.00040	0.00162	159.830	4.356	2.315	10.423	82.906	13.542	60.973	25.485	S:S-MA

0.00080	0.00050	0.00167	159.326	4.713	2.989	11.069	81.229	15.924	58.968	25.109	S:S-MA
0.00088	0.00066	0.00265	109.643	3.527	2.645	11.883	81.944	14.652	65.813	19.536	S:S-MA
0.00093	0.00068	0.00285	103.072	3.513	2.555	12.016	81.916	14.130	66.447	19.423	S:S-MA+S-MA
0.00045	0.00037	0.00224	97.896	1.362	1.136	7.598	89.903	11.254	75.255	13.491	S-MA
0.00038	0.00032	0.00193	106.492	1.231	1.021	6.987	90.761	11.050	75.623	13.327	S-MA
0.00007	0.00011	0.00157	107.460	0.211	0.333	5.280	94.176	5.711	90.657	3.631	S-MA
0.00036	0.00013	0.00176	103.977	1.078	0.394	5.963	92.565	5.295	80.203	14.501	S-MA
0.00071	0.00046	0.00107	113.836	2.413	1.552	4.057	91.977	19.349	50.571	30.080	S:S-MA+RS
0.00087	0.00050	0.00130	109.018	2.926	1.674	4.882	90.518	17.650	51.493	30.857	S:S-MA+RS
0.00098	0.00058	0.00151	100.426	3.086	1.819	5.311	89.785	17.804	51.989	30.207	S:S-MA+RS
0.00113	0.00056	0.00174	118.247	4.626	2.277	7.952	85.145	15.330	53.527	31.142	S:S-MA+RS
0.00113	0.00043	0.00160	141.261	5.760	2.199	9.132	82.909	12.866	53.432	33.702	RS
0.00124	0.00036	0.00167	210.002	12.849	3.724	19.352	64.075	10.365	53.867	35.767	S:S-MA
0.00114	0.00029	0.00153	236.452	13.571	3.445	20.367	62.618	9.215	54.482	36.303	S:S-MA
0.00138	0.00038	0.00174	216.332	16.505	4.545	23.281	55.668	10.252	52.517	37.231	S:S-MA
0.00134	0.00035	0.00183	200.696	13.701	3.540	20.886	61.873	9.285	54.779	35.936	S:S-MA
0.00092	0.00035	0.00123	290.681	13.914	5.246	20.925	59.914	13.088	52.201	34.711	S:S-MA
0.00123	0.00047	0.00176	203.680	12.722	4.840	20.341	62.097	12.769	53.665	33.566	S:S-MA
0.00086	0.00036	0.00124	283.132	12.203	5.098	19.672	63.028	13.789	53.207	33.005	S:S-MA
0.00148	0.00035	0.00186	211.656	17.917	4.191	25.276	52.616	8.844	53.343	37.813	S:S-MA
0.00140	0.00036	0.00191	195.214	14.113	3.629	21.540	60.717	9.238	54.834	35.927	S:S-MA

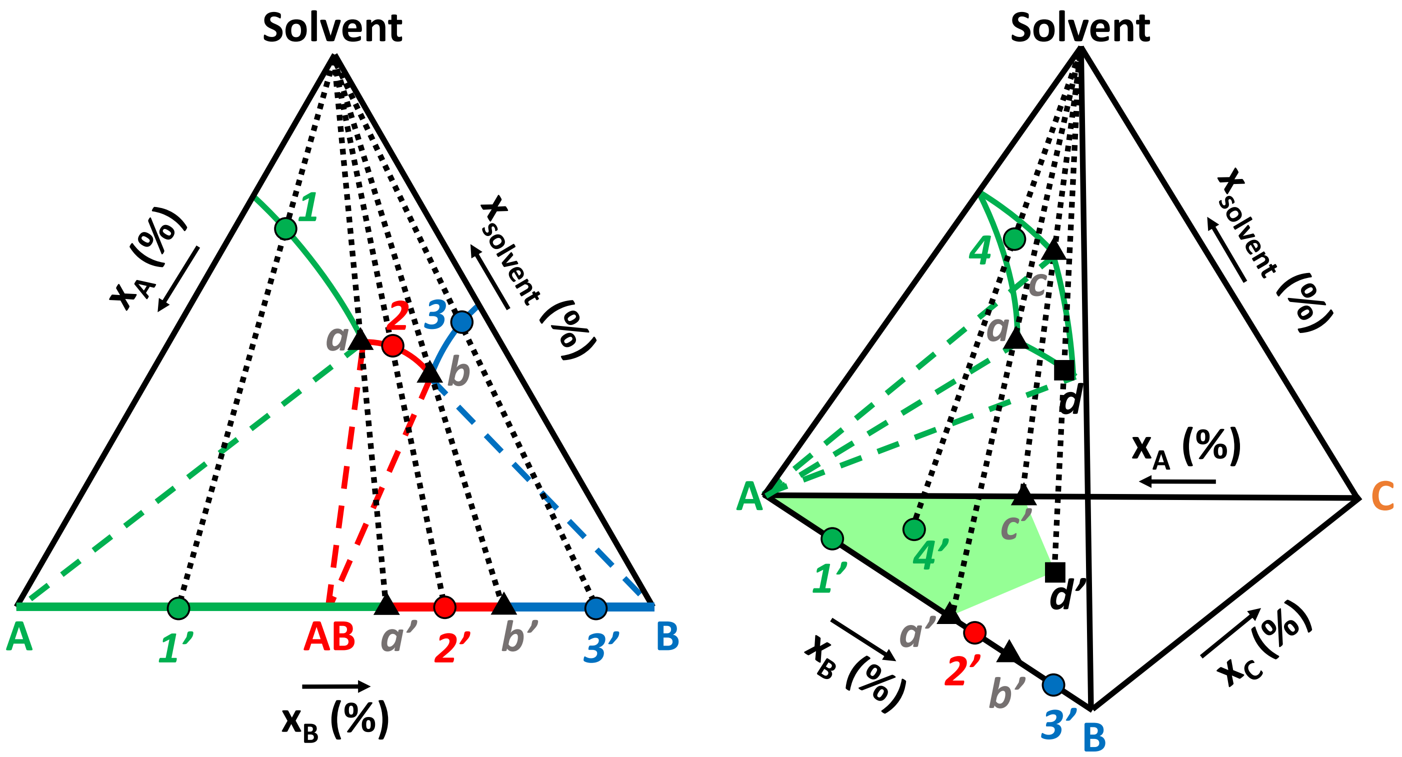

Figure B9: Left: projection of solubility curves (solid lines) of A (green), AB (red) and B (blue) on solvent-free axis AB in the isothermal ternary phase diagram A/B/Solvent. Dotted lines connect solubility compositions (1, 2, 3, a, b) to their solvent-free equivalent (1’, 2’, 3’, a’, b’). Dashed lines represent the boundaries of phase stability domains. Eutectic compositions a and b (black triangles) represent the liquid phase composition of a suspension equilibrating in a triphasic domain.

Right: projection of solubility surface of A (green) on solvent-free surface ABC in the isothermal quaternary phase diagram A/B/C/Solvent. Dotted lines connect solubility compositions (4, a, c, d) to their solvent-free equivalent (4’, a’, c’, d’). The data from the AB axis of the ternary phase diagram on the left are shown on the AB axis. Dashed lines represent the boundaries of the phase stability domain. The solubility surface of A is limited by solubility curves from ternaries A/B/Solvent and A/C/Solvent, and eutectic lines linking ternary eutectic compositions a and c (black triangles) to quaternary composition d (black square) involving A. Quaternary composition d represents the liquid phase composition of a suspension equilibrating in a quadriphasic domain.

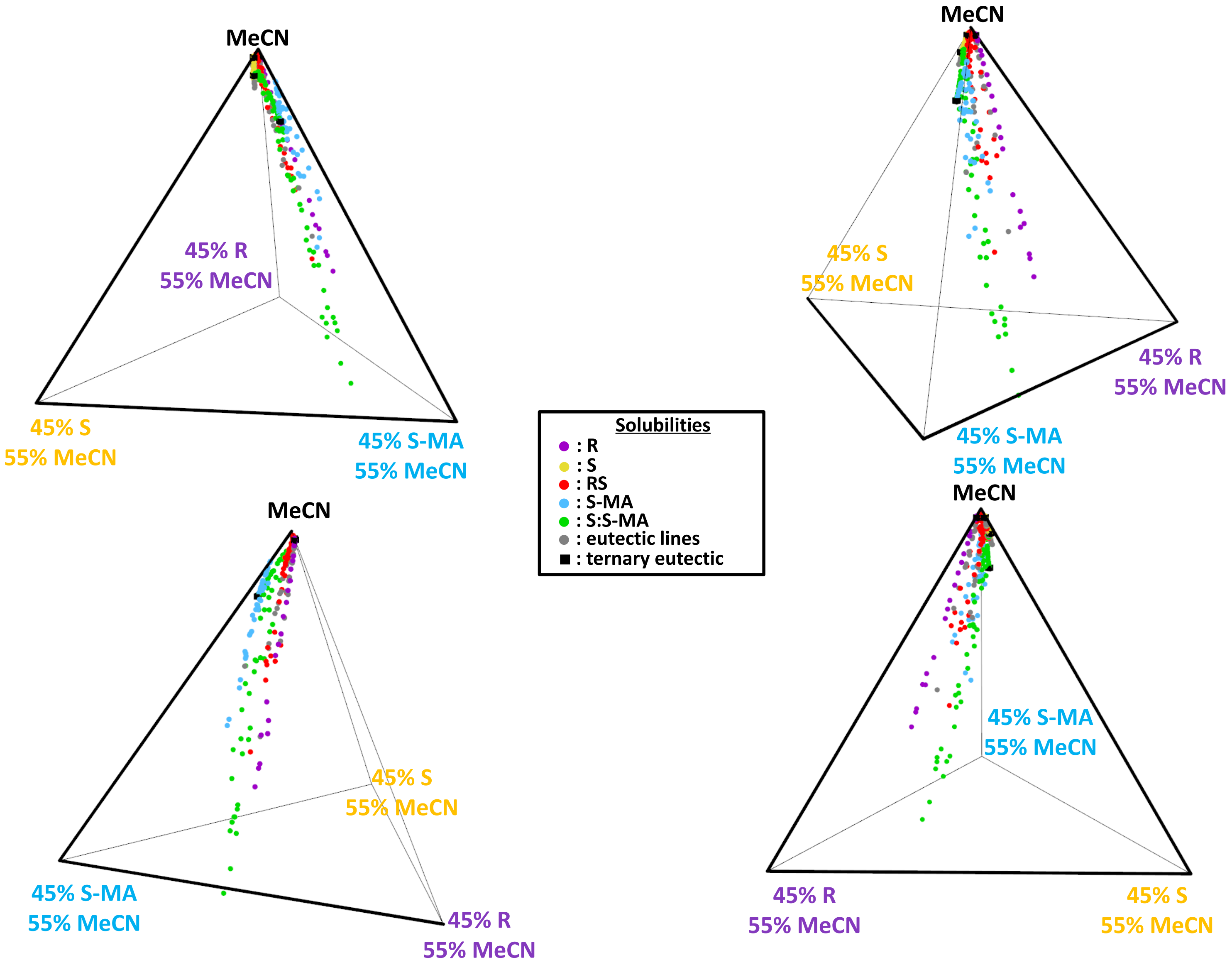

Figure B10: Zoom in the 55% MeCN to 100% MeCN tetrahedron region of the R/S/S-MA/MeCN quaternary phase diagram, with different viewing angles.

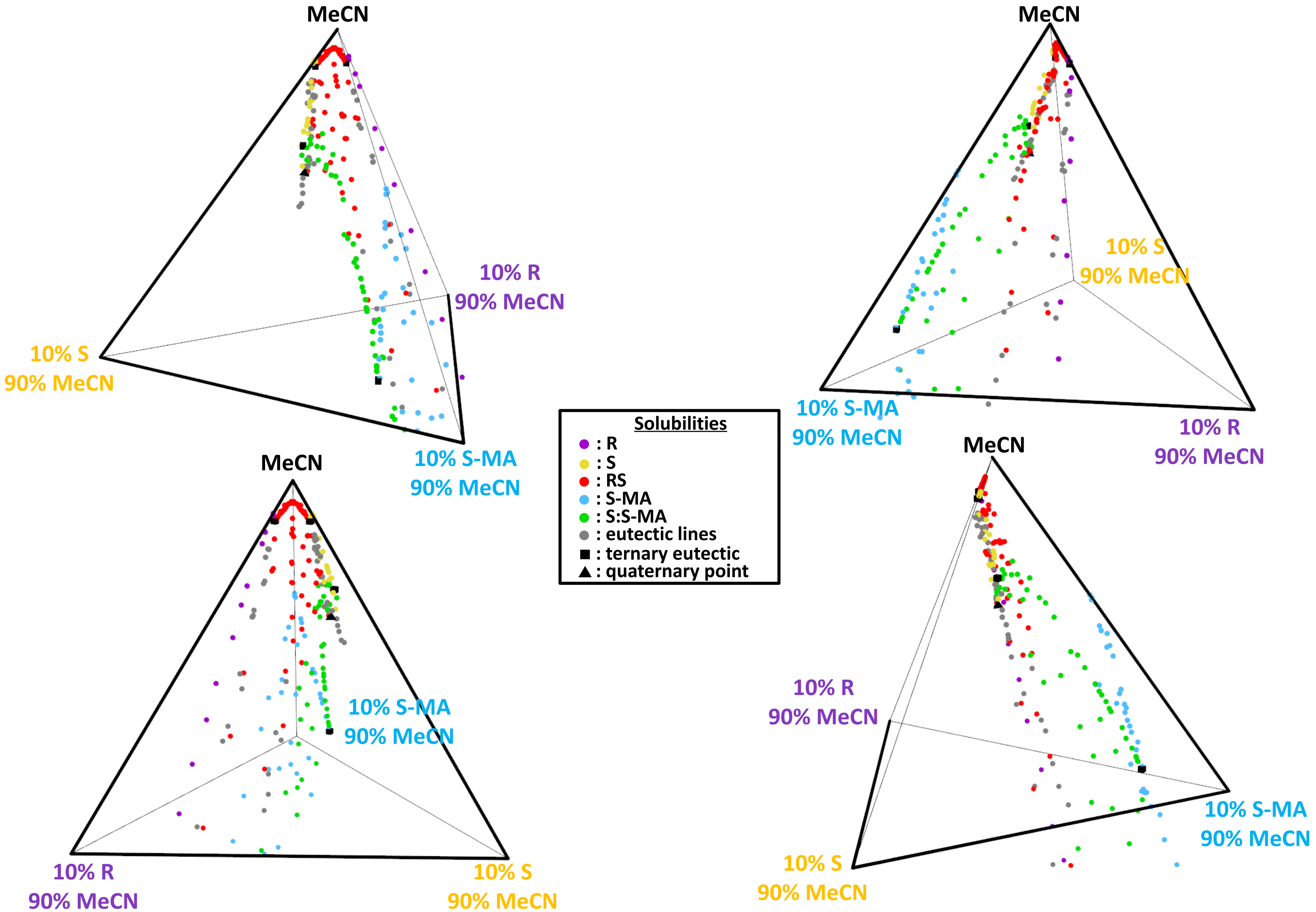

Figure B11: Zoom in the 90% MeCN to 100% MeCN tetrahedron region of the R/S/S-MA/MeCN quaternary phase diagram at 9°C, with different viewing angles.

Appendix C - Supporting Information of Chapter 5

Supporting Information of Chapter 5: "Enantioselective Cocrystallization and Enantiomer Recovery Guidelines from Phase Diagram Information"

Maxime D. Charpentier[1], Russell Miller[1,2], Karen Johnston[2], Joop H. ter Horst[1,3]

1. EPSRC Centre for Innovative Manufacturing in Continuous Manufacturing and Crystallization (CMAC), Strathclyde Institute of Pharmacy and Biomedical Sciences (SIPBS), University of Strathclyde

2. Department of Chemical and Process Engineering, University of Strathclyde, James Weir Building, 75 Montrose Street, Glasgow G1 1XJ, U.K.

3. Univ Rouen Normandie, Laboratoire Sciences et Méthodes Séparatives (SMS), UR 3233, F-76000 Rouen, France

Table of contents

C1 – Solvent-free Projection in a Quaternary Phase Diagram

A solvent-free projection is a representation of solubility surfaces from a quaternary phase diagram (i.e tetrahedron plot). By removing the dependency on the solvent concentration, solubility data can be shown in a two-dimensional plot where points are positioned based on their relative solvent-free molar ratio in dissolved components. Figure C1 provides a graphical explanation about how solvent-free projections are performed from phase diagram solubility points.

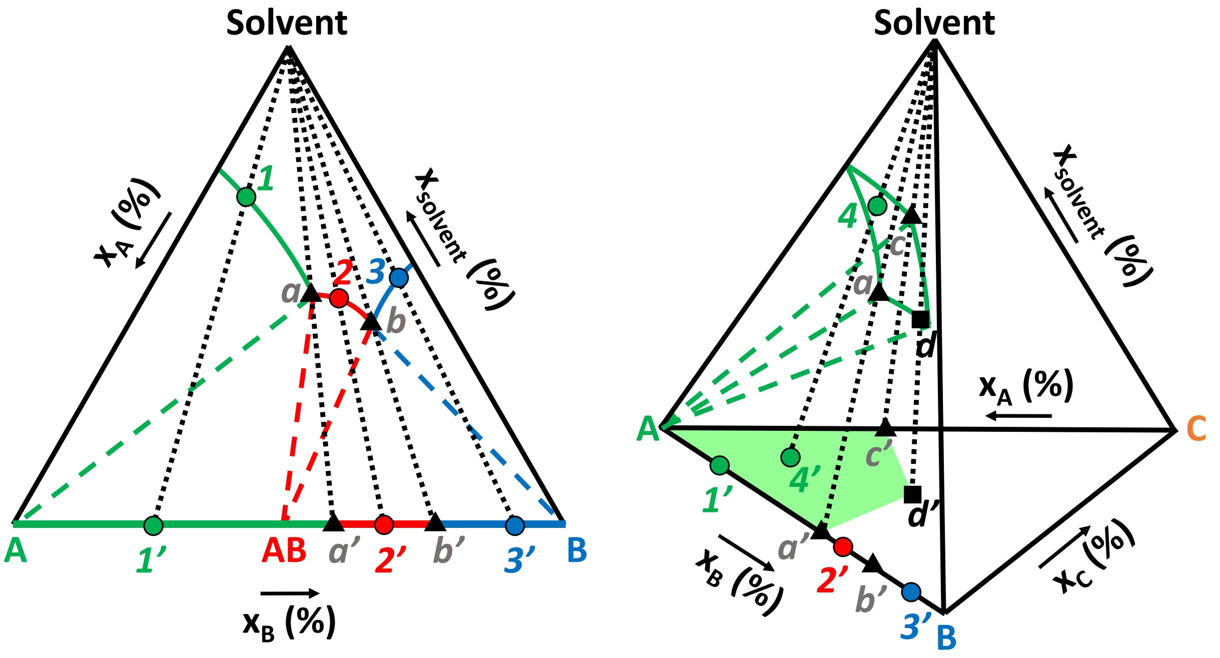

Figure C1: Left: projection of solubility curves (solid lines) of A (green), AB (red) and B (blue) on solvent-free axis AB in the isothermal ternary phase diagram A/B/Solvent. Dotted lines connect solubility compositions (*1*, *2*, *3*, *a*, *b*) to their solvent-free equivalent (*1'*, *2'*, *3'*, *a'*, *b'*). Dashed lines represent the boundaries of phase stability domains. Eutectic compositions *a* and *b* (black triangles) represent the liquid phase composition of a suspension equilibrating in a triphasic domain. Right: projection of solubility surface of A (green) on solvent-free surface ABC in the isothermal quaternary phase diagram A/B/C/Solvent. Dotted lines connect solubility compositions (*4*, *a*, *c*, *d*) to their solvent-free equivalent (*4'*, *a'*, *c'*, *d'*). The data from the AB axis of the ternary phase diagram on the left are shown on the AB axis. Dashed lines represent the boundaries of the phase stability domain. The solubility surface of A is limited by solubility curves from ternaries A/B/Solvent and A/C/Solvent, and eutectic lines linking ternary eutectic compositions *a* and *c* (black triangles) to quaternary composition *d* (black square) involving A. Quaternary composition *d* represents the liquid phase composition of a suspension equilibrating in a quadriphasic domain.

C2 – Quaternary Phase Diagram Data in Mass Fraction

Figure C2 and Table C1 summarise the experimental data of the quaternary phase diagram R/S/S-MA/MeCN at 9°C in mass fraction. Only the points of pure S:S-MA solubility surface are represented (green). The working composition ω, belonging to the racemic composition plane (grey) is selected for enantioselective cocrystallization batches. Its saturated solution λ at equilibrium is the most enriched in R because its position is the furthest from the racemic composition plane. This induces that the theoretical mass of pure cocrystal S:S-MA that can be crystallized at ω is the highest, therefore maximising the theoretical yield of recovery of pure Levetiracetam (S) from its initial amount input in the form of the racemic compound RS.

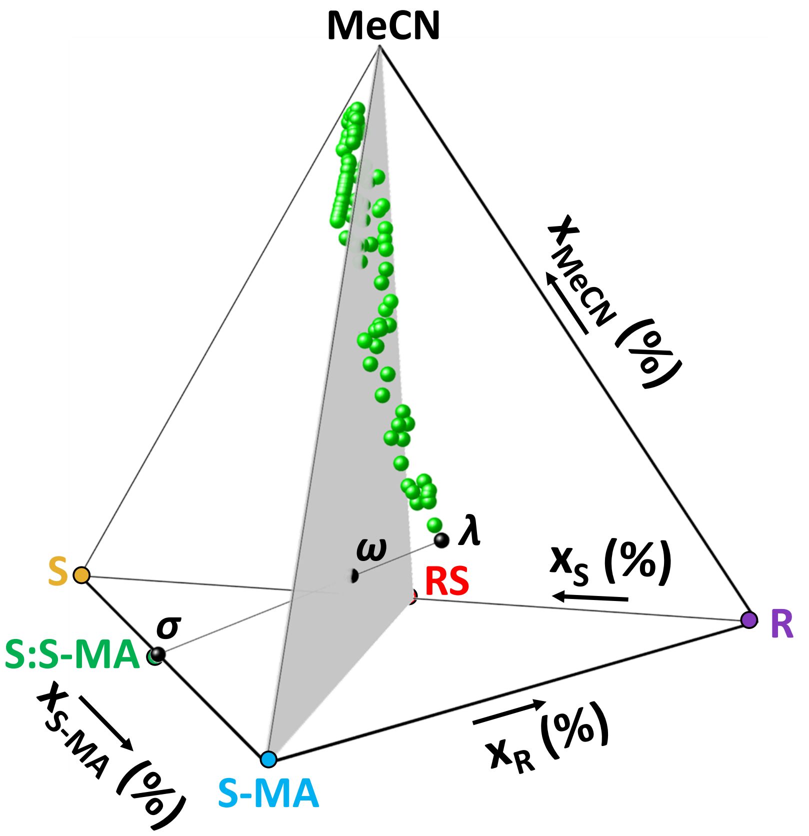

<u>Points coordinates:</u>

$\boldsymbol{\sigma}$: $x_R = 0\%$, $x_S = 52.80\%$, $x_{S\text{-}MA} = 47.20\%$, $x_{MeCN} = 0\%$

$\boldsymbol{\omega}$: $x_R = 21.12\%$, $x_S = 21.12\%$, $x_{S\text{-}MA} = 42.28\%$, $x_{MeCN} = 15.48\%$

$\boldsymbol{\lambda}$: $x_R = 31.22\%$, $x_S = 7.30\%$, $x_{S\text{-}MA} = 39.37\%$, $x_{MeCN} = 22.11\%$

Figure C2: Experimental data for isoplethal section at racemic composition, represented by plane S-MA/RS/MeCN (grey surface) in the isothermal quaternary phase diagram R/S/S-MA/MeCN at 9°C expressed in mass fractions. The experimental saturated solutions in equilibrium with S:S-MA are represented by green points. The solution λ is the saturated liquid, in equilibrium with pure S:S-MA solid (point σ), that is the most highly enriched in R and therefore the furthest from racemic composition. It is obtained by equilibrating a suspension of composition ω that is the working composition for chiral separation experiments by enantioselective cocrystallization.

Table C1: Experimental points used to plot experimental quaternary phase diagram in Figure C2.

Data points	x_R (%)	x_S (%)	$x_{S\text{-}MA}$ (%)	x_{MeCN} (%)
σ	0.0000	52.8015	47.1985	0.0000
ω	21.1158	21.1158	42.2814	15.4869
λ	31.2192	7.3021	39.3680	22.1107
Saturated solutions and eutectic lines points in equilibrium with S:S-MA	1.4023	7.5319	4.6950	86.3708
	0.9860	7.5494	4.6088	86.8558
	1.9172	5.8626	5.9382	86.2820
	1.3284	6.3784	5.3084	86.9848
	4.2518	5.3638	15.4454	74.9390
	2.4574	5.5840	12.5600	79.3985
	2.3060	5.3068	18.8339	73.5533
	2.2227	5.8160	21.8440	70.1172
	5.8500	6.2333	21.7021	66.2146
	7.3287	5.9723	18.0234	68.6756
	3.7678	5.9997	9.4729	80.7597
	1.2920	5.4151	7.2433	86.0496
	4.6727	5.6713	11.3375	78.3186
	4.7337	5.4675	17.1827	72.6160
	2.4698	4.6928	16.9431	75.8944
	5.5479	6.0397	19.7218	68.6906
	4.1024	5.2461	21.8081	68.8435
	11.9746	8.0933	29.7756	50.1564
	21.2523	8.3466	35.9366	34.4645
	18.3285	7.9962	35.0619	38.6134
	15.2013	7.8634	31.6959	45.2394
	12.4334	7.6268	24.0435	55.8963
	20.8665	8.3482	32.7688	38.0165
	19.2191	7.5621	32.7945	40.4244
	15.3100	7.1954	29.0794	48.4152
	11.7551	7.5912	25.4855	55.1682
	21.0639	7.7823	30.8293	40.3245
	19.8814	7.9287	30.0278	42.1622
	14.1244	7.2051	22.9249	55.7456
	11.2756	6.2095	17.9976	64.5173
	11.1695	6.9818	19.4376	62.4111
	12.1071	6.4331	25.8924	55.5673
	12.6744	8.0380	26.6074	52.6803
	9.6486	7.2364	29.0553	54.0597
	26.0507	7.5496	35.0703	31.3295
	26.9674	6.8453	36.1772	30.0101
	29.8538	8.2206	37.6417	24.2839
	26.9534	6.9641	36.7273	29.3552
	26.5973	10.0285	35.7538	27.6204
	25.0832	9.5424	35.8476	29.5269
	24.3635	10.1786	35.1083	30.3496

	31.2192	7.3021	39.3680	22.1107
	27.3299	7.0277	37.2858	28.3566
	0.0000	52.8015	47.1985	0.0000
	0.0000	5.0445	5.1772	89.7784
	0.0000	5.3056	12.7829	81.9114
	0.0000	4.9079	13.4789	81.6132
	0.0000	5.0247	14.3873	80.5880
	0.0000	5.0776	15.6677	79.2547
	0.0000	5.0742	15.6396	79.2862
	0.0000	5.1608	16.1348	78.7044
	0.0000	5.1583	16.4270	78.4147
	0.0000	5.3004	17.3434	77.3562
	0.0000	5.2982	18.8045	75.8973
	0.0000	5.6434	19.9834	74.3731
	0.0000	5.7946	20.5114	73.6940
	0.0000	5.7742	20.4590	73.7668
	0.0000	5.8892	20.6630	73.4478
	0.0000	5.8816	20.7063	73.4121
	0.0000	5.3257	17.5479	77.1264
	0.0000	5.1767	16.9277	77.8956
	0.0000	5.5859	19.3115	75.1027
	0.0000	6.5101	4.4538	89.0361
	0.0000	7.8395	4.6933	87.4672
	0.0000	7.0809	4.6861	88.2330
	0.0000	6.5844	4.7802	88.6354
	0.0000	5.9731	5.4538	88.5731
	0.0000	5.4075	5.9985	88.5941
	0.0000	5.4956	7.2938	87.2107
	0.0000	4.5090	7.2481	88.2428
	0.0000	4.8400	8.6602	86.4998
	0.0000	4.6056	9.3581	86.0363
	0.0000	4.7073	10.4935	84.7992
	0.0000	7.4679	4.2372	88.2949
	0.0000	5.9693	21.1536	72.8772
	0.0000	7.4693	4.2369	88.2938
	1.1860	7.2605	4.7035	86.8501
	1.0201	7.9855	4.7408	86.2536
	0.8043	8.6792	5.7700	84.7466
	0.6455	8.3970	5.5693	85.3883
	0.7300	8.8115	6.3273	84.1312
	0.7644	9.2033	6.7519	83.2804
	0.5705	9.5001	6.8669	83.0625
	1.3585	6.9378	5.1312	86.5726
	1.3785	7.7130	4.7423	86.1663
	10.3201	5.6019	16.3556	67.7225
	6.0197	4.8175	10.0752	79.0876

	7.7280	5.7153	12.7598	73.7969
	13.2359	7.8136	20.8811	58.0694
	8.1051	5.2137	12.1804	74.5008
	9.5009	5.4346	14.1724	70.8922
	9.8568	5.8096	15.1643	69.1693
	13.3915	6.5923	20.5751	59.4411
	9.6063	6.9883	29.3754	54.0301

C3 – Enantioselective Cocrystallization Batches Results

This section summarises the results of the enantioselective cocrystallization batches (ω_1 to ω_6) performed at the theoretical working composition ω. Table C2 displays the experimental masses that lead to the preparation of the initial compositions with care taken for repeatability. Figure C3 represents the XRPD patterns results for the final solid isolated in each batch. The washing protocols tried are discussed by referring to Table C3 information, and Figure C4 that shows as examples the visual aspect of wet final solids obtained for batches ω_1 to ω_3.

Table C2: Experimental ω compositions prepared for enantioselective cocrystallization batches experiments.

	Experimental masses for $\boldsymbol{\omega}$			**Overall composition $\boldsymbol{\omega}$ mass fractions**			
	m_{RS} (g)	**$m_{S\text{-}MA}$ (g)**	**m_{MeCN} (g)**	**x_R (%)**	**x_S (%)**	**$x_{S\text{-}MA}$ (%)**	**x_{MeCN} (%)**
$\boldsymbol{\omega}$				21.12	21.12	42.28	15.48
$\boldsymbol{\omega_1}$	10.7169	10.7291	3.9265	21.12	21.12	42.29	15.48
$\boldsymbol{\omega_2}$	10.7166	10.7297	3.9114	21.13	21.13	42.31	15.42
$\boldsymbol{\omega_3}$	10.7184	10.7290	3.9130	21.13	21.13	42.31	15.43
$\boldsymbol{\omega_4}$	10.7170	10.7302	3.9127	21.13	21.13	42.31	15.43
$\boldsymbol{\omega_5}$	10.7183	10.7316	3.9125	21.13	21.13	42.31	15.43
$\boldsymbol{\omega_6}$	10.7169	10.7301	3.9097	21.13	21.13	42.32	15.42

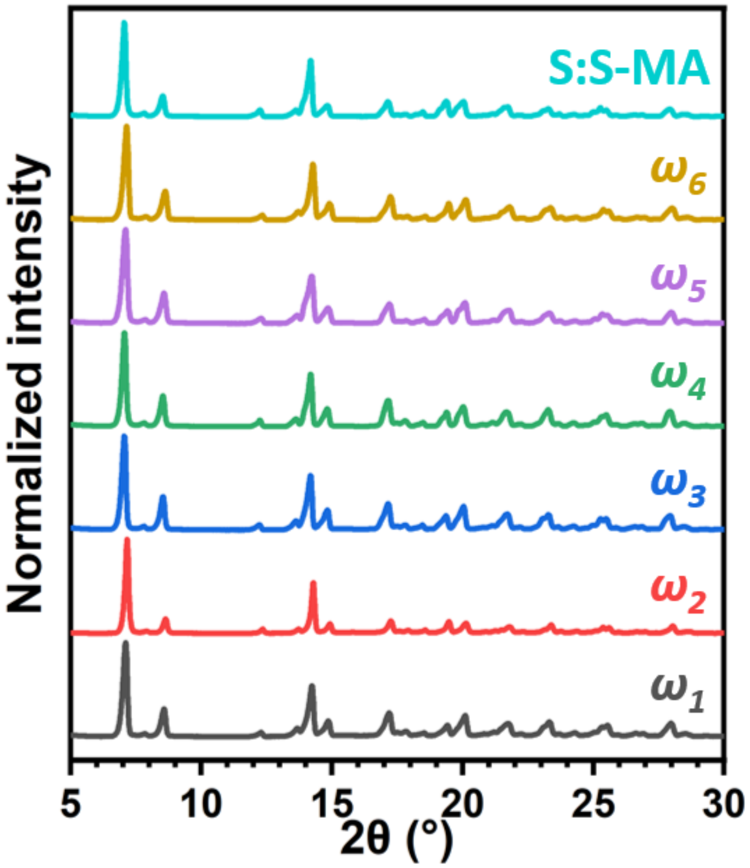

Figure C3: XRPD patterns for solid recovered from cocrystallization batches at composition ω, compared to the reference pattern of pure S:S-MA, that is the desired solid.

Washing protocols

Table C3 summarises the washing protocols tried for all batches and the results in terms of final solids obtained. The batches ω_1, ω_2, and ω_3 present final solids with a wet visual aspect. Despite 1 week drying at 50°C and no mass change measured, the solids continued to appear wet and agglomerated as shown in picture in Figure C4. Moreover, m_{solid}^{exp} measured for batches ω_2 and ω_3 is above $m_{S:S-MA}^{max}$, which is impossible if a pure and dry S:S-MA solid is obtained. These values confirm the presence of remaining liquor, also identified in final solid compositions measured. Therefore, these batches fail the chiral resolution because of inappropriate washing conditions. Indeed, only one washing was performed for ω_1 with $1\ \times 1.5V\ (30\text{mL})$ of MeCN at 9°C. This batch was the trial composition and highlight a risk of redissolution of the crystallized material during the washing. Because of a short equilibration time inducing small particle size, and a large amount of solvent required to rinse the viscous liquor, a notable mass loss of crystals was observed during the washing, which is verified by a low quantity of m_{solid}^{exp} obtained. An alternative method is applied for batch ω_2, in which we use filter papers between a press to remove the liquor until the filter paper does not show sign of liquid absorption. This proved to unsuccessful in removing the liquor. Batch ω_2 was equilibrated for a considerably longer time than batch ω_1, with an increase in the size of particles obtained. For batch ω_3, a long equilibration time is also performed but this time $1\ \times V\ (20\text{mL})$ of MeCN at 9°C is used. Results show less dissolution during the washing, confirmed by a higher quantity of m_{solid}^{exp} obtained. The visual aspect and the solid composition indicate that liquor is still present in the final solid. For the batches ω_4, ω_5, and ω_6, a larger amount of washing solvent is used by doing washes with $2\ \times V\ (20\text{mL})$ of MeCN.

Nevertheless, to avoid dissolution of the crystals, the washing fractions are kept in a freezer where they equilibrate to a temperature of about -10°C. This strategy is successful and allows to obtain pure S:S-MA, separated from the liquor, as highlighted by the completely dried solids and the solids composition measured. The crystallization yield $Y(\%)$ is higher than 90%, underlining only a small loss of solid during this washing protocol. Using two times the suspension volume V as a washing volume with MeCN at -10°C is therefore a satisfactory protocol to guarantee the purity of the final solid.

Table C3: Processes conditions and outcomes for the batch-wise cocrystallization experiments at overall compositions ω_i. The experimental volume V of the composition ω is of 20 mL in our experiments.

Batch	**Equilibration time of ω at 9°C**	**Washing protocol**	**Solid identification by XRPD**	**Final solid visual aspect**
$\boldsymbol{\omega_1}$	3h	1 x 1.5V MeCN 9°C	S:S-MA	Slightly wet
$\boldsymbol{\omega_2}$	>72h	Remaining solution absorbed between pressed filter papers	S:S-MA	Very wet
$\boldsymbol{\omega_3}$	>72h	1 x V MeCN 9°C	S:S-MA	Slightly wet
$\boldsymbol{\omega_4}$	>72h	2 x V MeCN -10°C	S:S-MA	Dry solid
$\boldsymbol{\omega_5}$	48h	2 x V MeCN -10°C	S:S-MA	Dry solid
$\boldsymbol{\omega_6}$	24h	2 x V MeCN -10°C	S:S-MA	Dry solid

Figure C4: Pictures of obtained solids from batches ω_1 and ω_2 that present a wet aspect as they are not completely washed from their viscous liquor. While ω_1 is described as slightly wet as it presents small agglomeration, ω_2 is characterized as very wet as large agglomerates can be observed.

C4 – Solubility Measurements Results

The solubility curves for (S)-mandelic acid (S-MA) and Levetiracetam (S) were measure in acetone, ethyl acetate and 1,4-dioxane. Table C4 summarises the experimental measurement that are used in the Van ‘t Hoff plots, and Table C5 reports the parameters of the fitted lines equations that are obtained. The latter are used to extrapolate solubility calculations at different temperatures.

Table C4: Experimental solubilities measured with Crystal16 used in Van’ t Hoff plots.

Compound	Solvent	Molar fraction X	Average T_{sat} (K)	ln X*	1/T (K^{-1})
S-MA	Acetone	0.1847	278.6	-1.689	0.003590
		0.2121	288.4	-1.551	0.003467
		0.2360	297.6	-1.444	0.003360
		0.2163	290.4	-1.531	0.003443
		0.2655	305.5	-1.326	0.003274
	Ethyl acetate	0.0974	296.5	-2.329	0.003373
		0.1323	309.6	-2.023	0.003230
		0.1514	318.5	-1.888	0.003140
		0.0981	297.8	-2.322	0.003359
		0.1150	304.1	-2.163	0.003288
		0.1356	310.8	-1.998	0.003218
		0.1550	316.5	-1.864	0.003159
	1,4-dioxane	0.3250	301.0	-1.124	0.003323
		0.3383	301.9	-1.084	0.003312
		0.3503	308.8	-1.049	0.003238
		0.3614	312.5	-1.018	0.003200
		0.3742	317.3	-0.983	0.003152
		0.3834	320.0	-0.959	0.003125
		0.3971	325.0	-0.923	0.003077
		0.4004	326.6	-0.915	0.003062
S	Acetone	0.0122	289.5	-4.403	0.003454
		0.0173	296.6	-4.057	0.003372
		0.0215	302.2	-3.842	0.003309
		0.0256	306.1	-3.666	0.003267
		0.0138	291.7	-4.282	0.003428
		0.0180	298.0	-4.020	0.003356
		0.0233	304.4	-3.759	0.003285
		0.0264	307.1	-3.635	0.003256
	Ethyl acetate	0.0183	320.2	-4.001	0.003123
		0.0204	322.1	-3.894	0.003105
		0.0230	324.2	-3.774	0.003084
		0.0244	325.7	-3.712	0.003070
		0.0103	308.5	-4.574	0.003242
		0.0124	312.6	-4.389	0.003199
		0.0147	315.6	-4.219	0.003168
		0.0162	317.4	-4.122	0.003150
	1,4-dioxane	0.0345	305.5	-3.365	0.003274
		0.0403	308.3	-3.212	0.003244

		0.0455	310.9	-3.091	0.003217
		0.0500	313.3	-2.995	0.003192
		0.0539	314.5	-2.921	0.003180
		0.0588	316.3	-2.834	0.003162
		0.0624	317.7	-2.775	0.003148
		0.0668	319.1	-2.707	0.003134

Table C5: Fitted line parameters for Van't hoff plots ($\ln X^* = \mathrm{a} \times \frac{1}{T} + \mathrm{b}$).

Compound	Solvent	a	b	R²
Levetiracetam (S)	Acetone	-3819.9	8.8044	0.9982
	Ethyl acetate	-5103.3	11.953	0.9985
	1,4-dioxane	-4667.2	11.918	0.9988
(S)-Mandelic acid (S-MA)	Acetone	-1129.6	2.3628	0.9968
	Ethyl acetate	-2085.6	4.6997	0.9868
	1,4-dioxane	-750.11	1.3832	0.9862

C5 – Eutectic Points E Estimations with Equilibration Method

Table C6: Eutectic points *E* estimations in acetone and ethyl acetate at 5°C. Suspensions in the triphasic domain equilibrating S and S:S-MA with a solution of eutectic composition *E* are equilibrated for 14 days. The saturated solutions are sampled and evaporated. The residue is dissolved in a known amount of solvent, and the solution composition is determined by UV-CD spectroscopy models using PLS calibrations for components quantification. From gravimetry and spectroscopy results, the saturated liquid compositions are computed. The nature of the solids in equilibrium is determined by XRPD and confirms S and S:S-MA in suspension. The eutectic points *E* are estimated from the centroid values of the five liquids, and their standard deviation σ in Euclidean distance to all points are computed.

	Suspensions compositions			**Evaporation of saturated solution**		**Dissolution of residue for analysis**		**UV-CD models quantification**		**Saturated liquid compositions**		
	x_S (%)	$x_{S\text{-}MA}$ (%)	$x_{solvent}$ (%)	$m_{residue}$ (mg)	$m_{solvent}$ (mg)	m_{MeCN} (mg)	m_{total} (mg)	x_S	$x_{S\text{-}MA}$	x_S (%)	$x_{S\text{-}MA}$ (%)	$x_{solvent}$ (%)
Acetone 5°C	36.10	24.40	39.50	24.4	127.4	7856	7880.4	0.001218	0.001858	6.33	9.66	84.02
	35.78	25.46	38.76	30.3	168	7779.1	7809.4	0.001480	0.002336	5.84	9.22	84.94
	35.80	26.47	37.73	22.1	118.7	7751	7773.1	0.001127	0.001696	6.23	9.37	84.40
	35.15	28.23	36.62	27.8	149.1	7746.6	7774.4	0.001389	0.002217	6.10	9.73	84.17
	34.62	29.35	36.03	30.5	164.8	7668.3	7698.8	0.001552	0.002352	6.13	9.29	84.58
	Eutectic point *E* estimation								**Centroid**	6.13	9.45	84.42
									σ	0.41		
Ethyl acetate 5°C	x_S (%)	$x_{S\text{-}MA}$ (%)	$x_{solvent}$ (%)	$m_{residue}$ (mg)	$m_{solvent}$ (mg)	m_{MeCN} (mg)	m_{total} (mg)	x_S	$x_{S\text{-}MA}$	x_S (%)	$x_{S\text{-}MA}$ (%)	$x_{solvent}$ (%)
	23.82	12.35	63.83	5.4	153.9	3306.8	3312.2	0.000720	0.000842	1.50	1.75	96.75
	24.35	12.35	63.30	7.7	230.5	3920.8	3928.5	0.000911	0.001117	1.50	1.84	96.66
	23.95	15.37	60.67	5.4	168.5	3926	3931.4	0.000549	0.000701	1.24	1.59	97.17
	23.57	17.58	58.85	4.8	162	3864.9	3869.7	0.000556	0.000676	1.29	1.57	97.14
	23.97	17.93	58.10	4.6	157.6	4192.7	4197.3	0.000514	0.000615	1.33	1.59	97.08
	Eutectic point *E* estimation								**Centroid**	1.37	1.67	96.96
									σ	0.26		

C6 – Detection of Deconstruction Point D with Online Raman Spectroscopy

Table C7: Compositions from the solvent addition line that lead to the estimation of point *D'*.

Composition	$V_{acetone}$ (mL)	x_S (%)	$x_{S\text{-}MA}$ (%)	$x_{acetone}$ (%)	$m_{\mathrm{suspension}}$ (g)
1	7	17.86	15.96	66.18	8.2983
2	10	13.91	12.43	73.66	10.6521
3	12	12.12	10.84	77.04	12.2213
4	14	10.74	9.60	79.65	13.7905
5 (D)'	16	9.65	8.62	81.73	15.3597
6	18	8.75	7.82	83.42	16.9289
7 (F)	30	5.62	5.03	89.35	26.3441

Appendix D - Supporting Information of Chapter 6

Supporting Information of Chapter 6: “Cocrystallization Opportunities for Chiral Resolution of Racemic Compounds”

Maxime D. Charpentier[1], Karen Johnston[2], Joop H. ter Horst[1,3]

1. EPSRC Centre for Innovative Manufacturing in Continuous Manufacturing and Crystallization (CMAC), Strathclyde Institute of Pharmacy and Biomedical Sciences (SIPBS), University of Strathclyde

2. Department of Chemical and Process Engineering, University of Strathclyde, James Weir Building, 75 Montrose Street, Glasgow G1 1XJ, U.K.

3. Univ Rouen Normandie, Laboratoire Sciences et Méthodes Séparatives (SMS), UR 3233, F-76000 Rouen, France

Table of contents

D1 – Thermal Database of Chiral Systems

Table D4: Thermal database of chiral systems with their IUPAC names, usual names, stable crystallization equilibria (conglomerate or racemic compound), enantiopure melting temperature T_R^f, stable racemic mixture melting temperature $T_{0.5}^f$, enantiopure melting enthalpy ΔH_R^f, and stable racemic mixture melting enthalpy $\Delta H_{0.5}^f$. When available, the corresponding space groups are indicated.

IUPAC name	Usual name	Stable equilibrium	Enantiopure data			Racemic mixture data			Source
			T_R^f (K)	ΔH_R^f (kJ/mol)	Space group	$T_{0.5}^f$ (K)	$\Delta H_{0.5}^f$ (kJ/mol)	Space group	
(3S)-(3-Fluorophenyl)-3-hydroxy propanoic acid	3-(3-fluorophenyl) hydracrylic acid	Conglomerate	311	24.27	$P2_1$	290	20.5	[redacted]	[1]
(+)-3-(4-chlorophenyl)-3-hydroxypropanoic acid	3-(4-Chlorophenyl)-hydracrylic acid	Conglomerate	385	29.7064	$P2_1$	357	28.0328	[redacted]	[1]
(S)-3-(4-Bromophenyl)-3-hydroxypropanoic acid	3-(4-Bromophenyl)-hydracrylic acid	Conglomerate	398	35.564	$P2_1$	371	28.8696	[redacted]	[1]
1(R),2(R)-1,2-diphenylethane-1,2-diol	Hydrobenzoin	Conglomerate	419.5	33.47	$P2_1$	394	30.12	[redacted]	[2]
1,7,7-trimethyl-3-[(4-methoxyphenyl)methylidene]bicyclo[2.2.1]heptan-2-one	Anisylidencampher	Conglomerate	399.5	30.12	$P2_12_12_1$	371.5	26.4	[redacted]	[1]
(S)-Fluoro-methyl-naphtalen-phenyl-1-ysilane		Conglomerate	340.5	23.4304	$P2_12_12_1$	312	22.5936	[redacted]	[1]
(R,S)-N-Methylephedrine	Methylephedrine	Conglomerate	361.2	30.5593	$P2_12_12_1$	335.9	26.6019	[redacted]	[3]
(S)-2-(2-Chlorophenyl)-2-(methylamino)-cyclohexanone	Ketamine	Conglomerate	394.1	26.6	$P2_12_12_1$	365.7		[redacted]	[4]
(S)-2-Hydroxy-3-phenylpropanoic acid	3-Phenyllactic acid	Conglomerate	395.25	30.5	$P2_12_12_1$	367.95	30.5	[redacted]	[5]
(2S)-1-butyl-N-(2,6-dimethylphenyl)piperidine-2-carboxamide	Levobupivacaine/ Bupivacaine	Conglomerate	413.1	26.25	$P2_12_12_1$	376.1	19.35	[redacted]	[6]

(R)-2-acetamido-4 -methylpentanoic acid	N-Acetyl-leucine	Conglomerate	453.65	31.5	$P2_12_12_1$	431.45		[redacted]	7
(S)-[6-(5-chloropyridin-2-yl)-5-oxo-7H-pyrrolo[3,4-b]pyrazin-7- yl]4-methylpipera zine-1- carboxylate	Zoplicone	Conglomerate	480	36.55	$P2_12_12_1$	446		[redacted]	8
3-(3-Fluorophenyl)-3-hydroxy propanoic acid	3-(3-Fluorophenyl) hydracrylic acid	Conglomerate	311	24.2672		290	20.5016	[redacted]	1
2-(4-methoxyphenyl)-1-phenylpropan-1-one	a-methyl-4-methoxy deoxybenzoin	Conglomerate	353	26.3592		326	21.7568	[redacted]	1
(1S,2S)-1,2-dichloro-1,2-dihydroacenaphthylene		Conglomerate	375	21.3384		339	20.5016	[redacted]	1
(R)-3-Hydroxy-3-phenylpropanoic acid	3-Phenyl hydracrylic acid	Conglomerate	391	32.6352		366	29.7064	[redacted]	1
1,7,7-trimethyl-3-[(4-methoxyphenyl)methylidene]bicyclo[2.2.1]heptan-2-one	Anisylidene-camphor	Conglomerate	399.5	30.1248		371.5	26.3592	[redacted]	1
(S)-4-Hydroxy-2-pyrrolidone		Conglomerate	429.7	28.493		394.7	26.7358	[redacted]	3
(3S)-3-hydroxy-2,2-dimethyl-3-phenylpropanoic acid		Conglomerate	431	39.748		407	37.2376	[redacted]	1
(2S,3S)-2acetamido-N,3-dimethylpentanimde	N-acetyl-isoleucine-N'-methylamide	Conglomerate	525.7	38.13		482	27.13	[redacted]	9
(1S,2S)-2-methylamino-1-phenylpropan-1-ol; hydrosulfide	Pseudoephedrine; hydrosulfide	Conglomerate	404.35	36.6184		381.35	32.5055	[redacted]	1, 3
(S)-1-[2-(3,4-dimethoxyphenyl)ethylamino]-3-(3-methylphenoxy)propan-2-ol; hydrochloride	Bevantolol; hydrochloride	Conglomerate	427.9	46.1498	C2	407.7	40.5006	[redacted]	3, 10, 11

(2S)-2-acetamido-3-methylbutanoic acid	N-acetyl-valine-N'-methylamide	Racemic compound	531.3	34.07		496.7	37.23	P-1	[9]
(-)5-(2-Hydroxypropan-2-yl)-2-methylcyclohex-2-en-1-ol	cis-Sobrerol	Racemic compound	382.9	23.1794		378.9	25.8571		[3]
(2R)-2-(4-Fluorophenyl)-2-hydroxyacetic acid	4-Fluoro mandelic acid	Racemic compound	425.9	28.8716	C2	405.9	29.644	Pbca	[1, 12]
2-(4-(2-methylpropyl)-phenyl) propanoic acid	Ibuprofen	Racemic compound	319.5	18.6996	$P2_1$	345.9	25.371	$P2_1/c$	[3, 13-16]
(1R,2S)-2-amino-1-phenyl-1-propanol	Norephedrine	Racemic compound	324.35	15.8657	$P2_1$	374.25	26.1123	$P2_1/c$	[3]
(1S,4S)-4-(3,4-Dichlorophenyl)-N-methyl-1,2,3,4-tetrahydronaphtalen-1-amine	Sertraline	Racemic compound	339.7	24.5	$P2_1$	342.7	21.44	$P2_1/n$	[17]
1-Naphthalen-1-yloxy-3-(propan-2-ylamino)propan-2-ol	Propranolol	Racemic compound	344.3	35.0271	$P2_1$	366.8	40.7754	P21/c	[3, 10, 11]
(2R)-2-Phenoxypropionic acid		Racemic compound	359	22.5936	$P2_1$	388	33.0536	A2/a	[1]
(2R)-(2-Fluorophenyl)-2-hydroxyacetic acid	2-fluoromandelic acid	Racemic compound	362.4	20.01	$P2_1$	389.2	30.5624	$P2_1/c$	[1, 12]
(2R)-(2-Chlorophenyl)(hydroxy)acetic acid	2-chloromandelic acid	Racemic compound	363.45	25	$P2_1$	391.85	23.87	$P2_1/c$	[18]
(-)-2-hydroxybutanedioic acid	Malic acid	Racemic compound	373.1	26.477	$P2_1$	401.6	31.9128	$P2_1/c$	[19, 20]
(S)-(3-chlorophenyl)(hydroxy)acetic acid	3-chloromandelic acid	Racemic compound	379.7	24.7746	$P2_1$	388.7	26.1357	$P2_1/c$	[21, 22]

(3R)-3-(4-Fluorophenyl)-3-hydroxypropanoic acid	3-(4-fluorophenyl)hydracrylic acid	Racemic compound	381	30.9616	$P2_1$	362	27.6144	$Pna2_1$	[1]
(S)-2-(2-oxopyrrolidin-1-yl)butanamide	Levetiracetam	Racemic compound	389.3	27.2334	$P2_1$	392.5	31.1482	$P2_1/c$	[16, 23-26]
(2R)-2-(3-fluorophenyl)-2-hydroxyacetic acid	3-Fluoromandelic acid	Racemic compound	394.1	23.2836	$P2_1$	369.2	22.8428	$P2_1/c$	[1]
(S)-(+)-2-Hydroxy-2-phenylacetic acid	Mandelic acid	Racemic compound	404.7	24.5	$P2_1$	393.3	25.8562	$P2_1/c$	[3, 27, 28]
(+)-2-(6-methoxynaphthalen-2-yl) propanoic acid	Naproxen	Racemic compound	429.3	31.7	$P2_1$	428.9	33.2	Pbca	[16, 29]
(S)-7-(2,3-Dihydroxypropyl)-1,3-dimethylpurine-2,6-dione	Diprophylline	Racemic compound	437.5	31.7	$P2_1$	433.1	32.8	$P2_1/c$	[30]
4-[(2S)-2-(3,5-dioxopiperazin-1-yl)propyl]piperazine-2,6-dione	Dexrazoxane	Racemic compound	467.5	37.8234	$P2_1$	507.3	44.978		[3]
(2R)-1-Naphthalen-1-yloxy-3-(propan-2-ylamino)propan-2-ol; hydrochloride	Propranolol; Hydrochloride	Racemic compound	467.7	33.31	$P2_1$	435.8	29.83	$P2_1/c$	[3, 10, 31-33]
(1R,2S)-2-(Methylamino)-1-phenylpropan-1-ol	Ephedrine	Racemic compound	312.9	17.3259	$P2_12_12_1$	350.7	29.0913		[3]
(2S)-2-(3-benzoylphenyl)propanoic acid	Ketoprofen	Racemic compound	345.4	14.6858	$P2_12_12_1$	367.2	20.9618	P-1	[16, 34, 35]
(4S)-(2-methylpropyl)-1,3-oxazolidine-2,5-dione	N-Carboxyleucine anhydride	Racemic compound	349.15		$P2_12_12_1$	321.15		$P2_1/a$	[36]
(3S)-3-(3-Bromophenyl)-3-hydroxypropanoic acid	3-(3-Bromophenyl)hydracrylic acid	Racemic compound	350	23.85	$P2_12_12_1$	349	6.78	$P2_1/c$	

(+)-(2S,3S)-Phenylglyceric acid		Racemic compound	371.5	23.4304	$P2_12_12_1$	395	31.38		[1]
(+)-2-Methylamino-1-phenylpropan-1-ol	Pseudoephedrine	Racemic compound	392.35	31.95	$P2_12_12_1$	391.05	34.1		[3]
N-[[(2S)-1-ethylpyrrolidin-2-yl]methyl]-2-methoxy-5-sulfamoylbenzamide	Sulpiride	Racemic compound	459.5	42.0074	$P2_12_12_1$	450.9	46.1495	P-1	[3]
1-(Propan-2-ylamino)-3-(2-prop-2-enyphenoxy)propan-2-ol	Alprenolol	Racemic compound	298.5	23.7819		331.1	35.6142		[3]
alpha-2-(1-Naphthyl)propanoic acid		Racemic compound	342	14.2256		422.5	30.5432	$P2_1/c$	[1, 37]
(3R)-(2-Fluorophenyl)-3- hydroxy propanoic acid		Racemic compound	348	22.5936		342	27.196		[1]
(-)-1-[2-(3,4-Dimethoxyphenyl)ethylamino]-3-(3-methylphenoxy)propan-2- ol	Bevantolol	Racemic compound	348.25	44.2104		360.55	45.8985		[3, 10, 11]
3-(3-Bromo-3-phenyl)-3-hydroxy propanoic acid	3-(3-Bromophenyl) hydracrylic acid	Racemic compound	350	23.8488		349	26.7776		[1]
1,5-Dichloro-9,10-dihydro-9,10-ethano anthracene		Racemic compound	353.5	12.552		424	27.6144		[1]
(S,S)-3,5- Dimercaptoheptanedioic acid	2',6'-pipecoloxylidide	Racemic compound	355	20.92		429	39.33		[1]
3,5-imercaptoheptanedioic acid	Methylenebis-thiopropanoic acid	Racemic compound	355	20.92		429	39.3296		[1]
beta-3-Hydroxy-3-phenylbutanoic acid		Racemic compound	357	22.5936		330	19.6648		[1]
2R-Chloro-3-methyl-2-phenoxy propionic acid		Racemic compound	359.5	22.1752		391.5	30.5432		[1]

(2R)-4-Nitro-2-phenoxypropionic acid		Racemic compound	362	20.92		412	31.22		[1]
4-Nitro 2-phenoxy propionic acid		Racemic compound	362	20.92		411.5	32.2168		[1]
9,10-Dihydro-9,10ethano-11,12-dicarbomethoxyanthracene		Racemic compound	363	16.736		380	23.4304		[1]
2-(3-Chlorophenyl)-2-hydroxy acetic acid	3-chloromandelic acid	Racemic compound	366.9	21.1951		379.7	20.9468		[21]
(+)-2-(3-Chlorophenoxy)-propionic acid		Racemic compound	367.5	29.71		386	33.05	C2/c	[38]
2-(m-Chlorophenoxy) propanoic acid		Racemic compound	367.5	29.7064		386	33.0536		[1]
3-(m-Chlorophenyl)-3-hydroxy propanoic acid	3-(m-Chlorophenyl) hydracrylic acid	Racemic compound	368	28.0328		340	23.8488		[1]
(+)-2-(2-Chlorophenoxy)-propionic acid		Racemic compound	369	26.7776		388	32.2168	$P2_1/n$	[1]
(1S,3E,4R)-3-benzylidene-1,7,7-trimethylbicyclo[2.2.1]heptan-2-one	Benzylidene camphor	Racemic compound	371	23.4304		350.5	23.012		[1]
2S-Dimethyl-diacetyl tartaric acid		Racemic compound	377.5	27.196		357.5	27.6144	$P2_1/c$	[1]
(3R)-3-Hydroxy-3-phenylpentanoic acid		Racemic compound	379	30.9616		384	35.1456		[1]
2-(4-Chlorophenyl)-2-hydroxy acetic acid	4-chloromandelic acid	Racemic compound	379.3	19.6272		383.7	22.9373		[21]
2-(2-Chlorophenyl)-2-hydroxy acetic acid	2-chloromandelic acid	Racemic compound	379.9	20.6774		345.5	19.909		[21]

(2R)-2-(4-bromo phenoxy) propanoic acid		Racemic compound	380	27.6144		385	31.7984		[1]
(R,S)-2-[(2-aminoethoxy)methyl]-4-(2-chlorophenyl)-ethoxycarbonyl-5-methoxycarbonyl-6-methyl-1,4-dihydropyridine	Amlodipine	Racemic compound	384.2	16.86		414.3	20.22		[39]
9,10-Dimethyl-9,10 dihydro-9,10- ethano-11,12-dicarbomethoxyanthracene trans		Racemic compound	393	18.828		465	41.0032		[1]
2-(2-chlorophenyl)-2-hydroxy acetic acid	2-chloromandelic acid	Racemic compound	393.5	24.9969		363.6	23.8698		[18, 21, 40]
(2R)-2-(4-Chlorophenyl)-2-hydroxy acetic acid	4-chloromandelic acid	Racemic compound	394.7	21.04		394.75	27.2542	P-1	[21]
(S)-N-(2,6-dimethylphenyl)-1-piperidine-2-carboxamide		Racemic compound	403.1	24.19		385.1	23.13		[6]
11,12-Di(hydroxymethyl)-9,10-dihydro-9,10-ethanoanthracene		Racemic compound	405.5	23.8488		474.5	41.2124		[1]
(2S)-N-(2,6-dimethylphenyl)-1-ethylpiperidine-2-carboxamide		Racemic compound	408.1	19.9		405.1	18.1		[6]
Dibenzoylmethyl-tartaric acid		Racemic compound	409	46.024		422.5	48.9528		[1]
(2S)-N-(2,6-dimethylphenyl)-1-propylpiperidine-2-carboxamide	Ropivacaine	Racemic compound	414.1	44.5		391.15	23.8		[6]
1,2-Dibromoacenaphtene/5,6-Dibromoacenaphthene		Racemic compound	416	26.3592		397	25.104	$P2_1/n$	[1]
5-O-ethyl 3-O-methyl (4R)-4-(2,3-dichlorophenyl)-2,6-dimethyl-1,4-dihydropyridine-3,5-dicarboxylate	Felodipine	Racemic compound	417.1	25.4		416.55	31.5	$P2_1/c$	[41-43]

5-(2-Hydroxypropan-2-yl)-2-methylcyclohex-2-en-1-ol	trans-Sobrerol	Racemic compound	423.5	34.6853		404.8	34.3925			[3]
1,5-Dichloro-9,10-dihyro-9,10 ethano- 11,12-dicarbomethoxyanthracene (exo)		Racemic compound	424	23.2212		465	36.8192			[1]
(2R)-N-(2,6-dimethylphenyl)-1-methylpiperidine-2-carboxamide	Mepivacaine	Racemic compound	426.1	17.77		423.1	16.94			[6]
1,5-Dichloro-9,10-dihyro-9,10-ethano-11,12dicarbomethoxyanthracene (endo)		Racemic compound	427	24.6856		436	26.3592			[1]
(S)-2-acetamido-N,4-dimethylpentanamide	N-acetyl-leucine-N'-methylamide	Racemic compound	428.2	23.19		432.1	27.16			[9]
(2R)-5-[2-(3,4-Dimethoxyphenyl)ethyl](methyl)amino}-2-isopropyl-2-(3,4,5-trimethoxyphenyl)pentanenitrile	Gallopamil	Racemic compound	434.4	54.395		426.7	51.32			[44]
1,5-Dichloro-11,12-dihydroxymethyl-9,10-dihydro-9,10 ethanoanthracene trans (endo)		Racemic compound	435	19.6648		441	33.0536			[1]
(2R)-2-[(3-amino-2,4,6-triiodophenyl)methyl]butanoic acid	Iopanoic acid	Racemic compound	438.7	25.9826		426.9	27.6981			[3]
(3R)-2,2,3-Triphenylpentanoic acid		Racemic compound	441.5	26.7776		480	37.2376			[1]
2-acetamido-N-methylacetamide	N-acetyl-alanine-N'-methylamide	Racemic compound	454.8	23.64		411.9	15.91			[9]
(2R)-2-(1-Nitronaphthalen-2-yl)oxypropanamide		Racemic compound	461.5	30.5432		431	29.288			[1]
1-(1-Phenylethyl)thiourea		Racemic compound	471.5	35.9824		410.5	33.0536			[1]
(2S)-2-[4-(3-oxo-1H-isoindol-2-yl)phenyl]butanoic acid	Indobufen	Racemic compound	471.9	33.4		455.3	39.4			[45]

Naphtoxy-2 propionamide		Racemic compound	475	38.0744		445	37.656	$C2/c$	1
(2R)-2-[4-(3-oxo-1H-isoindol-2-yl)phenyl]propanoic acid	Indoprofen	Racemic compound	483.3	51.6542		485.5	41.94	$P2_1/n$	46, 47
11,12-Di(iodo-methyl)-9,10-dihydro-9,10-ethanoanthracene		Racemic compound	491	35.1456		468.5	33.472		1
1,5-Dichloro-11,12 dihydroxymethyl-9,10 dihydro-9,10 ethanoanthracene trans (exo)		Racemic compound	527	53.5552		519.5	53.5552		1
(2R)-1-(Propan-2-ylamino)-3-(2-prop-2-enyphenoxy) propan-2-ol; hydrochloride	Alprenolol; hydrochloride	Racemic compound	298.5	23.78		331.1	35.61	$P2_1/c$	3
2-Amino-1-phenylpropan-1-ol; hydrosulfide	Norephedrine; hydrosulfide	Racemic compound	374.5	23.2589		390.5	29.7901		3
(2S)-2-(3,4-Dimethoxyphenyl)-5-[2-(3,4-dimethoxyphenyl)ethyl-methylamino]-2-propan-2-ylpentanenitrile; hydrochloride	Verapamil; Hydrochloride	Racemic compound	408.3	40.675		416.7	64.41	P-1	44
2-(Methylamino)-1-phenylpropan-1-ol; napsylate	Ephedrine; napsylate	Racemic compound	443.7	32.9615		443.5	38.5053		3
(1S,2S)-2-amino-1-phenyl-1-propanol; hydrochloride	Norephedrine; hydrochloride	Racemic compound	445.95	20.2464	$P2_1$	469.05	28.97		3, 48
(+)-2-methylamino-1-phenylpropan-1-ol; hydrochloride	Pseudoephedrine; hydrochloride	Racemic compound	456.05	22.8083	$P2_12_12_1$	439.15	21.9111	*Pcab*	3, 49
2-(Methylamino)-1-phenylpropan-1-ol; hydrochloride	Ephedrine; hydrochloride	Racemic compound	492.3	31.7022	$P2_1$	463.9	34.928	$P2_1/a$	3
2-(cyclohexanecarbonyl)-3,6,7,11b-tetrahydro-1H-pyrazino[2,1-a]isoquinolin-4-one	Praziquantel	Racemic compound	383.75	18.4835	C2	409.35	25.7334	P-1	50

Table D5: Comparison of experimental eutectic temperatures $T_{0.5}^{f}$ and theoretical ones computed with Schröder-Van Laar equation for the 22 stable conglomerate systems.

IUPAC name	Usual name	T_R^f (K)	ΔH_R^f (kJ/mol)	$T_{0.5}^{f}$ (K)		
				Experimental	Theoretical	Absolute difference
(3S)-(3-Fluorophenyl)-3-hydroxy propanoic acid	3-(3-fluorophenyl) hydracrylic acid	311	24.27	290	289.61	0.39
(+)-3-(4-chlorophenyl)-3-hydroxypropanoic acid	3-(4-Chlorophenyl)-hydracrylic acid	385	29.7064	357	358.24	1.24
(S)-3-(4-Bromophenyl)-3-hydroxypropanoic acid	3-(4-Bromophenyl)-hydracrylic acid	398	35.564	371	373.89	2.89
1(R),2(R)-1,2-diphenylethane-1,2-diol	Hydrobenzoin	419.5	33.47	394	391.24	2.76
1,7,7-trimethyl-3-[(4-methoxyphenyl)methylidene]bicyclo[2.2.1]heptan-2-one	Anisylidencampher	399.5	30.12	371.5	371.13	0.37
(S)-Fluoro-methyl-naphtalen-phenyl-1-ysilane		340.5	23.4304	312	314.19	2.19
(R,S)-N-Methylephedrine	Methylephedrine	361.2	30.5593	335.9	338.17	2.27
(S)-2-(2-Chlorophenyl)-2-(methylamino)-cyclohexanone	Ketamine	394.1	26.6	365.7	363.10	2.60
(S)-2-Hydroxy-3-phenylpropanoic acid	3-Phenyllactic acid	395.25	30.5	367.95	367.78	0.17
	Levobupivacaine/ Bupivacaine	413.1	26.25	376.1	378.75	2.65
(R)-2-acetamido-4 -methylpentanoic acid	N-Acetyl-leucine	453.65	31.5	431.45	418.89	12.56
(S)-[6-(5-chloropyridin-2-yl)-5-oxo-7H-pyrrolo[3,4- b]pyrazin-7- yl]4-methylpiperazine-1- carboxylate	Zoplicone	480	36.55	446	446.23	0.23
3-(3-Fluorophenyl)-3-hydroxy propanoic acid	3-(3-Fluorophenyl) hydracrylic acid	311	24.2672	290	289.61	0.39

2-(4-methoxyphenyl)-1-phenylpropan-1-one	a-methyl-4-methoxy deoxybenzoin	353	26.3592	326	327.71	1.71
(1S,2S)-1,2-dichloro-1,2-dihydroacenaphthylene		375	21.3384	339	340.51	1.51
(R)-3-Hydroxy-3-phenylpropanoic acid	3-Phenyl hydracrylic acid	391	32.6352	366	365.75	0.25
1,7,7-trimethyl-3-[(4-methoxyphenyl)methylidene]bicyclo[2.2.1]heptan-2-one	Anisylidene-camphor	399.5	30.1248	371.5	371.14	0.36
(S)-4-Hydroxy-2-pyrrolidone		429.7	28.493	394.7	395.34	0.64
(3S)-3-hydroxy-2,2-dimethyl-3-phenylpropanoic acid		431	39.748	407	405.65	1.35
(2S,3S)-2acetamido-N,3-dimethylpentanimde	N-acetyl-isoleucine-N’-methylamide	525.7	38.13	482	487.01	5.01
(1S,2S)-2-methylamino-1-phenylpropan-1-ol; hydrosulfide	Pseudoephedrine; hydrosulfide	404.35	36.6184	381.35	380.16	1.19
(S)-1-[2-(3,4-dimethoxyphenyl)ethylamino]-3-(3-methylphenoxy)propan-2-ol; hydrochloride	Bevantolol; hydrochloride	427.9	46.1498	407.7	406.20	1.50
				Average		2.01
				Standard deviation		2.65

D2 – Sources for the Thermal Database

(1) Leclercq, M.; Collet, A.; Jacques, J. Etude des melanges d'antipodes optiques—XII: mesure de la stabilite des racemiques vrais. *Tetrahedron* **1976**, *32* (7), 821-828.
(2) Pennington, W. T.; Chakraborty, S.; Paul, I. C.; Curtin, D. Crystal structures of D-(+)-and meso-hydrobenzoin. Absolute direction of the dipole moment of D-and L-hydrobenzoin in the crystal and correlation with crystal morphology, pyroelectric effect, and absolute configuration. *Journal of the American Chemical Society* **1988**, *110* (19), 6498-6504.
(3) Li, Z. J.; Zell, M. T.; Munson, E. J.; Grant, D. J. Characterization of racemic species of chiral drugs using thermal analysis, thermodynamic calculation, and structural studies. *Journal of pharmaceutical sciences* **1999**, *88* (3), 337-346.
(4) Tamagawa, R. E.; Miranda, E. A.; Santana, C. C.; Giulietti, M. Determination of the Binary and Ternary Phase Diagrams of R (+)-/S (−)-Ketamine Using Differential Scanning Calorimetry. *Journal of Chemical & Engineering Data* **2009**, *54* (1), 16-21.
(5) Navare, P. S.; MacDonald, J. C. Investigation of stability and structure in three homochiral and heterochiral crystalline forms of 3-phenyllactic acid. *Crystal growth & design* **2011**, *11* (6), 2422-2428.
(6) Nemák, K.; Ács, M.; Kozma, D.; Fogassy, E. Racemic compound formation-conglomerate formation: Part 4. Optical resolution and determination of the melting phase diagrams of 2′, 6′-pipecoloxylidide and four 1-alkyl-2′, 6′-pipecoloxylidides. *Journal of Thermal Analysis and Calorimetry* **1997**, *48* (3), 691-696.
(7) Estime, N.; Pena, R.; Teychené, S.; Autret, J. M.; Biscans, B. Characterization of the conglomerate form of acetyl-dl-leucine by thermal analysis and solubility measurements. *Journal of crystal growth* **2012**, *342* (1), 28-33.
(8) Giovannini, J.; Céolin, R.; Perrin, M.-A.; Toscani, S.; Louër, D.; Leveiller, F. Polymorphism and hydration of zopiclone: Determination of crystal structures, and thermodynamic studies as a function of temperature and water vapor pressure. *Le Journal de Physique IV* **2001**, *11* (PR10), Pr10-93-Pr10-97.
(9) Badea, E.; Della Gatta, G.; Pałecz, B. Thermal properties of some small peptides (N-acetyl-amino acid-N′-methylamides) with non-polar side groups. *The Journal of Chemical Thermodynamics* **2014**, *73*, 178-182.
(10) Polenske, D.; Lorenz, H.; Seidel-Morgenstern, A. The binary phase diagram of propranolol hydrochloride and crystallization-based enantioseparation. *Journal of pharmaceutical sciences* **2010**, *99* (4), 1762-1773.
(11) Neau, S. H.; Shinwari, M. K.; Hellmuth, E. W. Melting point phase diagrams of free base and hydrochloride salts of bevantolol, pindolol and propranolol. *International journal of pharmaceutics* **1993**, *99* (2-3), 303-310.
(12) Larsen, S.; Marthi, K. Structures of the optically active monofluoro-substituted mandelic acids: Relation to their racemic counterparts and thermochemical properties. *Acta Crystallographica Section B: Structural Science* **1997**, *53* (2), 280-292.
(13) Dwivedi, S.; Sattari, S.; Jamali, F.; Mitchell, A. Ibuprofen racemate and enantiomers: phase diagram, solubility and thermodynamic studies. *International journal of pharmaceutics* **1992**, *87* (1-3), 95-104.

(14) Lerdkanchanaporn, S.; Dollimore, D.; Evans, S. J. Phase diagram for the mixtures of ibuprofen and stearic acid. *Thermochimica acta* **2001**, *367*, 1-8.
(15) Bouillot, B.; Teychené, S.; Biscans, B. An evaluation of thermodynamic models for the prediction of drug and drug-like molecule solubility in organic solvents. *Fluid Phase Equilibria* **2011**, *309* (1), 36-52.
(16) Machado, S. M.; Castro, R. A.; Maria, T. M.; Canotilho, J.; Eusébio, M. E. S. Levetiracetam+ nonsteroidal anti-inflammatory drug binary systems: A contribution to the development of new solid dosage forms. *International Journal of Pharmaceutics* **2017**, *533* (1), 1-13.
(17) He, Q.; Rohani, S.; Zhu, J.; Gomaa, H. Sertraline racemate and enantiomer: solid-state characterization, binary phase diagram, and crystal structures. *Crystal growth & design* **2010**, *10* (4), 1633-1645.
(18) He, Q.; Zhu, J.; Gomaa, H.; Jennings, M.; Rohani, S. Identification and Characterization of Solid-State Nature of 2-Chloromandelic Acid. *Journal of Pharmaceutical Sciences* **2009**, *98* (5), 1835-1844.
(19) Kotelnikova, E. N.; Isakov, A. I.; Lorenz, H. Non-equimolar discrete compounds in binary chiral systems of organic substances. *CrystEngComm* **2017**, *19* (14), 1851-1869.
(20) Jacques, J.; Collet, A.; Wilen, S. H. *Enantiomers, racemates, and resolutions*; Wiley, 1981.
(21) Kőrösi, M.; Béri, J.; Hanu, A.; Kareth, S.; Székely, E. High-pressure melting equilibrium of chiral compounds: A practical study on chlorinated mandelic acids under carbon dioxide atmosphere. *Journal of CO2 Utilization* **2020**, *37*, 173-179.
(22) Hylton, R. K.; Tizzard, G. J.; Threlfall, T. L.; Ellis, A. L.; Coles, S. J.; Seaton, C. C.; Schulze, E.; Lorenz, H.; Seidel-Morgenstern, A.; Stein, M. Are the crystal structures of enantiopure and racemic mandelic acids determined by kinetics or thermodynamics? *Journal of the American Chemical Society* **2015**, *137* (34), 11095-11104.
(23) Herman, C.; Vermylen, V.; Norberg, B.; Wouters, J.; Leyssens, T. The importance of screening solid-state phases of a racemic modification of a chiral drug: thermodynamic and structural characterization of solid-state phases of etiracetam. *Acta Crystallographica Section B: Structural Science, Crystal Engineering and Materials* **2013**, *69* (4), 371-378.
(24) Herman, C.; Leyssens, T.; Vermylen, V.; Halloin, V.; Haut, B. A new approach for the estimation of the melting enthalpy of metastable crystalline compounds using differential scanning calorimetry: Application to the two crystallographic forms of Etiracetam. *Journal of thermal analysis and calorimetry* **2012**, *107* (2), 777-788.
(25) Herman, C.; Haut, B.; Aerts, L.; Leyssens, T. Solid–liquid phase diagrams for the determination of the solid state nature of both polymorphs of (RS)-2-(2-oxo-pyrrolidin-1-yl)-butyramide. *International journal of pharmaceutics* **2012**, *437* (1-2), 156-161.
(26) Herman, C.; Leyssens, T.; Vermylen, V.; Halloin, V.; Haut, B. Towards an accurate and precise determination of the solid–solid transition temperature of enantiotropic systems. *The Journal of Chemical Thermodynamics* **2011**, *43* (5), 677-682.
(27) Emel'yanenko, V. N.; Turovtsev, V. V.; Fedina, Y. A. Experimental and theoretical thermodynamic properties of RS-(±)-and S-(+)-mandelic acids. *Thermochimica Acta* **2018**, *665*, 37-42.

(28) Lorenz, H.; Sapoundjiev, D.; Seidel-Morgenstern, A. Enantiomeric mandelic acid system melting point phase diagram and solubility in water. *Journal of Chemical & Engineering Data* **2002**, *47* (5), 1280-1284.

(29) Braun, D. E.; Ardid-Candel, M.; D'Oria, E.; Karamertzanis, P. G.; Arlin, J.-B.; Florence, A. J.; Jones, A. G.; Price, S. L. Racemic naproxen: a multidisciplinary structural and thermodynamic comparison with the enantiopure form. *Crystal growth & design* **2011**, *11* (12), 5659-5669.

(30) Brandel, C.; Amharar, Y.; Rollinger, J. M.; Griesser, U. J.; Cartigny, Y.; Petit, S.; Coquerel, G. r. Impact of molecular flexibility on double polymorphism, solid solutions and chiral discrimination during crystallization of diprophylline enantiomers. *Molecular Pharmaceutics* **2013**, *10* (10), 3850-3861.

(31) Bartolomei, M.; Bertocchi, P.; Ramusino, M. C.; Signoretti, E. C. Thermal studies on the polymorphic modifications of (R, S) propranolol hydrochloride. *Thermochimica acta* **1998**, *321* (1-2), 43-52.

(32) Polenske, D.; Lorenz, H.; Seidel-Morgenstern, A. Separation of propranolol hydrochloride enantiomers by preferential crystallization: thermodynamic basis and experimental verification. *Crystal growth & design* **2007**, *7* (9), 1628-1634.

(33) Elsabee, M.; Prankerd, R. Solid-state properties of drugs. III. Differential scanning calorimetry of chiral drug mixtures existing as racemic solid solutions, racemic mixtures or racemic compounds. *International journal of pharmaceutics* **1992**, *86* (2-3), 221-230.

(34) Ravikumar, K. Non-steroidal anti-inflammatory drugs. III. Structure of indoprofen: 2-[4-(1-oxo-2-isoindolinyl) phenyl] propionic acid. *Acta Crystallographica Section C: Crystal Structure Communications* **1994**, *50* (4), 589-592.

(35) Kommuru, T. R.; Khan, M. A.; ReddyX, I. K. Racemate and enantiomers of ketoprofen: phase diagram, thermodynamic studies, skin permeability, and use of chiral permeation enhancers. *Journal of pharmaceutical sciences* **1998**, *87* (7), 833-840.

(36) Kanazawa, H. N-Carboxy-dl-leucine anhydride. *Acta Crystallographica Section E: Structure Reports Online* **2003**, *59* (9), o1309-o1311.

(37) Riis, E.; Larsen, S. 2-(1-Naphthyl) propionic acid. *Acta Crystallographica Section E: Structure Reports Online* **2005**, *61* (5), o1396-o1397.

(38) Sørensen, H. O.; Larsen, S. Hydrogen bonding in enantiomeric versus racemic mono-carboxylic acids; a case study of 2-phenoxypropionic acid. *Acta Crystallographica Section B: Structural Science* **2003**, *59* (1), 132-140.

(39) Zeng, A.; Wang, C.; Yuan, B.; Yang, G.; Fu, Q. The influence of chirality, physicochemical properties, and permeation enhancers on the transdermal permeation of amlodipine across rat skin. *Drug Development and Industrial Pharmacy* **2010**, *36* (6), 724-734.

(40) He, Q.; Rohani, S.; Zhu, J.; Gomaa, H. Crystallization of the racemic compound and conglomerate of (RS)-2-chloromandelic acid. *Crystal growth & design* **2010**, *10* (12), 5136-5145.

(41) Fossheim, R. Crystal structure of the dihydropyridine calcium antagonist felodipine. Dihydropyridine binding prerequisites assessed from crystallographic data. *Journal of medicinal chemistry* **1986**, *29* (2), 305-307.

(42) Rollinger, J. M.; Burger, A. Polymorphism of racemic felodipine and the unusual series of solid solutions in the binary system of its enantiomers. *Journal of pharmaceutical sciences* **2001**, *90* (7), 949-959.

(43) Surov, A. O.; Solanko, K. A.; Bond, A. D.; Perlovich, G. L.; Bauer-Brandl, A. Crystallization and polymorphism of felodipine. *Crystal Growth & Design* **2012**, *12* (8), 4022-4030.
(44) Rustichelli, C.; Gamberini, M. C.; Ferioli, V.; Gamberini, G. Properties of the racemic species of verapamil hydrochloride and gallopamil hydrochloride. *International journal of pharmaceutics* **1999**, *178* (1), 111-120.
(45) Vigevani, A.; Zampieri, M. Thermal behaviour, phase diagram, and spectroscopic properties of rac-indobufen and its enantiomers. *Chirality* **1995**, *7* (8), 575-579.
(46) Wassvik, C. M.; Holmén, A. G.; Bergström, C. A.; Zamora, I.; Artursson, P. Contribution of solid-state properties to the aqueous solubility of drugs. *European journal of pharmaceutical sciences* **2006**, *29* (3-4), 294-305.
(47) Pella, E.; Restelli, R. Binary phase diagram of the enantiomers of indoprofen. *Microchimica Acta* **1983**, *79* (1), 65-74.
(48) Egli, M.; Dobler, M. Structural Aspects of the Enantioselectivity of Tartrates with α-Amino-alcohol Salts. Part II. Crystal structures of (1R, 2S)-norephedrine hydrochloride and (1R, 2R)-norpseudoephedrine hydrochloride. *Helvetica chimica acta* **1989**, *72* (5), 1151-1157.
(49) Prankerd, R.; Elsabee, M. Thermal analysis of chiral drug mixtures: the DSC behavior of mixtures of ephedrine HCl and pseudoephedrine HCl enantiomers. *Thermochimica acta* **1995**, *248*, 147-160.
(50) Liu, Y.; Wang, X.; Wang, J. K.; Ching, C. B. Investigation of the phase diagrams of chiral praziquantel. *Chirality: The Pharmacological, Biological, and Chemical Consequences of Molecular Asymmetry* **2006**, *18* (4), 259-264.